Fluorescence imaging methodologies towards the study of charge transfer processes and ensuing dynamics in model lipid membranes

Aya Sakaya

A Thesis submitted to McGill University in partial fulfilment of the requirements for the degree of

Doctor of Philosophy

Department of Chemistry

McGill University, Montréal, Québec, Canada

June 2023

I dedicate this thesis

To my supermom Ghada, and my brothers Jamal and Khaled

Thank you for the endless love and support

In the memory of Jihad Sakaya

(1952 – 2005)

Abstract

Charge transfer processes are essential to both material design and applications as well as in biological functions, where precisely regulated redox reactions are central to cellular homeostasis and function. Interfacing biological systems with electronic devices through bioelectronic materials provides opportunities to manipulate interactions between biotic and abiotic surfaces, gaining insights into key biological redox reactions. However, this interface poses some key physical, chemical, and biological challenges. The complex composition of lipid membranes hinders the selective investigation of specific reactions of interest. Additionally, integrating bioelectronic materials within lipid membranes may trigger undesired chemical reactions and damage.

This thesis focuses on the development and application of platforms and tools that enable the control and accurate reporting on select redox reactions in lipid bilayers, towards the development of novel bioelectronic devices. Particularly, we report the development and benchmarking of high-sensitivity fluorescence imaging methodologies that enable the study and observation of select charge transfer processes in model lipid membranes and shed light on key resulting membrane dynamics.

We first report on the fluorescence imaging of singlet oxygen ($^1O_2$) flux and the associated lipid membrane deformation dynamics. Here, we demonstrate that a fluorogenic α-tocopherol analogue probe (H_4BPMHC) serves as a highly sensitive sensor of $^1O_2$ flux owing to its extremely efficient $^1O_2$ quenching rate constant (k_q). This high k_q results in linear zero-order reaction kinetics with $^1O_2$, accompanied by an impressive >360-fold enhancement in emission intensity, which enables straightforward and accurate determination of the flux of $^1O_2$ impinging on the lipid membrane. This $^1O_2$ flux is then correlated with the resulting membrane deformation and expansion dynamics, visualized on giant unilamellar vesicles and discussed in the context of lipid peroxidation rate and the effect of water-borne vs. membrane-borne $^1O_2$.

We next provide a platform to map α-tocopherol redox activity in supported lipid bilayers. This work involves developing and benchmarking the limits of sensitivity of an electrochemical fluorescence microscopy (ECFM) setup for the study of charge transfer through ITO-supported lipid bilayers. This setup was used to decipher and provide a molecular mechanism behind the redox transitions undergone by H_4BPMHC. We show that our ECFM setup allows for the sensitive

detection of electrochemical transitions exploiting the amplification of electron transfer processes via fluorescence, where the equivalent of femtoamperes currents leading to probe conversion can be readily recorded.

Finally, motivated by the aim of utilizing acceptor-donor-acceptor (ADA) oligomers as transmembrane molecular wires for eventual bioelectronic-interfacing applications, we investigated the molecular mechanism behind the observed photo-induced deformation and tubulation of supported lipid bilayers embedded with these ADA oligomers. We show that this membrane remodeling is $^1O_2$-mediated and occurs following the onset of lipid peroxidation. Utilizing the $^1O_2$ flux sensor reported above, we reveal a key correlation between the measured $^1O_2$ flux and the resulting membrane deformation and discuss it in the context of the membrane's response to chemical oxidative insult.

Overall, our work provides novel tools and methodologies for the control and study of charge transfer processes in lipid membranes. Our ability to selectively modulate and image these in-membrane redox reactions in real-time has allowed us to extract and correlate key kinetic and dynamic information relating to the membrane's response to precise oxidative insult. These new methodologies open the way for new investigations into the effect of select chemical and electrochemical charge transfer processes on membrane dynamics and integrity.

Résumé

Les processus de transfert de charge sont essentiels pour la conception des matériaux, leurs applications et les fonctions biologiques. Connecter des systèmes biologiques à des dispositifs électroniques à travers des matériaux bioélectroniques permet de manipuler les interactions entre les surfaces biotiques et abiotiques et d'élucider les réactions redox biologiques essentielles. Cependant, cette interface pose des défis physiques, chimiques et biologiques. La composition complexe des membranes lipidiques entrave l'étude sélective des réactions d'intérêt, et l'intégration de matériaux bioélectroniques dans les membranes lipidiques peut déclencher des réactions chimiques indésirables.

Cette thèse se concentre sur le développement et l'application d'outils permettant de contrôler et de rapporter avec précision des réactions redox dans les bicouches lipidiques, en vue de créer de nouveaux dispositifs bioélectroniques. Particulièrement, nous rapportons le développement de méthodologies d'imagerie de fluorescence à haute sensibilité pour l'étude sélective de processus de transfert de charge dans des membranes lipidiques modèles et l'élucidation des dynamiques membranaires résultantes.

Nous rapportons au départ l'imagerie par fluorescence du flux d'oxygène singulet ($^1O_2$) et des dynamiques de déformation des membranes lipidiques qui en suivent. Une sonde fluorogène analogue à l'α-tocophérol (H_4BPMHC) se révèle être un capteur très sensible du flux de $^1O_2$ grâce à sa constante de vitesse d'extinction du $^1O_2$ (k_q) élevée. Ce k_q élevé se traduit par une cinétique de réaction linéaire avec le $^1O_2$, accompagnée d'une augmentation impressionnante de l'intensité d'émission, permettant de mesurer précisément le flux de $^1O_2$ impactant la membrane lipidique. Ce flux de $^1O_2$ est corrélé aux dynamiques de déformation de la membrane, visualisée sur des vésicules unilamellaires géantes et discutée dans le contexte du taux de peroxydation des lipides et de l'origine du $^1O_2$.

Nous fournissons ensuite une plateforme pour cartographier l'activité redox de l'α-tocophérol dans les bicouches lipidiques soutenues. Ceci implique le développement et l'évaluation d'une configuration de microscopie à fluorescence électrochimique (ECFM) pour l'étude du transfert de charge à travers des bicouches lipidiques supportées par l'ITO. Ce dispositif permet de détecter et déchiffrer le mécanisme des transitions redox du H_4BPMHC avec une sensibilité élevée en exploitant l'amplification des processus de transfert d'électrons via la fluorescence, où

l'équivalent des courants femtoampères conduisant à la conversion de la sonde peuvent être enregistrés.

Enfin, motivés par notre but d'utiliser les oligomères accepteurs-donneurs-accepteurs (ADA) comme fils moléculaires transmembranaires pour d'éventuelles applications d'interfaçage bioélectronique, nous avons étudié le mécanisme moléculaire à l'origine de la déformation photo-induite observée des bicouches lipidiques supportées contenants ces oligomères. Nous montrons que le remodelage de la membrane est médié par le $^1O_2$ et se produit suite à la peroxydation des lipides. En utilisant le capteur de flux de $^1O_2$ mentionné avant, nous établissons une corrélation entre le flux de $^1O_2$ mesuré et la déformation membranaire et nous l'analysons dans le contexte de la réponse de la membrane à une attaque chimique oxydante.

En somme, cette thèse présente de nouveaux outils et méthodologies pour contrôler et étudier les processus de transfert de charge dans les membranes lipidiques. Nous pouvons moduler et visualiser en temps réel les réactions redox, nous permettant d'extraire des informations cinétiques et dynamiques clés sur la réponse de la membrane à une insulte oxydative spécifique. Ces nouvelles méthodologies ouvrent la voie à de futures recherches sur l'impact des processus de transfert de charge chimiques et électrochimiques sur la dynamique et l'intégrité des membranes.

Acknowledgements

"You should enjoy the little detours to the fullest. Because that's where you'll find things more important than what you want."
- Yoshihiro Togashi

I am eternally grateful to have taken on my PhD journey at McGill, and in the beautiful city of Montréal. I cannot and do not want to imagine how my life would have been and who I would be had I not met all the amazing people that I was fortunate to meet throughout my degree.

I am immensely grateful to my supervisor, Prof. Gonzalo Cosa. Thank you for the guidance and mentorship, for the chats over coffee, for all the "quick" hours-long discussions in your office about science and research that somehow often turned into sociological discussions, for the impromptu photophysics lessons over the whiteboard, and for never saying no when I ask you if you have time to chat. Your attention to detail and your constant questioning of every scientific statement I make has not only translated into how I conduct science but also into my daily life. Thank you for always being receptive to any disagreement with an open mind, and for being understanding and helpful in stressful situations. Finally, thank you for always being available on short notice and always making time for us even when that time didn't necessarily exist.

I would like to thank my committee members, Prof. Hanadi Sleiman and Prof. Dima Perepichka, for all their valuable guidance and feedback throughout the years. Thank you as well to Chantal, Linda, Nikoo, Chelsea, and every member of the Chemistry office and administrative team. Thank you for your contagious positivity and kindness, and for going above and beyond to make our graduate studies go as smoothly as possible. A special thank you goes to Mohini Ramkaran, not only for helping me with the AFM measurements (i.e., doing it by yourself while I watched), but also for the immensely informative teaching throughout our sessions. Your knowledge and excitement were contagious, and I still remember your teachings many years later.

I am not sure where to begin with thanking all the Cosa lab members, past and present, for making my time there truly unforgettable and for providing a wonderful working environment. Thank you, Andrés, Mayra, Kasia, Sol, Terri, Alejandro, Lana, Christina, Viktorija, Ricky, Yasser, Casey, Julia, Kevin, Anthony, Jorge, Florencia, Andy, Alex, Paty, Laiyi, Heidi, Denys, Oleksii, Morgan, and all exchange and summer students, for creating such a fun environment. Thank you

for all the birthday cakes (with clapping, please), all the outings, all the rants, and all the laughter. Thank you for providing a very supportive environment where everyone cares and strives for each other's success.

Andrés, thank you for being my scientific mentor when I first started and for teaching me the way around the (not frustrating at all) field of spectroelectrochemistry. Mayra, thank you for taking me in and being so kind and supportive throughout all the good and the bad in my first year. Thank you, Tara and José, not only for your contributions to my research but for your cherished friendship. I will forever hold dearly all those times we spent together in that dark microscope room.

I am so fortunate to have encountered amazing role models for women in science in the Cosa lab. Terri, thank you for being such a force. Your leadership, intelligence, confidence, assertiveness, and kindness are something to look up to. Thank you for always being available for a chat despite your busy schedule, for always speaking up for other people, and for being our voice of reason. Also, thank you so much for proofreading all my research chapters. Kasia, my bestie, I have learned so much from you. Thank you for always questioning the status quo, for teaching me not to settle for less than I deserve and to strive for better, for being an example of what a meticulous scientist should be like, for being so supportive and encouraging, for all the therapeutic coffee breaks and car rides (I thank you for that, miserable Montréal parking situation), and for not being afraid to question the fundamentals of our science and pushing us to be excellent researchers. Sol, my adoptive mother, I feel so lucky to have overlapped with your visits at different stages of my degree. Thank you for being so kind, welcoming, and supportive. Thank you for all the "vibras positivas" that you bring to the lab, for introducing us to clapping while singing "happy birthday", for always encouraging me and pushing me forward, for sharing my excitement of science, and overall, for being such a gentle and loving soul.

Yasser, thank you for being my scientific mentor and replacement big brother. Thank you for all the exciting conversations about science and society, for all the laughs, and for dishing out some tough love when needed. Your intelligence and work ethic are something I admire.

Thank you, Florencia and Jorge, for being the best labmates and friends anyone could wish to have. Thank you for bringing such a positive attitude and work ethic to the lab, for being so kind and supportive to everyone, for being the first to act when anything is needed, for always listening

to my rants, for providing a safe and welcoming space, for the love and laughter, and for all the empanada nights (watch out for the squirrel though).

I feel so lucky to have had the opportunity to be a part of the NSERC CREATE PROMOTE program. Although I was suspicious at first, all those networking events and workshops really were formative. In particular, I would like to thank the PROMOTE coordinator, Anne Noronha, for being a one-woman machine. Thank you so much, Anne, for taking care of every aspect of the program all by yourself and for always being kind, encouraging, supportive, and pushing us towards new opportunities. I am most thankful to the PROMOTE program for introducing me to my amazing mentor, Jida El Hajjar. Jida, you are a truly wonderful person and an amazing example of what a strong Lebanese woman can achieve.

Finally, I would love to thank my family, to whom I owe everything I have and will ever achieve. To my brothers, Jamal and Khaled, thank you for always being so loving and supportive. Jamal, I feel so lucky to have undergone this difficult PhD journey at the same time as you. It meant a lot to have someone to share all the struggles and frustrations with. Thank you for all the weekly hours-long phone calls filled with laughter, engaging conversations, and (one-sided) rants. Khaled, your warmth and kindness are truly contagious. Thank you for always providing a safe and supportive space when I needed it. Last but most definitely not least, I would like to thank my mom, Ghada, to whom I owe everything in my life. You are the strongest woman I have ever met. You single-handedly raised three young kids despite immense personal pain and grief. You sacrificed everything to make sure we have the best life possible. You are my definition of a superwoman. You made sure to raise us to embody Dad's qualities and ethics, but I am certain that the day I become half of the strong, smart, kind, patient, resilient, and resourceful woman that you are, I am set for life. I love you so so much.

Author Contributions

This thesis consists of five chapters. **Chapter 1** provides an introduction of the concepts and methodologies covered in the body of work. **Chapter 2** has been published in *Langmuir*. **Chapter 3** has been published in *ACS Applied Materials & Interfaces*. **Chapter 4** is based on a manuscript that is currently in preparation. **Chapter 5** includes and overview to our contributions to original knowledge and provides an outlook and suggestions for future work. All articles presented in **Chapters 2 to 4** were co-authored with Prof. Gonzalo Cosa (Department of Chemistry, McGill University), who guided and coordinated the studies and participated in project design, data interpretation, and manuscript preparation.

Chapter 2: Sakaya, A.; Bacellar, I. O. L.; Fonseca, J. L.; Durantini, A. M.; McCain, J.; Xu, L.; Vignoni, M.; Thomas, A. H.; Baptista, M. S.; Cosa, G. "Singlet Oxygen Flux, Associated Lipid Photooxidation, and Membrane Expansion Dynamics Visualized on Giant Unilamellar Vesicles", *Langmuir* **2023**, *39* (1), 442-452.

Aya Sakaya contributed to project design, performed bulk solution-based measurements, and acquired microscopy measurements on GUVs in the presence of the photosensitizer I_2BOAc. Contributions also include data analysis and interpretation, discussions, manuscript writing and editing.

Isabel O. L. Bacellar contributed to project design, manuscript writing and editing, and performed, analyzed, and interpreted initial essential (unpublished) spectroscopy and microscopy measurements with a previous version of the reported $^1O_2$ sensor.

José L. Fonseca acquired fluorescence microscopy measurements of GUVs photosensitized by methylene blue and contributed to the analysis and interpretation of that data and to manuscript editing.

Andrés M. Durantini contributed to initial project design and manuscript editing.

Julia McCain synthesized the probe H_4BPMHC, conducted (unpublished) informative experiments on the kinetics of $^1O_2$ sensing by H_4BPMHC in organic solutions, and contributed to manuscript editing.

Laiyi Xu measured the partition coefficient (log(P)) of I_2BOAc and H_4BPMHC and contributed to manuscript editing.
Mariana Vignoni, Andrés H. Thomas, and Mauricio S. Baptista contributed to discussions and manuscript editing.

Chapter 3: Sakaya, A.; Durantini, A. M.; Gidi, Y.; Šverko, T.; Wieczny, V.; McCain, J.; Cosa, G. "Fluorescence Amplified Detection of Redox Turnovers in Supported Lipid Bilayers Illuminates Redox Processes of α-Tocopherol", *ACS Appl. Mater. Interfaces* **2022,** *14* (11), 13872-13882.

Aya Sakaya contributed to project design and acquisition of electrochemical fluorescence microscopy data. Contributions also include data analysis and interpretation, discussions, manuscript writing and editing.
Andrés M. Durantini contributed to project design, the acquisition, analysis and interpretation of initial (unpublished) data, and to manuscript editing.
Yasser Gidi performed the DFT calculations, contributed to manuscript editing, and provided useful insight towards the project.
Tara Šverko contributed to initial experimental design and data acquisition and analysis as well as manuscript editing.
Vincent Wieczny contributed experimentally towards the formation of the electrode-supported lipid bilayers in addition to manuscript editing.
Julia McCain synthesized the probe and contributed to manuscript editing.

Chapter 4: Sakaya, A.; Che, Y.; Perepichka, D. F.; Cosa, G. "$^1O_2$-mediated remodeling of supported lipid membranes". *In preparation.*

Aya Sakaya contributed to project design and acquired all data reported in the manuscript. Contributions also include data analysis in and interpretation, manuscript writing and editing.
Yuxuan Che synthesized all ADA oligomers.
Dmytro F. Perepichka contributed to project guidance and data interpretation.

Table of Contents

List of Figures

List of Schemes

List of Tables

List of abbreviations and acronyms

β	Factor reflecting the distance dependence of the rate of electron transfer/exchange
ε	Molar extinction coefficient
ε_0	Vacuum permittivity
θ	Angle of incident beam
θ_c	Critical angle for total internal reflection
κ^2	Geometric factor accounting for the relative donor-acceptor dipole orientation
λ	Wavelength
λ	Solvent reorganization energy
λ_0	Wavelength of the incident light in vacuum
λ_{ex}	Excitation wavelength
σ	Fluorophore cross section
τ	Time till full consumption of H_4BPMHC
Φ_f	Fluorescence quantum yield
ϕ_Δ, Φ_Δ	Singlet oxygen photosensitization quantum yield
ω	Radius of photobleached area
APD	Avalanche photodiode
BDT	Benzodithiophene
BODIPY	Boron-dipyrromethene
C	Charge
CCD	Charge-coupled device
CE	Counter electrode
CPE	Conjugated polyelectrolyte
cw, CW	Continuous wave
d	Diameter
D	Diffusion coefficient
D_2O	Deuterium oxide
DFT	Density functional theory
DiD	1,1′-dioctadecyl-3,3,3′,3′- tetramethylindodicarbocyanine perchlorate
DMA	9,10-dimethylanthracene
DMPC	1,2-dimyristoyl-sn-glycero-3-phosphocholine
DOPC	1,2- Dioleoyl-*sn*-glycero-3-phosphocholine
DOTAP	1,2-dioleoyl-3-trimethylammoniumpropane
DPBS	Phosphate buffer prepared in D_2O
DPPE-bio	1,2-dipalmitoyl-sn-glycero- 3-phosphoethanolamine-*N*-(biotinyl) (sodium salt)
e	Elementary charge

E°	Standard reduction potential
ECFM	Electrochemical fluorescence microscopy
E_{ET}	Efficiency of energy transfer
Egg PC	L-*α*-phosphatidylcholine (95%) (Egg, Chicken)
EGOFETs	Electrolyte-gated organic field effect transistors
EMCCD	Electron multiplying charge-coupled device
EP	Electron affinity
E_{pa}	Anodic peak potential
f	Fractional recovery after FRAP
F	Faraday's constant
FOV	Field of view
FRAP	Fluorescence recovery after photobleaching
FRET	Förster resonance energy-transfer
FWHM	Full width at half-maximum
GODCAT	Oxygen scavenging mixture of glucose, glucose oxidase, and catalase
GUV	Giant unilamellar vesicle
HOMO	Highest occupied molecular orbital
i	Current
I_0	Intensity of evanescent field at glass-water interface
I_a	Rate of photosensitizer excitation
IC	Internal conversion
ICT	Intramolecular charge transfer
IDT	Indacenodithiophene
I_{ex}	Rate of incident photons
I_{max}	Intensity maximum
IP	Ionization potential
IR	Infrared
ISC	Intersystem crossing
ITO	Indium tin oxide
I_z	Intensity of evanescent field at perpendicular distance z
J	Electron exchange energy
J(λ)	Spectral overlap integral between the donor and acceptor
K	Parameter dependent of the interactions between the orbitals involved in Dexter electron exchange
k_0	Maximum value of the rate constant of Dexter electron exchange or P*e*T
k_d	Singlet oxygen unimolecular decay rate constant in solvent
k_{decay}	Decay rate constant of singlet excited state
k_{DeT}	Rate constant of Dexter electron exchange

k_{ene}	Rate constant of *ene* reaction between lipids and singlet oxygen
k_{ET}	Rate constant of energy transfer
k_{ex}	Rate constant of excitation
k_{IC}	Rate constant of internal conversion
k_{ISC}	Rate constant of intersystem crossing
k_{op}	Rate constant of chromanol ring opening
k_{ox}	Oxidation rate constant
k_{PeT}	Rate constant of photoinduced electron transfer
k_{phos}	Rate constant of phosphorescence
k_{phy}	Singlet oxygen physical quenching rate constant
k_q	Quenching rate constant
k_q^Q	Quenching rate constant by quencher Q
k_r	Radiative decay rate constant
k_{red}	Reduction rate constant
k_{VR}	Rate constant of vibrational relaxation
LED	Light emitting diode
LSCM	Laser scanning confocal microscopy
LUMO	Lowest unoccupied molecular orbital
MeCN	Acetonitirle
MEHPPV	Poly[2-methoxy-5-(2-ethylhexyloxy)-1,4-phenylenevinylene]
MICOE	Membrane intercalating conjugated oligoelectrolytes
n	Refractive index
NA	Numerical aperture
N_A	Avogadro's number
OECT	Organic electrochemical transistor
OEIP	Organic electronic ion pumps
OMO	Occupied molecular orbital
P3HT	Poly(3-hexylthiophene)
PBS	Phosphate-buffered saline
PEDOT	Poly(3,4-ethylenedioxythiophene)
P*e*T	Photoinduced electron transfer
PFS	Perfect Focus System
PMHC	2,2,5,6,7-pentamethyl-6-hydroxychroman
PMT	Photomultiplier tube
POPC	1- palmitoyl-2-oleoyl-glycero-3-phosphocholine
PS	Photosensitizer
PSS	Polystyrene sulfonate
PVA	Poly(vinyl alcohol)

Q	Quencher
r	Radius
R	Universal gas constant
R_0	Förster radius
RE	Reference electrode
ROS	Reactive oxygen species
S	Surface
S_0	Singlet ground state
S_1	First singlet excited state
SCE	Standard calomel electrode
sCMOS	Scientific complementary metal oxide semiconductor
SEC	Spectro-electrochemistry
SECM	Scanning electrochemical microscopy
SEIRAS	Surface enhanced infrared absorption spectroscopy
SERS	Surface enhanced Raman spectroscopy
S_l	Total lipid area in solution
SLB	Supported lipid bilayer
SMFM	Singlet molecule fluorescence microscopy
S_n	Singlet excited state
SOMO	Semi-occupied molecular orbital
SOSG	Singlet Oxygen Sensor Green
SOSG-EP	Singlet Oxygen Sensor Green endoperoxide
SR	Super-resolution
SVL	Supported vesicular layer
T	Temperature
T_1	First triplet excited state
t_{deform}	Time till GUV deformatiom
TIRF	Total internal reflection fluorescence
T_n	Triplet excited state
$t_{shedding}$	Time till GUV shedding
UMO	Unoccupied molecular orbital
UV	Ultraviolet
v_n	Frequency for nuclear motion along the reaction coordinate
VR	Vibrational relaxation
WE	Working electrode

Chapter 1

Introduction

"The greatest challenge to any thinker is stating the problem in a way that will allow a solution."

- Bertrand Russell

Charge transfer processes are ubiquitous. They play a pivotal role in areas of physical, chemical, and biological relevance. Judicious control of charge transfer processes is at the core of material design and applications. In turn, controlled and concerted reduction-oxidation (redox) reactions are fundamental to cellular function and homeostasis. A tremendous opportunity exists to integrate the material and biological realms, through bioelectronic materials, to manipulate and control biological outcomes, to develop integrated sensing devices, and fundamentally, to study and explore biological redox reactions. To meet their full potential, advancements in the field of bioelectronic devices are required that in turn necessitate the development of innovative tools and methodologies to enhance the electronic connectivity between biological systems and external electronic materials, to investigate the effects of such interfaces on cellular integrity, and to facilitate the extraction of relevant information from the system.

This thesis highlights our contributions to the early-stage development of innovative bioelectronic platforms, in the form of new tools to study and monitor redox processes in lipid membranes. Thus, **Chapter 2** presents a novel fluorescence imaging methodology for the real-time quantitative sensing of oxidative damage to lipid membranes and the visualization of subsequent membrane deformation dynamics. In **Chapter 3**, we introduce a new fluorescence microscopy platform that enables electrochemical control and investigation of redox reactions in lipid membranes. Building upon the knowledge and methodologies from **Chapter 2** and **Chapter 3**, **Chapter 4** delves into the incorporation, photostability, and phototoxicity analysis of novel organic bioelectronic building blocks within lipid membranes.

In this introduction, we provide an overview of the fundamental aspects to consider when integrating biological systems and electronic materials under optical stimulus. 1.1 thus presents fundamental concepts in photophysics and photochemistry that govern the design and use of fluorescence probes to report on redox reactions. **Section 1.2** examines the current state of organic bioelectronic devices and highlights existing challenges that need to be addressed. **Section 1.3** introduces current fundamental and advanced methodologies for electrochemically controlling and investigating charge transfer processes in lipid membranes. **Section 1.4** centers on singlet oxygen, a significant source of photoinduced chemical damage that can occur when incorporating optically active bioelectronic materials into lipid membranes. This section discusses the generation and detection of singlet oxygen and the resulting photosensitized damage within lipid membranes. Finally, **Section 1.5** introduces fundamental concepts in fluorescence and spectroelectrochemical

microscopy, which offer powerful platforms for the spatiotemporal control and monitoring of chemically and electrochemically induced redox reactions in lipid membranes.

1.1. Fundamentals in photophysics and photochemistry

Fluorescence is a physical phenomenon that occurs when a chromophore undergoes electronic excitation, resulting in the dissipation of energy in the form of an emitted photon (light). This process follows strict conservation of spin, such as in transition from a singlet excited state to a singlet ground state. The fluorescence characteristics, including intensity, wavelength, lifetime, and polarization can be controlled by manipulating the chemical structure of the chromophore and its surroundings. This control enables for chromophores to be used effectively as markers/molecular probes in the investigation of physical, chemical and biological processes. Fluorescence spectroscopy and microscopy provide a means to acquire both static and dynamic information about a specific system of interest, to extract thermodynamic and kinetic parameters associated with physical, chemical, and biological processes, as well as to examine features and alterations in the microenvironment surrounding a fluorophore.

In this section, we first introduce the fundamentals of excited state photophysical processes that govern the fate of molecules in excited electronic states, including the ability of a molecule to fluoresce. We then discuss the principles behind some intramolecular processes that can be used to tune the fluorescence and other photophysical properties of fluorophores. Finally, we explore various intermolecular pathways for fluorescence quenching, which offer the means to modulate the intensity of a fluorophore in response to chemical and environmental cues.

1.1.1. Excited state processes

Upon exposure to electromagnetic radiation (light) of appropriate energy, a molecule can absorb an incident photon and transition from an initial ground state to an electronically excited state. This absorption process occurs on the femtosecond timescale (10^{-15} s) and results in the promotion of an electron from an occupied molecular orbital (OMO) to a higher energy, previously unoccupied molecular orbital (UMO). This electronic excitation normally involves a transition from the highest occupied molecular orbital (HOMO) to the lowest unoccupied molecular orbital (LUMO), yet transitions may occur from lower occupied molecular orbitals or to higher electronic

states (**Figure 1.1**). Organic molecules typically exist in a singlet configuration when in the ground state (S_0), with all OMOs containing two electrons of opposite spin states. Electronic excited states can have either a singlet or a triplet spin multiplicity, depending on the orientation and phase of the spin vectors of the two unpaired electrons. The two spin vectors are said to be oriented in the same direction (parallel) when both unpaired electrons are in the same spin state, and in opposite directions (antiparallel) when one electron is in a "spin up" state while the second is in a "spin down" state. A molecule has a singlet spin multiplicity and a zero net spin magnetic moment when the two spin vectors are antiparallel and out of phase, making a 180° angle. Conversely, a molecule has a triplet spin multiplicity and a non-zero spin magnetic moment when the two spin vectors form a ~70° angle while being oriented either in the same or in opposite directions while in phase.

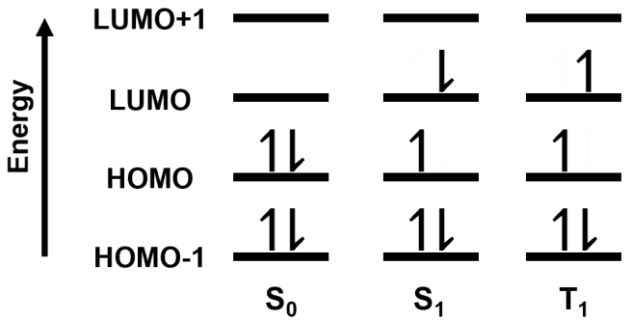

Figure 1.1. Electronic configuration of the occupied and unoccupied molecular orbitals of a typical singlet ground state (S_0), first singlet excited state (S_1), and one possible configuration of the first triplet excited state (T_1). Each arrow represents an electron in a "spin up" or a "spin down" state.

The transitions undergone by an electron, from photon absorption to relaxation back to the ground state, are well depicted using a Perrin-Jablonski diagram (**Figure 1.2**).[1-3] Due to selection rules, a molecule must conserve its spin multiplicity during electronic transitions.[4] Upon absorption of a photon, a molecule is promoted from its S_0 ground state to one of the vibrational levels of an excited singlet state S_n (**Figure 1.2**, blue arrows). Molecules promoted to higher vibrational levels quickly relax to the lowest vibrational level ($v = 0$) of the same electronic state through a radiationless process called vibrational relaxation (VR), taking place within 10^{-12} – 10^{-10} s (**Figure 1.2**, purple arrows). When promoted to a higher excited state S_n with n>1, molecules undergo a horizontal (energy conserving) radiationless transition to a high vibrational level of the n-1 electronic state, a process called internal conversion (IC, **Figure 1.2**, grey arrows), followed

by vibrational relaxation to the $v = 0$ level of the n-1 state. These internal conversion + vibrational relaxation steps repeat until the $v = 0$ level of the first singlet excited state S_1 is reached ($S_{1,v=0}$).

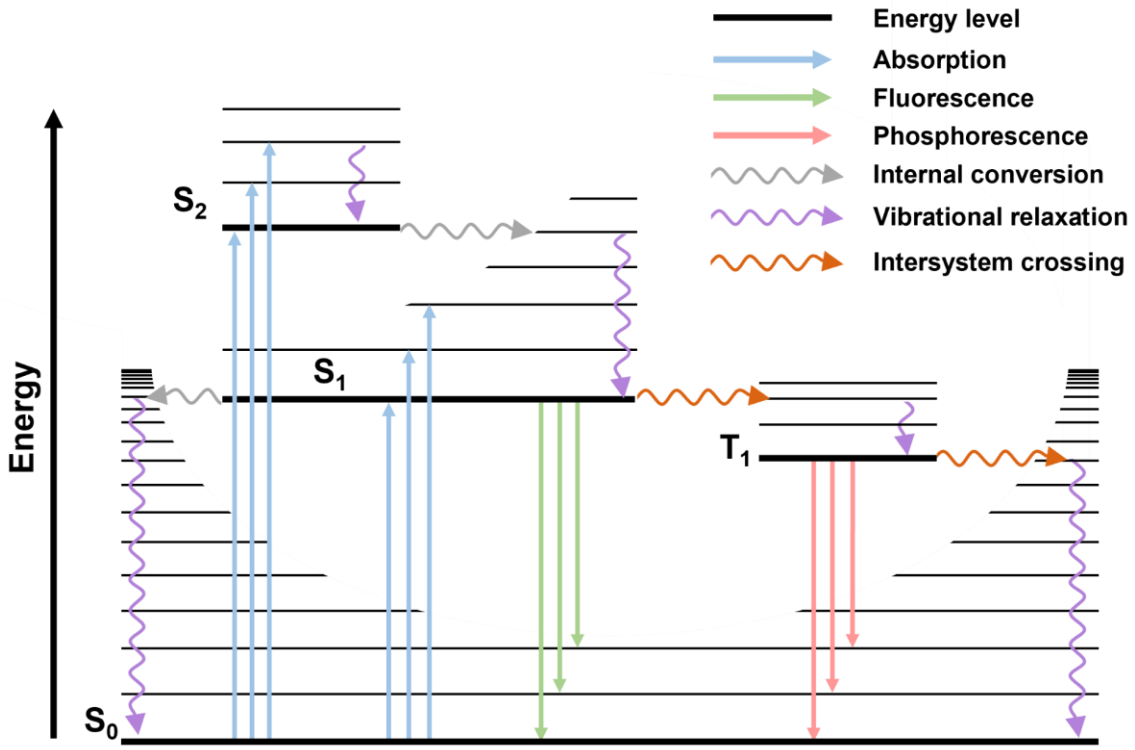

Figure 1.2. Perrin-Jablonski state energy diagram depicting radiative and radiationless transitions between singlet and triplet states.

Once in the $S_{1,v=0}$ state, a molecule can relax back to its ground state though multiple competing pathways. One pathway involves the radiative transition to one of the vibrational levels of the S_0 state through the emission of a photon (fluorescence, **Figure 1.2**, green arrows). Due to energy loss through vibrational relaxation, the energy of the emitted photon is typically lower than that of the absorbed photon. This loss of energy results in the emission spectrum of the molecule to be red-shifted compared to its absorption spectrum, where the difference in energy is known as a Stokes shift.[5] Alternatively, the molecule can relax non-radiatively to the ground state though internal conversion to a high vibrational energy level of the S_0 state followed by vibrational relaxation.

Less frequently, a molecule can undergo a conversion in its spin multiplicity from the singlet $S_{1,v=0}$ state to a triplet T_n state through a process called intersystem crossing (ISC, **Figure**

1.2, orange arrows). ISC requires one of the unpaired electrons of the excited molecule to change its spin, a quantum-mechanically "forbidden", and thus highly improbable, process. However, the rate and probability of ISC can be controlled through certain molecular design considerations discussed in more details in **Section 1.1.2.2**. Upon ISC and following radiationless (IC and/or VR) transition to the $T_{1,v=0}$ state, the molecule can relax back to the ground S_0 state radiatively through photon emission (phosphorescence, **Figure 1.2**, pink arrows) or non-radiatively through ISC to a high vibrational level of S_0 followed by vibrational relaxation. As ISC is a "spin forbidden" process, the rates of all radiative and radiationless transitions between states of different spin multiplicity are orders of magnitude slower than the rates of transitions between electronic states of the same multiplicity (**Table 1.1**). As a result, a triplet state of a conventional organic fluorophore is extremely long lived compared to its singlet state (10^3 – 10^6-fold longer lifetime). This renders the triplet state an important intermediate in photochemical processes as its prolonged lifetime grants it enough time to encounter and react with external reagents.

Table 1.1. Typical timescales for the photophysical transitions depicted in the Perrin-Jablonski diagram. [4, 6]

Process	Transition	Rate constant symbol	Rate constant (s^{-1})
Absorption	$S_0 \rightarrow S_n$	k_{ex}	10^{15}
Vibrational relaxation	$S_{n,v=n} \rightarrow S_{n,v=0}$	k_{VR}	$10^{10} – 10^{12}$
Internal conversion	$S_n \rightarrow S_1$, $T_n \rightarrow T_1$	k_{IC}	$10^{10} – 10^{14}$
Fluorescence	$S_1 \rightarrow S_0$	k_r	$10^{7} – 10^{10}$
Internal conversion	$S_1 \rightarrow S_0$	k_{IC}	$10^{6} – 10^{7}$
Intersystem crossing	$S_n \rightarrow T_n$, $T_n \rightarrow S_n$	k_{ISC}	$10^{5} – 10^{10}$
Phosphorescence	$T_1 \rightarrow S_0$	k_{phos}	$10^{-2} – 10^{6}$

In a solution containing only the fluorophore and solvent (i.e., in the absence of external quenchers), the efficiency by which a molecule relaxes via fluorescence is given by its fluorescence quantum yield Φ_f (**eq 1.1**), a ratio of emitted photons over those absorbed, a magnitude that may be equated to the ratio of fluorescence decay rate (k_r) over the total decay rate (k_{decay}) arising from all $S_1 \rightarrow S_0/T_n$ transitions.

$$\Phi_f = \frac{\#\text{ emitted photons}}{\#\text{ absorbed photons}} = \frac{k_r}{k_{decay}} = \frac{k_r}{k_r + k_{IC} + k_{ISC}} \quad (1.1)$$

1.1.2. Intramolecular fluorescence quenching

When in a solution containing only the fluorophore, relaxation via fluorescence emission is in direct competition with intramolecular processes, namely internal conversion and intersystem crossing (ISC). The probability (and thus rates) of these processes can be tuned by molecular design principles to either increase or decrease them as needed.

1.1.2.1. Internal conversion

Certain vibrational modes in a molecule can promote the non-radiative deactivation of an excited state through the conversion of electronic energy into vibrational energy of an electronic ground state. The resulting large vibrational energy of the ground state is then released as heat to the surrounding media. Vibrational modes that are able to both trigger the radiationless transition by providing an appropriate vibronic interaction between the two electronic states as well as carry the excess energy resulting from this transition are particularly effective at promoting internal conversion.[7]

Scheme 1.1. Examples of molecules with efficient and inhibited internal conversion decay pathways

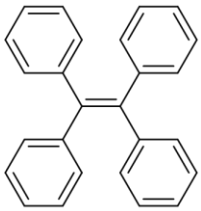

Tetraphenylethene (TPE)

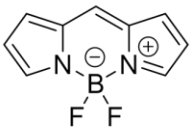

Boron dipyrromethene (BODIPY)

Two vibrational modes that efficiently promote internal conversion are C−C bond stretching ("loose bolt" effect) and the C=C bond twisting ("free rotor" effect).[7] As such, one can promote internal conversion by introducing carbon-carbon double bonds that are freely rotating in the excited state, such as in the tetraphenylethene (TPE) group used in many aggregation-induced

emission fluorophores (**Scheme 1.1**).[8] Alternatively, internal conversion can be very efficiently prevented in highly structurally constrained molecules, such as boron dipyrromethene (BODIPY) fluorophores whose fluorescence quantum yield is ~1 (**Scheme 1.1**) when boron chelation is introduced in the otherwise non-emissive dipyrrin framework.

1.1.2.2. Intersystem crossing

Intersystem crossing is a radiationless process by which an electronically excited molecule undergoes a transition from a singlet to a triplet spin multiplicity (or vice versa). This process, requiring one of the two unpaired electrons to "flip" its spin, is a forbidden process and thus is very unlikely to occur. Nevertheless, this process can become more favorable when strong vibronic coupling exists between the singlet and triplet states as a result of significant overlap between the vibrational energy levels of the two states. The structure of the fluorophore can also be specifically designed to promote or prevent ISC. Molecules that are able to undergo efficient ISC to generate triplet states, known as triplet photosensitizers, have a wide range of applications as the long lifetime and excited state energy of triplet excited states allows their critical use in important photochemical processes such as in photovoltaics,[9] photocatalysis,[10] and photodynamic therapy.[11]

The spin states ("up" or "down") of the two unpaired electrons in an excited molecule are very strongly coupled to each other. The strength of the coupling is determined by the electron exchange energy *J*. The "spin" of an electron is its intrinsic angular momentum (confusingly not resulting from an angular/rotational motion) and as such is associated to a magnetic moment. The coupling of the spins of the two unpaired electrons of an excited molecule is thus a form of magnetic coupling. As such, the two spins can be decoupled in the presence of other magnetic moments, which act as magnetic "torques" that change the direction or phase of one of the electron spin vectors with respect to the other. These magnetic interactions should be strong enough to overcome *J*. The most common sources of magnetic torques are (1) coupling to an externally applied magnetic field (Zeeman coupling), (2) coupling to the magnetic moment generated by the motion of the electron in an orbital (spin-orbit coupling), and (3) coupling to the magnetic moment of a nuclear spin (hyperfine coupling). Regardless of which coupling mechanism is used, the change in spin magnetic moment following change in spin angular momentum, must be offset by an equal change in magnetic moment in order to conserve the total angular momentum of the

molecule. This most commonly occurs in the form of a change in orbitals, and thus in orbital angular momentum/magnetic moment.[7]

In the absence of an external magnetic field, ISC is most often promoted through coupling of an electron's spin magnetic moment to its orbital magnetic moment. While the former is a fixed quantity, the latter is variable and – considering a simplified relativistic picture of an electron moving within an orbital – is proportional to the speed of the electron. The larger the orbital magnetic moment, the stronger the spin-orbit coupling. When in the vicinity of a "heavy atom", the electron is attracted towards the strong positive charge of the nucleus and must greatly accelerate its speed to avoid being pulled into the nucleus, creating a strong orbital magnetic moment. Spin-orbit coupling (and ISC) is thus very efficiently catalyzed in the presence of a large nuclear charge, a phenomenon known as the "heavy atom effect".[7]

An alternative approach to requiring the presence of a heavy atom to create a spin-orbit magnetic coupling that is strong enough to overcome the electron exchange energy J is to simply decrease the magnitude of J, and thus decrease the extent of spin coupling between the two unpaired electrons. As the magnitude of J decreases exponentially with distance, one approach for enhancing ISC is to spatially separate the two unpaired electrons.[7] This is commonly done by forming electron withdrawing (acceptor) and electron donating (donor) dyads or polyads, which undergo intramolecular charge transfer upon photoexcitation, effectively generating a diradical.[12, 13] The decrease in J upon the spatial separation of the two unpaired electrons not only strongly decreases their extent of coupling, but also decreases the energy gap between the singlet and triplet states ($\Delta E_{ST} = 2J$), which further promotes the transition between these two states. When the spatial separation between the two electrons exceeds 5 – 10 Å, the coupling between their spins can be easily overcome through hyperfine coupling, where the nuclear spin magnetic moment acts as a torque that promotes a change in the direction of the spin of either electron.[7, 14]

1.1.3. Mechanisms of fluorescence quenching

The fluorescence emission of a molecule can be quenched upon interacting with other components in its environment through multiple pathways, including quenching by resonance energy transfer, collisional quenching between the excited state fluorophore and a quencher, and static quenching upon the formation of a stable complex between the ground state fluorophore and a quencher. The latter is not an excited state process and will not be further addressed in this

section. The thermodynamics and kinetics of these quenching processes are very sensitive to the molecular nature of the fluorophore and quencher, their intra- or intermolecular distance, and their surrounding environment. As such, a system can be designed to capitalize on and modulate these quenching interactions in order to report on certain molecular and biological processes.

1.1.3.1. Förster resonance energy transfer

Förster resonance energy transfer (FRET) is a mechanism by which a photoexcited donor fluorophore transfers its excitation energy to a nearby acceptor molecule. The energy is transferred non-radiatively via through-space dipole-dipole interactions that take place over a range of 1 – 10 nm. The rate of energy transfer (k_{ET}) depends on key photophysical properties of the donor and the acceptor molecules and is given by **eq 1.2** below.[5] Here, Φ_f^D is the fluorescence quantum yield of the donor, τ_D is the singlet excited state lifetime of the donor in the absence of the acceptor, r is the donor-acceptor distance, κ^2 is a value that depends on the relative orientation of the donor and acceptor dipoles and ranges between 0 and 4, n is the refractive index of the solvent, N_A is Avogadro's number, and $J(\lambda)$ is the overlap integral between the donor emission and acceptor absorption spectra.

$$k_{ET} = \frac{\Phi_f^D \kappa^2}{\tau_D r^6}\left(\frac{9000\ln(10)}{128\pi^5 N_A n^4}\right)J(\lambda) \tag{1.2}$$

κ^2 is frequently given a value of 2/3, corresponding to freely tumbling donor and acceptor molecules (i.e., having randomly oriented dipole moments). κ^2 has a value of 1 when the donor and acceptor molecules are oriented parallel but not colinear to each other, a value of 4 when the two dipoles are parallel, colinear, and oriented in a head-to-tail fashion, and a value of 0 when the two dipoles are perpendicular orientations.[5] The efficiency of energy transfer (E_{ET}) reflects the fraction of donor excitations events that are deactivated by FRET and is given by given by **eq 1.3**, where k°_{decay} is the decay rate constant of the donor from the singlet excited state in the absence of the acceptor.

$$E_{ET} = \frac{k_{ET}}{k_{ET} + k^{\circ}_{decay}} \tag{1.3}$$

One useful and commonly referred to parameter of a donor-acceptor FRET pair is their Förster radius R_0 (**eq 1.4**), the separation at which the FRET efficiency is 50%. The Förster radius is a key parameter to consider when developing FRET-based chemical sensing systems, and is typically in around 30 – 60 Å.[5] The long range distance dependence of FRET earned it the term "spectroscopic ruler",[15] and underlines its use as a reporter on molecular dynamics. Recently, our research group revised the expressions of FRET efficiency and Förster radius described in **eqs 1.3** and **1.4**, respectively, and adapted them towards the analysis of single-molecule FRET experiments.[16] The new analysis method removed the dependence on the quantum yield of the donor, as the latter is sensitive to its microenvironment and can thus change over the course of an experiment.

$$R_0 = \left(\Phi_f^D \kappa^2 \left(\frac{9000 \ln(10)}{128\pi^5 N_A n^4} \right) J(\lambda) \right)^{\frac{1}{6}} \quad (1.4)$$

1.1.3.2. Dexter energy transfer

Like FRET, Dexter energy transfer, also known as Dexter electron transfer and Dexter electron exchange, is a mechanism by which an excited state donor returns to the ground state by transferring its excitation energy to a ground state acceptor. Unlike FRET however, this energy exchange results from a short-range (<10 Å) electron exchange process between the donor and the acceptor, as opposed to a long range (10 – 100 Å) dipole-dipole interaction between the two molecules (**Figure 1.3**). The two-electron exchange steps depicted in **Figure 1.3** can occur either simultaneously or in a stepwise fashion.[5, 17]

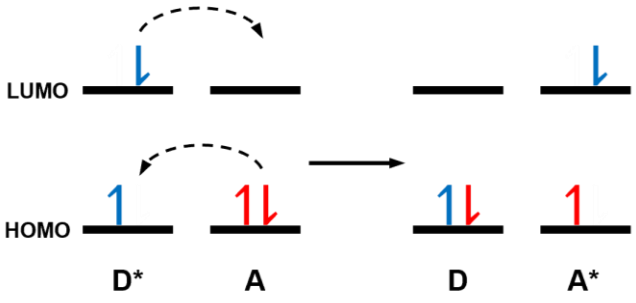

Figure 1.3. Schematic of Dexter energy exchange interaction. Curved dashed arrows depict the electron transfer steps between the donor (D) and acceptor (A) molecules.

Dexter energy transfer is a quantum mechanical effect that requires significant overlap between the wavefunctions of the orbitals involved in the electron exchange steps. Accordingly, Dexter interactions require very close contact between the donor and acceptor and is classified as a type of collisional quenching. Similar to FRET, the rate of Dexter energy transfer depends on the spectral overlap integral *J(λ)* between the two molecules, however, a major difference is that here both spectra are normalized, so Dexter energy transfer is independent of the transition dipole moment for absorption or emission. The distance dependence of Dexter interactions is however much stronger than in FRET, with the rate of energy transfer (k_{DeT}) decreasing exponentially with increasing donor-acceptor separation, as depicted in **eq 1.5**.[17] Here, *L* is the center-to-center separation between the donor and acceptor when they are in full contact (sum of their van der Waals radii) and *K* is a parameter dependent of the interactions between the orbitals involved in the process, such as instantaneous orbital orientation.[17]

$$k_{DeT} = KJ(\lambda)e^{-\frac{2r}{L}} \tag{1.5}$$

A convenient way to express the distance dependence of k_{DeT} is in the form of **eq 1.6**. Here, k_0 is the rate of energy transfer when the donor and acceptor are in van der Waals contact (r = L). The maximum value k_0 can have is ~ 10^{13} s^{-1}. β reflects the sensitivity of k_{DeT} to *r* ($\beta \approx 1$ $Å^{-1}$) for a given donor-acceptor pair. The smaller the value of β, the less sensitive k_{DeT} is to donor-acceptor distance.[17]

$$k_{DeT} \sim k_0 e^{-\beta(r-L)} \tag{1.6}$$

A specific example of Dexter energy transfer is triplet-triplet annihilation (TTA). TTA is a photophysical process by which a donor molecule in the triplet excited state returns to the singlet ground state upon collision with a triplet state acceptor molecule by transferring its excitation energy to the acceptor via Dexter electron exchange. The acceptor is then promoted to a higher energy singlet excited state. TTA plays a central role in various applications across different fields, ranging from optoelectronic devices to biomedical applications.[18, 19] Perhaps the most important example of TTA is the interaction between molecular oxygen, which naturally exists in a triplet manifold, and an excited triplet state photosensitizer (see **Section 1.1.2.2**). This interaction results

in the return of the triplet excited state photosensitizer back to its singlet ground state, and the promotion of molecular oxygen to a higher energy singlet excited form, known as singlet oxygen ($^1O_2$). $^1O_2$ is a highly reactive molecule that generates irreversible chemical damage in its surrounding environment. $^1O_2$ and its biological implications are discussed in more details in **Section 1.4**.

1.1.3.3. Photoinduced electron transfer

While both Dexter energy transfer and photoinduced electron transfer (P*e*T) are mechanisms by which the fluorescence of a dye is quenched by electron transfer following photoexcitation, the mechanism and driving force of these two collisional quenching pathways are quite different. P*e*T is a process favored by the higher ability of a ground state closed shell molecule to, once in the excited state, become both a better electron acceptor and electron donor. This is best illustrated through changes in the electron affinity (EA) and ionization potential (IP) of a molecule in the gas phase, before and after excitation, as depicted in **Figure 1.4**.

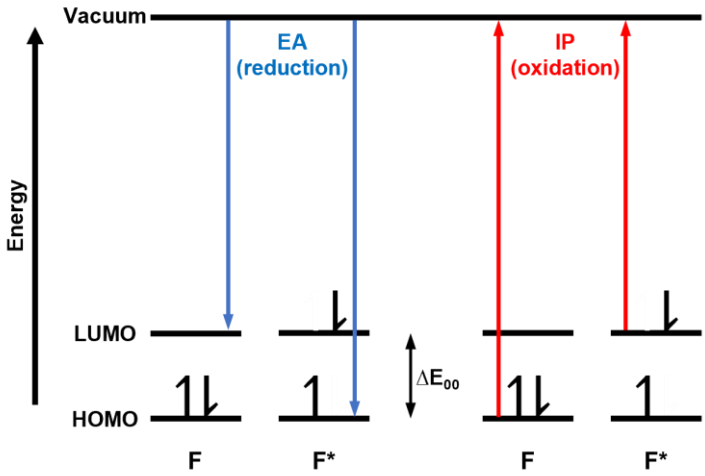

Figure 1.4. Comparison of the electron affinity (EA) and ionization potential (IP) between a ground state (F) and excited state (F*) fluorophore in the gas phase.[17]

During P*e*T, an excited chromophore (a fluorophore herein) can act as either the electron donor (D) or the electron acceptor (A), depending on the relative orbital energies of the fluorophore compared to that of a close lying redox active compound **(Figure 1.5)**. P*e*T can only spontaneously take place if the Gibbs free energy ($\Delta G°$) for photoinduced electron transfer is negative. Hence,

for the fluorophore to undergo a photoinduced oxidation and donate an electron to the LUMO of the quencher, its LUMO (effectively, its semi-occupied orbital originally corresponding to the LUMO) must be higher in energy than that of a quencher. Conversely, for the fluorophore to undergo a photoinduced reduction by accepting an electron from a quencher, its HOMO (effectively, its semi-occupied orbital originally corresponding to the HOMO) must be lower in energy than that of a quencher (**Figure 1.5**).

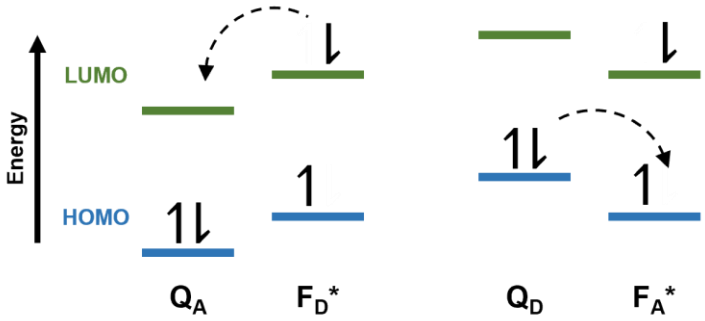

Figure 1.5. P*e*T between a photoexcited fluorophore (F*) and a quencher (Q). The fluorophore can be the electron donor (left) or the electron acceptor (right). Curved dashed arrows indicate an electron transfer process.

In the gas phase, $\Delta G°$ of the P*e*T reaction can be determined from the IP of the donor and the EA of the acceptor. However, when in solution, interaction between the solvent molecules and the charged species change the energetics of the reaction. Consequently, the measured reduction potentials of the acceptor and the donor are used instead. Here, $\Delta G°$ is given by the equation for the Gibbs free energy of photoinduced electron transfer (**eq 1.7**, wrongly, though typically referred to as the Rehm-Weller equation).[17, 20, 21] Here, $E^{\circ}_{D^{\bullet+}/D}$ and $E^{\circ}_{A/A^{\bullet-}}$ are the standard reduction potentials of the donor and the acceptor, respectively, ΔE_{00} is the electronic excitation energy of the fluorophore (HOMO-LUMO gap), n is the number of electrons transferred (typically $n = 1$ in P*e*T processes), F is Faraday's constant, N_A is Avogadro's number, e is the elementary charge of the electron, ε_0 is the vacuum permittivity, ε is the solvent dielectric constant, and r is the distance between the two charges. The last term in **eq 1.7** is a Coulombic correction factor accounting for the energy gain associated with bringing two opposite charges close together.

$$\Delta G^{\circ} = nF\left(E^{\circ}_{D^{\bullet+}/D} - E^{\circ}_{A/A^{\bullet-}}\right) - \Delta E_{00} - N_A \frac{e^2}{4\pi\varepsilon_0 \varepsilon r} \qquad (1.7)$$

The P*e*T rate constant (k_{PeT}) is determined from the Marcus theory of electron transfer.[22] Here the energy $\Delta G^{\ddagger}$ required to reach the transition state of the electron transfer reaction – intersection of the reactant and product potential energy surfaces – depends on the total Gibbs free energy of the reaction ΔG° and on the reorganization energy λ, the energy difference between a geometry where the products (redox active partners and surrounding solvent) adopt a similar nuclear arrangement as that of the stabilized reactants and the geometry where products have been allowed to relax.[23] **Eqs 1.8** and **1.9** provide expressions for the transition state energy and P*e*T rate constant, respectively.[17, 23] In **eq 1.9**, *R* is the universal gas constant, *T* is the absolute temperature, κ is a transmission coefficient reflecting the probability that the reactant, upon reaching the transition state configuration, would proceed to form the product, and ν_n is an electronic factor representing the theoretical maximum value that k_{PeT} can have.

$$\Delta G^{\ddagger} = \frac{(\Delta G^{\circ} + \lambda)^2}{4\lambda} \tag{1.8}$$

$$k_{PeT} = \nu_n \kappa e^{-\frac{\Delta G^{\ddagger}}{RT}} \tag{1.9}$$

It is important to note that the P*e*T rate constant expressed in **eq 1.9** is expected to have a similar distance dependence as the one expressed in **eq 1.6**, where the term ν_n incorporates the distance dependence.[5, 24] P*e*T is frequently used in the design of fluorogenic probes, fluorophores that undergo a change in intensity upon exposure to certain redox active chemical cues. Here, upon the oxidation of a quencher that prevents fluorescence emission via photoinduced reduction of a fluorophore, the P*e*T mechanism is deactivated, and fluorescence is restored, thus providing a sensing mechanism for oxidizing agents.[25-30] Likewise, the reduction of a quencher that operates via the photoinduced oxidation of a fluorophore inactivates this P*e*T mechanism, thus reporting on the activity of reducing agents.[31-34]

1.2. Organic bioelectronics

The fast-growing field of bioelectronics, serving as an interface between living systems and modern electronic devices, has the potential to revolutionize multiple fields, ranging from medical devices for the diagnosis and treatment of diseases to philosophical investigations into the origins of consciousness. Since Luigi Galvani's famous 18th century experiment in which a frog's leg twitched when a small voltage was applied,[35] experiments combining living organisms and electricity have elucidated the inner workings of the brain and led to the development of implantable devices such as pacemakers and cochlear implants.[36]

Bioelectronic materials are charge carriers that connect the biotic and abiotic and allow to establish, monitor, and control the interaction between biological systems and external electronic materials. Initially dominated by inorganic conductors and semiconductors, organic semiconductor devices are now at the forefront of bioelectronic research, largely owing to their superior biocompatibility.[36-41]

In this section, we provide an overview of the materials and structures of some main organic semiconductors and the properties central to their superior performance as bioelectronics. We then discuss recent advances in organic bioelectronic devices. Finally, we address challenges and limitations in the current applications of organic bioelectronic materials.

1.2.1. Organic bioelectronic materials

1.2.1.1. Conjugated polymers

Conjugated polymers are organic macromolecules characterized by a backbone of alternating single and double carbon bonds. The overlapping p-orbitals along this backbone result in delocalized π-electrons, granting conjugated polymers attractive optical and electronic properties. Conjugated polymers employed in optoelectronic and bioelectronic devices typically consist of repeating aromatic ring units. The structures of the conjugated oligomers most commonly used in bioelectronic applications are depicted in **Scheme 1.2**. Polyaniline and polypyrrole are some of the earliest studied organic semiconductors.[42-44] Polythiophene and its derivatives (including P3HT and PEDOT) have been extensively used in optoelectronic and bioelectronic applications. Polyphenylene vinylene is one of the most frequently used backbones for conjugated poly- and oligoelectrolytes (discussed in **sections 1.2.1.2** and 1.2.1.3).

Unlike covalently bonded "hard" silicon, the most frequently used material in inorganic bioelectronics, "soft" conjugated polymers are held together through weak van der Waals interactions. This difference in packing arrangement is the root behind the advantages of organic electronics over their inorganic counterparts. The weak packing of conjugated polymers provides a flexibility close to that of biological organisms compared to inorganic material. Moreover, the lack of an intermolecular covalent bond constraint allows for the facile functionalization of conjugated polymers. As such, structures can be functionalized to improve their biocompatibility, thermal and electrochemical stability, and mechanical and optoelectronic properties.[37, 45-47]

Scheme 1.2. Structures of the conjugated polymers most frequently used in bioelectronic applications.

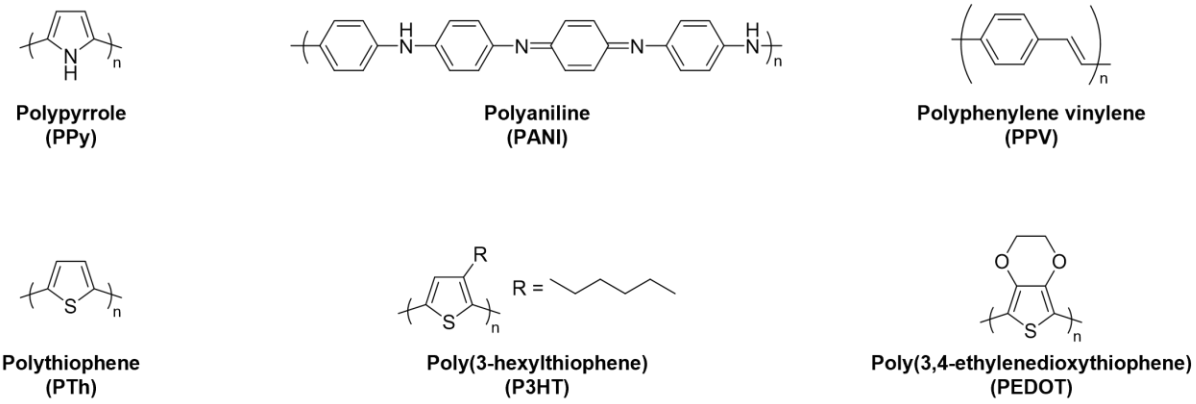

Importantly, conjugated polymers provide an oxide-free interface with the aqueous biological environment. As depicted in **Figure 1.6**, the cleaved top layer of silicon gives rise to an oxide layer that acts as a physical barrier between the silicon and ions in the electrolyte.[37] The oxide-free interface of conjugated polymers, on the other hand, allows for direct contact with the biological environment. This, along with the ability of ions to penetrate the volume of conjugated polymers (owing to their weak van der Waals interactions), enables a three-dimensional interaction between conjugated polymers and the electrolytes.[48] Unlike silicon, whose three-dimensional organization and conductive properties remain largely unaffected by the presence of a charge, the uptake or release of ions from conjugated polymers is accompanied by large changes in their packing and charge transport properties. Hydrophilic polymers can also absorb water and swell, further increasing their ion transport abilities. As such, a change in ion flux in the biological environment (e.g., following a neuron firing) can strongly affect the conductance of (and flow of

current through) the conjugated polymer. The oxide-free interface and ion transport properties of conjugated polymers are the fundamental design principles of organic electrochemical transistors (OECT), first reported in 1984,[49] and recently shown to vastly outperform inorganic field effect transistors in detecting small potential fluctuations.[50] Organic transistor devices are at the center of biosensing applications of organic bioelectronics, which will be discussed in more detail in **section 1.2.2**.

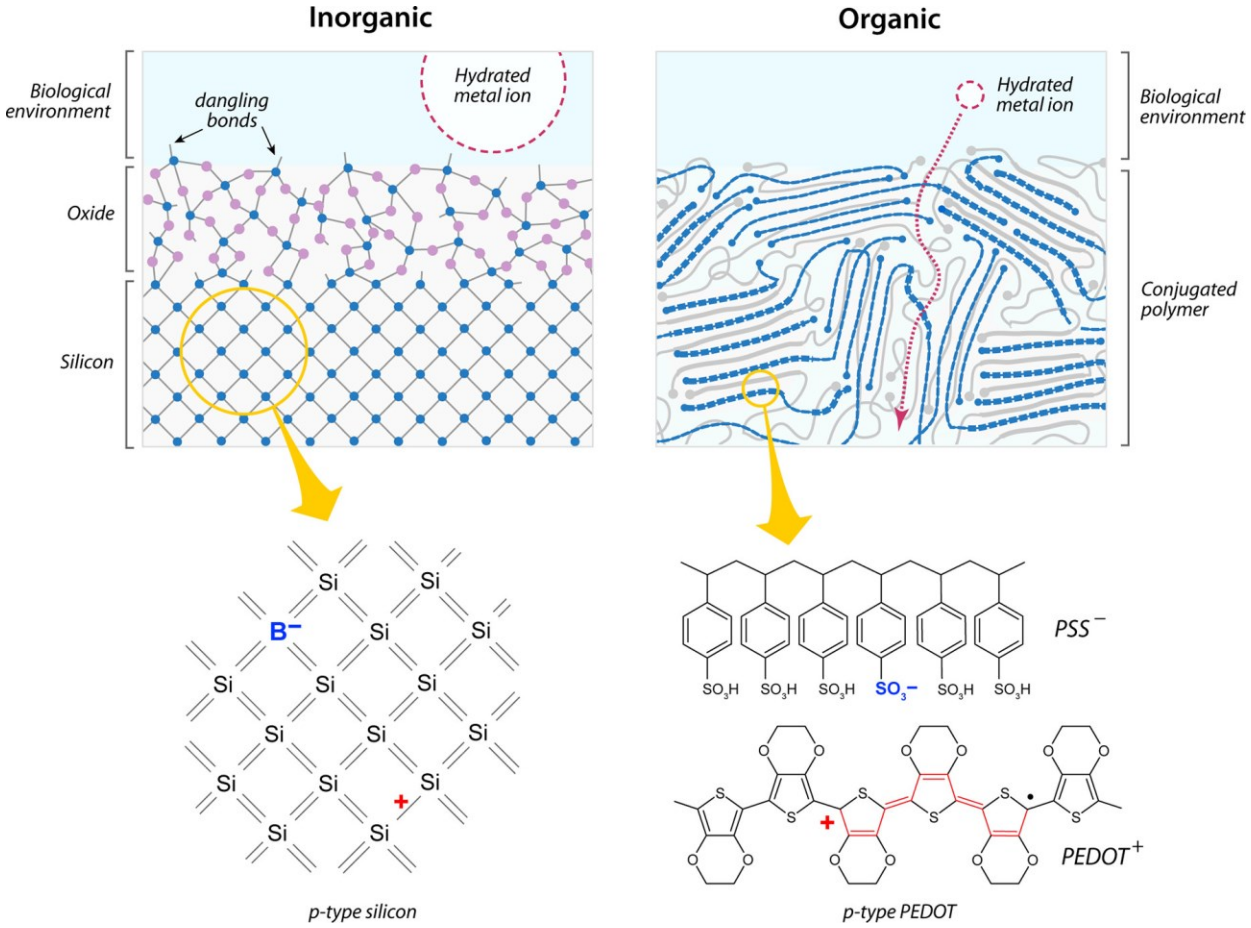

Figure 1.6. Schematics depicting silicon and PEDOT semiconductors interfaced with an electrolyte. The hydrated ion in both schematics is of the same size and is intended to depict the relative scale of both constructs. The insets depict the molecular structures of the p-doped silicon and PEDOT, doped with boron and polystyrene sulfonate (PSS), respectively. Figure reproduced with permission from reference 37.

Similar to inorganic semiconductors, the semiconducting properties of conjugated polymers manifest at the bulk material level, as opposed to the scale of individual monomers or chains. In their innate state, conjugated polymers behave as semiconductors with low electric

conductivity (10^{-7} – 10^{-3} S cm^{-1}) and require doping in order to increase their charge carrier density and attain electric conductivities similar to those of metals (> 1 – 10^{3} S cm^{-1}).[39] Conjugated polymers can become electron carriers upon n-doping or hole carriers upon p-doping. Different doping mechanisms are employed to increase the conductivity of conjugated polymers, the most frequent being chemical and electrochemical doping.[38, 48, 51] Electrochemical doping of conjugated polymers is achieved by injecting or removing electrons through an external electrode connected to the polymer. Counterions from the surrounding electrolyte compensate the generated charge in the polymer.[48] Chemical doping, on the other hand, typically consists of the addition of highly electron-accepting molecules that oxidize the polymer backbone, the most famous example being the doping of PEDOT with polystyrene sulfonate (PSS, **Figure 1.6**).[51, 52] Conjugate polymers that are chemically doped by the addition of external agents form composite hole and cation transporting materials. On the other hand, the doping charged group can be covalently linked to the polymer backboned, forming single component mixed conductors known as conjugated polyelectrolytes.

1.2.1.2. Conjugated polyelectrolytes

Conjugated polyelectrolytes (CPEs) consist of a conjugated polymer backbone with ionic pendants (typically short alkyl chains ending with charged groups) covalently bonded to the aromatic repeat units. Besides their attractive properties as single-component mixed conductors, the polar pendants of CPEs increase their hydrophilicity. This improved hydrophilicity enables using CPEs as interfacial layers in multilayer organic devices.[53, 54] The charged nature of CPEs has also been shown to enhance the performance of organic electronic devices by improving charge injection between the electrodes and organic layers.[54-56]

Besides their use in optoelectronic devices, the interesting optical and electrochemical properties of CPEs have been used in various biological and sensing applications.[57-59] However, it is difficult to accurately predict and determine how a change in CPE (or non-charge conjugated polymers) structure will affect its properties due to the large polydispersity exhibited by their polymeric structure.[60] The large structure of conjugated polymers and CPEs also restricts their application as bioelectronic materials to a physical interface between biological systems and external electronic components, preventing a more intimate interaction with cell membranes. To

circumvent these limitations, bioelectronics research has shifted to using membrane intercalating conjugated oligoelectrolytes.[60, 61]

1.2.1.3. Membrane intercalating conjugated oligoelectrolytes

Membrane intercalating conjugated oligoelectrolytes (MICOEs) are short conjugated structures of fixed and controlled length, typically consisting of 3-6 phenylene vinylene repeat units, bearing polar pendants at both terminals of the conjugated backbone (**Figure 1.7**).[60-62]

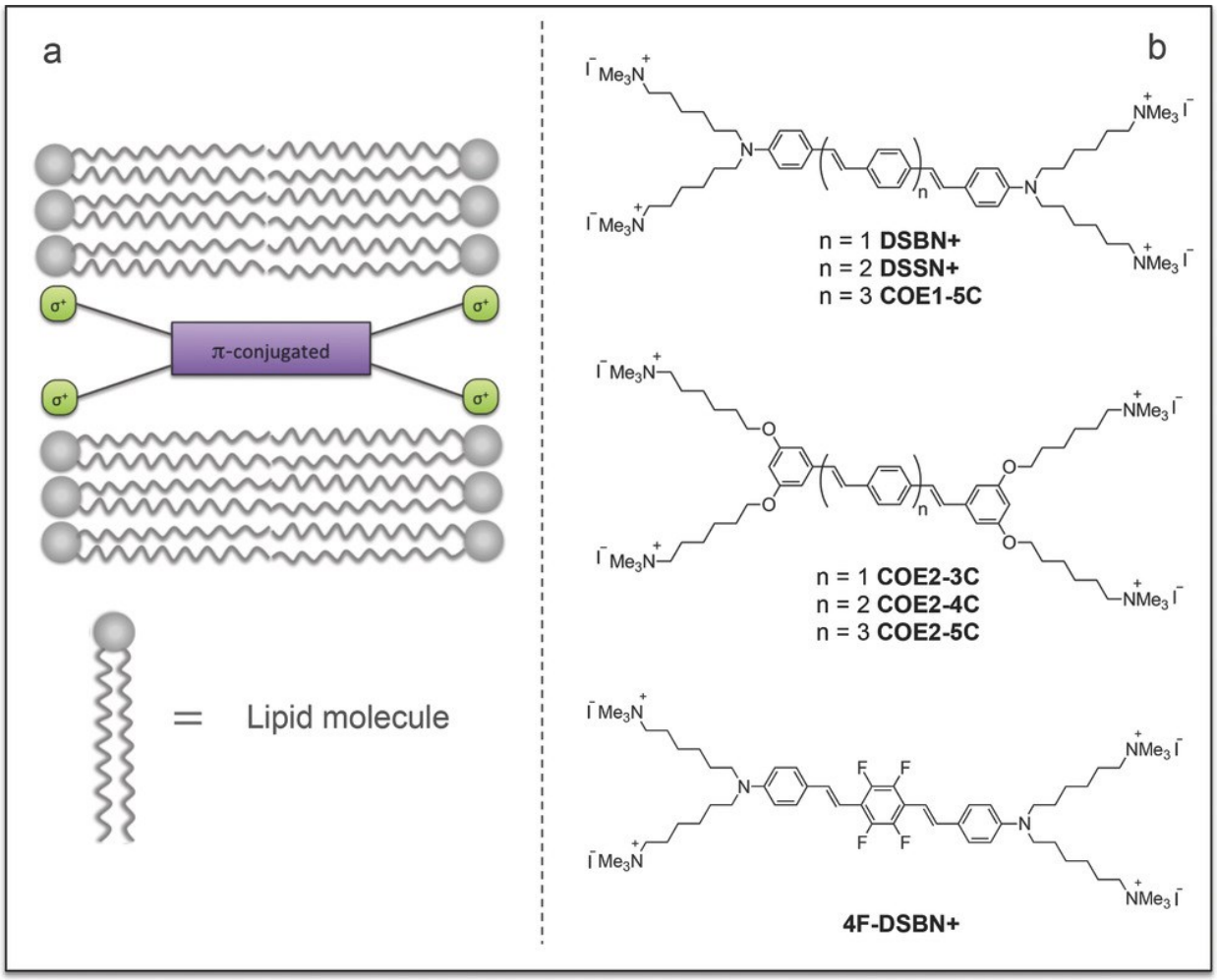

Figure 1.7. Membrane intercalating conjugated oligoelectrolytes. (a) Schematic of a MICOE bearing a π-conjugated backbone (purple) and polar terminal pendant groups (black lines and green circles) intercalating within a lipid bilayer (grey). (b) Structures of most frequently studied MICOEs. Reproduced with permission from reference 61.

The unique structure of MICOEs, similar to that of lipids (hydrophobic core with hydrophilic pendants), allows them to spontaneously intercalate and partition within lipid bilayers.[60, 61] The limited and addressable structure of MICOEs enables direct assessment of their structure-property relationship. For instance, the effect on membrane integrity arising from the incorporation of MICOEs within lipid membranes has been identified to be strongly dependent on the length of the oligomer. Increasing the number of phenylene vinylene repeat units from 3 to 4 significantly decreases the antimicrobial membrane-disrupting properties of the MICOE.[63] In contrast, a further increase to 5 repeat units grants the MICOE with membrane rigidifying and stabilizing properties.[64]

Acting as transmembrane molecular wires, the incorporation of MICOEs in membranes has greatly improved charge transfer in bioelectronic devices such as microbial fuel cells,[65, 66] bioelectrosynthesis,[67] and photocurrent production.[68]

1.2.2. Recent applications in bioelectronics

Capitalizing on the versatility, excellent optoelectronic properties, and low production costs of organic semiconductor materials, a vast range of bioelectronic devices have been developed to monitor and stimulate cellular activity (**Figure 1.8**).

Coating electrodes with conjugated polymers reduces their impedance by several orders of magnitude owing to their ability to transport ions[69] and improves the electrode-biosystem interface for both short- and long-term operations.[70] Owing to the decreased electrode impedance (opposition to electron flow, equal to resistance under DC current), microelectrode arrays coated with PEDOT:PSS were successfully used to monitor neuronal activity with improved sensitivity.[71]

The use of organic semiconductors in thin film transistors constitutes perhaps their most impressive application. Conjugated polymers and polyelectrolytes are used as channel material between two electrodes (source and drain electrodes). Applying a voltage between the source and drain electrodes generates a current flow in the organic channel material, known as the drain current. The latter is exposed to the biological environment, and cells can be cultured on the transistor surface. Biological signals accompanied by a change in ion flux (e.g., neuron firing, binding events) result in a change in the current flowing through the semiconductor and, thus in the drain current.[72] Monitoring changes in the drain current is therefore used to detect biological signals sensitively. Conjugated, ion permeable polymers are used in organic electrochemical

transistors (OECTs).[48] As described in the section above, ion flow through the bulk of the conjugated polymer changes its doping state and is accompanied by large changes in its bulk capacitance (capability to store electric charge), resulting in large changes in drain current. OECTs can thus sensitively detect changes in the biological environment they are exposed to.[48] On the other hand, organic semiconductors that pack in a more rigid and crystalline fashion are not permeable to ions. These materials constitute electrolyte-gated organic field effect transistors (EGOFETs) and detect biological signals through changes in the double layer capacitance along the electrolyte-semiconductor interface.[73, 74]

Organic thin film transistors, EGOFET-based devices in particular, are the central construct behind the biosensing applications of organic bioelectronics. Biological, chemical, and electrical events are accurately sensed through changes in the doping state and conductivity of organic semiconductors down to the single molecule detection of analyte.[75] Selective sensing of specific analytes can be achieved by functionalizing the semiconducting surface of EGOFETs with certain biorecognition elements such as enzymes, antibodies, and aptamers.[76]

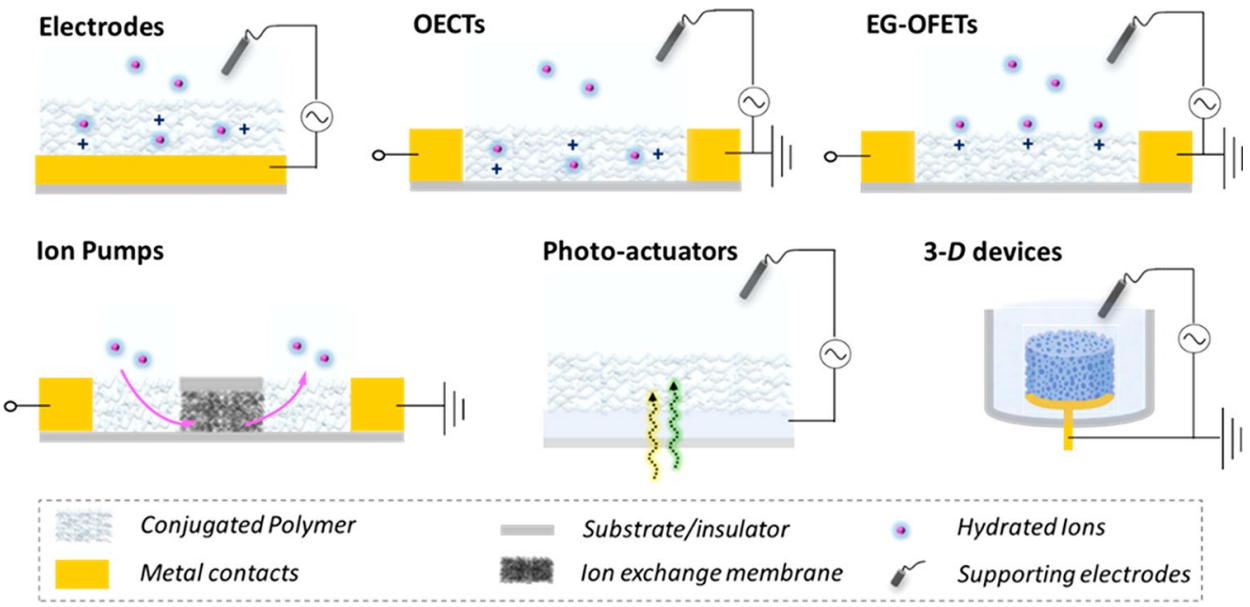

Figure 1.8. Schematic representation of some organic bioelectronic devices. Reproduced with permission from reference 39.

The ability of conjugated polymers to transport ions is beneficial not only to detect an influx of ions into the bulk of the polymer, but also to selectively pump ions and small molecules out towards the biological environment. Organic semiconducting polymers thus serve as ion

exchange membranes in organic electronic ion pumps (OEIPs) and are used for the selective delivery of small molecule drugs and therapeutics between two separated regions.[77] A typical OEIP device consists of a biological system separated by an ion exchange membrane (organic semiconductor) from a reservoir containing the drug to be delivered. Voltage application across the membrane enables the delivery of the drug from the reservoir to the biological organism.[78]

Conjugated polymers, polyelectrolytes, and MICOEs have been shown to improve the performance of microbial fuel cells. By acting as electron relay systems, the organic semiconductors enhance the efficiency of transmission of the protons and electrons produced by bacteria to the electrodes.[79, 80] Song et al. recently reported increasing the bioelectricity generation in microbial fuel cells composed of *S. oneidensis* bacteria by 14-fold upon coating with polypyrrole.[80] Coating the cathode material with polyaniline derivatives was also shown to improve the power densities of microbial fuel cells by 180%.[79]

Conjugated polymers have also been employed to stimulate certain reactions in cells. Organic semiconductors were first shown to regulate cell growth by the pivotal work of Wong and coworkers, in which they showed that the shape and growth of endothelial cells cultured on a polypyrrole thin film could be controlled by modulating the redox state of the semiconductor film.[81] The optical and electronic properties of conjugated polymers have also been extensively employed in the optical stimulation and modulation of cellular and neuronal activity.[82, 83] Conjugate semiconductors can transduce light into an electrical input and modulate the membrane potential of cells in direct contact with the polymer layer. The most impressive example of such photoactuation activity is perhaps the work reported by the Lanzani and Benfenati research groups on the restoration of vision in blind animal models.[84-86] P3HT polymers have also been recently reported to enable the spatially and temporally controlled photomodulation of the growth and fate of endothelial colony-forming cells.[87]

1.2.3. Limitations of conventional bioelectronic materials

Despite impressive advancements in the performance of conjugated semiconductors in bioelectronic devices, their transition from *in vitro* systems to marketable devices for *in vivo* use remains limited. Limitations in the use of conjugated polymers and electrolytes can be broadly classified into three categories: electrochemical stability, charge transport properties, and

biotoxicity. The most frequently used semiconductors in bioelectronic applications, listed in **Scheme 1.2**, all fall into at least one of these three categories in terms of their limitations.

The stability of organic semiconductors has been shown to decline when incorporated into bioelectronic devices and exposed to aqueous biological media for extended periods of time.[88] P3HT, polythiophene, polyaniline, and MEHPPV (and polyphenylene vinylene-based polymers in general) were all found to be electrochemically unstable in aqueous media.[89-92] Moreover, the charge transport properties of these conjugated polymers are greatly limited by their significant structural and energetic disorder arising from their flexible backbone.[93, 94]

The biggest concern, however, is the potential toxicity of these bioelectronic materials towards the biological system they are interfaced with. For instance, the thickness, roughness, and dopant nature of polypyrrole films were reported to affect the semiconducting film's biocompatibility.[95, 96] EDOT (monomer of PEDOT) was reported to decrease the viability of *S. oneidensis* upon continuous exposure.[97] DFSO+, a frequently used membrane intercalating conjugated oligoelectrolyte, was also reported to be fairly toxic even at low concentrations.[98] While the toxicity and biocompatibility of conjugated organic semiconductors are frequently assessed before application in bioelectronic devices, such assessment is typically limited to the exact conditions of the reported application, and a broader analysis of the effect organic bioelectronic materials have on the viability, integrity, and function of biological systems is often lacking. As such, one major concern is that the reported "dark" biocompatibility of key conjugated polymers and oligomers would not necessarily translate into applications involving exposure to light. Conjugated structures, being excellent fluorophores, could possibly undergo excited state processes that lead to their degradation, that of the surrounding biological system, or both.

While it is evident that novel organic bioelectronic materials are needed to achieve desired outcomes in terms of sensing and actuation in the emerging field of bioelectronics, it is also true that the design and synthesis of new bioelectronic structures must be accompanied by a thorough assessment of their biocompatibility and stability under various conditions. These conditions should include, not just electrochemical and thermal responses, but also assessment of their response (and potential toxicity) to optical stimuli.

1.3. Measuring charge transfer and redox reactions in lipid membranes

Cellular redox reactions consist of precisely balanced and concerted oxidation and reduction (redox) reactions and are critical in maintaining cellular homeostasis and regulating critical biological functions. Energy production,[99, 100] cellular signaling,[101] gene expression,[102, 103] and cellular detoxification[103, 104] all rely on redox processes. Electrochemical investigation of the precise function and properties of individual redox agents in cell membranes is challenging owing to the complex composition of cell membranes and their insulating properties.[105]

As discussed in **section 1.2.1**, organic bioelectronic materials are highly efficient electron relay systems. In particular, membrane intercalating conjugated oligoelectrolytes (MICOEs) serve as transmembrane molecular wires and were reported to improve the efficiency of electron transfer between bacterial cells and external electrodes.[65-67] Their incorporation in cell membranes holds great potential in facilitating the investigation of in- and cross-membrane redox reactions by reducing the insulation barrier presented by lipid membranes.[62] Their utilization, however, would still need to be accompanied by further characterization techniques to enable the selective induction and monitoring of biological redox reactions of interest.

This section provides a brief overview of current electrochemical characterization techniques employed in studying biological and membrane-bound redox reactions, their challenges, and promising avenues for mapping and visualizing membrane redox processes.

1.3.1. Electrochemical techniques

1.3.1.1. Bulk electrochemical measurements

Bulk electrochemical measurements consist of conventional three-electrode electrochemical systems, where electron transfers occurring between a working electrode and an analyte are monitored. Electrochemical potentials (voltages) are applied between the working electrode and a reference electrode, while currents (electron flow per unit time) are monitored between the working and counter electrodes. Redox reactions in lipid membranes are investigated by extracting the cell membrane of prokaryotic or eukaryotic cells and depositing it atop the

working electrode,[106, 107] or by assembling planar or vesicular model lipid membranes containing the redox agent of interest on top of the electrode.[108, 109]

Among other techniques, investigation of redox processes in lipid membranes consists of cycling the applied potential and monitoring the resulting changes in current as a function of applied potential (cyclic voltammetry) or applying a fixed potential (expected to result in a redox reaction) and monitoring the change in current over time (chronoamperometry).[109, 110] These measurements, in ideal cases, allow the extraction of thermodynamic and kinetic parameters associated with the redox process that occurred.[111] Potential reaction intermediates can be detected, and the occurrence of simultaneous or sequential side reactions, such as a proton transfer or chemical reaction/rearrangement following electron transfer, can be identified.[111]

While conventional bulk electrochemical measurements have the potential to provide rich information, they are limited by the large lipid membrane capacitance and require large concentrations of analyte to provide a detectable and differentiable signal. Bulk measurements are also not suitable for systems containing more than one redox agent and do not account for any spatial heterogeneity across the electrode surface.

1.3.1.2. Scanning electrochemical microscopy

First reported in 1986,[112, 113] scanning electrochemical microscopy (SECM) utilizes ultramicroelectrodes to detect localized electrochemical reactions on top of an electroactive substrate. The microelectrode tip (~ 5 µm radius) is brought within a few micrometers from the substrate, and the current resulting from redox reactions at the surfaces of the tip and substrate (both serving as independent working electrodes) is detected.[111] SECM allows to extract information on the electron transfer kinetics of the detected redox reactions. Scanning the microelectrode over the substrate surface in a raster scan fashion enables the extraction of information on surface heterogeneity with down to a 15 nm spatial resolution, depending on the tip size.[114]

SECM has been widely used to image charge transfer in biological systems,[115] including for the study of the insulation and permeation of lipid membranes,[116] mapping the production of hydrogen peroxide in biofilms,[117] and investigation of ion channel behaviors in supported lipid bilayers.[118]

1.3.2. Spectroelectrochemical techniques

While conventional electrochemical techniques are great for extracting information on analyte concentration (e.g., for sensor applications), reaction thermodynamics and kinetics, and for providing insight into potential reaction mechanisms, these techniques alone do not allow the identification of unknown intermediate species and products. The generated information is further complicated when more than one redox active species is present in the system.[119] This can be circumvented by combining reaction-focused electrochemical measurements with species-focused spectroscopic characterization, a field known as spectroelectrochemistry.

Spectroelectrochemistry is a broad field where electrochemical measurements are combined with a wide range of spectroscopic techniques, including UV-visible absorbance and fluorescence,[120, 121] infrared (IR),[122] X-ray,[123] Raman scattering,[124] and magnetic resonance.[125] This section however will focus on spectroelectrochemical techniques used to investigate biological and membrane redox reactions in lipid membranes.

1.3.2.1. Vibrational spectroelectrochemistry

Electrochemical measurements have frequently been combined with IR or Raman vibrational spectroscopy to study redox reactions in lipid membranes.[126, 127] IR spectroscopy broadly consists of irradiating a sample with a wide range of IR, typically 2500 – 25000 nm (4000 – 400 cm^{-1}) wavelengths. Only IR photons that match the vibrational energies of the sample will be absorbed, and the resulting IR absorbance spectrum reveals information on the chemical composition and structure of the molecule. IR-spectroelectrochemistry typically operates by difference spectroscopy, where the IR spectrum of the sample is taken before and after applying a potential to induce a redox reaction, and only the difference between the two spectra is analyzed to identify resulting chemical changes upon reduction/oxidation. Difference spectroscopy eliminates any contributions arising from the bulk of the sample and only shows changes resulting from the applied electrochemical potential.[128, 129] Standard IR-spectroelectrochemical difference spectroscopy, however, is limited by the weakness of the detected signal, which is often difficult to distinguish from background noise.

The signal-to-noise ratio of IR spectroscopy is enhanced 10 – 1000-fold when the sample is deposited on certain metal surfaces, such as silver and gold.[130] This technique, called surface enhanced infrared absorption spectroscopy (SEIRAS),[131, 132] consists of generating plasmonic

resonances in the metal upon interaction with the incident IR irradiation, which results in a localized enhancement of the electromagnetic field sensed by the sample at the electrode surface, and thus an enhancement in the absorbance signal. SEIRAS-spectroelectrochemistry has been the go-to method for studying redox reactions in lipid membranes, particularly for investigating membrane redox proteins.[127, 133-136]

Raman spectroscopy, like IR spectroscopy, is used to determine the molecular vibrations of a sample. Briefly, the sample is typically irradiated with a (monochromatic) laser of a wavelength ranging from ultraviolet to near-infrared, and the light scattered by the sample is captured. While the majority of scattered light will be elastic Rayleigh scattering of the same wavelength as the incident light, a tiny portion will be inelastic Raman scattering with a wavelength shift. The magnitude of the shift is determined by the molecule's vibrational modes. Raman spectroelectrochemical applications in biological processes often employ surface enhanced Raman spectroscopy (SERS),[137] which relies on a similar localized electric field enhancement process as described above for SEIRAS.[138] SERS-spectroelectrochemistry has been employed in the investigation of the oxidation mechanism of nucleobases,[139] in the study of protein interactions with lipid membranes,[140] and in the study of bacterial cells,[141] among other applications.

The major drawback of vibrational spectroelectrochemistry is that its application has been mainly confined to bulk applications, with sparce applications in IR or Raman microscopy.[142-144] Bulk measurements do not enable spatiotemporal investigations of surface heterogeneities or to map where reactions are taking place on the surface of a biological sample.

1.3.2.2. Fluorescence spectroelectrochemical microscopy

Fluorescence spectroelectrochemistry measures redox processes by following changes in the fluorescence spectra and/or intensities of reporter fluorophores. Unlike vibrational spectroelectrochemistry, where the recorded vibrational information could arise from a range of redox-active molecules in a complex biological system, fluorescence spectroelectrochemistry allows, upon careful and rational design, to report on the redox transition undergone only by the analyte of interest. As a one- or two-electron redox reaction is amplified in the form of hundreds of emitted photons, fluorescence spectroelectrochemistry is a highly sensitive technique that greatly reduces the required concentration of analyte.

The most essential and challenging step in fluorescence spectroelectrochemistry is to determine the best mechanism by which to report on the desired redox reaction. In most cases, reporting occurs via fluorogenic reactions, where the occurrence of the desired redox reaction is accompanied by an onset of fluorescence signal. Such fluorogenic reactions typically fall into one of three categories, depicted in **Figure 1.9**.[145]

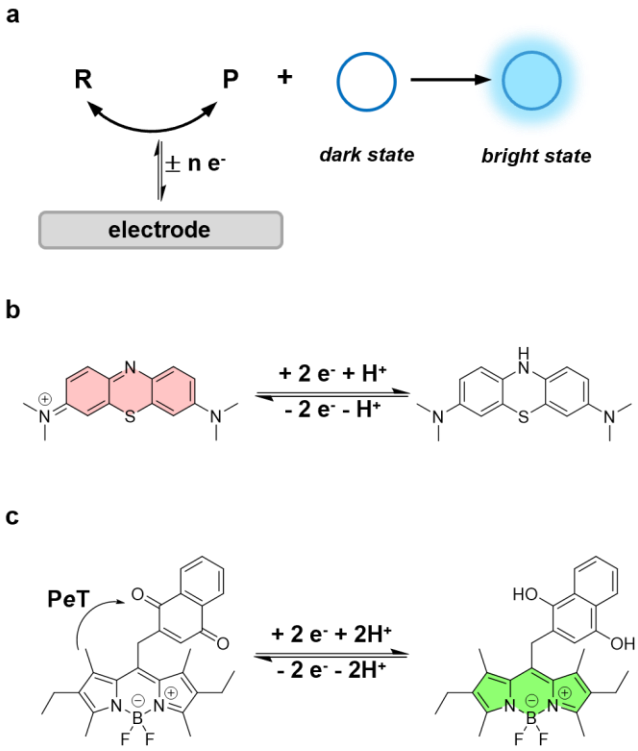

Figure 1.9. Three mechanisms of fluorescence monitoring of a redox reaction.(a)The redox conversion of an analyte of interest induces the conversion of the fluorogenic reporter from a non-emissive to an emissive state. Figure adapted from reference 146.(b) The redox reaction converts the analyte of interest from a non-emissive to an emissive form (or vice-versa). (c) The analyte of interest in tagged by a quenched fluorophore. The quenching mechanism is inactivated upon the redox conversion.

In the first case (**Figure 1.9a**), a fluorogenic reporter is added to the sample containing the analyte of interest. The reporter is initially in a non-emissive state. However, upon the redox conversion of the analyte of interest to an active form, the latter can induce the conversion of the fluorogenic reporter to its fluorescent form.[146] The activation of the fluorogenic probe can result from changes in its microenvironment or direct interaction with the product of the redox reaction. The most common applications of this redox sensing mechanism include the use of pH-sensitive

fluorescein dyes to report of proton-coupled electron transfer reactions (accompanied by a local changes in pH levels),[147, 148] as well as the sensing of ion gradients in batteries via the use of fluorophores that undergo a change in their emission intensity upon forming a complex with ionic components such as Li^+ or Mn^{2+}.[149, 150] A second fluorescent reporting mechanism involves directly reporting on the desired redox reaction, where the reactant and product exhibit different emission intensities and/or spectra (**Figure 1.9b**). Two widely used redox reporters that fall in this category are methylene blue and resazurin, which have been frequently used to report on biochemical redox reactions,[151, 152] cell viability,[153] catalytic activity of nanoparticle,[154] and heterogenous electron transfer at electrode interfaces.[155, 156] The third commonly used mechanism is labeling the analyte of interest by a fluorogenic probe, where one of the redox states of the analyte leads to the quenching of the fluorophore by energy or electron transfer, while the other state does not. Unlike the first two scenarios, this case does not involve any chemical conversions of the fluorophore and simply uses the latter to report on the desired redox reaction (**Figure 1.9c**). In this regard, our research group has developed a range of fluorogenic probes that operate through a photoinduced electron transfer (P*e*T) mechanism, and report on a variety of biologically relevant redox activity, such as that of ubiquinone,[32] menadione (Vitamin K_3),[31] and α-tocopherol.[27-30]

Since its initial inception in 1997 by Schröder and Scholz,[157] the integration of electrochemistry with fluorescence microscopy has evolved to enable the detection of redox conversions at the single molecule level,[145, 158] first reported by Bard and Barbara in 2006.[159] Electrochemical fluorescence microscopy (ECFM) enables the extraction of spatiotemporal information on the redox reactions occurring on top of the electrodes. This permits detecting surface heterogeneities and elucidating the heterogeneous behaviors within the sample, information typically lost in bulk measurements.[160] ECFM also allows to extract the thermodynamic and kinetic parameters of redox reactions.[161, 162]

ECFM has been frequently used for the investigation of the electrochemical characteristics of conducting and semiconducting materials and surfaces. Its applications are diverse and include the assessment of electrode surfaces modified by molecular adsorbates,[160] the examination of how electrode topography and structure affect the formation of self-assembled monolayers,[163] the investigation of charge transfer dynamics in dye-sensitized solar cells and polymer nanoparticles,[164, 165] and the characterization of optoelectronic properties in polymer thin films.[166] ECFM has also proven valuable in studying biological and biomimetic systems, such as visualizing

of membrane potentials,[167-170] calcium imaging,[171] mapping ion transport,[172] and examining membrane stability and deformation.[173, 174] However, surprisingly, only a couple studies report the use of ECFM for the investigation of redox reactions in lipid membranes.[175, 176] There is thus vast room to explore the utilization of this highly sensitive method for the selective control and investigation of membrane redox reactions.

1.4. Singlet oxygen and lipid peroxidation

Lipid peroxidation is a critical biomarker observed in a wide range of human diseases characterized by the prevalence of oxidative stress, a condition where there is an imbalance between the rate of generation of reactive oxygen species (ROS) and the rate of depletion/detoxification of these species and their associated products. Initially regarded as exclusively detrimental, emerging evidence suggests that lipid peroxidation plays a vital role in preserving cellular homeostasis and facilitating essential signaling pathways.[177-179] However, when unregulated, the accumulation of lipid oxidation products can result in cellular death and the development of pathological conditions.[180] Notably, lipid peroxidation has been associated with neurodegenerative disorders such as Alzheimer's, Parkinson's, and amyotrophic lateral sclerosis (ALS).[181-184] Lipid peroxidation was also shown to play an essential role in regulated cell death pathways such as apoptosis, necrosis, and the more recently reported ferroptosis.[185-187]

Lipid peroxidation can be triggered by multiple mechanisms, such as enzymatic pathways,[188] ROS-initiated lipid chain autooxidation,[189] and reaction with singlet oxygen ($^1O_2$).[190, 191] The production of $^1O_2$ can occur through photosensitization when molecular oxygen reacts with a photoexcited triplet state photosensitizer, as discussed in **Section 1.1.3.2**. Consequently, caution should be exercised when considering the incorporation of photoactive molecules, such as optoelectronic materials, into lipid membranes, and the potential phototoxicity of such additives must be carefully evaluated.

This section introduces the physical and chemical properties of $^1O_2$, including its mechanisms of generation and deactivation. Furthermore, it delves into the impact and outcomes of the reaction of singlet oxygen with lipid membranes. Additionally, the section briefly examines the physical principles governing the current tools used for detecting $^1O_2$ and addresses their limitations.

1.4.1. Chemistry and reactivity of singlet oxygen

1.4.1.1. Electronic configuration and reactivity of molecular oxygen

The ground state of molecular oxygen has an unusual electronic configuration. Unlike most molecules which exist in a closed shell configuration in their ground state with no unpaired electrons and a singlet spin multiplicity, ground state molecular oxygen exists as a biradical with a triplet spin multiplicity, with two unpaired electrons occupying two degenerate antibonding π* orbitals.[192] The first two electronic excited states of molecular oxygen, $^1\Delta_g$ and $^1\Sigma_g^+$, are singlet states lying 95 and 158 kJ mol^{-1} above the ground state, respectively, with the two unpaired electrons of opposite and out of phase spins occupying either one of or both antibonding π^* orbitals (**Figure 1.10**).[193] The $^1\Sigma_g^+$ state of oxygen is extremely short-lived and rapidly decays to the $^1\Delta_g$ state, the latter being metastable due to the spin-forbidden relaxation to the ground state.[194] As such, the term "singlet oxygen" ($^1O_2$) typically refers to the $^1\Delta_g$ excited state.[193, 195]

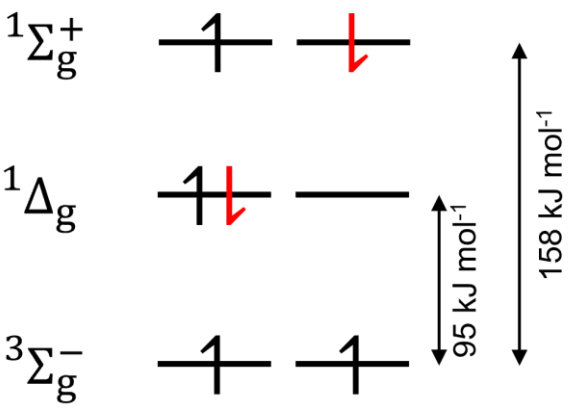

Figure 1.10. Electronic configuration of the two degenerate π* antibonding orbitals of molecular oxygen in its ground and two lowest excited states.

Ground state triplet oxygen $^3O_2$ can readily undergo one-electron reactions with radicals. However, for $^3O_2$ to spontaneously react with a non-radical molecule, it would need to accept two electrons with spins in a triplet state configuration. Since most ground state non-radical organic molecules are diamagnetic with paired electrons of opposite and out of phase spins, $^3O_2$ is essentially (and fortunately) unreactive. On the other hand, the electrophilicity, excited state energy, and singlet multiplicity of $^1O_2$ renders it a highly reactive molecule that readily oxidizes surrounding organic molecules.[190, 191]

1.4.1.2. Formation of singlet oxygen

$^1O_2$ can be generated through multiple chemical and photochemical pathways. For example, $^1O_2$ is endogenously chemically generated through enzymatic pathways catalyzed by peroxidases and oxygenases and is produced by neutrophils during phagocytosis, typically through a reaction of H_2O_2 with HOCl or $O_2^{\bullet-}$ (**Scheme 1.3**).[196, 197] As described in **Section 1.1.3.2**, $^1O_2$ can also be photochemically generated through a triplet-triplet annihilation (Dexter energy transfer) reaction between $^3O_2$ and a photosensitizer (PS) in its excited triplet state ($^3PS^*$). Energy transfer between $^3PS^*$ and $^3O_2$ to generate $^1O_2$ is known as a Type II photosensitization mechanism (**Scheme 1.4**). An alternative photosensitization mechanism (Type I) involves an electron or a hydrogen atom transfer between $^3PS^*$ and a substrate, where newly formed products further react with $^3O_2$ to yield different ROS species (**Scheme 1.4**).[198] It is worth mentioning that both Type I and Type II photosensitization may occur from the singlet excited state of the photosensitizer ($^1PS^*$), however such processes are unlikely given the short lifetime of $^1PS^*$, and most photosensitization typically occurs from the triplet excited state $^3PS^*$.

Scheme 1.3. Chemical generation of $^1O_2$.

$$H_2O_2 + HOCl \rightarrow {}^1O_2 + H_2O + Cl^- + H^+$$

$$H_2O_2 + O_2^{\bullet-} \rightarrow {}^1O_2 + {\bullet}OH + OH^-$$

$^1O_2$ can be photochemically generated in a biological system by endogenous photosensitizers such as flavins, pterins, and porphyrins, or by addition of an exogenous photosensitizers.[199] The efficiency by which a photosensitizer generates $^1O_2$ is characterized by its $^1O_2$ photosensitization quantum yield, Φ_Δ. The Φ_Δ depends on the efficiency of two processes: the intersystem crossing (ISC) from $^1PS^*$ to $^3PS^*$, and the energy transfer from $^3PS^*$ to $^3O_2$. One way to control the $^1O_2$ generation capability of a photosensitizer is by controlling its ISC rate. As described in detail in **Section 1.1.2.2**, the rate of ISC can be controlled through molecular design approaches, such as catalyzing spin-orbit coupling through additions of heavy atoms to the molecular structure of the PS, or through reducing the singlet-triplet energy gap of the PS by spatially separating its HOMO and LUMO orbitals.[7, 200]

Scheme 1.4. Type I and Type II mechanisms of photosensitized oxidation[a]

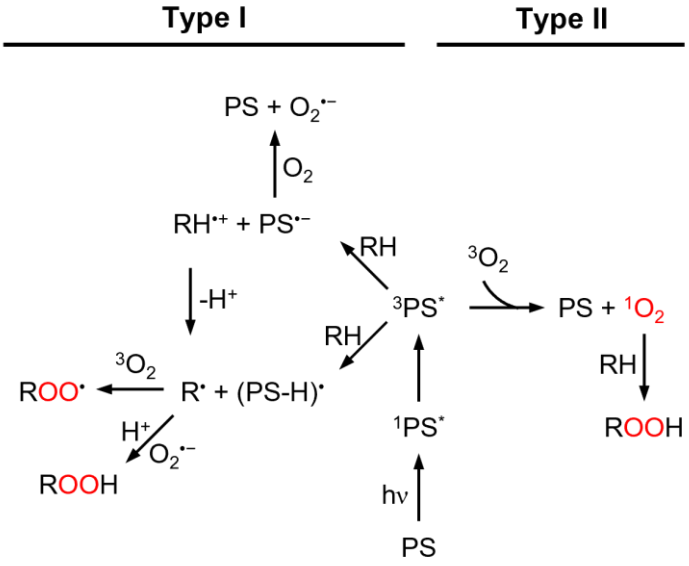

[a] Adapted from reference 191.

1.4.1.3. Singlet oxygen decay pathways

Upon its formation, $^1O_2$ can be deactivated through several pathways,[201] summarized in **Scheme 1.5** below. $^1O_2$ can relax back to ground state $^3O_2$ radiatively by emission of a photon (phosphorescence) at ~ 1275 nm. The phosphorescence signal of $^1O_2$ is however very weak due to the spin forbidden nature of the transition and the competing non-radiative deactivation of $^1O_2$ by surrounding solvent molecules. The latter occurs through an electronic-to-vibrational energy transition, whereupon the electronic excitation energy of $^1O_2$ is transformed into vibrational energy in O_2 and surrounding solvent molecules. The efficiency of this deactivation mode is solvent-dependent and correlates with the energy of the highest-frequency vibrational mode of the solvent. As such, $^1O_2$ decay rate increase with increasing "concentration" of C-H bonds, and is the highest in solvents containing O-H bonds, with k_d values ranging from 3×10^5 s^{-1} in H_2O to ~20 s^{-1} in CS_2.[201] With $^1O_2$ being readily deactivated in H_2O, its phosphorescence quantum yield is estimated to be around 10^{-6}.[195]

The presence of a quencher Q in solution further increases the deactivation rate of $^1O_2$ through a physical and/or chemical quenching mechanism. Physical quenching of $^1O_2$ results in the regeneration of ground state $^3O_2$ and an intact Q. This quenching pathway typically proceeds through the formation of an excited state charge transfer complex (exciplex) between $^1O_2$ and Q,

$^1(Q^1O_2)$, which decays by undergoing ISC to a ground state triplet complex, $^3(Q^1O_2)$, followed by dissociation to ground state Q and $^3O_2$.[201] Reaction-less decay of the $^1(Q^1O_2)$ exciplex directly competes with the highly reactive nature of $^1O_2$, whereupon $^1O_2$ is chemically quenched upon oxidizing the quencher.

Scheme 1.5. $^1O_2$ deactivation pathways

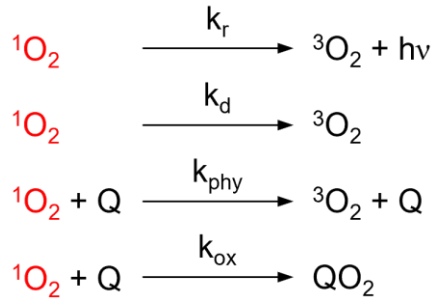

1.4.2. Lipid peroxidation mechanism and outcomes

1.4.2.1. Oxidation of lipids by $^1O_2$

Given its lifetime in aqueous media (~3.5 µs in pure H_2O, ~2 µs in cells),[195] $^1O_2$ can only react with targets present within ~200 nm from the location of its generation. When produced in biological systems, $^1O_2$ can readily oxidize biomolecules and unsaturated compounds such as proteins, nucleic acids, and unsaturated lipids.[190, 191] The peroxidation of lipids composed of mono- and polyunsaturated fatty acids proceeds via the *ene* reaction, whereupon addition of $^1O_2$ to either end of the carbon-carbon double bond results in the shift of the double bond to an allylic position and the production of a lipid hydroperoxide (**Scheme 1.6**).

Scheme 1.6. $^1O_2$ *ene* reaction

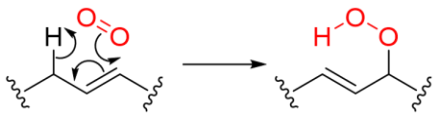

The bimolecular rate constant of $^1O_2$ quenching by unsaturated fatty acids (k_q) depends on the nature of the fatty acids, and ranges from $1.7 \times 10^4\ M^{-1}\ s^{-1}$ for the monounsaturated oleic acid to $15 \times 10^4\ M^{-1}\ s^{-1}$ for docosahexaenoic acid, bearing 6 double bonds.[202] Quenching of $^1O_2$ by

lipids occurs through both physical and chemical (*ene* reaction) quenching pathways, with the latter typically dominating and accounting for 60-95% of the total quenching rate constant.[202]

The formation of lipid hydroperoxides is accompanied by changes to the physical properties of the lipid membrane. The hydrophilic nature of the hydroperoxide group results in its migration closer to the water-lipid interface. This leads to an increase in the area occupied by the lipid, and thus an increase in the total membrane surface area accompanied by a decrease in membrane thickness and the generation of "floppy", fluctuating membranes (**Figure 1.11**).[203] The percentage of area increase depends on the nature and degree of unsaturation of the lipid, with values ranging between 15-50% increase in area per lipid having been reported.[204, 205]

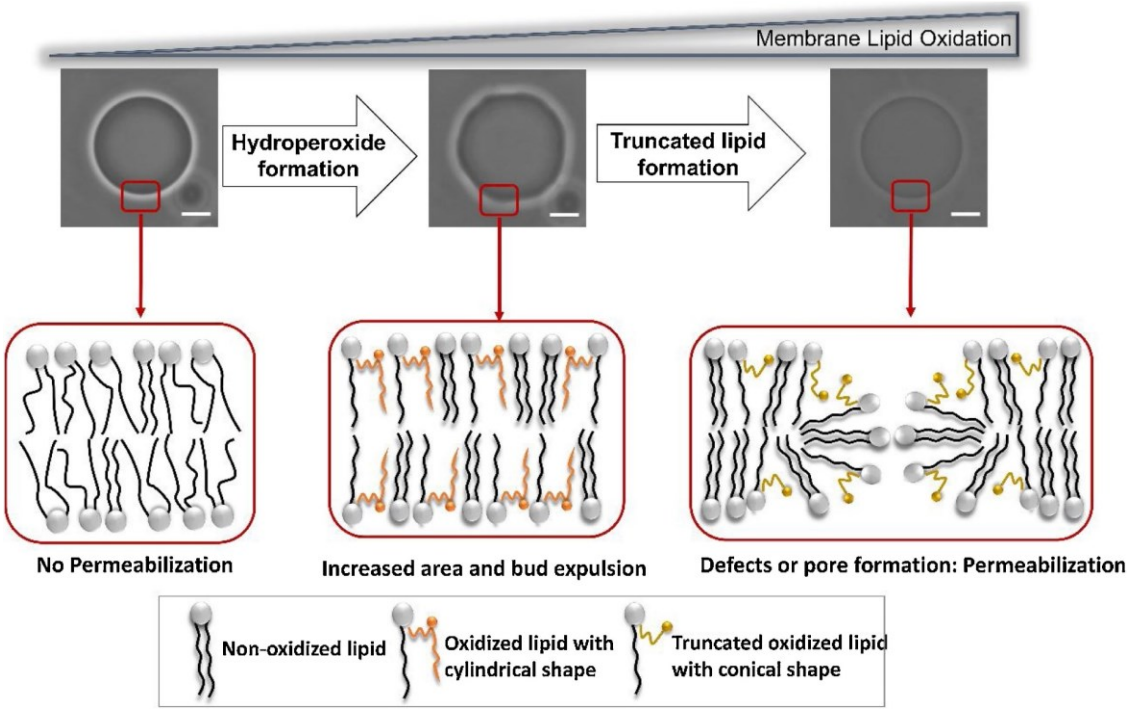

Figure 1.11. Schematic illustration of the dynamic morphological changes underwent by lipid membranes upon their photooxidation. Images correspond to phase contrast microscopy of a giant unilamellar vesicle composed of unsaturated lipids. The vesicle interior and exterior solutions are equimolar sucrose and glucose solutions, respectively. The different densities of the two solutions drive the vesicles down towards the substrate. The sketches under the microscopy images highlight the role of lipid shape and packing on the physical properties on the lipid membrane. Scale bar = 10 μm. Reproduced with permission from reference 203.

1.4.2.2. Membrane permeabilization

Despite inducing morphological changes in membranes, lipid hydroperoxides, generated upon oxidation by $^1O_2$ or other radical-mediated pathways, interestingly do not compromise the integrity of the membrane or lead to its permeabilization.[203] This was evident by phase-contrast microscopy studies on giant unilamellar vesicles containing interior and exterior solutions of different refractive indexes (sucrose and glucose, respectively), where the phase contrast was maintained upon formation of lipid hydroperoxides, indicating a lack of mixing between the two solutions (**Figure 1.11**). However, the formation of secondary oxidation products following lipid peroxidation was accompanied by a reduction in vesicle size and fluctuation, and the loss of phase contrast between the vesicle interior and exterior, indicating the formation of pores along the membrane, allowing mixing the contents of the two solutions.[206]

Product studies done following the oxidation of giant and large unilamellar vesicles (liposomes) composed of unsaturated lipids indicated that the formation of membrane pores and subsequent membrane permeabilization requires the formation of lipid alkoxyl radicals that undergo β-scission and generate truncated oxidized lipids bearing short chain aldehydes and carboxylic acids.[207, 208] The conical shape of these truncated lipids (compared to the cylindrical shape of non-oxidized lipids and lipid hydroperoxides) results in a change in membrane packing and the formation of pores,[207] leading to membrane permeabilization.[209, 210] The remodeling of lipid membranes following their photosensitized oxidation has been shown to trigger multiple cell death pathways.[203]

1.4.2.3. $^1O_2$ quenching by α-tocopherol

To combat the detrimental consequences of photosensitized lipid oxidation, biological systems possess their own protective mechanisms. One such mechanism is the Vitamin E antioxidant family. The most metabolic active form of Vitamin E is α-tocopherol (**Scheme 1.7**), which has been shown to efficiently inhibit the oxidative action of free radicals and $^1O_2$.

α-tocopherol quenches $^1O_2$ with a bimolecular quenching rate constant (k_q) ranging between $1.48 – 6.7 \times 10^8$ M^{-1} s^{-1}, depending on the solvent,[211-215] strongly outcompeting the quenching of $^1O_2$ by fatty acids ($k_q = 10^4 – 10^5$ M^{-1} s^{-1}). The quenching of $^1O_2$ by α-tocopherol occurs through a predominantly physical quenching mechanism, with chemical quenching (oxidation of α-tocopherol) accounting for only 1 – 7% of the total quenching rate constant.[212-215]

Chemical quenching of $^1O_2$ by α-tocopherol produces an unstable hydroperoxide (referred to as tocopherone or hydroperoxydienone), which rapidly decomposes to form a tocopherol-quinone (**Scheme 1.7**).[216, 217] The exact mechanism by which the tocopherol-hydroperoxide forms is not known, but has however been suggested to proceed via an *ene*-type reaction as opposed to through the previously suggested formation of an endoperoxide.[216, 218]

Scheme 1.7. Product of chemical quenching of $^1O_2$ by α-tocopherol

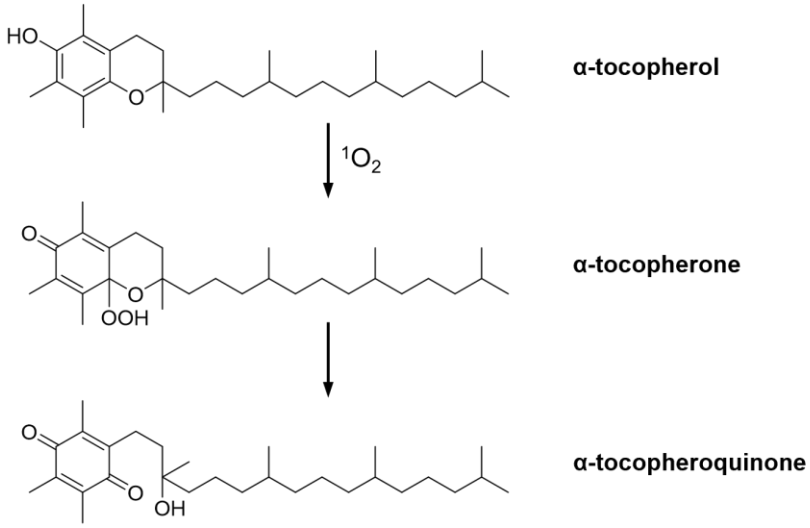

1.4.3. Singlet oxygen sensing

Given the important role that $^1O_2$ plays in cell signaling and pathologies, a wide range of probes have been developed to detect its formation.[219, 220] These probes rely on a change in their photophysical properties upon oxidation by $^1O_2$, such as changes to their absorbance or photoluminescence (fluorescence, phosphorescence, or chemiluminescence) intensity and/or spectra.[219] Among those, fluorescence turn-on probes (fluorogenic probes) have gained the most attention and use owing to their larger signal and superior sensitivity.

To serve as quantitative $^1O_2$ sensors in biological systems, as opposed to qualitative indicators of its generation, $^1O_2$ probes must meet certain requirements. The probe should be biocompatible and selectively react with $^1O_2$ over other reactive oxygen species (ROS). The reaction of the probe with $^1O_2$ should generate an easily detectable signal that allows to monitor the reaction kinetics of $^1O_2$. To guarantee the latter, $^1O_2$ quenching by the probe should outcompete all other $^1O_2$ deactivation pathways, including its reaction with other biomolecules and its natural

decay in solvent. Importantly, the probe should not itself generate any $^1O_2$ or other ROS, either before or after reacting with $^1O_2$.[221]

The up to date reported and commercially available fluorogenic $^1O_2$ sensors predominantly consist of a receptor-reporter construct, where the reporter is a fluorophore covalently linked to an organic receptor moiety that demonstrates fast reaction kinetics with $^1O_2$. The fluorescence of the reporter fluorophore is quenched by the non-oxidized receptor segment, typically through an electron or energy transfer mechanism. However, upon the trapping of $^1O_2$ by the receptor, the quenching mechanism is deactivated, and the fluorescence of the reporter fluorophore is restored. The vast majority of reported fluorogenic $^1O_2$ sensors utilize anthracene derivatives as $^1O_2$ traps, owing to their selective and fast quenching of $^1O_2$. The reaction kinetics of anthracene-derivatives is however strongly dependent on their substitutions, as switching from a 9,10-dimethyl anthracene to a 9,10-diphenyl anthracene decreases the $^1O_2$ quenching rate constant by 100 – 1000-fold (depending on the solvent used).[222] Other trapping moieties such as tetracene and 5-membered heteroarenes have also been employed.[219, 220] A wide range of fluorophores have been utilized as reporter segments, such as boron dipyrromethene (BODIPY), cyanines, and silicon-rhodamines, although xanthene-based dyes remain largely the most frequently used fluorophore structures. The most commonly used example of such probes is the commercially available Singlet Oxygen Sensor Green (SOSG), composed of a fluorescein fluorophore that is quenched through a photoinduced electron transfer (P*e*T) mechanism by a covalently linked anthracene trap. Upon the oxidation of the anthracene moiety and formation of an endoperoxide (SOSG-EP), the P*e*T quenching pathway is deactivated, and the probe becomes emissive (**Scheme 1.8**). Here, the emission intensity enhancement of ~48-fold is expected upon the oxidation of SOSG to SOSG-EP, given the reported emission quantum yields for both species of 0.009 and 0.43 respectively.[223]

To date, most reported and commercially available $^1O_2$ sensors suffer some drawbacks, such as slow turn-on response, pH sensitivity, low incorporation into biological systems, and vulnerability to photooxidation.[219] The major pitfall however is that a large number of reported $^1O_2$ sensors are themselves capable of sensitizing the formation of $^1O_2$, leading to an overestimation of the amount and rate of $^1O_2$ generation.[219, 223, 224] Reported $^1O_2$ sensors that do not themselves have any photosensitization properties tend to fall short in other required criteria, such as having a limited enhancement in fluorescence intensity upon $^1O_2$ trapping.[225] It is thus evident that novel $^1O_2$ sensors that meet the above listed criteria are needed.

Scheme 1.8. Reaction of SOSG with $^1O_2$[a]

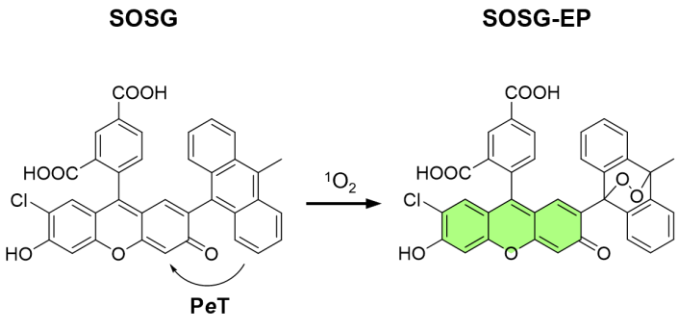

[a] Adapted from reference 223

1.5. Techniques in epifluorescence microscopy

Fluorescence microscopy is a valuable tool that enables the extraction of both static and dynamic information of a system. Owing to its versatility, fluorescence microscopy is used for the investigation of a plethora of physical, chemical, and biological systems. This includes the characterization of exciton transport in quantum dots,[226] the stoichiometric and dynamic study of DNA self-assembled materials,[227, 228] and the quantification of the catalytic properties of nanoparticles and enzymes,[229] to name a few. Additionally, fluorescence microscopy allows to visualize and report on the chemical dynamics and resulting morphological changes within biological and biomimetic systems such as supported lipid bilayers,[230] giant unilamellar vesicles,[231] eukaryotic cells,[27] and bacteria.[232] These examples constitute only a small overview of the extensive range of applications of fluorescence imaging.

Advancements in fluorescence microscopy have facilitated the observation of reactions at the single molecule level, allowing to extract statistical distributions pertaining to static and dynamic heterogeneities within a system and to better elucidate the structure-property relationship of materials. Among its vast applications, single molecule fluorescence microscopy (SMFM) techniques have allowed to map single chemical reactions in cells,[233] to investigate supramolecular assemblies,[234] and to contribute to the elucidation of photophysical processes and photochemical reaction mechanisms.[235] SMFM is however diffraction limited and unable to resolve features smaller that the diffraction limit of light (~250 nm).[236] Impressive super-resolution (SR) techniques have emerged in the past three decades to circumvent this limitation.[237-239] Recognized with a

Nobel Prize in Chemistry in 2014 for Eric Betzig, Stefan Hell, and W. E. Moerner,[240] SR microscopy enables to resolve features ~10-20 nm apart. SR microscopy has significantly advanced our understanding of complex, sub-diffraction limited systems. As such, SR microscopy is now commonly used for the characterization of complex materials such as supramolecular fibers, block copolymers, and DNA origami,[241, 242] and has enabled the visualization subcellular structures with unprecedented details.[243, 244] Most recently, the Jungmann group reported an impressive breakthrough in fluorescence microscopy, achieving unprecedented Ångström resolution,[245] and one can only imagine the possibilities and scientific advancements to follow.

In this section, we introduce the fundamental principles and configurations of epifluorescence microscopy, which serve as the foundation for advanced imaging techniques. Specifically, we will focus on fluorescence imaging methodologies employed throughout this thesis, including total internal reflection fluorescence microscopy and electrochemical fluorescence microscopy.

1.5.1. Fundamentals in epifluorescence microscopy

Fluorescence microscopy setups consist of four essential components: a light source for exciting molecules/fluorophores, an objective lens, a detector for capturing emitted photons, and the sample. In epifluorescence microscopy, a single microscope objective serves the dual purpose of directing excitation light towards the sample and collecting emitted photons. This epifluorescence configuration minimizes the collection of excitation photons by the detector. Various light sources can be used for excitation as long as they provide photons of the appropriate wavelength to be absorbed by the fluorophores in the sample. Monochromatic lasers however have the advantage of offering precise control over the excitation wavelength and greatly minimize unwanted cross excitation in samples with multiple fluorophores. The choice of detector depends on the illumination method used for the sample. In epifluorescence microscopy, the excitation methods can be broadly classified into two categories: confocal microscopy and widefield microscopy.

Confocal microscopy utilizes point illumination where the excitation light is focused to a diffraction-limited spot that is approximately Gaussian in intensity profile with dimensions of ~200 nm (lateral) and 500 nm (axial) for a high numerical aperture objective (e.g. NA ~ 1.4) (**Figure 1.12a**). Collected photons are passed through a pinhole placed before the detector, which

effectively rejects all out of focus light such that only photons from the focal spot in the sample are collected by the detector.[246] Detectors used in confocal microscopy are single point detectors, such as avalanche photodiodes (APDs) or photomultiplier tubes (PMTs). The single point excitation and detection configuration of confocal microscopy enables excellent signal-to-background ratios and temporal resolutions (down to ~10 μs).[247] However, image construction in traditional laser scanning confocal microscopy (LSCM) relies on the gradual construction of an image upon raster scanning, a time-consuming process that can take several seconds per image depending on the desired resolution. As a result, LSCM may not be suitable for studying systems with rapid dynamic transitions when simultaneous acquisition of multiple points in space is required. However, more advanced confocal microscopy setups circumvent this problem, such as in spinning disk confocal microscopy which uses a rotating disk of pinholes to image multiple points at once.[248]

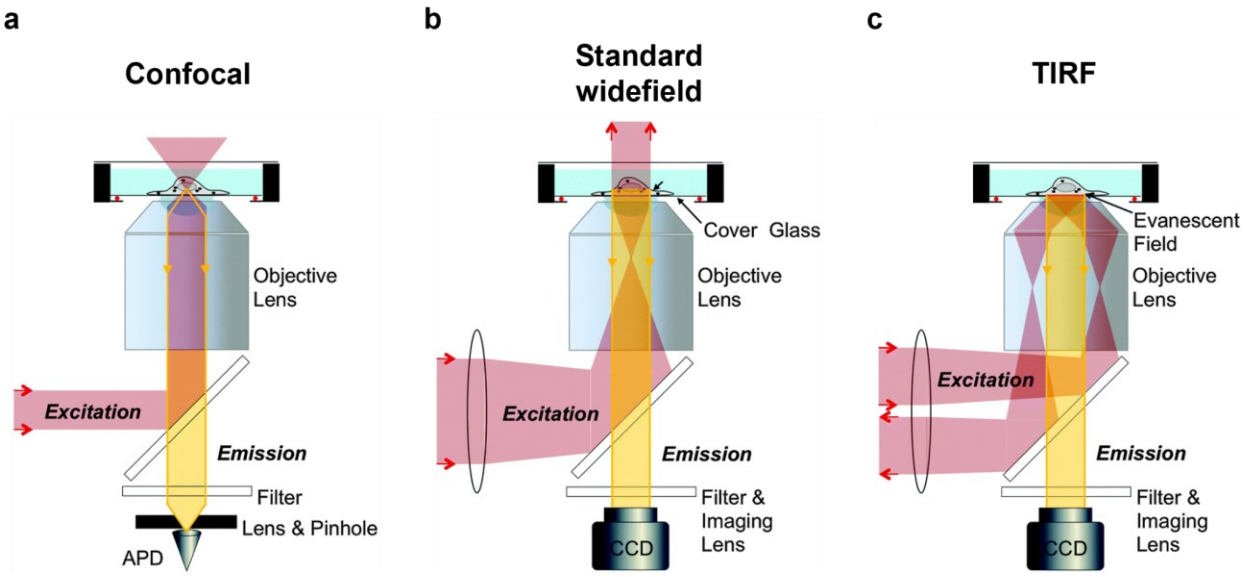

Figure 1.12. Confocal and widefield microscopy setups. (a) Standard confocal microscopy setup. (b) Standard widefield microscopy setup. (c) Total internal reflection fluorescence (TIRF) microscopy setup. Adapted with permission from reference 249.

In contrast, widefield microscopy illuminates a large area of the sample at once, ranging from ~ 82 × 82 μm^2 using a 100× objective to ~ 400 × 400 μm^2 with a 20× objective, enabling simultaneous acquisition of spatial and temporal information (**Figure 1.12b**). The emitted photons are collected, filtered, and directed towards a multi-point detector, such as an electron multiplying

charged couple device (EMCCD) or a scientific complementary metal oxide semiconductor (sCMOS) camera. Imaging frequencies of 20-50 Hz are typically used (20-50 ms per frame) when imaging over the entire area of as EMCCD pixel array, and faster acquisition frequencies can be achieved upon decreasing the imaging area. In standard widefield microscopy, the collimated Gaussian-shaped excitation beam is directed perpendicular to the coverslip surface, ensuring maximum illumination volume (**Figure 1.12b**).[250] This configuration is well-suited for imaging thick samples, such as cells or giant unilamellar vesicles. However, when imaging thin samples or single molecules positioned directly on the sample coverslip, a large excitation volume can be problematic. Unwanted background emission originating from above the coverslip focal plane can overshadow the desired emission from the sample.[250]

1.5.2. Total internal reflection fluorescence microscopy

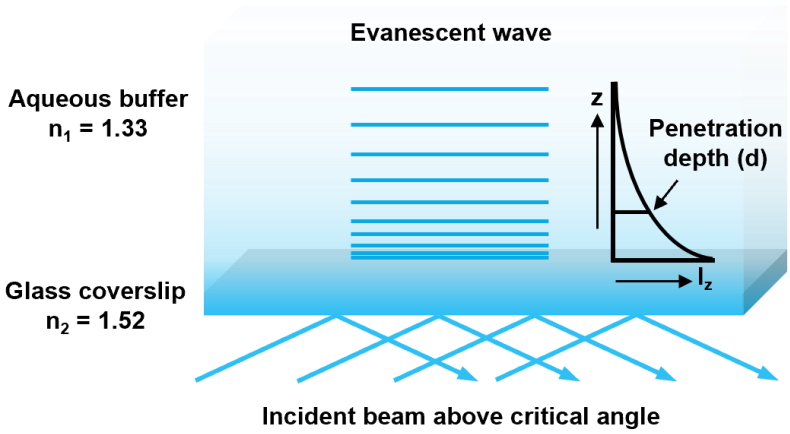

Figure 1.13. Evanescent wave generated upon total internal reflection of incident beam. Adapted with permission from reference 251.

Total internal reflection fluorescence (TIRF) microscopy is a subtype of widefield microscopy that confines the imaging volume to a thin sheet above the sample coverslip (**Figure 1.12c**).[249, 251] In TIRF microscopy, the excitation beam is focused off-axis onto the back focal plane of the objective, causing the beam to be directed towards the sample at an angle. At the interface glass/water interface, the change in refractive index (1.52 for glass and 1.33 for water) results in a change in the direction of the beam. If the incident angle exceeds the critical angle θ_c, the beam undergoes total internal reflection and is redirected back towards the objective (**Figure 1.13**). The

critical angle can be calculated using Snell's law (**eqs 1.10** and **1.11**), where the subscripts 1 and 2 refer to the aqueous media and glass coverslip, respectively, θ denotes the beam propagation angle, and n represents the refractive index of the medium. The critical angle θ_c is determined by setting $\theta_1 = 90°$, yielding $sin(\theta_1) = 1$.[252]

$$n_1 \sin(\theta_1) = n_2 \sin(\theta_2) \tag{1.10}$$

$$\theta_c = \sin^{-1}\left(\frac{n_1}{n_2}\right) \tag{1.11}$$

The central feature of TIRF microscopy is that while the excitation beam undergoes total internal reflection when directed at an angle above the critical angle, some of the incident energy penetrates the glass/water interface and generates a standing wave called an evanescent field or evanescent wave. The intensity of this evanescent wave (I_z) exponentially decreases with increasing distance (z) from the interface, as described by **eq 1.12**.[251, 252] Here, I_0 denotes the intensity of the evanescent field at the glass/water interface ($z = 0$) and d represents the penetration depth of the evanescent field, given by **eq 1.13**.[251, 252] The penetration depth depends on the angle of incidence, the refractive indices of the propagating media, and the wavelength of the incident light in vacuum (λ_0). The intensity decay of the evanescent field leads to a confinement of the excitation volume to the coverslip surface. Consequently, only fluorophores located within this limited region (d ~300 nm) are effectively excited, while fluorophores or impurities away from the coverslip plane are not excited (not detected, thus minimizing background). This confinement enhances the signal-to-background ratio, allowing for the detection of minute features, including single molecules.

$$I_z = I_0 e^{-z/d} \tag{1.12}$$

$$d = \frac{\lambda_0}{4\pi(n_2^2 \sin^2(\theta_2) - n_1^2)^{1/2}} \tag{1.13}$$

1.5.3. Electrochemical fluorescence microscopy

Electrochemical fluorescence microscopy (ECFM) is a powerful technique that allows for simultaneous acquisition of spatiotemporal photophysical and electrochemical information. By correlating changes in the redox state of a system with corresponding changes in fluorescence intensity, ECFM provides indirect and highly sensitive insight into the electrochemical properties of the system, as discussed in **Section 1.3.2.2**.

ECFM is a versatile tool applicable to various systems. The only fundamental requirement is that the sample surface be optically transparent for excitation and photon collection, as well as electrically active to enable the application of an electrochemical potential and induce redox reactions. Indium tin oxide (ITO)-coated glass coverslips are commonly used substrates due to their favorable optical and electronic properties,[159, 165, 253-256] although any optically transparent semiconducting coating is theoretically a suitable substrate.

ECFM imaging can be conducted using both TIRF[159, 165, 253] and confocal microscopy[254-256] configurations (**Figure 1.14**), with the choice of imaging modality depending on the nature of required measurements. The imaging chamber consists of a three-electrode system. The sample surface substrate functions as the working electrode (WE), where the desired redox reactions occur. Electrochemical potentials are applied between the WE and a reference electrode (RE) to drive the redox reactions, and the resulting currents are measured between the WE and the counter electrode (CE).[111] An external potentiostat is used to control and connect all three electrodes (**Figure 1.14**).

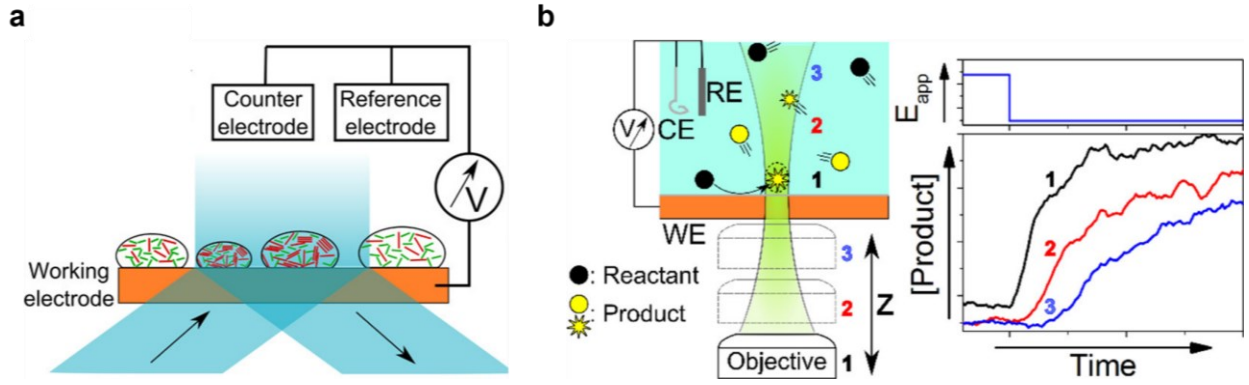

Figure 1.14. ECFM setups and measurements. (a) Configuration of a TIRF-ECFM setup. (b) Confocal-ECFM configuration and representative data that could be extracted from ECFM measurements. Figures adapted with permission from references 165 and 256.

Reference electrodes are designed such that their composition and electrochemical properties remain constant throughout the measurements. This stability ensures precise control over the potential applied at the surface of the working electrode (WE). The choice of RE depends on the solvent used in ECFM measurements. In aqueous media, silver/silver chloride (Ag/AgCl) and standard calomel electrodes (SCE) are commonly employed due to their high stability and accurate half-cell potentials. However, measurements in organic solvents pose some challenges as robust reference electrodes prepared in organic solvents are not readily available. In such cases, an Ag/Ag^+ quasi-reference electrode (Ag wire immersed in an AgNO3 + supporting electrolyte solution) is often used but requires calibration using a ferrocene/ferrocenium internal standard immediately before or after ECFM measurements. CEs typically consist of platinum wire or platinum mesh.

The electrochemical cell containing the deposited sample is mounted atop the fluorescence microscope and is often purged and maintained under argon flow to create an oxygen-free environment. The sample is then excited, and its fluorescence intensity is recorded before, during, and after the application of an electrochemical potential (**Figure 1.14b**). The recorded intensity-time profiles are then analyzed in relation to the applied potential. Depending on the nature of the applied potential (e.g., constant or varying over time), statistical distributions of the thermodynamics and kinetics of the redox process can be obtained at analyte concentrations significantly lower than those required for conventional bulk electrochemical measurements.

1.6. Objectives and scope

The integration of biological systems with external bioelectronic materials enables the investigation of crucial biological redox processes involved in cellular function and homeostasis. Successful interfacing of biotic and abiotic components relies on the utilization of biocompatible organic bioelectronic materials, which facilitate interconnectivity and enable selective control and monitoring of biological redox processes. Despite notable advancements in bioelectronic devices, several challenges remain. These include the limited stability and charge transport properties of commonly used organic bioelectronic materials, uncertainties regarding the photostability and phototoxicity of these optically active materials when subjected to optical stimuli, and the difficulty of measuring redox signals in lipid membranes.

This thesis aims to achieve two primary objectives. The first is to develop advanced fluorescence microscopy platforms that enable the selective and controlled induction and monitoring of redox processes in lipid membranes, both chemically and electrochemically. These platforms will also allow the investigation of the resulting impact on membrane integrity and dynamics. The second aim is to implement the developed platforms to study the properties and effects of novel bioelectronic materials embedded within lipid membranes.

To that end, **Chapter 2** reports a new fluorescence imaging platform for the quantitative sensing of the oxidative damage to lipid membranes. In this work, we demonstrate the ability of an α-tocopherol (Vitamin E)-based fluorogenic probe (H_4BPMHC) to quantitatively report in real-time on the flux of photosensitized singlet oxygen ($^1O_2$) impinging on giant unilamellar vesicles (GUVs), and the associated GUV morphological changes. This sensor undergoes a large linear enhancement in its emission intensity (> 350-fold in liposomes) upon trapping $^1O_2$, allowing for a straightforward quantitative assessment of the amount of photosensitized $^1O_2$ generated over time. The flux of $^1O_2$ is then correlated with the ensuing membrane deformation dynamics and explored as a function of water-born vs membrane-born $^1O_2$.

Chapter 3 presents the development of an innovative electrochemical fluorescence microscopy (ECFM) platform designed for the controlled induction and mapping of redox turnovers in supported lipid bilayers. The study utilizes H_4BPMHC as a case study, where its redox conversions are amplified and monitored as changes in fluorescence intensity in response to the application of an electrochemical potential. The platform demonstrates remarkable sensitivity, enabling the detection of redox conversions equivalent to femtoampere currents with excellent signal-to-background ratios. Moreover, the ECFM platform enables the extraction of reaction thermodynamic (such as half-wave potentials) and kinetic information.

The motivation behind **Chapter 4** of the thesis was to utilize the platforms developed in **Chapters 2** and **3** to enhance the electrical connectivity between lipid membranes and electrode surfaces using novel bioelectronic molecular wires. As an initial step, we investigate in **Chapter 4** the membrane photostability and phototoxicity of semiconducting acceptor-donor-acceptor (ADA) constructs as potential building blocks of novel bioelectronic materials. Through imaging studies, unexpected and abrupt glass-supported lipid membrane deformation and reorganization were observed upon photoexcitation of the ADA oligomers. Detailed investigation into the underlying chemical mechanism revealed the involvement of ADA-photosensitized $^1O_2$-mediated

membrane peroxidation. Leveraging the $^1O_2$-sensing platform established in **Chapter 2**, the studies demonstrated the requirement of a threshold level of $^1O_2$ flux to induce membrane reorganization.

Overall, this thesis has presents innovative methodologies that significantly contribute to the understanding of chemically and electrochemically induced redox processes in lipid membranes and that have the capacity to drive the progress of bioelectronic interfaces and open avenues for future explorations into the dynamic characteristics of lipid membranes when subjected to chemical insults.

1.7. References

1. Perrin, F. In *La fluorescence des solutions-Induction moléculaire.–Polarisation et durée d'émission.–Photochimie*, Annales de physique, EDP Sciences: 1929; pp 169-275.
2. Jablonski, A., Efficiency of anti-Stokes fluorescence in dyes. *Nature* **1933,** *131* (3319), 839-840.
3. Jabłoński, A., Über den mechanismus der photolumineszenz von farbstoffphosphoren. *Z. Phys.* **1935,** *94* (1-2), 38-46.
4. Valeur, B.; Berberan-Santos, M. N., *Molecular fluorescence: principles and applications*. John Wiley & Sons: 2012.
5. Lakowicz, J. R., *Principles of fluorescence spectroscopy*. Springer: 2006.
6. Basic Principles of Fluorescence Spectroscopy. In *Handbook of Fluorescence Spectroscopy and Imaging*, 2011; pp 1-30.
7. Turro, N. J.; Ramamurthy, V.; Scaiano, J. C., *Principles of molecular photochemistry: an introduction*. University science books: 2009.
8. Mei, J.; Hong, Y.; Lam, J. W. Y.; Qin, A.; Tang, Y.; Tang, B. Z., Aggregation-Induced Emission: The Whole Is More Brilliant than the Parts. *Adv. Mater.* **2014,** *26* (31), 5429-5479.
9. Luppi, B. T.; Majak, D.; Gupta, M.; Rivard, E.; Shankar, K., Triplet excitons: improving exciton diffusion length for enhanced organic photovoltaics. *J. Mater. Chem. A* **2019,** *7* (6), 2445-2463.
10. Shaw, M. H.; Twilton, J.; MacMillan, D. W. C., Photoredox Catalysis in Organic Chemistry. *J. Org. Chem.* **2016,** *81* (16), 6898-6926.
11. Abrahamse, H.; Hamblin, Michael R., New photosensitizers for photodynamic therapy. *Biochem. J* **2016,** *473* (4), 347-364.
12. Hou, Y.; Zhang, X.; Chen, K.; Liu, D.; Wang, Z.; Liu, Q.; Zhao, J.; Barbon, A., Charge separation, charge recombination, long-lived charge transfer state formation and intersystem crossing in organic electron donor/acceptor dyads. *J. Mater. Chem. C* **2019,** *7* (39), 12048-12074.
13. Filatov, M. A., Heavy-atom-free BODIPY photosensitizers with intersystem crossing mediated by intramolecular photoinduced electron transfer. *Org. Biomol. Chem.* **2020,** *18* (1), 10-27.
14. May, S. R.; Climent, C.; Tao, Z.; Vinogradov, S. A.; Subotnik, J. E., Spin–Orbit versus Hyperfine Coupling-Mediated Intersystem Crossing in a Radical Pair. *J. Phys. Chem. A* **2023,** *127* (16), 3591-3597.
15. Stryer, L.; Haugland, R. P., Energy transfer: a spectroscopic ruler. *Proc. Natl. Acad. Sci.* **1967,** *58* (2), 719-726.
16. Gidi, Y.; Götte, M.; Cosa, G., Conformational Changes Spanning Angstroms to Nanometers via a Combined Protein-Induced Fluorescence Enhancement–Förster Resonance Energy Transfer Method. *J. Phys. Chem. B* **2017,** *121* (9), 2039-2048.
17. Turro, N. J.; Ramamurthy, V.; Scaiano, J. C., *Modern molecular photochemistry of organic molecules*. University Science Books Sausalito, CA: 2010; Vol. 188.
18. Gao, C.; Wong, W. W. H.; Qin, Z.; Lo, S.-C.; Namdas, E. B.; Dong, H.; Hu, W., Application of Triplet–Triplet Annihilation Upconversion in Organic Optoelectronic Devices: Advances and Perspectives. *Adv. Mater.* **2021,** *33* (45), 2100704.
19. Zeng, L.; Huang, L.; Han, J.; Han, G., Enhancing Triplet–Triplet Annihilation Upconversion: From Molecular Design to Present Applications. *Acc. Chem. Res.* **2022,** *55* (18), 2604-2615.

20. Rehm, D.; Weller, A., Kinetics of Fluorescence Quenching by Electron and H-Atom Transfer. *Isr. J. Chem.* **1970,** *8* (2), 259-271.
21. Braslavsky, S. E., Glossary of terms used in photochemistry, 3rd edition (IUPAC Recommendations 2006). *Pure Appl. Chem.* **2007,** *79* (3), 293-465.
22. Marcus, R. A., On the Theory of Oxidation—Reduction Reactions Involving Electron Transfer. V. Comparison and Properties of Electrochemical and Chemical Rate Constants1. *J. Phys. Chem.* **1963,** *67* (4), 853-857.
23. Marcus, R. A., Electron transfer reactions in chemistry theory and experiment. *J. Electroanal. Chem.* **1997,** *438* (1), 251-259.
24. Closs, G. L.; Miller, J. R., Intramolecular Long-Distance Electron Transfer in Organic Molecules. *Science* **1988,** *240* (4851), 440-447.
25. Burmistrova, N. A.; Meier, R. J.; Schreml, S.; Duerkop, A., Reusable optical sensing microplate for hydrogen peroxide using a fluorescent photoinduced electron transfer probe (HP Green). *Sensors Actuators B: Chem.* **2014,** *193*, 799-805.
26. Shieh, P.; Dien, V. T.; Beahm, B. J.; Castellano, J. M.; Wyss-Coray, T.; Bertozzi, C. R., CalFluors: A Universal Motif for Fluorogenic Azide Probes across the Visible Spectrum. *J. Am. Chem. Soc.* **2015,** *137* (22), 7145-7151.
27. Greene, L. E.; Lincoln, R.; Cosa, G., Rate of Lipid Peroxyl Radical Production during Cellular Homeostasis Unraveled via Fluorescence Imaging. *J. Am. Chem. Soc.* **2017,** *139* (44), 15801-15811.
28. Krumova, K.; Cosa, G., Bodipy Dyes with Tunable Redox Potentials and Functional Groups for Further Tethering: Preparation, Electrochemical, and Spectroscopic Characterization. *J. Am. Chem. Soc.* **2010,** *132* (49), 17560-17569.
29. Krumova, K.; Friedland, S.; Cosa, G., How Lipid Unsaturation, Peroxyl Radical Partitioning, and Chromanol Lipophilic Tail Affect the Antioxidant Activity of α-Tocopherol: Direct Visualization via High-Throughput Fluorescence Studies Conducted with Fluorogenic α-Tocopherol Analogues. *J. Am. Chem. Soc.* **2012,** *134* (24), 10102-10113.
30. Krumova, K.; Greene, L. E.; Cosa, G., Fluorogenic α-Tocopherol Analogue for Monitoring the Antioxidant Status within the Inner Mitochondrial Membrane of Live Cells. *J. Am. Chem. Soc.* **2013,** *135* (45), 17135-17143.
31. Belzile, M.-N.; Godin, R.; Durantini, A. M.; Cosa, G., Monitoring Chemical and Biological Electron Transfer Reactions with a Fluorogenic Vitamin K Analogue Probe. *J. Am. Chem. Soc.* **2016,** *138* (50), 16388-16397.
32. Greene, L. E.; Godin, R.; Cosa, G., Fluorogenic Ubiquinone Analogue for Monitoring Chemical and Biological Redox Processes. *J. Am. Chem. Soc.* **2016,** *138* (35), 11327-11334.
33. Zhang, N.; Wang, Y.; Leng, S.; Xu, S.; Zhang, L.; Wang, Q.; Zhang, Q.; Hu, H.-Y., An efficient fluorescence sensor for nitroreductase selective imaging based on intramolecular photoinduced electron transfer. *Talanta* **2019,** *205*, 120133.
34. Wang, J.; Zhou, C.; Zhang, J.; Zhu, X.; Liu, X.; Wang, Q.; Zhang, H., A new fluorescence turn-on probe for biothiols based on photoinduced electron transfer and its application in living cells. *Spectrochim. Acta A Mol. Biomol. Spectrosc.* **2016,** *166*, 31-37.
35. Galvani, A., *De viribus electricitatis in motu musculari Commentarius cum Joannis Aldini dissertatione et notis*. Junk: 1925.
36. Inal, S.; Rivnay, J.; Suiu, A.-O.; Malliaras, G. G.; McCulloch, I., Conjugated Polymers in Bioelectronics. *Acc. Chem. Res.* **2018,** *51* (6), 1368-1376.

37. Rivnay, J.; Owens, R. M.; Malliaras, G. G., The Rise of Organic Bioelectronics. *Chem. Mater.* **2014,** *26* (1), 679-685.
38. Higgins, S. G.; Lo Fiego, A.; Patrick, I.; Creamer, A.; Stevens, M. M., Organic Bioelectronics: Using Highly Conjugated Polymers to Interface with Biomolecules, Cells, and Tissues in the Human Body. *Adv. Mater. Technol.* **2020,** *5* (11), 2000384.
39. Pitsalidis, C.; Pappa, A.-M.; Boys, A. J.; Fu, Y.; Moysidou, C.-M.; van Niekerk, D.; Saez, J.; Savva, A.; Iandolo, D.; Owens, R. M., Organic Bioelectronics for In Vitro Systems. *Chem. Rev.* **2022,** *122* (4), 4700-4790.
40. McCuskey, S. R.; Chatsirisupachai, J.; Zeglio, E.; Parlak, O.; Panoy, P.; Herland, A.; Bazan, G. C.; Nguyen, T.-Q., Current Progress of Interfacing Organic Semiconducting Materials with Bacteria. *Chem. Rev.* **2022,** *122* (4), 4791-4825.
41. Berggren, M.; Głowacki, E. D.; Simon, D. T.; Stavrinidou, E.; Tybrandt, K., In Vivo Organic Bioelectronics for Neuromodulation. *Chem. Rev.* **2022,** *122* (4), 4826-4846.
42. Jozefowicz, M.; Yu, L. T.; Belorgey, G.; Buvet, R., Conductivité Electronique et Propriétés Chimiques de Polyanilines Oligomères. *J. Polym. Sci., Part C: Polym. Symp.* **1967,** *16* (5), 2943-2954.
43. Macdiarmid, A. G.; Chiang, J. C.; Richter, A. F.; Epstein, A. J., Polyaniline: a new concept in conducting polymers. *Synth. Met.* **1987,** *18* (1), 285-290.
44. MacDiarmid, A. G., Polyaniline and polypyrrole: Where are we headed? *Synth. Met.* **1997,** *84* (1), 27-34.
45. Rivers, T. J.; Hudson, T. W.; Schmidt, C. E., Synthesis of a Novel, Biodegradable Electrically Conducting Polymer for Biomedical Applications. *Adv. Funct. Mater.* **2002,** *12* (1), 33-37.
46. Moser, M.; Savagian, L. R.; Savva, A.; Matta, M.; Ponder, J. F., Jr.; Hidalgo, T. C.; Ohayon, D.; Hallani, R.; Reisjalali, M.; Troisi, A.; Wadsworth, A.; Reynolds, J. R.; Inal, S.; McCulloch, I., Ethylene Glycol-Based Side Chain Length Engineering in Polythiophenes and its Impact on Organic Electrochemical Transistor Performance. *Chem. Mater.* **2020,** *32* (15), 6618-6628.
47. Bhagwat, N.; Murray, R. E.; Shah, S. I.; Kiick, K. L.; Martin, D. C., Biofunctionalization of PEDOT films with laminin-derived peptides. *Acta Biomater.* **2016,** *41*, 235-246.
48. Rivnay, J.; Inal, S.; Salleo, A.; Owens, R. M.; Berggren, M.; Malliaras, G. G., Organic electrochemical transistors. *Nat. Rev. Mater.* **2018,** *3* (2), 17086.
49. Kittlesen, G. P.; White, H. S.; Wrighton, M. S., Chemical derivatization of microelectrode arrays by oxidation of pyrrole and N-methylpyrrole: fabrication of molecule-based electronic devices. *J. Am. Chem. Soc.* **1984,** *106* (24), 7389-7396.
50. Khodagholy, D.; Rivnay, J.; Sessolo, M.; Gurfinkel, M.; Leleux, P.; Jimison, L. H.; Stavrinidou, E.; Herve, T.; Sanaur, S.; Owens, R. M.; Malliaras, G. G., High transconductance organic electrochemical transistors. *Nat. Commun.* **2013,** *4* (1), 2133.
51. Yurash, B.; Cao, D. X.; Brus, V. V.; Leifert, D.; Wang, M.; Dixon, A.; Seifrid, M.; Mansour, A. E.; Lungwitz, D.; Liu, T.; Santiago, P. J.; Graham, K. R.; Koch, N.; Bazan, G. C.; Nguyen, T.-Q., Towards understanding the doping mechanism of organic semiconductors by Lewis acids. *Nat. Mater.* **2019,** *18* (12), 1327-1334.
52. Groenendaal, L.; Jonas, F.; Freitag, D.; Pielartzik, H.; Reynolds, J. R., Poly(3,4-ethylenedioxythiophene) and Its Derivatives: Past, Present, and Future. *Adv. Mater.* **2000,** *12* (7), 481-494.
53. Hoven, C. V.; Garcia, A.; Bazan, G. C.; Nguyen, T.-Q., Recent Applications of Conjugated Polyelectrolytes in Optoelectronic Devices. *Adv. Mater.* **2008,** *20* (20), 3793-3810.

54. Lee, W.; Seo, J. H.; Woo, H. Y., Conjugated polyelectrolytes: A new class of semiconducting material for organic electronic devices. *Polymer* **2013,** *54* (19), 5104-5121.
55. Seo, J. H.; Namdas, E. B.; Gutacker, A.; Heeger, A. J.; Bazan, G. C., Conjugated polyelectrolytes for organic light emitting transistors. *Appl. Phys. Lett.* **2010,** *97* (4).
56. Huang, F.; Wu, H.; Cao, Y., Water/alcohol soluble conjugated polymers as highly efficient electron transporting/injection layer in optoelectronic devices. *Chem. Soc. Rev.* **2010,** *39* (7), 2500-2521.
57. Zhu, C.; Liu, L.; Yang, Q.; Lv, F.; Wang, S., Water-Soluble Conjugated Polymers for Imaging, Diagnosis, and Therapy. *Chem. Rev.* **2012,** *112* (8), 4687-4735.
58. Zhou, L.; Lv, F.; Liu, L.; Wang, S., Water-Soluble Conjugated Organic Molecules as Optical and Electrochemical Materials for Interdisciplinary Biological Applications. *Acc. Chem. Res.* **2019,** *52* (11), 3211-3222.
59. Chen, L.; McBranch, D. W.; Wang, H.-L.; Helgeson, R.; Wudl, F.; Whitten, D. G., Highly sensitive biological and chemical sensors based on reversible fluorescence quenching in a conjugated polymer. *Proc. Natl. Acad. Sci.* **1999,** *96* (22), 12287-12292.
60. Zhou, C.; Chia, G. W. N.; Yong, K.-T., Membrane-intercalating conjugated oligoelectrolytes. *Chem. Soc. Rev.* **2022,** *51* (24), 9917-9932.
61. Yan, H.; Catania, C.; Bazan, G. C., Membrane-Intercalating Conjugated Oligoelectrolytes: Impact on Bioelectrochemical Systems. *Adv. Mater.* **2015,** *27* (19), 2958-2973.
62. Garner, L. E.; Park, J.; Dyar, S. M.; Chworos, A.; Sumner, J. J.; Bazan, G. C., Modification of the Optoelectronic Properties of Membranes via Insertion of Amphiphilic Phenylenevinylene Oligoelectrolytes. *J. Am. Chem. Soc.* **2010,** *132* (29), 10042-10052.
63. Yan, H.; Rengert, Z. D.; Thomas, A. W.; Rehermann, C.; Hinks, J.; Bazan, G. C., Influence of molecular structure on the antimicrobial function of phenylenevinylene conjugated oligoelectrolytes. *Chem. Sci.* **2016,** *7* (9), 5714-5722.
64. Hinks, J.; Wang, Y.; Matysik, A.; Kraut, R.; Kjelleberg, S.; Mu, Y.; Bazan, G. C.; Wuertz, S.; Seviour, T., Increased Microbial Butanol Tolerance by Exogenous Membrane Insertion Molecules. *ChemSusChem* **2015,** *8* (21), 3718-3726.
65. Wang, V. B.; Du, J.; Chen, X.; Thomas, A. W.; Kirchhofer, N. D.; Garner, L. E.; Maw, M. T.; Poh, W. H.; Hinks, J.; Wuertz, S.; Kjelleberg, S.; Zhang, Q.; Loo, J. S. C.; Bazan, G. C., Improving charge collection in Escherichia coli–carbon electrode devices with conjugated oligoelectrolytes. *PCCP* **2013,** *15* (16), 5867-5872.
66. Garner, L. E.; Thomas, A. W.; Sumner, J. J.; Harvey, S. P.; Bazan, G. C., Conjugated oligoelectrolytes increase current response and organic contaminant removal in wastewater microbial fuel cells. *Energy Environ. Sci.* **2012,** *5* (11), 9449-9452.
67. Thomas, A. W.; Garner, L. E.; Nevin, K. P.; Woodard, T. L.; Franks, A. E.; Lovley, D. R.; Sumner, J. J.; Sund, C. J.; Bazan, G. C., A lipid membrane intercalating conjugated oligoelectrolyte enables electrode driven succinate production in Shewanella. *Energy Environ. Sci.* **2013,** *6* (6), 1761-1765.
68. Saboe, P. O.; Lubner, C. E.; McCool, N. S.; Vargas-Barbosa, N. M.; Yan, H.; Chan, S.; Ferlez, B.; Bazan, G. C.; Golbeck, J. H.; Kumar, M., Two-Dimensional Protein Crystals for Solar Energy Conversion. *Adv. Mater.* **2014,** *26* (41), 7064-7069.
69. Leleux, P.; Badier, J.-M.; Rivnay, J.; Bénar, C.; Hervé, T.; Chauvel, P.; Malliaras, G. G., Conducting Polymer Electrodes for Electroencephalography. *Adv. Healthc. Mater.* **2014,** *3* (4), 490-493.

70. Schander, A.; Teßmann, T.; Strokov, S.; Stemmann, H.; Kreiter, A. K.; Lang, W. In *In-vitro evaluation of the long-term stability of PEDOT:PSS coated microelectrodes for chronic recording and electrical stimulation of neurons*, 2016 38th Annual International Conference of the IEEE Engineering in Medicine and Biology Society (EMBC), 16-20 Aug. 2016; 2016; pp 6174-6177.
71. Khodagholy, D.; Doublet, T.; Quilichini, P.; Gurfinkel, M.; Leleux, P.; Ghestem, A.; Ismailova, E.; Hervé, T.; Sanaur, S.; Bernard, C.; Malliaras, G. G., In vivo recordings of brain activity using organic transistors. *Nat. Commun.* **2013,** *4* (1), 1575.
72. Strakosas, X.; Bongo, M.; Owens, R. M., The organic electrochemical transistor for biological applications. *J. Appl. Polym. Sci.* **2015,** *132* (15).
73. Toss, H.; Suspène, C.; Piro, B.; Yassar, A.; Crispin, X.; Kergoat, L.; Pham, M.-C.; Berggren, M., On the mode of operation in electrolyte-gated thin film transistors based on different substituted polythiophenes. *Org. Electron.* **2014,** *15* (10), 2420-2427.
74. Spanu, A.; Martines, L.; Bonfiglio, A., Interfacing cells with organic transistors: a review of in vitro and in vivo applications. *Lab on a Chip* **2021,** *21* (5), 795-820.
75. Macchia, E.; Tiwari, A.; Manoli, K.; Holzer, B.; Ditaranto, N.; Picca, R. A.; Cioffi, N.; Di Franco, C.; Scamarcio, G.; Palazzo, G.; Torsi, L., Label-Free and Selective Single-Molecule Bioelectronic Sensing with a Millimeter-Wide Self-Assembled Monolayer of Anti-Immunoglobulins. *Chem. Mater.* **2019,** *31* (17), 6476-6483.
76. Mulla, M. Y.; Torsi, L.; Manoli, K., Chapter Seventeen - Electronic biosensors based on EGOFETs. In *Methods Enzymol.*, Pelosi, P.; Knoll, W., Eds. Academic Press: 2020; Vol. 642, pp 403-433.
77. Uguz, I.; Proctor, C. M.; Curto, V. F.; Pappa, A.-M.; Donahue, M. J.; Ferro, M.; Owens, R. M.; Khodagholy, D.; Inal, S.; Malliaras, G. G., A Microfluidic Ion Pump for In Vivo Drug Delivery. *Adv. Mater.* **2017,** *29* (27), 1701217.
78. Williamson, A.; Rivnay, J.; Kergoat, L.; Jonsson, A.; Inal, S.; Uguz, I.; Ferro, M.; Ivanov, A.; Sjöström, T. A.; Simon, D. T.; Berggren, M.; Malliaras, G. G.; Bernard, C., Controlling Epileptiform Activity with Organic Electronic Ion Pumps. *Adv. Mater.* **2015,** *27* (20), 3138-3144.
79. Li, C.; Ding, L.; Cui, H.; Zhang, L.; Xu, K.; Ren, H., Application of conductive polymers in biocathode of microbial fuel cells and microbial community. *Bioresour. Technol.* **2012,** *116*, 459-465.
80. Song, R.-B.; Wu, Y.; Lin, Z.-Q.; Xie, J.; Tan, C. H.; Loo, J. S. C.; Cao, B.; Zhang, J.-R.; Zhu, J.-J.; Zhang, Q., Living and Conducting: Coating Individual Bacterial Cells with In Situ Formed Polypyrrole. *Angew. Chem. Int. Ed.* **2017,** *56* (35), 10516-10520.
81. Wong, J. Y.; Langer, R.; Ingber, D. E., Electrically conducting polymers can noninvasively control the shape and growth of mammalian cells. *Proc. Natl. Acad. Sci.* **1994,** *91* (8), 3201-3204.
82. Hopkins, J.; Travaglini, L.; Lauto, A.; Cramer, T.; Fraboni, B.; Seidel, J.; Mawad, D., Photoactive Organic Substrates for Cell Stimulation: Progress and Perspectives. *Adv. Mater. Technol.* **2019,** *4* (5), 1800744.
83. Medagoda, D. I.; Ghezzi, D., Organic semiconductors for light-mediated neuromodulation. *Commun. Mater.* **2021,** *2* (1), 111.
84. Ghezzi, D.; Antognazza, M. R.; Maccarone, R.; Bellani, S.; Lanzarini, E.; Martino, N.; Mete, M.; Pertile, G.; Bisti, S.; Lanzani, G.; Benfenati, F., A polymer optoelectronic interface restores light sensitivity in blind rat retinas. *Nat. Photon.* **2013,** *7* (5), 400-406.
85. Tortiglione, C.; Antognazza, M. R.; Tino, A.; Bossio, C.; Marchesano, V.; Bauduin, A.; Zangoli, M.; Morata, S. V.; Lanzani, G., Semiconducting polymers are light nanotransducers in eyeless animals. *Sci. Adv.* **2017,** *3* (1), e1601699.

86. Maya-Vetencourt, J. F.; Ghezzi, D.; Antognazza, M. R.; Colombo, E.; Mete, M.; Feyen, P.; Desii, A.; Buschiazzo, A.; Di Paolo, M.; Di Marco, S.; Ticconi, F.; Emionite, L.; Shmal, D.; Marini, C.; Donelli, I.; Freddi, G.; Maccarone, R.; Bisti, S.; Sambuceti, G.; Pertile, G.; Lanzani, G.; Benfenati, F., A fully organic retinal prosthesis restores vision in a rat model of degenerative blindness. *Nat. Mater.* **2017,** *16* (6), 681-689.
87. Lodola, F.; Rosti, V.; Tullii, G.; Desii, A.; Tapella, L.; Catarsi, P.; Lim, D.; Moccia, F.; Antognazza, M. R., Conjugated polymers optically regulate the fate of endothelial colony-forming cells. *Sci. Adv.* **2019,** *5* (9), eaav4620.
88. Bobbert, P. A.; Sharma, A.; Mathijssen, S. G. J.; Kemerink, M.; de Leeuw, D. M., Operational Stability of Organic Field-Effect Transistors. *Adv. Mater.* **2012,** *24* (9), 1146-1158.
89. Picca, R. A.; Manoli, K.; Macchia, E.; Tricase, A.; Di Franco, C.; Scamarcio, G.; Cioffi, N.; Torsi, L., A Study on the Stability of Water-Gated Organic Field-Effect-Transistors Based on a Commercial p-Type Polymer. *Front. Chem.* **2019,** *7*.
90. Quigley, A. F.; Wagner, K.; Kita, M.; Gilmore, K. J.; Higgins, M. J.; Breukers, R. D.; Moulton, S. E.; Clark, G. M.; Penington, A. J.; Wallace, G. G.; Officer, D. L.; Kapsa, R. M. I., In vitro growth and differentiation of primary myoblasts on thiophene based conducting polymers. *Biomater. Sci.* **2013,** *1* (9), 983-995.
91. Bidez, P. R.; Li, S.; MacDiarmid, A. G.; Venancio, E. C.; Wei, Y.; Lelkes, P. I., Polyaniline, an electroactive polymer, supports adhesion and proliferation of cardiac myoblasts. *J. Biomater. Sci. Polym. Ed.* **2006,** *17* (1-2), 199-212.
92. Vaquero, S.; Bossio, C.; Bellani, S.; Martino, N.; Zucchetti, E.; Lanzani, G.; Antognazza, M. R., Conjugated polymers for the optical control of the electrical activity of living cells. *J. Mater. Chem. B* **2016,** *4* (31), 5272-5283.
93. Noriega, R.; Rivnay, J.; Vandewal, K.; Koch, F. P. V.; Stingelin, N.; Smith, P.; Toney, M. F.; Salleo, A., A general relationship between disorder, aggregation and charge transport in conjugated polymers. *Nat. Mater.* **2013,** *12* (11), 1038-1044.
94. Venkateshvaran, D.; Nikolka, M.; Sadhanala, A.; Lemaur, V.; Zelazny, M.; Kepa, M.; Hurhangee, M.; Kronemeijer, A. J.; Pecunia, V.; Nasrallah, I.; Romanov, I.; Broch, K.; McCulloch, I.; Emin, D.; Olivier, Y.; Cornil, J.; Beljonne, D.; Sirringhaus, H., Approaching disorder-free transport in high-mobility conjugated polymers. *Nature* **2014,** *515* (7527), 384-388.
95. Fonner, J. M.; Forciniti, L.; Nguyen, H.; Byrne, J. D.; Kou, Y.-F.; Syeda-Nawaz, J.; Schmidt, C. E., Biocompatibility implications of polypyrrole synthesis techniques. *Biomed. Mater.* **2008,** *3* (3), 034124.
96. Varesano, A.; Vineis, C.; Aluigi, A.; Rombaldoni, F.; Tonetti, C.; Mazzuchetti, G., Antibacterial efficacy of polypyrrole in textile applications. *Fibers Polym.* **2013,** *14* (1), 36-42.
97. Zajdel, T. J.; Baruch, M.; Méhes, G.; Stavrinidou, E.; Berggren, M.; Maharbiz, M. M.; Simon, D. T.; Ajo-Franklin, C. M., PEDOT:PSS-based Multilayer Bacterial-Composite Films for Bioelectronics. *Sci. Rep.* **2018,** *8* (1), 15293.
98. Kirchhofer, N. D.; Rengert, Z. D.; Dahlquist, F. W.; Nguyen, T.-Q.; Bazan, G. C., A Ferrocene-Based Conjugated Oligoelectrolyte Catalyzes Bacterial Electrode Respiration. *Chem* **2017,** *2* (2), 240-257.
99. Pedersen, P. L.; Amzel, L. M., ATP synthases. Structure, reaction center, mechanism, and regulation of one of nature's most unique machines. *J. Biol. Chem.* **1993,** *268* (14), 9937-9940.
100. Ramirez, B. E.; Malmström, B. G.; Winkler, J. R.; Gray, H. B., The currents of life: the terminal electron-transfer complex of respiration. *Proc. Natl. Acad. Sci.* **1995,** *92* (26), 11949-11951.

101. Holmström, K. M.; Finkel, T., Cellular mechanisms and physiological consequences of redox-dependent signalling. *Nat. Rev. Mol. Cell Biol.* **2014,** *15* (6), 411-421.
102. Bauer, C. E.; Elsen, S.; Bird, T. H., Mechanisms for Redox Control of Gene Expression. *Annu. Rev. Microbiol.* **1999,** *53* (1), 495-523.
103. Hammond, C. L.; Lee, T. K.; Ballatori, N., Novel roles for glutathione in gene expression, cell death, and membrane transport of organic solutes. *J. Hepatol.* **2001,** *34* (6), 946-954.
104. Miret, J. A.; Munné-Bosch, S., Redox signaling and stress tolerance in plants: a focus on vitamin E. *Ann. N. Y. Acad. Sci.* **2015,** *1340* (1), 29-38.
105. Żebrowska, A.; Krysiński, P.; Łotowski, Z., Electrochemical studies of blocking properties of solid supported tethered lipid membranes on gold. *Bioelectrochemistry* **2002,** *56* (1), 179-184.
106. Liu, H.-Y.; Pappa, A.-M.; Pavia, A.; Pitsalidis, C.; Thiburce, Q.; Salleo, A.; Owens, R. M.; Daniel, S., Self-Assembly of Mammalian-Cell Membranes on Bioelectronic Devices with Functional Transmembrane Proteins. *Langmuir* **2020,** *36* (26), 7325-7331.
107. Pappa, A.-M.; Liu, H.-Y.; Traberg-Christensen, W.; Thiburce, Q.; Savva, A.; Pavia, A.; Salleo, A.; Daniel, S.; Owens, R. M., Optical and Electronic Ion Channel Monitoring from Native Human Membranes. *ACS Nano* **2020,** *14* (10), 12538-12545.
108. Labbé, E.; Buriez, O., Electrode-supported and free-standing bilayer lipid membranes: Formation and uses in molecular electrochemistry. *Electrochem. Sci. Adv.* **2022,** *2* (6), e2100170.
109. Hoyo, J.; Guaus, E.; Oncins, G.; Torrent-Burgués, J.; Sanz, F., Incorporation of Ubiquinone in Supported Lipid Bilayers on ITO. *J. Phys. Chem. B* **2013,** *117* (25), 7498-7506.
110. Vacek, J.; Zatloukalova, M.; Novak, D., Electrochemistry of membrane proteins and protein–lipid assemblies. *Curr. Opin. Electrochem.* **2018,** *12*, 73-80.
111. Bard, A. J.; Faulkner, L. R., Fundamentals and applications. *Electrochemical methods* **2001,** *2* (482), 580-632.
112. Engstrom, R. C.; Weber, M.; Wunder, D. J.; Burgess, R.; Winquist, S., Measurements within the diffusion layer using a microelectrode probe. *Anal. Chem.* **1986,** *58* (4), 844-848.
113. Liu, H. Y.; Fan, F. R. F.; Lin, C. W.; Bard, A. J., Scanning electrochemical and tunneling ultramicroelectrode microscope for high-resolution examination of electrode surfaces in solution. *J. Am. Chem. Soc.* **1986,** *108* (13), 3838-3839.
114. Sun, T.; Wang, D.; Mirkin, M. V.; Cheng, H.; Zheng, J.-C.; Richards, R. M.; Lin, F.; Xin, H. L., Direct high-resolution mapping of electrocatalytic activity of semi-two-dimensional catalysts with single-edge sensitivity. *Proc. Natl. Acad. Sci.* **2019,** *116* (24), 11618-11623.
115. Conzuelo, F.; Schulte, A.; Schuhmann, W., Biological imaging with scanning electrochemical microscopy. *Proc. R. Soc. A: Math. Phys. Eng. Sci.* **2018,** *474* (2218), 20180409.
116. Tsionsky, M.; Zhou, J.; Amemiya, S.; Fan, F.-R. F.; Bard, A. J.; Dryfe, R. A. W., Scanning Electrochemical Microscopy. 38. Application of SECM to the Study of Charge Transfer through Bilayer Lipid Membranes. *Anal. Chem.* **1999,** *71* (19), 4300-4305.
117. Liu, X.; Ramsey, M. M.; Chen, X.; Koley, D.; Whiteley, M.; Bard, A. J., Real-time mapping of a hydrogen peroxide concentration profile across a polymicrobial bacterial biofilm using scanning electrochemical microscopy. *Proc. Natl. Acad. Sci.* **2011,** *108* (7), 2668-2673.
118. Zhang, Z.; Shi, J.; Huang, W., Study of the ion-channel behavior on glassy carbon electrode supported bilayer lipid membranes stimulated by perchlorate anion. *Mater. Sci. Eng. C* **2015,** *55*, 431-435.
119. Kaim, W.; Fiedler, J., Spectroelectrochemistry: the best of two worlds. *Chem. Soc. Rev.* **2009,** *38* (12), 3373-3382.

120. Yu, J.-S.; Zhou, T.-Y., The electrochemistry and thin-layer luminescence spectroelectrochemistry of rhodamine 6G at a 4,4′-bipyridine-modified gold electrode. *J. Electroanal. Chem.* **2001,** *504* (1), 89-95.
121. Dias, M.; Hudhomme, P.; Levillain, E.; Perrin, L.; Sahin, Y.; Sauvage, F.-X.; Wartelle, C., Electrochemistry coupled to fluorescence spectroscopy: a new versatile approach. *Electrochem. Commun.* **2004,** *6* (3), 325-330.
122. Iwasita, T.; Nart, F. C., In situ infrared spectroscopy at electrochemical interfaces. *Prog. Surf. Sci.* **1997,** *55* (4), 271-340.
123. Sharpe, L. R.; Heineman, W. R.; Elder, R. C., EXAFS spectroelectrochemistry. *Chem. Rev.* **1990,** *90* (5), 705-722.
124. Corio, P.; Santos, P. S.; Brar, V. W.; Samsonidze, G. G.; Chou, S. G.; Dresselhaus, M. S., Potential dependent surface Raman spectroscopy of single wall carbon nanotube films on platinum electrodes. *Chem. Phys. Lett.* **2003,** *370* (5), 675-682.
125. Harder, S. R.; Feinberg, B. A.; Ragsdale, S. W., A spectroelectrochemical cell designed for low temperature electron paramagnetic resonance titration of oxygen-sensitive proteins. *Anal. Biochem.* **1989,** *181* (2), 283-287.
126. de Souza, J. C. P.; Macedo, L. J. A.; Hassan, A.; Sedenho, G. C.; Modenez, I. A.; Crespilho, F. N., In Situ and Operando Techniques for Investigating Electron Transfer in Biological Systems. *ChemElectroChem* **2021,** *8* (3), 431-446.
127. Melin, F.; Hellwig, P., Recent advances in the electrochemistry and spectroelectrochemistry of membrane proteins. *Biol. Chem.* **2013,** *394* (5), 593-609.
128. Rothschild, K. J.; Zagaeski, M.; Cantore, W. A., Conformational changes of bacteriorhodopsin detected by Fourier transform infrared difference spectroscopy. *Biochem. Biophys. Res. Commun.* **1981,** *103* (2), 483-489.
129. Zscherp, C.; Barth, A., Reaction-Induced Infrared Difference Spectroscopy for the Study of Protein Reaction Mechanisms. *Biochemistry* **2001,** *40* (7), 1875-1883.
130. Ataka, K.; Heberle, J., Biochemical applications of surface-enhanced infrared absorption spectroscopy. *Anal. Bioanal. Chem.* **2007,** *388* (1), 47-54.
131. Hartstein, A.; Kirtley, J. R.; Tsang, J. C., Enhancement of the Infrared Absorption from Molecular Monolayers with Thin Metal Overlayers. *Phys. Rev. Lett.* **1980,** *45* (3), 201-204.
132. Ataka, K.-i.; Yotsuyanagi, T.; Osawa, M., Potential-Dependent Reorientation of Water Molecules at an Electrode/Electrolyte Interface Studied by Surface-Enhanced Infrared Absorption Spectroscopy. *J. Phys. Chem.* **1996,** *100* (25), 10664-10672.
133. Makarchuk, I.; Santos Seica, A. F.; Melin, F.; Hellwig, P., Probing the reaction of membrane proteins via infrared spectroscopies, plasmonics, and electrochemistry. *Curr. Opin. Electrochem.* **2021,** *30*, 100770.
134. Millo, D.; Hildebrandt, P.; Pandelia, M.-E.; Lubitz, W.; Zebger, I., SEIRA Spectroscopy of the Electrochemical Activation of an Immobilized [NiFe] Hydrogenase under Turnover and Non-Turnover Conditions. *Angew. Chem. Int. Ed.* **2011,** *50* (11), 2632-2634.
135. Jiang, X.; Zaitseva, E.; Schmidt, M.; Siebert, F.; Engelhard, M.; Schlesinger, R.; Ataka, K.; Vogel, R.; Heberle, J., Resolving voltage-dependent structural changes of a membrane photoreceptor by surface-enhanced IR difference spectroscopy. *Proc. Natl. Acad. Sci.* **2008,** *105* (34), 12113-12117.
136. Gutiérrez-Sanz, O.; Marques, M.; Pereira, I. A. C.; De Lacey, A. L.; Lubitz, W.; Rüdiger, O., Orientation and Function of a Membrane-Bound Enzyme Monitored by Electrochemical

Surface-Enhanced Infrared Absorption Spectroscopy. *J. Phys. Chem. Lett.* **2013,** *4* (17), 2794-2798.
137. Fleischmann, M.; Hendra, P. J.; McQuillan, A. J., Raman spectra of pyridine adsorbed at a silver electrode. *Chem. Phys. Lett.* **1974,** *26* (2), 163-166.
138. Aroca, R., *Surface-enhanced vibrational spectroscopy*. John Wiley & Sons: 2006.
139. Ibañez, D.; Santidrian, A.; Heras, A.; Kalbáč, M.; Colina, A., Study of Adenine and Guanine Oxidation Mechanism by Surface-Enhanced Raman Spectroelectrochemistry. *J. Phys. Chem. C* **2015,** *119* (15), 8191-8198.
140. Karaballi, R. A.; Merchant, S.; Power, S. R.; Brosseau, C. L., Electrochemical surface-enhanced Raman spectroscopy (EC-SERS) study of the interaction between protein aggregates and biomimetic membranes. *PCCP* **2018,** *20* (6), 4513-4526.
141. McLeod, K. E. R.; Lynk, T. P.; Sit, C. S.; Brosseau, Christa L., On the origin of electrochemical surface-enhanced Raman spectroscopy (EC-SERS) signals for bacterial samples: the importance of filtered control studies in the development of new bacterial screening platforms. *Anal. Methods* **2019,** *11* (7), 924-929.
142. Kurouski, D.; Mattei, M.; Van Duyne, R. P., Probing Redox Reactions at the Nanoscale with Electrochemical Tip-Enhanced Raman Spectroscopy. *Nano Lett.* **2015,** *15* (12), 7956-7962.
143. Zeng, Z.-C.; Huang, S.-C.; Wu, D.-Y.; Meng, L.-Y.; Li, M.-H.; Huang, T.-X.; Zhong, J.-H.; Wang, X.; Yang, Z.-L.; Ren, B., Electrochemical Tip-Enhanced Raman Spectroscopy. *J. Am. Chem. Soc.* **2015,** *137* (37), 11928-11931.
144. Li, J.-T.; Chen, Q.-S.; Sun, S.-G., In situ microscope FTIR studies of methanol adsorption and oxidation on an individually addressable array of nanostructured Pt microelectrodes. *Electrochim. Acta* **2007,** *52* (18), 5725-5732.
145. Jeuken, L.; Orrit, M.; Canters, G., Single-molecule fluorescence in redox chemistry. *Curr. Opin. Electrochem.* **2023,** *37*, 101196.
146. Doneux, T., Visualisation of electrochemical processes by coupled electrochemistry and fluorescence microscopy. *Curr. Opin. Electrochem.* **2022,** *34*, 101013.
147. Engstrom, R. C.; Ghaffari, S.; Qu, H., Fluorescence imaging of electrode-solution interfacial processes. *Anal. Chem.* **1992,** *64* (21), 2525-2529.
148. Cannan, S.; Douglas Macklam, I.; Unwin, P. R., Three-dimensional imaging of proton gradients at microelectrode surfaces using confocal laser scanning microscopy. *Electrochem. Commun.* **2002,** *4* (11), 886-892.
149. Qiao, Y.; Zhou, Z.; Chen, Z.; Du, S.; Cheng, Q.; Zhai, H.; Fritz, N. J.; Du, Q.; Yang, Y., Visualizing ion diffusion in battery systems by fluorescence microscopy: A case study on the dissolution of LiMn2O4. *Nano Energy* **2018,** *45*, 68-74.
150. Padilla, N. A.; Rea, M. T.; Foy, M.; Upadhyay, S. P.; Desrochers, K. A.; Derus, T.; Knapper, K. A.; Hunter, N. H.; Wood, S.; Hinton, D. A.; Cavell, A. C.; Masias, A. G.; Goldsmith, R. H., Tracking Lithium Ions via Widefield Fluorescence Microscopy for Battery Diagnostics. *ACS Sensors* **2017,** *2* (7), 903-908.
151. Farjami, E.; Clima, L.; Gothelf, K. V.; Ferapontova, E. E., DNA interactions with a Methylene Blue redox indicator depend on the DNA length and are sequence specific. *Analyst* **2010,** *135* (6), 1443-1448.
152. Kerman, K.; Ozkan, D.; Kara, P.; Meric, B.; Gooding, J. J.; Ozsoz, M., Voltammetric determination of DNA hybridization using methylene blue and self-assembled alkanethiol monolayer on gold electrodes. *Anal. Chim. Acta* **2002,** *462* (1), 39-47.

153. Czekanska, E. M., Assessment of Cell Proliferation with Resazurin-Based Fluorescent Dye. In *Mammalian Cell Viability: Methods and Protocols*, Stoddart, M. J., Ed. Humana Press: Totowa, NJ, 2011; pp 27-32.
154. Zhou, X.; Xu, W.; Liu, G.; Panda, D.; Chen, P., Size-Dependent Catalytic Activity and Dynamics of Gold Nanoparticles at the Single-Molecule Level. *J. Am. Chem. Soc.* **2010,** *132* (1), 138-146.
155. Doneux, T.; Bouffier, L.; Goudeau, B.; Arbault, S., Coupling Electrochemistry with Fluorescence Confocal Microscopy To Investigate Electrochemical Reactivity: A Case Study with the Resazurin-Resorufin Fluorogenic Couple. *Anal. Chem.* **2016,** *88* (12), 6292-6300.
156. Gatland, Z.; Madrid, D.; Siegel, M.; Kisley, L., Reduction reactions at metal/non-aqueous interfaces can be sensed with the turn-on fluorophore resazurin. *Mater. Chem. Front.* **2023,** *7* (11), 2260-2265.
157. Schröder, U.; Scholz, F., Microscopic in situ diffuse reflectance spectroelectrochemistry of solid state electrochemical reactions of particles immobilized on electrodes. *J. Solid State Electrochem.* **1997,** *1* (1), 62-67.
158. Hao, R.; Peng, Z.; Zhang, B., Single-Molecule Fluorescence Microscopy for Probing the Electrochemical Interface. *ACS Omega* **2020,** *5* (1), 89-97.
159. Palacios, R. E.; Fan, F.-R. F.; Bard, A. J.; Barbara, P. F., Single-Molecule Spectroelectrochemistry (SMS-EC). *J. Am. Chem. Soc.* **2006,** *128* (28), 9028-9029.
160. Bizzotto, D., In situ spectroelectrochemical fluorescence microscopy for studying electrodes modified by molecular adsorbates. *Curr. Opin. Electrochem.* **2018,** *7*, 161-171.
161. Salverda, J. M.; Patil, A. V.; Mizzon, G.; Kuznetsova, S.; Zauner, G.; Akkilic, N.; Canters, G. W.; Davis, J. J.; Heering, H. A.; Aartsma, T. J., Fluorescent Cyclic Voltammetry of Immobilized Azurin: Direct Observation of Thermodynamic and Kinetic Heterogeneity. *Angew. Chem. Int. Ed.* **2010,** *49* (33), 5776-5779.
162. Krzemiński, Ł.; Ndamba, L.; Canters, G. W.; Aartsma, T. J.; Evans, S. D.; Jeuken, L. J. C., Spectroelectrochemical Investigation of Intramolecular and Interfacial Electron-Transfer Rates Reveals Differences Between Nitrite Reductase at Rest and During Turnover. *J. Am. Chem. Soc.* **2011,** *133* (38), 15085-15093.
163. Yu, Z. L.; Casanova-Moreno, J.; Guryanov, I.; Maran, F.; Bizzotto, D., Influence of Surface Structure on Single or Mixed Component Self-Assembled Monolayers via in Situ Spectroelectrochemical Fluorescence Imaging of the Complete Stereographic Triangle on a Single Crystal Au Bead Electrode. *J. Am. Chem. Soc.* **2015,** *137* (1), 276-288.
164. Godin, R.; Sherman, B. D.; Bergkamp, J. J.; Chesta, C. A.; Moore, A. L.; Moore, T. A.; Palacios, R. E.; Cosa, G., Charge-Transfer Dynamics of Fluorescent Dye-Sensitized Electrodes under Applied Biases. *J. Phys. Chem. Lett.* **2015,** *6* (14), 2688-2693.
165. Godin, R.; Palacios, R. E.; Cosa, G., Heterogeneous Charge Mobility in Individual Conjugated Polyelectrolyte Nanoparticles Revealed by Two-Color Single Particle Spectroelectrochemistry Studies. *J. Phys. Chem. C* **2015,** *119* (23), 12875-12886.
166. Ayranci, R.; Ak, M., A Fluorescence and Electroactive Surface Design: Electropolymerization of Dansyl Fluorophore Functionalized PEDOT. *J. Electrochem. Soc.* **2017,** *164* (13), H925.
167. Peterka, D. S.; Takahashi, H.; Yuste, R., Imaging Voltage in Neurons. *Neuron* **2011,** *69* (1), 9-21.
168. Miller, E. W., Small molecule fluorescent voltage indicators for studying membrane potential. *Curr. Opin. Chem. Biol.* **2016,** *33*, 74-80.

169. Miller, E. W.; Lin, J. Y.; Frady, E. P.; Steinbach, P. A.; Kristan, W. B.; Tsien, R. Y., Optically monitoring voltage in neurons by photo-induced electron transfer through molecular wires. *Proc. Natl. Acad. Sci.* **2012,** *109* (6), 2114-2119.
170. Yudovich, S.; Marzouqe, A.; Kantorovitsch, J.; Teblum, E.; Chen, T.; Enderlein, J.; Miller, E. W.; Weiss, S., Electrically controlling and optically observing the membrane potential of supported lipid bilayers. *Biophys. J.* **2022,** *121* (13), 2624-2637.
171. Grienberger, C.; Konnerth, A., Imaging Calcium in Neurons. *Neuron* **2012,** *73* (5), 862-885.
172. Omatsu, T.; Hori, K.; Naka, Y.; Shimazaki, M.; Sakai, K.; Murakami, K.; Maeda, K.; Fukuyama, M.; Yoshida, Y., Dynamic behavior analysis of ion transport through a bilayer lipid membrane by an electrochemical method combined with fluorometry. *Analyst* **2020,** *145* (11), 3839-3845.
173. Ben Trad, F.; Delacotte, J.; Guille-Collignon, M.; Lemaître, F.; Arbault, S.; Sojic, N.; Burlina, F.; Labbé, E.; Buriez, O., Electrochemiluminescence Imaging of Liposome Permeabilization by an Antimicrobial Peptide: Melittin. *Chem. Biomed. Imaging* **2023,** *1* (1), 58-65.
174. Ben Trad, F.; Wieczny, V.; Delacotte, J.; Morel, M.; Guille-Collignon, M.; Arbault, S.; Lemaître, F.; Sojic, N.; Labbé, E.; Buriez, O., Dynamic Electrochemiluminescence Imaging of Single Giant Liposome Opening at Polarized Electrodes. *Anal. Chem.* **2022,** *94* (3), 1686-1696.
175. Schmidt, I.; Pieper, A.; Wichmann, H.; Bunk, B.; Huber, K.; Overmann, J.; Walla, P. J.; Schröder, U., In Situ Autofluorescence Spectroelectrochemistry for the Study of Microbial Extracellular Electron Transfer. *ChemElectroChem* **2017,** *4* (10), 2515-2519.
176. Perez Jimenez, A. I.; Challier, L.; Aït-Yahiatène, E.; Delacotte, J.; Labbé, E.; Buriez, O., Selective Electrochemical Bleaching of the Outer Leaflet of Fluorescently Labeled Giant Liposomes. *Chem. Eur. J.* **2017,** *23* (28), 6781-6787.
177. Rudolph, T. K.; Freeman, B. A., Transduction of Redox Signaling by Electrophile-Protein Reactions. *Sci. Signal.* **2009,** *2* (90), re7-re7.
178. Agmon, E.; Stockwell, B. R., Lipid homeostasis and regulated cell death. *Curr. Opin. Chem. Biol.* **2017,** *39*, 83-89.
179. Leonarduzzi, G.; Arkan, M. C.; Başağa, H.; Chiarpotto, E.; Sevanian, A.; Poli, G., Lipid oxidation products in cell signaling. *Free Radical Biol. Med.* **2000,** *28* (9), 1370-1378.
180. Foret, M. K.; Lincoln, R.; Do Carmo, S.; Cuello, A. C.; Cosa, G., Connecting the "Dots": From Free Radical Lipid Autoxidation to Cell Pathology and Disease. *Chem. Rev.* **2020,** *120* (23), 12757-12787.
181. Arlt, S.; Beisiegel, U.; Kontush, A., Lipid peroxidation in neurodegeneration: new insights into Alzheimer's disease. *Curr. Opin. Lipidol.* **2002,** *13* (3), 289-294.
182. Jenner, P., Oxidative stress in Parkinson's disease. *Ann. Neurol.* **2003,** *53* (S3), S26-S38.
183. Barber, S. C.; Mead, R. J.; Shaw, P. J., Oxidative stress in ALS: A mechanism of neurodegeneration and a therapeutic target. *Biochim. Biophys. Acta - Mol. Basis Dis.* **2006,** *1762* (11), 1051-1067.
184. Peña-Bautista, C.; Vento, M.; Baquero, M.; Cháfer-Pericás, C., Lipid peroxidation in neurodegeneration. *Clin. Chim. Acta* **2019,** *497*, 178-188.
185. Timucin, A. C.; Basaga, H., Pro-apoptotic effects of lipid oxidation products: HNE at the crossroads of NF-κB pathway and anti-apoptotic Bcl-2. *Free Radical Biol. Med.* **2017,** *111*, 209-218.
186. Haugaard, S. B.; Andersen, O.; Pedersen, S. B.; Dela, F.; Fenger, M.; Richelsen, B.; Madsbad, S.; Iversen, J., Tumor necrosis factor α is associated with insulin-mediated suppression

of free fatty acids and net lipid oxidation in HIV-infected patients with lipodystrophy. *Metabolism* **2006,** *55* (2), 175-182.
187. Angeli, J. P. F.; Shah, R.; Pratt, D. A.; Conrad, M., Ferroptosis inhibition: mechanisms and opportunities. *Trends Pharmacol. Sci.* **2017,** *38* (5), 489-498.
188. Ackermann, J. A.; Hofheinz, K.; Zaiss, M. M.; Krönke, G., The double-edged role of 12/15-lipoxygenase during inflammation and immunity. *Biochim. Biophys. Acta - Mol. Cell Biol. Lipids* **2017,** *1862* (4), 371-381.
189. Yin, H.; Xu, L.; Porter, N. A., Free radical lipid peroxidation: mechanisms and analysis. *Chem. Rev.* **2011,** *111* (10), 5944-5972.
190. Baptista, M. S.; Cadet, J.; Greer, A.; Thomas, A. H., Photosensitization Reactions of Biomolecules: Definition, Targets and Mechanisms. *Photochem. Photobiol.* **2021,** *97* (6), 1456-1483.
191. Di Mascio, P.; Martinez, G. R.; Miyamoto, S.; Ronsein, G. E.; Medeiros, M. H. G.; Cadet, J., Singlet Molecular Oxygen Reactions with Nucleic Acids, Lipids, and Proteins. *Chem. Rev.* **2019,** *119* (3), 2043-2086.
192. Mulliken, R. S., Interpretation of the Atmospheric Oxygen Bands; Electronic Levels of the Oxygen Molecule. *Nature* **1928,** *122* (3075), 505-505.
193. DeRosa, M. C.; Crutchley, R. J., Photosensitized singlet oxygen and its applications. *Coord. Chem. Rev.* **2002,** *233-234*, 351-371.
194. Scurlock, R. D.; Wang, B.; Ogilby, P. R., Chemical Reactivity of Singlet Sigma Oxygen (b1Σg+) in Solution. *J. Am. Chem. Soc.* **1996,** *118* (2), 388-392.
195. Ogilby, P. R., Singlet oxygen: there is indeed something new under the sun. *Chem. Soc. Rev.* **2010,** *39* (8), 3181-3209.
196. Kiryu, C.; Makiuchi, M.; Miyazaki, J.; Fujinaga, T.; Kakinuma, K., Physiological production of singlet molecular oxygen in the myeloperoxidase-H2O2-chloride system. *FEBS Lett.* **1999,** *443* (2), 154-158.
197. Hampton, M. B.; Kettle, A. J.; Winterbourn, C. C., Inside the Neutrophil Phagosome: Oxidants, Myeloperoxidase, and Bacterial Killing. *Blood* **1998,** *92* (9), 3007-3017.
198. Baptista, M. S.; Cadet, J.; Di Mascio, P.; Ghogare, A. A.; Greer, A.; Hamblin, M. R.; Lorente, C.; Nunez, S. C.; Ribeiro, M. S.; Thomas, A. H.; Vignoni, M.; Yoshimura, T. M., Type I and Type II Photosensitized Oxidation Reactions: Guidelines and Mechanistic Pathways. *Photochem. Photobiol.* **2017,** *93* (4), 912-919.
199. Wondrak, G. T.; Jacobson, M. K.; Jacobson, E. L., Endogenous UVA-photosensitizers: mediators of skin photodamage and novel targets for skin photoprotection. *Photochem. Photobiol. Sci.* **2006,** *5* (2), 215-237.
200. Zhang, X.; Wang, Z.; Hou, Y.; Yan, Y.; Zhao, J.; Dick, B., Recent development of heavy-atom-free triplet photosensitizers: molecular structure design, photophysics and application. *J. Mater. Chem. C* **2021,** *9* (36), 11944-11973.
201. Schweitzer, C.; Schmidt, R., Physical Mechanisms of Generation and Deactivation of Singlet Oxygen. *Chem. Rev.* **2003,** *103* (5), 1685-1758.
202. Krasnovsky, A. A.; Kagan, V. E.; Minin, A. A., Quenching of singlet oxygen luminescence by fatty acids and lipids: Contribution of physical and chemical mechanisms. *FEBS Lett.* **1983,** *155* (2), 233-236.
203. Tsubone, T. M.; Baptista, M. S.; Itri, R., Understanding membrane remodelling initiated by photosensitized lipid oxidation. *Biophys. Chem.* **2019,** *254*, 106263.

204. Weber, G.; Charitat, T.; Baptista, M. S.; Uchoa, A. F.; Pavani, C.; Junqueira, H. C.; Guo, Y.; Baulin, V. A.; Itri, R.; Marques, C. M.; Schroder, A. P., Lipid oxidation induces structural changes in biomimetic membranes. *Soft Matter* **2014,** *10* (24), 4241-4247.
205. van den Berg, J. J. M.; Op den Kamp, J. A. F.; Lubin, B. H.; Kuypers, F. A., Conformational changes in oxidized phospholipids and their preferential hydrolysis by phospholipase A2: A monolayer study. *Biochemistry* **1993,** *32* (18), 4962-4967.
206. Mertins, O.; Bacellar, Isabel O. L.; Thalmann, F.; Marques, Carlos M.; Baptista, Maurício S.; Itri, R., Physical Damage on Giant Vesicles Membrane as a Result of Methylene Blue Photoirradiation. *Biophys. J.* **2014,** *106* (1), 162-171.
207. Bacellar, I. O. L.; Oliveira, M. C.; Dantas, L. S.; Costa, E. B.; Junqueira, H. C.; Martins, W. K.; Durantini, A. M.; Cosa, G.; Di Mascio, P.; Wainwright, M.; Miotto, R.; Cordeiro, R. M.; Miyamoto, S.; Baptista, M. S., Photosensitized Membrane Permeabilization Requires Contact-Dependent Reactions between Photosensitizer and Lipids. *J. Am. Chem. Soc.* **2018,** *140* (30), 9606-9615.
208. Vignoni, M.; Urrutia, M. N.; Junqueira, H. C.; Greer, A.; Reis, A.; Baptista, M. S.; Itri, R.; Thomas, A. H., Photo-Oxidation of Unilamellar Vesicles by a Lipophilic Pterin: Deciphering Biomembrane Photodamage. *Langmuir* **2018,** *34* (50), 15578-15586.
209. Boonnoy, P.; Jarerattanachat, V.; Karttunen, M.; Wong-ekkabut, J., Bilayer Deformation, Pores, and Micellation Induced by Oxidized Lipids. *J. Phys. Chem. Lett.* **2015,** *6* (24), 4884-4888.
210. Sakuma, Y.; Taniguchi, T.; Imai, M., Pore Formation in a Binary Giant Vesicle Induced by Cone-Shaped Lipids. *Biophys. J.* **2010,** *99* (2), 472-479.
211. Fragata, M.; Bellemare, F., Model of singlet oxygen scavenging by α-tocopherol in biomembranes. *Chem. Phys. Lipids* **1980,** *27* (2), 93-99.
212. Fahrenholtz, S. R.; Doleiden, F. H.; Trozzolo, A. M.; Lamola, A. A., On the quenching of singlet oxygen by α-tocopherol. *Photochem. Photobiol.* **1974,** *20* (6), 505-509.
213. Christopher, S.; Ching, T.-Y.; Geller, G. G., Chemistry of singlet oxygen—XVIII. Rates of reaction and quenching of α-tocopherol and singlet oxygen*. *Photochem. Photobiol.* **1974,** *20* (6), 511-513.
214. Kaiser, S.; Di Mascio, P.; Murphy, M. E.; Sies, H., Physical and chemical scavenging of singlet molecular oxygen by tocopherols. *Arch. Biochem. Biophys.* **1990,** *277* (1), 101-108.
215. Stevens, B.; Small Jr, R.; Perez, S. J. P.; Photobiology, The Photoperoxidation of Unsaturated Organic Molecules-XIII. O2 1 Δg Quenching By α-Tocopherol. *Photochem. Photobiol.* **1974,** *20* (6), 515-517.
216. Clough, R.; Yee, B.; Foote, C., Chemistry of singlet oxygen. 30. The unstable primary product of tocopherol photooxidation. *J. Am. Chem. Soc.* **1979,** *101* (3), 683-686.
217. NEELY, W. C.; MARTIN, J. M.; BARKER, S. A., Products and Relative Reaction Rates of the Oxidation of Tocopherols with Singlet Molecular Oxygen. *Photochem. Photobiol.* **1988,** *48* (4), 423-428.
218. Kumar, A.; Prasad, A.; Pospíšil, P., Formation of α-tocopherol hydroperoxide and α-tocopheroxyl radical: relevance for photooxidative stress in Arabidopsis. *Sci. Rep.* **2020,** *10* (1), 19646.
219. You, Y., Chemical tools for the generation and detection of singlet oxygen. *Org. Biomol. Chem.* **2018,** *16* (22), 4044-4060.
220. Gunduz, H.; Kolemen, S.; Akkaya, E. U., Singlet oxygen probes: Diversity in signal generation mechanisms yields a larger color palette. *Coord. Chem. Rev.* **2021,** *429*, 213641.

221. Westberg, M.; Bregnhøj, M.; Banerjee, C.; Blázquez-Castro, A.; Breitenbach, T.; Ogilby, P. R., Exerting better control and specificity with singlet oxygen experiments in live mammalian cells. *Methods* **2016,** *109*, 81-91.
222. Wilkinson, F.; Brummer, J. G., Rate constants for the decay and reactions of the lowest electronically excited singlet state of molecular oxygen in solution. *J. Phys. Chem. Ref. Data* **1981,** *10* (4), 809-999.
223. Gollmer, A.; Arnbjerg, J.; Blaikie, F. H.; Pedersen, B. W.; Breitenbach, T.; Daasbjerg, K.; Glasius, M.; Ogilby, P. R., Singlet Oxygen Sensor Green®: Photochemical Behavior in Solution and in a Mammalian Cell. *Photochem. Photobiol.* **2011,** *87* (3), 671-679.
224. Ragàs, X.; Jiménez-Banzo, A.; Sánchez-García, D.; Batllori, X.; Nonell, S., Singlet oxygen photosensitisation by the fluorescent probe Singlet Oxygen Sensor Green®. *Chem. Commun.* **2009,** (20), 2920-2922.
225. Pedersen, S. K.; Holmehave, J.; Blaikie, F. H.; Gollmer, A.; Breitenbach, T.; Jensen, H. H.; Ogilby, P. R., Aarhus Sensor Green: A Fluorescent Probe for Singlet Oxygen. *J. Org. Chem.* **2014,** *79* (7), 3079-3087.
226. Liu, H.; Wang, T.; Wang, C.; Liu, D.; Luo, J., Exciton Radiative Recombination Dynamics and Nonradiative Energy Transfer in Two-Dimensional Transition-Metal Dichalcogenides. *J. Phys. Chem. C* **2019,** *123* (15), 10087-10093.
227. Jiang, S.; Pal, N.; Hong, F.; Fahmi, N. E.; Hu, H.; Vrbanac, M.; Yan, H.; Walter, N. G.; Liu, Y., Regulating DNA Self-Assembly Dynamics with Controlled Nucleation. *ACS Nano* **2021,** *15* (3), 5384-5396.
228. Saccà, B.; Ishitsuka, Y.; Meyer, R.; Sprengel, A.; Schöneweiß, E.-C.; Nienhaus, G. U.; Niemeyer, C. M., Reversible Reconfiguration of DNA Origami Nanochambers Monitored by Single-Molecule FRET. *Angew. Chem. Int. Ed.* **2015,** *54* (12), 3592-3597.
229. De Cremer, G.; Sels, B. F.; De Vos, D. E.; Hofkens, J.; Roeffaers, M. B. J., Fluorescence micro(spectro)scopy as a tool to study catalytic materials in action. *Chem. Soc. Rev.* **2010,** *39* (12), 4703-4717.
230. Thid, D.; Benkoski, J. J.; Svedhem, S.; Kasemo, B.; Gold, J., DHA-Induced Changes of Supported Lipid Membrane Morphology. *Langmuir* **2007,** *23* (11), 5878-5881.
231. Riske, K. A.; Sudbrack, T. P.; Archilha, N. L.; Uchoa, A. F.; Schroder, A. P.; Marques, C. M.; Baptista, M. S.; Itri, R., Giant Vesicles under Oxidative Stress Induced by a Membrane-Anchored Photosensitizer. *Biophys. J.* **2009,** *97* (5), 1362-1370.
232. Martínez, S. R.; Durantini, A. M.; Becerra, M. C.; Cosa, G., Real-Time Single-Cell Imaging Reveals Accelerating Lipid Peroxyl Radical Formation in Escherichia coli Triggered by a Fluoroquinolone Antibiotic. *ACS Infect. Dis.* **2020,** *6* (9), 2468-2477.
233. Lincoln, R.; Greene, L. E.; Zhang, W.; Louisia, S.; Cosa, G., Mitochondria Alkylation and Cellular Trafficking Mapped with a Lipophilic BODIPY–Acrolein Fluorogenic Probe. *J. Am. Chem. Soc.* **2017,** *139* (45), 16273-16281.
234. Hariri, A. A.; Hamblin, G. D.; Gidi, Y.; Sleiman, H. F.; Cosa, G., Stepwise growth of surface-grafted DNA nanotubes visualized at the single-molecule level. *Nat. Chem.* **2015,** *7* (4), 295-300.
235. Gidi, Y.; Payne, L.; Glembockyte, V.; Michie, M. S.; Schnermann, M. J.; Cosa, G., Unifying Mechanism for Thiol-Induced Photoswitching and Photostability of Cyanine Dyes. *J. Am. Chem. Soc.* **2020,** *142* (29), 12681-12689.
236. Abbe, E., Beiträge zur Theorie des Mikroskops und der mikroskopischen Wahrnehmung. *Archiv für Mikroskopische Anatomie* **1873,** *9* (1), 413-468.

237. Hell, S. W.; Wichmann, J., Breaking the diffraction resolution limit by stimulated emission: stimulated-emission-depletion fluorescence microscopy. *Opt. Lett.* **1994,** *19* (11), 780-782.
238. Betzig, E.; Patterson, G. H.; Sougrat, R.; Lindwasser, O. W.; Olenych, S.; Bonifacino, J. S.; Davidson, M. W.; Lippincott-Schwartz, J.; Hess, H. F., Imaging Intracellular Fluorescent Proteins at Nanometer Resolution. *Science* **2006,** *313* (5793), 1642-1645.
239. Rust, M. J.; Bates, M.; Zhuang, X., Sub-diffraction-limit imaging by stochastic optical reconstruction microscopy (STORM). *Nat. Methods* **2006,** *3* (10), 793-796.
240. Möckl, L.; Lamb, D. C.; Bräuchle, C., Super-resolved Fluorescence Microscopy: Nobel Prize in Chemistry 2014 for Eric Betzig, Stefan Hell, and William E. Moerner. *Angew. Chem. Int. Ed.* **2014,** *53* (51), 13972-13977.
241. Pujals, S.; Feiner-Gracia, N.; Delcanale, P.; Voets, I.; Albertazzi, L., Super-resolution microscopy as a powerful tool to study complex synthetic materials. *Nat. Rev. Chem.* **2019,** *3* (2), 68-84.
242. Dhiman, S.; Andrian, T.; Gonzalez, B. S.; Tholen, M. M. E.; Wang, Y.; Albertazzi, L., Can super-resolution microscopy become a standard characterization technique for materials chemistry? *Chem. Sci.* **2022,** *13* (8), 2152-2166.
243. Schermelleh, L.; Ferrand, A.; Huser, T.; Eggeling, C.; Sauer, M.; Biehlmaier, O.; Drummen, G. P. C., Super-resolution microscopy demystified. *Nat. Cell Biol.* **2019,** *21* (1), 72-84.
244. Sigal, Y. M.; Zhou, R.; Zhuang, X., Visualizing and discovering cellular structures with super-resolution microscopy. *Science* **2018,** *361* (6405), 880-887.
245. Reinhardt, S. C. M.; Masullo, L. A.; Baudrexel, I.; Steen, P. R.; Kowalewski, R.; Eklund, A. S.; Strauss, S.; Unterauer, E. M.; Schlichthaerle, T.; Strauss, M. T.; Klein, C.; Jungmann, R., Ångström-resolution fluorescence microscopy. *Nature* **2023,** *617* (7962), 711-716.
246. Jonkman, J.; Brown, C. M., Any Way You Slice It-A Comparison of Confocal Microscopy Techniques. *J Biomol Tech* **2015,** *26* (2), 54-65.
247. Campos, L. A.; Liu, J.; Wang, X.; Ramanathan, R.; English, D. S.; Muñoz, V., A photoprotection strategy for microsecond-resolution single-molecule fluorescence spectroscopy. *Nat. Methods* **2011,** *8* (2), 143-146.
248. Elliott, A. D., Confocal Microscopy: Principles and Modern Practices. *Curr. Protoc. Cytom.* **2020,** *92* (1), e68.
249. Park, Y. I.; Lee, K. T.; Suh, Y. D.; Hyeon, T., Upconverting nanoparticles: a versatile platform for wide-field two-photon microscopy and multi-modal in vivo imaging. *Chem. Soc. Rev.* **2015,** *44* (6), 1302-1317.
250. Webb, D. J.; Brown, C. M., Epi-Fluorescence Microscopy. In *Cell Imaging Techniques: Methods and Protocols*, Taatjes, D. J.; Roth, J., Eds. Humana Press: Totowa, NJ, 2013; pp 29-59.
251. Fish, K. N., Total Internal Reflection Fluorescence (TIRF) Microscopy. *Curr. Protoc.* **2022,** *2* (8), e517.
252. Mattheyses, A. L.; Simon, S. M.; Rappoport, J. Z., Imaging with total internal reflection fluorescence microscopy for the cell biologist. *J. Cell Sci.* **2010,** *123* (21), 3621-3628.
253. Fan, S.; Webb, J. E. A.; Yang, Y.; Nieves, D. J.; Gonçales, V. R.; Tran, J.; Hilzenrat, G.; Kahram, M.; Tilley, R. D.; Gaus, K.; Gooding, J. J., Observing the Reversible Single Molecule Electrochemistry of Alexa Fluor 647 Dyes by Total Internal Reflection Fluorescence Microscopy. *Angew. Chem. Int. Ed.* **2019,** *58* (41), 14495-14498.
254. Lei, C.; Hu, D.; Ackerman, E. J., Single-molecule fluorescence spectroelectrochemistry of cresyl violet. *Chem. Commun.* **2008,** (43), 5490-5492.

255. Lei, C.; Hu, D.; Ackerman, E., Clay Nanoparticle-Supported Single-Molecule Fluorescence Spectroelectrochemistry. *Nano Lett.* **2009,** *9* (2), 655-658.
256. Godin, R.; Cosa, G., Counting Single Redox Turnovers: Fluorogenic Antioxidant Conversion and Mass Transport Visualization via Single Molecule Spectroelectrochemistry. *J. Phys. Chem. C* **2016,** *120* (28), 15349-15353.

Chapter 2

Singlet Oxygen Flux, Associated Lipid Photooxidation and Membrane Expansion Dynamics Visualized on Giant Unilamellar Vesicles

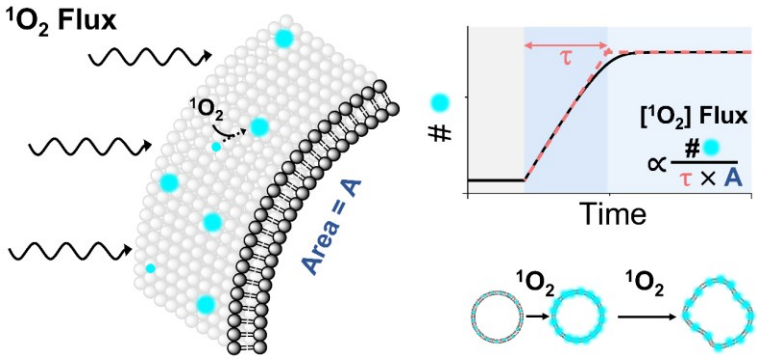

"Important thing in science is not so much to obtain new facts as to discover new ways of thinking about them"

- Sir William Bragg

2.1. Preface

In **Chapter 1**, we discussed the mechanism by which fluorophores can photosensitize the generation of singlet oxygen ($^1O_2$) and the pathways by which $^1O_2$ is deactivated. In particular, we addressed how $^1O_2$ induces lipid peroxidation, and how lipid hydroperoxides and their by-products result in changes to the physical properties of a lipid membrane, including membrane surface area, packing, and permeability. **Chapter 1** also provides the chemical principles underlying the activity of $^1O_2$ sensors and introduces the need of new sensitive and quantitative sensors. In **Chapter 2**, we demonstrate the capabilities of an α-tocopherol based fluorogenic probe, H_4BPMHC, as quantitative sensor of $^1O_2$ flux. Fluorescence imaging studies were conducted using giant unilamellar vesicles embedded with H_4BPMHC and were used to correlate the flux of photosensitized $^1O_2$ with ensuing membrane deformation dynamics. The work reported in **Chapter 2** provides a roadmap for the investigation of the dose-dependent response of lipid membranes to chemical oxidative stimuli.

Chapter 2 has been reproduced with permission from "Singlet Oxygen Flux, Associated Lipid Photooxidation, and Membrane Expansion Dynamics Visualized on Giant Unilamellar Vesicles", Aya Sakaya, Isabel O. L. Bacellar, José Luis Fonseca, Andrés M. Durantini, Julia McCain, Laiyi Xu, Mariana Vignoni, Andrés H. Thomas, Mauricio S. Baptista, and Gonzalo Cosa, *Langmuir* **2023**, *39* (1), 442-452. Copyright 2023 American Chemical Society. Aya Sakaya and Isabel O. L. Bacellar are co-first authors on this manuscript.

2.2. Abstract

The physical properties of lipid membranes depend on their lipid composition. Photosensitized singlet oxygen ($^1O_2$) provides a handle to spatiotemporally control the generation of lipid hydroperoxides via the *ene* reaction, enabling fundamental studies on membrane dynamics in response to chemical composition changes. Critical to relating the physical properties of the lipid membrane to hydroperoxide formation is the availability of a sensitive reporter to quantify the arrival of $^1O_2$. Here, we show that a fluorogenic α- tocopherol analogue, H_4BPMHC, undergoes a >360-fold emission intensity enhancement in liposomes following a reaction with $^1O_2$. Rapid quenching of $^1O_2$ by the probe (k_q = 4.9 × 10^8 M^{-1} s^{-1}) ensures zero-order kinetics of probe consumption. The remarkable intensity enhancement of H_4BPMHC upon $^1O_2$ trapping, its linear temporal behavior, and its protective role in outcompeting membrane damage provide a sensitive and reliable method to quantify the $^1O_2$ flux on lipid membranes. Armed with this probe, fluorescence microscopy studies were devised to enable (i) monitoring the flux of photosensitized $^1O_2$ into giant unilamellar vesicles (GUVs), (ii) establishing the onset of the *ene* reaction with the double bonds of monounsaturated lipids, and (iii) visualizing the ensuing collective membrane expansion dynamics associated with molecular changes in the lipid structure upon hydroperoxide formation. A correlation was observed between the time for antioxidant H_4BPMHC consumption by $^1O_2$ and the onset of membrane fluctuations and surface expansion. Together, our imaging studies with H_4BPMHC in GUVs provide a methodology to explore the intimate relationship between photosensitizer activity, chemical insult, membrane morphology, and its collective dynamics.

2.3. Introduction

The physical properties of lipid membranes, such as molecular surface area, thickness, curvature, permeability, and lateral organization, depend on their lipid composition. Photosensitized singlet oxygen ($^1O_2$) provides a handle to spatiotemporally control the generation of lipid hydroperoxides via the *ene* reaction with mono and polyunsaturated fatty acids, [1, 2] enabling fundamental studies on membrane dynamics in response to chemical composition changes.[3-6]

Molecular changes associated with lipid peroxidation may be amplified to collective physical properties of the lipid membrane, such as surface area expansion and associated membrane thinning,[6-10] as well as lateral phase separation.[11-14]

Fluorescence microscopy studies offer the possibility of relating, at the nanometer scale, the dynamics of lipid membrane surface area expansion and associated morphological changes to the rate of lipid peroxidation by means of membrane visualization via positional fluorescent markers. Critical to relating the physical properties of the lipid membrane to lipid hydroperoxide formation is the availability of a sensitive fluorescent probe that provides a direct readout of the $^1O_2$ flux. Essentially, a probe that undergoes intensity enhancement or emission wavelength change upon trapping $^1O_2$ and whose temporal response is well established is needed in order to quantify in real-time the flux of $^1O_2$ impinging on the membranes. Additionally, such a probe should readily outcompete $^1O_2$-mediated lipid oxidation and all other $^1O_2$ decay pathways. Critically, such a probe should not in itself generate singlet oxygen upon photoexcitation, either prior to or after activation.[15]

Here, we show that the two-segment trap-reporter fluorogenic α-tocopherol analogue, H_4BPMHC,[16] fulfills the sensitivity and reactivity requirements toward sensing $^1O_2$ in lipid membranes in bulk and at the nanometer scale (**Figure 2.1**). H_4BPMHC bears the chromanol moiety of α-tocopherol (trap), an extremely efficient quencher of $^1O_2$ through combined physical and chemical pathways (**Figure 2.1d**).[17] It also bears a lipophilic BODIPY-fluorophore tail (reporter), where intramolecular photoinduced electron transfer (P*e*T) from the chromanol segment renders the probe non-emissive.[16, 18] Probe oxidation occurs with zero-order kinetics, readily observed through a >360-fold intensity enhancement, and provides a direct readout of $^1O_2$ flux (molecules of $^1O_2$ per unit area and unit time) through lipid membranes (**Figure 2.1a,b**). The probe thus offers remarkable sensitivity and straightforward analysis (**Figure 2.1b**). H_4BPMHC further offers a membrane-protecting role, inhibiting $^1O_2$-mediated lipid peroxidation/membrane damage until its consumption/intensity enhancement is achieved, thus serving as an internal clock for the onset of the *ene* reaction (**Figure 2.1b,c**).

Imaging studies on single giant unilamellar vesicles (GUVs) conducted with H_4BPMHC and water- and lipid-soluble $^1O_2$ photosensitizers enabled probing real-time $^1O_2$ flux, the ensuing onset of lipid peroxidation by $^1O_2$, and the associated changes to membrane surface area and

morphology (**Figure 2.1c**). Our imaging studies offer a way for examining the close connection between membrane morphology and dynamics, chemical damage, and photosensitizer activity.

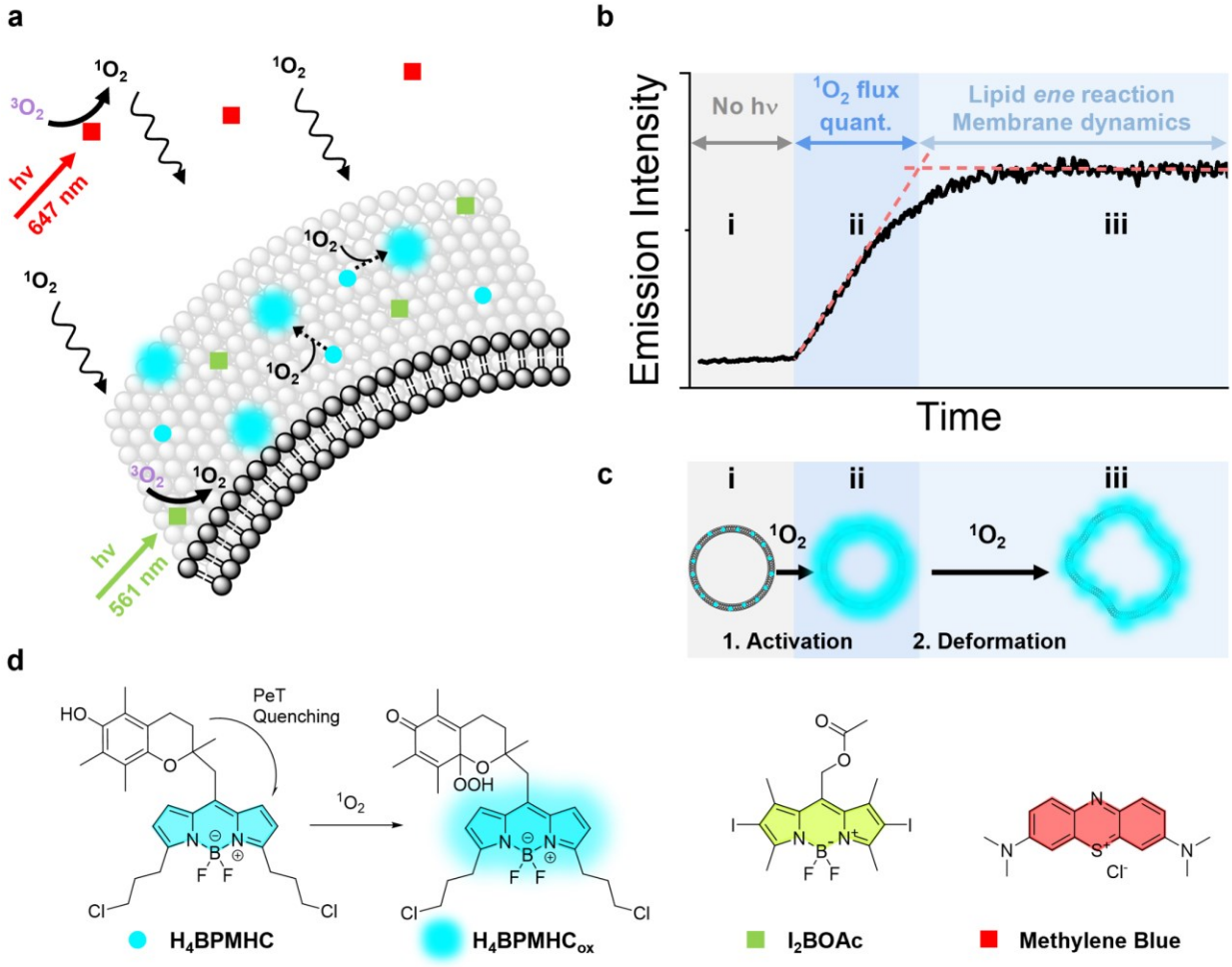

Figure 2.1. Singlet oxygen ($^1O_2$) flux and the ensuing conversion of nonemissive H$_4$BPMHC to emissive H$_4$BPMHCox. (a) Schematic of $^1O_2$ production by either a lipophilic or a hydrophilic photosensitizer. Flux toward the lipid membrane in the latter case is illustrated with wiggly arrows. $^1O_2$ reaction with H$_4$BPMHC is further shown. (b) Intensity-time profile of membrane-embedded H$_4$BPMHC: (i) prior to photosensitizer irradiation, (ii) following $^1O_2$ photosensitization-mediated probe activation, and (iii) following the onset of lipid *ene* reaction upon full consumption of the antioxidant probe. (c) Cartoon illustrating expected observation through the abovementioned three phases. (d) Structures of H$_4$BPMHC, a proposed fluorescent oxidized counterpart, H$_4$BPMHC$_{ox}$, and the photosensitizers employed in this study.

2.4. Experimental Section

2.4.1. Materials

H_4BPMHC, H_2BPMHC, and I_2BOAc were synthesized as previously described.[16, 18, 19] Methylene blue, poly(vinyl alcohol) (PVA, average M_w 130,000), D-(+)-glucose(≥99.5% GC), sucrose (≥99.5%, HPLC, for molecular biology), 9,10-dimethylanthracene (DMA), formamide, benzene, toluene, anthracene, pyrene, hexachlorobenzene, 1,3,5-tri-*tert*-butylenzene, and HPLC grade chloroform (≥99.8%, amylene stabilized) were purchased from Sigma Aldrich. HPLC solvents (acetone and acetonitrile), sulfuric acid, 10× phosphate-buffered saline (pH 7.4, Invitrogen), HyClone Water (Molecular Biology Grade, Cytiva), and naphthalene were purchased from Thermo Fisher Scientific. Anhydrous ethanol was purchased from Greenfield Global, Inc. (Brampton, ON, Canada). Hydrogen peroxide was purchased from ACP chemicals. Deuterium oxide (D_2O, 99.9%) was purchased from Cambridge Isotope Laboratories, Inc. 1,2- Dioleoyl-*sn*-glycero-3-phosphocholine (DOPC), L-*α*-phosphatidylcholine (95%) (Egg PC) (Egg, Chicken), 1,2-dipalmitoyl-sn-glycero- 3-phosphoethanolamine-*N*-(biotinyl) (sodium salt, DPPE-bio), 1,2-dimyristoyl-sn-glycero-3-phosphocholine (DMPC), and 1- palmitoyl-2-oleoyl-glycero-3-phosphocholine (POPC) were purchased from Avanti Polar Lipids. All materials were used without further purification.

2.4.2. Fluorescence assays in the presence of photosensitizers

Oxidation of H_4BPMHC (H_2BPMHC when specified) by photosensitized singlet oxygen was measured in a liposome suspension (see **Section** 2.7.1 for liposome preparation). Generation of H_4BPMHC_{ox} was monitored by following the evolution of its emission intensity as a function of photosensitizer irradiation time.

Liposome solutions were made by diluting H_4BPMHC-containing liposomes in air-equilibrated PBS or DPBS (phosphate buffer prepared in D_2O) to a final concentration of 1 mM in lipid and 1 μM in H_4BPMHC. Photosensitizers were added from concentrated stock solutions (in acetonitrile for I_2BOAc and water for methylene blue), ensuring to add a maximum of 2 μL of the concentrated photosensitizer solution to a final sample volume of 2000 μL.

Samples containing 0.4 μM I_2BOAc were irradiated using green LED lamps (LED-GR, Luzchem), with a 520 nm peak wavelength, a full width at half-maximum (FWHM) of 31 nm, and an irradiance of 2.6 mW cm^{-2} in the peak wavelength range. Samples containing 1 μM methylene blue were irradiated using red LED lamps (LED-RD, Luzchem), with a 635 nm peak wavelength, an FWHM of 17 nm, and an irradiance of 1.85 mW cm^{-2} in the peak wavelength range.

Emission scans were recorded as a function of irradiation time using a Photon Technology International (PTI) Quanta Master fluorimeter and 1.0 cm × 1.0 cm glass cuvettes. The excitation wavelength was set at 480 nm and the emission range from 490 to 650 or 700 nm. The excitation and emission slits were set to 2 nm in all the experiments. Recorded emission spectra are automatically corrected for wavelength-dependent detector (PMT) sensitivity upon acquisition with the PTI Felix32 software (version 1.2).

2.4.3. GUV preparation

GUVs were grown by the gel-assisted method.[20] Rectangular microscope glass slides (3″ × 1″ × 1 mm, Fischer Scientific) were cleaned by sonication in a piranha solution (3:1 H_2SO_4/H_2O_2). A polymer film was prepared by spreading 100 μL of a 5% (w/w) PVA solution in HyClone water over the surface of the dry glass slides, obtaining a *ca.* 1.0 × 2.5 cm rectangle. The glass slides were then placed into an oven at 50 °C for 1 h until a dry PVA film was obtained. Next, 10 μL of a 20 mM lipid solution in chloroform (98% DOPC, 2% DPPE-bio) also carrying H_4BPMHC in a 1:100 H_4BPMHC/lipid ratio were spread over the PVA film. After evaporation of the solvent in a vacuum-filled chamber for 30 min, an O-ring was fixed around the PVA film, and the resulting compartment was filled with 600 μL of a 0.1 M sucrose solution. After 2 min, the GUV suspension was transferred to an Eppendorf tube. The compartment was then washed with an extra 100 μL of sucrose solution, which was also added to the tube. Prior to the experiments, the content of the tube was homogenized by gentle mixing of the suspension, and 100 μL of GUV suspension was transferred to the imaging chamber of the microscope containing 400 μL of 0.1 M glucose solution. The GUVs were allowed to sediment in the dark for *ca.* 10 min and thus reach the glass coverslip bottom (25 mm × 25 mm, Fischer scientific, piranha cleaned). No coverslip surface functionalization was employed. Sedimentation of GUVs is favored by the fact that the inner compartment of the GUVs is filled with sucrose solution, while the outer medium is enriched

in glucose. Photosensitizers were added to the glucose solution from concentrated stocks in water (MB) or acetonitrile (I_2BOAc).

2.4.4. Microscopy imaging of GUVs

Fluorescence images were acquired using an inverted microscope (Nikon Eclipse Ti) equipped with a Perfect Focus System (PFS) to compensate for axial drift and an oil immersion objective (Nikon CFI SR Apochromat TIRF 100×, numerical aperture (NA) = 1.49) with an effective pixel size of 160 nm. A widefield configuration was adopted, where the incident beam was brought in perpendicular to the sample surface. H_4BPMHC, I_2BOAC, and methylene blue were excited with the 488, 561, and 647 nm laser outputs of an Agilent MLC400B Monolithic laser combiner, respectively. We note that under the excitation conditions applied, the direct excitation of H_4BPMHC with the 488 nm laser line led to a minimal direct excitation of I_2BOAC. Under our imaging conditions, the rate of excitation of I_2BOAc with the 561 nm laser was ~19-fold larger than its rate of excitation with the 488 nm laser (considering I_2BOAc extinction coefficient and photon flux at both wavelengths, see **Figure 2.5** for extinction coefficient spectra of H_4BPMHC, I_2BOAC, and methylene blue). The laser beam was cleaned up with a ZET 405/488/561/647× multiband excitation filter (Chroma Technology) and coupled to the microscope with a ZT405/488/561/647rpc multiband beam splitter (Chroma Technology). The fluorescence emission collected through the objective was spectrally filtered using a ZET405/488/561/647m emission filter (Chroma Technology). Emission from H_4BPMHC was further cleaned using a 540/80× bandpass filter (Chroma Technology) to reject any emission arising from I_2BOAC or methylene blue. H_4BPMHC emission was collected on the 512 × 512 pixels region of a back-illuminated electron multiplying charge-coupled device (EMCCD) camera (Andor iXon Ultra DU-897). Images were acquired with a pixel size of 160 nm/pixel and at a frame rate of 10 frames/s (I_2BOAc) or 5 frames/s (methylene blue). The difference in acquisition rate between the two photosensitizers is due to the faster kinetics observed with I_2BOAc. The objective was focused at the equatorial plane of the GUVs. Emissions from spherical GUVs thus appear as rings on the camera plane. The microscope was controlled through the NIS element software from Nikon, while the camera was controlled using Micro-Manager Software (Micro-Manager 1.4.13, San Francisco, CA, USA). GUV data analysis is described in detail in **Section** 2.7.1.

2.5. Results and Discussion

2.5.1. Mechanistic underpinning behind H_4BPMHC choice

We chose H_4BPMHC as a fluorogenic sensor based on (i) its anticipated sensitivity toward $^1O_2$, (ii) its partition within lipid membranes where $^1O_2$ is to be sensed, (iii) its reporting mechanism based on the fluorescence enhancement of a properly substituted BODIPY dye, and (iv) the lack of $^1O_2$ generation characteristic of BODIPY dyes, yet encountered in e.g. xanthene chromophore singlet oxygen sensors.[15, 21-23] We hypothesized that $^1O_2$ addition to the chromanol moiety in the probe would deactivate the otherwise efficient intramolecular P*e*T from the trap to the reporter segment, thus restoring the BODIPY emission in newly formed H_4BPMHC$_{ox}$.[16, 18]

Most importantly, we anticipated H_4BPMHC to have a high reactivity toward $^1O_2$, expected to be on the same order as that of α-tocopherol, the most potent naturally occurring lipid-soluble antioxidant.[24] The chromanol moiety of α-tocopherol present in H_4BPMHC provides a highly efficient quenching mechanism for $^1O_2$ (**Scheme 2.1**, steps 3−4), where a close to diffusion-controlled quenching rate constant ($k_q = k_{ox} + k_{phy}$), in the range of 2−7 × 10^8 M^{-1} s^{-1}, has been reported for α-tocopherol.[25-28] Notably, a large fraction of the quenching (93−99% depending on the solvent[17, 26, 27]) occurs via a physical pathway (k_{phy}), relying on intersystem crossing within an exciplex (step 4 in **Scheme 2.1**).[27, 28] The remaining fraction of the quenching in turn results in the oxidation of the chromanol moiety (step 3 in **Scheme 2.1**).

Scheme 2.1. Elementary Steps involved in singlet oxygen ($^1O_2$) generation through a sensitizer photoirradiation and subsequent decay steps.[a]

$$\text{Sensitizer} \xrightarrow{\phi_\Delta x I_a} {}^1O_2 \qquad 1$$

$$^1O_2 \xrightarrow{k_d} {}^3O_2 + h\nu + \Delta \qquad 2$$

$$^1O_2 + Q \xrightarrow{k^Q_{ox}} Q_{ox} \qquad 3$$

$$^1O_2 + Q \xrightarrow{k^Q_{phy}} {}^3O_2 + Q \qquad 4$$

$$^1O_2 + L \xrightarrow{k^L_{ene}} LOOH \qquad 5$$

$$^1O_2 + L \xrightarrow{k^L_{phy}} {}^3O_2 + L \qquad 6$$

[a]Step 1, sensitization may arise from either singlet or triplet excited states, where I_a stands for the rate of excitation of the photosensitizer, and ϕ_Δ is the yield of $^1O_2$ sensitization from the photoexcited sensitizer. Step 2, unimolecular processes (k_d) involving either heat or phosphorescence emission. Steps 3 and 4, chemical (k_{ox}) and physical (k_{phy}) interactions, respectively, with a generic quencher (Q), where $k_q = k_{ox} + k_{phy}$. Similar chemical and physical deactivation steps are illustrated with lipids (steps 5 and 6).

Provided that quenching of $^1O_2$ by H4BPMHC outcompetes $^1O_2$ decay through other pathways (i.e., $^1O_2$ quenching by lipids (**Scheme 2.1**, steps 5 and 6, where $k_q^L = k_{ene}^L + k_{phy}^L \approx 1-10 \times 10^4$ M^{-1} s^{-1} [29-31]) as well as the fast $^1O_2$ decay rate in water ($k_d \approx 2.7-2.9 \times 10^5$ s^{-1}, **Scheme 2.1**, step 2)[32, 33]), a kinetic analysis shows that the rate of $^1O_2$ addition (oxygenation) to H4BPMHC and formation of emissive H_4BPMHC_{ox} (**Scheme 2.1**, **eqs 2.1** and **2.2**) will be zero order with respect to the probe (see **Section 2.7.2** for the derivation of **eq 2.1**).[34] Thus, under continuous photosensitizer irradiation conditions, e.g. lamp or laser continuous wave (cw) illumination, and provided $k_q^{H_4BPMHC} \times [H_4BPMHC] \gg \left(k_d + k_q^L \times [L]\right)$, a linear time dependence is expected for the generation of emissive H_4BPMHC_{ox} as seen in **eq 2.2**, where I_a is the rate of excitation of the photosensitizer, and ϕ_Δ is its quantum yield of singlet oxygen sensitization.

$$-\frac{d[H_4BPMHC]}{dt} = \frac{d[H_4BPMHC_{ox}]}{dt} = \frac{\phi_\Delta \times I_a \times k_{ox}^{H_4BPMHC} \times [H_4BPMHC]}{\left(k_d + k_q^L \times [L]\right) + k_q^{H_4BPMHC} \times [H_4BPMHC]} \quad (2.1)$$

$$\frac{d[H_4BPMHC_{ox}]}{dt} = \frac{\phi_\Delta \times I_a \times k_{ox}^{H_4BPMHC}}{k_q^{H_4BPMHC}} \quad (2.2)$$

This anticipated temporal response provides a direct readout of the consumption time for the probe (**Figure 2.1b**), and the associated flux of $^1O_2$ provided the amount of probe is known (vide infra).

2.5.2. H4BPMHC reactivity and sensitivity to $^1O_2$

Following the mechanism-based choice of the probe, we first established the reactivity of H4BPMHC to $^1O_2$ in acetonitrile solutions via a competition assay involving $^1O_2$-mediated discoloration of the trap DMA, see **Section 2.7.1** and **Figure 2.6**. The assay yielded a value of $k_q^{H_4BPMHC} = 4.9 \times 10^8$ M^{-1} s^{-1} for the quenching of $^1O_2$ by H4BPMHC. This value is comparable to the k_q value obtained by Gorman et al. and others using α-tocopherol.[25-27] The value also

compares well with the one we have previously reported for the scavenging of $^1O_2$ by PMHC (2,2,5,6,7-pentamethyl-6-hydroxychroman, an α-tocopherol analogue lacking the phytyl tail) and by Br_2BPMHC, a BODIPY based dormant photosensitizer structurally related to H_4BPMHC (4×10^8 and 2×10^8 M^{-1} s^{-1}, respectively).[19] Given that only 1%−7% of the quenching is expected to yield oxidation of the chromanol moiety with a concomitant enhancement of fluorescence, these values place the rate constant for chemical trapping of $^1O_2$ by tocopherol (k_{ox}) in the range of 4.9×10^6 to 3.4×10^7 M^{-1} s^{-1}.

Importantly, the rate constant for $^1O_2$ quenching and trapping by chromanol are approximately four and two orders of magnitude larger, respectively, than that recorded for $^1O_2$ quenching by monounsaturated lipids in organic solvents ($k_q^L \sim 1 \times 10^4$ M^{-1} s^{-1}),[29-31] where an estimated 60% arises from chemical trapping contributions ($k_{ene}^L \sim 0.6 \times 10^4$ M^{-1} s^{-1}).[29] This would indicate that the probe protects unsaturated lipids from photooxidation by $^1O_2$ and that zero-order kinetics are applicable, provided the lipid to probe molar excess is not larger than three orders of magnitude.

We subsequently conducted emission intensity studies over time to monitor the response of H_4BPMHC to $^1O_2$ when the probe is embedded in liposomes. Liposomes were prepared with DOPC at a final concentration of 1 mM and having a *ca*. 1:1000 H_4BPMHC/lipid mole ratio (**Figure 2.2**). Photosensitizers, either I_2BOAc or methylene blue (log P = 5.87 (this work, see **Section 2.7**) and −0.10,[35] respectively), were chosen based on their differing hydrophobicity (**Figure 2.1d**). A linear increase in fluorescence intensity with increasing I_2BOAc irradiation times was observed with liposome suspensions illustrating zero-order kinetics with respect to the probe in this media (see **Figure 2.2a**). Analysis of the data shows that the activation of the probe was dependent on the presence of photosensitizer, light, and oxygen (**Figure 2.2a,b**). Activation of H_4BPMHC in liposomes is thus associated with the chemical trapping of $^1O_2$, see **Figure 2.2a,b**.

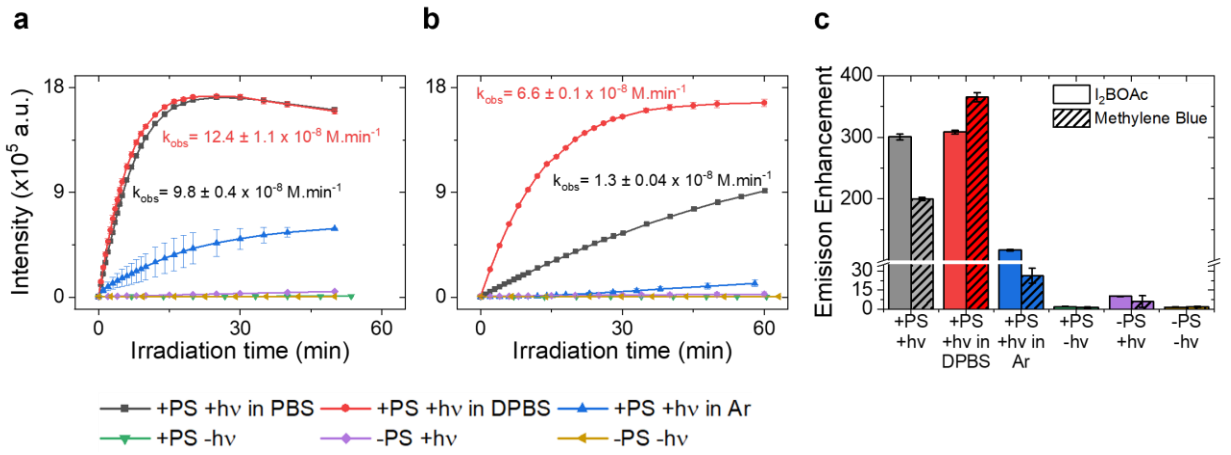

Figure 2.2. H_4BPMHC sensitivity to $^1O_2$ in DOPC liposomes. (a,b) H_4BPMHC fluorescence intensity−time profiles in DOPC liposomes using 0.4 μM I_2BOAc (a) or 1 μM methylene blue (b) as a photosensitizer under different conditions: air-equilibrated in PBS buffer, air equilibrated in a DPBS buffered solution (phosphate buffer prepared in D_2O), argon purged, and negative controls lacking photosensitizers, light, or both. The zero-order rate constants of emission enhancement in PBS (black) and DPBS (red) are listed in the graphs. (c) Maximum enhancement of H_4BPMHC emission intensity upon its oxidation by photosensitized $^1O_2$ obtained from data listed in (a,b). Data correspond to the average ± standard deviation of independent triplicates (duplicates for argon-purged samples). [DOPC] = 1 mM, [H_4BPMHC] = 1 μM. Excitation and emission slits were set at 2 nm. H_4BPMHC was excited at λ_{ex} = 480 nm and its emission was collected between 490 and 700 nm. Time 0 min corresponds to the time when the photosensitizer was added for the samples where photosensitizers were not irradiated. We utilized 0.4 μM of I_2BOAC irradiated with a 520 nm LED lamp or 1 μM of methylene blue irradiated with a 635 nm LED lamp in these studies.

The >360-fold enhancement recorded in these experiments is remarkable and emphasizes the sensitivity of H_4BPMHC to $^1O_2$ within lipid environments (**Figure 2.2c**, see **Section 2.7.3.1** for emission enhancement calculations). Intensity enhancement values and rates of probe oxidation were basically the same in either water or deuterium oxide, even though $^1O_2$ experiences considerably different lifetimes in these media, 3.5−3.7 μs in water to 68−69 μs in D_2O.[32, 33] The similar rates and maximum enhancements recorded in both media highlight the lipophilic nature of both the photosensitizer and the probe (see **Section 2.7.3.2** for oxidation rate calculation). Here, $^1O_2$ molecules are produced and consumed within the same lipid membrane microenvironment, minimizing the detrimental role that quenching by water may have on product yield (rate of probe activation). Extended irradiation times under the abovementioned conditions lead to a decrease in the emission intensity of the activated probe, possibly due to the reaction of $^1O_2$ with the BODIPY core or degradation of H_4BPMHC_{ox} to less emissive products.[36]

The effect that different degrees of lipid unsaturation have on the rates of enhancement was also explored by recording the response to $^1O_2$ of an H_4BPMHC analogue that differs in the degree of BODIPY methylation and sensitivity, H_2BPMHC.[18] Results were obtained working with liposomes prepared with either DMPC, POPC, or EggPC (a mixture of natural lipids). No major differences in the rates or value of probe enhancement were observed when the photosensitizer used was I_2BOAc, regardless of the degree of lipid unsaturation (see **Figure 2.7**), consistent with the probe outcompeting lipids in its quenching of $^1O_2$ and offering a protective role while in its reduced form (where *ene* reaction is expected with polyunsaturated lipids but not in DMPC).

When the hydrophilic photosensitizer methylene blue was utilized, we recorded a 5-fold increase in the rates of H_4BPMHC emission enhancement when going from water to deuterium oxide. This is consistent with $^1O_2$ molecules sensitized in the bulk solution more efficiently reaching the membrane in D_2O versus H_2O, unless otherwise identical conditions (**Figure 2.2b**). No intensity plateau was reached during the recorded time window explored. One may estimate at 18 the value for the relative rate of probe oxidation ($k_{ox}^{H_4BPMHC}$) by $^1O_2$ when generated by membrane-embedded I_2BOAc versus by methylene blue in the liposome surrounding solution (within the mean square displacement of $^1O_2$). This value was calculated after correcting for excitation rate, sensitization quantum yield, and photosensitizer effective concentration (see **Section 2.7.4.1**) and is within a factor of two of the value we recorded experimentally ~7.5. Notably, for methylene blue, the enhancement rate retrieved was smaller with the saturated lipid DMPC than with either POPC or EggPC (that bear unsaturated lipids). Methylene blue can both sensitize the formation of $^1O_2$ as well as initiate free radical reactions, leading to competing probe activation pathways as the probe is also sensitive to lipid peroxyl radicals.[37-39] In the latter case, lipid unsaturation will favor free radical chain autooxidation, leading to faster enhancements with EggPC and POPC than with DMPC. Analysis of the results thus requires partly invoking type I photosensitization for methylene blue. The larger activation of H_4BPMHC under oxygen-deprived (argon-purged) conditions when using I_2BOAc as a photosensitizer (compared to minimal activation with methylene blue) is attributed to oxygen leaking into the samples throughout the extended experimental time (>2 h after degassing), combined with the more effective excitation of and $^1O_2$ photosensitization by I_2BOAc (see **Section** 2.7.4.1).

The zero-order kinetics recorded in liposomes is consistent with oxidation of the chromanol trap segment outcompeting the decay of $^1O_2$ through other pathways, including both its

unimolecular decay in solution and quenching by lipids (see **eqs 2.1** and **2.2**, with $k_q^{H_4BPMHC}$ = 4.9 × 10^8 M^{-1} s^{-1} as reported above, $k_q^L \sim 10^4$ M^{-1} s^{-1}, k_d = 2.7–2.9 × 10^5 s^{-1} in water, [L] = 1 × 10^{-3} M, and [H_4BPMHC] = 1 × 10^{-6} M).

The observed zero-order kinetics provided a convenient way to estimate "τ," the endpoint for H_4BPMHC consumption through oxidation, and as a corollary, a straightforward way to estimate the flux of $^1O_2$ through the membranes where the probe locates. Analysis of the intensity−time trajectories, such as those shown in **Figure 2.2a,b**, enables the determination of experimental values of τ, corresponding to the time at the intersection of the straight lines tangential to the linear increase in the intensity of the probe and the subsequent drop in intensity arising from probe degradation (see **Figure 2.1b**).[18, 40, 41] The flux of $^1O_2$ was next estimated. Here, in a period τ, an amount of $^1O_2$ has reached/been produced within the membrane sufficient to fully consume the initial amount of probe in the membrane (see **eqs 2.3** and **2.4**, where H_4BPMHC_0 stands for the initial amount of probe and the ratio of rate constants reflects the fraction of $^1O_2$-mediated quenching that leads to oxidation (intensity enhancement) of the probe). Dividing next this estimated $^1O_2$ amount by the time τ it took for the $^1O_2$ to react with the probe and by the total lipid area in solution (S_l), one obtains the $^1O_2$ flux, under steady irradiation conditions, through all the membranes in a solution containing H_4BPMHC (see **eq 2.4** and **Table 2.2**).

$$H_4BPMHC_0 = \frac{k_{ox}^{H_4BPMHC}}{k_q^{H_4BPMHC}} \times {}^1O_2 \tag{2.3}$$

$$\text{Flux}_{{}^1O_2} = \frac{{}^1O_2}{\tau \times S_l} \tag{2.4}$$

2.5.3. Correlating $^1O_2$ flux, associated lipid photooxidation and membrane expansion dynamics

Having established the sensitivity and reactivity of H_4BPMHC toward $^1O_2$, we next sought to explore the relationship between chemical insult, membrane morphology, and its collective dynamics. To that end, we devised widefield fluorescence microscopy studies on single GUVs to establish: (i) the flux of $^1O_2$ through the membrane, (ii) the onset of the *ene* reaction with the double

bonds of monounsaturated lipids, and (iii) the ensuing membrane fluctuations and GUV surface area expansion.

Individual DOPC GUVs were imaged with an inverted fluorescence microscope with the incident beam perpendicular to the imaging surface, employing a 100× magnification objective. The 488 nm, 561, and 647 nm output laser lines were employed to excite H_4BPMHC, I_2BOAc, and methylene blue, respectively. The experiments involved an initial "prephotosensitization" period, where only the probe was excited, a period necessary to establish the physical parameters of the nonoxidized GUVs (diameter and initial intensity, see **Figure 2.3c**). Then, irradiation of the probe and either photosensitizer was simultaneously performed in a continuous manner by the respective lasers. An emission filter was chosen to reject any emission coming from the photosensitizers while letting the emission of H_4BPMHC reach the detector, enabling monitoring of the intensity enhancement of the fluorogenic antioxidant in GUVs over time as a steady state generation of $^1O_2$ took place. Images were recorded on an EMCCD camera. A 1:100 H_4BPMHC/lipid mole ratio was found to yield optimum experimental conditions for the GUV studies in terms of sensitivity and lag time to full enhancement, with minimal probe photobleaching or preactivation (oxidation prior to the start of photosensitization of $^1O_2$).

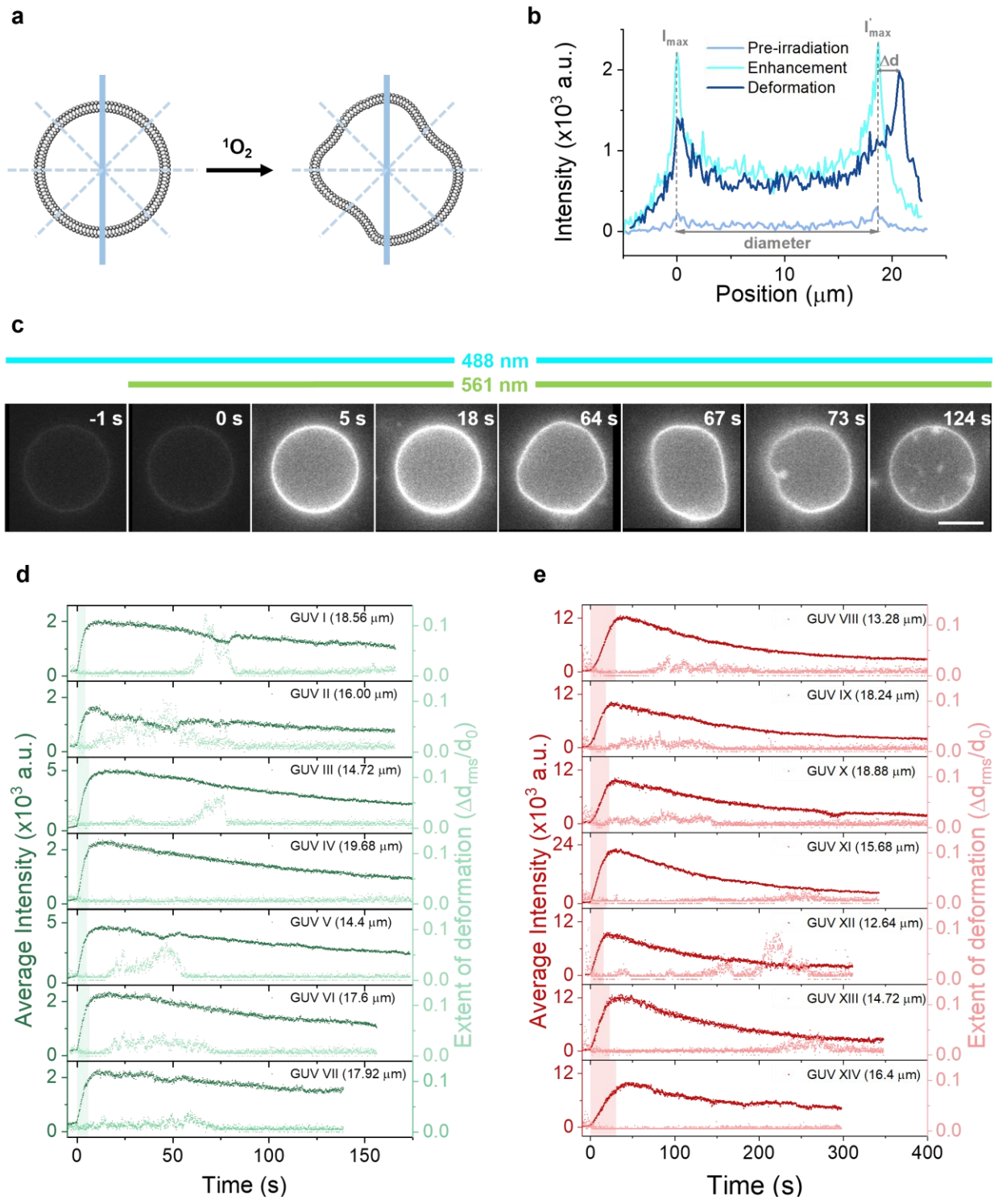

Figure 2.3. GUVs allow the recording of H_4BPMHC emission enhancement and membrane surface area expansion due to lipid photooxidation. (a) Four concentric lines were traced across the projection of each GUV, which were used to extract intensity profiles along each axis. (b) Evolution of the intensity profile along the vertical axis (highlighted in panel (a)) of the GUV shown in panel (c); three salient times are depicted: (i) before irradiating the photosensitizers (light

blue trace), (ii) at maximum emission enhancement (cyan trace), and (iii) at maximum deformation along the vertical axis (dark blue trace). The dashed grey lines indicate the profile maxima (I_{max} and I_{max}'), after background subtraction. The distance between both maxima corresponds to the GUV diameter "*d*". (c) Example of imaging studies on a DOPC GUV containing I_2BOAc as a photosensitizer. GUV depicted in this film strip corresponds to GUV I in (d) and **Supporting Information Video "SV1-GUV I"**. (d,e) Temporal profiles of H_4BPMHC emission intensity and GUV extent of deformation ($\Delta d_{rms}/d_0$). Results in (d) were obtained upon irradiation in the presence of 0.3 μM I_2BOAc. Results in (e) were obtained with 1.7 μM methylene blue. Photosensitizers were irradiated with the 50 μW output of a 561 nm laser (I_2BOAc) or 647 nm laser (methylene blue). H_4BPMHC was irradiated with the 15 μW (d) or 50 μW (e) output of a 488 nm laser. H_4BPMHC/lipid ratio was 1:100. Time 0 s corresponds to the start of photosensitizer irradiation. Light green (d) and light red (e) shaded regions represent τ, the time till full probe consumption. The value of the initial diameter is additionally provided for each GUV.

Irradiation of GUVs with H_4BPMHC and either photosensitizer led to a linear increase in fluorescence intensity with time, as observed in bulk studies in liposome dispersions (see **Figure 2.3d,e**, and the accompanying **Supporting Information Video files**). No enhancement was, in turn, observed in control studies upon irradiation of GUVs with no photosensitizer (see **Figure 2.8**). Both the values for maximum intensity (**Figure 2.3d,e**) and maximum enhancement (**Table 2.1**) achieved were comparable for different GUVs when recorded under identical conditions, indicating that the data is consistent with similar dye surface density and similar reactivity between different individually analyzed GUVs (see **Table 2.1**, and **Section 2.7.1** for details on obtaining the intensity over time profiles). Notably, the intensity enhancement values retrieved, ranging from 10- to 30-fold with I_2BOAc and 40- to 60-fold with methylene blue (**Table 2.1**), were significantly smaller than for liposome experiments (>360-fold, vide supra). We attribute the smaller enhancement value recorded in GUVs over liposomes to the larger initial intensity (prior to photosensitizer irradiation) arising from the experimental setup and scattered light. Preactivation occurring during sample preparation or early activation due to the generation of $^1O_2$ upon cross-excitation of the photosensitizer at 488 nm before its direct excitation (before time zero in **Figure 2.3d**), may also lead to larger initial intensity values and thus a loss of sensitivity/smaller enhancement values. Differences in preactivation would further account for the spread in enhancement values recorded for individual GUVs. Following the linear enhancement of the probe, a slow decay in emission intensity was recorded. This decay may be attributed to (i) a decrease in fluorophore density following lipid peroxidation and membrane shedding (vide infra),

(ii) photobleaching of the BODIPY, and (iii) oxidized H_4BPMHC escaping the lipid membrane environment, given the higher polarity expected for the newly formed adduct.[42, 43]

To obtain the flux of $^1O_2$ into the membrane, we next calculated the time required for full probe consumption, τ, from the intersection between the linear intensity growth and subsequent decay and the initial number of H_4BPMHC molecules per GUV determined from geometric considerations (total GUV surface, lipid molecular surface area, and probe to lipid mole ratio). Utilizing **eqs 2.3** and **2.4**, the flux of $^1O_2$ was obtained upon dividing the initial H_4BPMHC load in a given GUV by its associated τ and area for that GUV, see **Table 2.1**.

While studies conducted with the more hydrophilic photosensitizer methylene blue provided similar observations to those reported with I_2BOAc (see **Figure 2.3d,e**), we note the superior $^1O_2$ flux recorded with I_2BOAc once the excitation power and absorption of the photosensitizer are factored in, see **Section 2.7.4.2**. This can be attributed to the preferential partitioning of I_2BOAc within the lipid membrane phase, as discussed in bulk studies with liposome dispersions. We additionally note that larger H_4BPMHC intensity enhancements were recorded with methylene blue versus I_2BOAc (**Table 2.1**). This is consistent with reduced activation of H_4BPMHC during the imaging period preceding the photosensitizer excitation, as methylene blue has a markedly red-shifted absorption.

Table 2.1. Singlet oxygen flux, H_4BPMHC emission enhancement, and extent of membrane deformation recorded with photosensitizers I_2BOAc and methylene blue.

Photosensitizer	I_2BOAc[a]	methylene blue[b]
$^1O_2$ flux (molecules nm^{-2} s^{-1})	0.43 ± 0.08	0.11 ± 0.02
Enhancement	21.3 ± 9.7	50.1 ± 9.7
Maximum deformation (%)	6.26 ± 3.04	4.1 ± 2.3

[a]Values are the average ± standard deviation of 13 values. [b]Values are the average ± standard deviation of 10 values.

Qualitatively, H_4BPMHC consumption (as determined in **Figure 2.1b**) marked the onset of the *ene* reaction, with membrane expansion being observed on visual inspection of filmstrips acquired for single GUVs. This expansion was at times in the form of a strong membrane fluctuation. GUV membrane shedding in the form of budding vesicles or membrane strings was

also observed after the onset of the *ene* reaction (after time τ). While membrane shedding was recorded in all cases, expansion was observed in roughly 80% of GUVs studied with I_2BOAc and ~54% of the GUVs studied with methylene blue as a photosensitizer. No shedding or expansion was observed in control experiments lacking the photosensitizer studied under otherwise identical conditions (see **Figure 2.8** for representative film strips and intensity time trajectories).

To estimate the relative increase in diameter of the GUV associated with its surface "*S*" expansion ($S = \pi d^2$, where d = diameter), we calculated the root mean square of the difference of the diameters at the initial time $d_{(0)}$ and at subsequent times following irradiation $d_{(t)}$ normalized to the initial diameter, for the four cross sections of the GUV 2D projection, as illustrated in **Figure 2.3a** and using **eq 2.5** below. Here the diameter values were estimated from the maximum intensities on the line profile of the ring image, see **Figure 2.3b**. A similar approach was utilized for recording morphological fluctuations, where we individually monitored the fluctuations of the four diameters arising from the four concentric lines (see **Figure 2.9**). **Figure 2.3d,e** illustrates in parallel the intensity enhancement and the root mean square diameter change as a function of time for single GUVs recorded upon exciting either photosensitizer.

$$\frac{\Delta d_{rms}}{d_{(0)}} = \frac{\langle \Delta d^2 \rangle_{(t)}^{\frac{1}{2}}}{d_{(0)}} = \frac{\langle \left(d_{(t)} - d_{(0)}\right)^2 \rangle^{\frac{1}{2}}}{d_{(0)}} \qquad (2.5)$$

We observed enlargement in relative diameters of 6 and 4%, on average, for GUVs studied with I_2BOAc and methylene blue, respectively, and undergoing expansion (**Table 2.1**). Considering that following the *ene* reaction with $^1O_2$, the molecular area of DOPC enlarges by 19%,[7-9, 44] and one would expect an increase of ~1.2-fold for the overall DOPC GUV surface area once all lipids have undergone *ene* reaction, and a corresponding increase of ~1.09-fold, or 9%, for its diameter. These estimates are comparable to the 6 and 4% average enlargements in relative diameters we observed. Fluctuations in GUV morphology while apparent from the $\langle \Delta d^2 \rangle_{(t)}^{1/2} / d_{(0)}$ versus time trajectories displayed in **Figure 2.3d,e**, are more prominently observed when looking at fluctuations over time in each of the four diameters, see **Figure 2.9** for an example with GUVs number I and II, and also accompanying **Supporting Information Videos**.

Following the onset of the *ene* reaction, a significant fraction of GUVs underwent expansion/shedding in a short time span comparable to τ (see **Figure 2.4**), yet other GUVs registered such events at times up to 30-fold those recorded for τ. The rate of lipid oxidation via the *ene* reaction is expected to follow **eq 2.6**. Here, upon a drop of the membrane-embedded $^1O_2$ quencher H_4BPMHC to negligible amounts (the H_4BPMHC term in the denominator becomes negligible, compared to **eqs 2.1** and **2.2**), rapid lipid oxidation occurs. Values for k_{ene}^L in the range of 0.6×10^4 and 3×10^6 M^{-1} s^{-1} have been reported via $^1O_2$ NIR luminescence studies in organic solvents[29] and by quantifying GUV area expansion by micropipette aspiration,[7] respectively. Accordingly, either first- or zero-order kinetics are expected, respectively, for lipid oxidation in water. That we have observed zero-order kinetics for H_4BPMHC reactions with $^1O_2$ places an upper bound on the rate constant for the *ene* reaction of $k_{ene}^L < 4.9 \times 10^6$ M^{-1} s^{-1}. Effectively, for zero-order kinetics to be observed, the inequality $k_q^{H_4BPMHC} \times [H_4BPMHC] \gg k_q^L \times [L]$ must hold. Given that [L] = 100 × [H_4BPMHC], this would indicate that $k_q^{H_4BPMHC} \gg 100 \times k_q^L$. Considering the $k_q^{H_4BPMHC} = 4.9 \times 10^8$ M^{-1} s^{-1} value we recorded in acetonitrile (vide supra), k_q^L (and thus k_{ene}^L) is thus placed as smaller than 4.9×10^6 M^{-1} s^{-1}.

Considering that the recorded times for expansion/shedding were mostly longer than, yet within a time span of one order of magnitude from those measured for probe oxidation τ (see **Figure 2.4** and its expanded version **Figure 2.10**), further insight may be provided on the rate of lipid oxidation. Inspection of **eq 2.6** (and **eq 2.2** for comparison) would indicate that upon $^1O_2$ reaction with the probe, lipid photooxidation can be as fast as the rate of $^1O_2$ generation ($\phi_\Delta \times I_a$) provided that $^1O_2$ is efficiently quenched by lipids before its physical decay (k_d) takes place. That we observe relatively long times (larger than τ) for lipid membrane expansion/shedding would be consistent with singlet oxygen deactivation by water partially dampening the rate of lipid oxidation.

$$-\frac{d[L]}{dt} = \frac{d[LOOH]}{dt} = \frac{\Phi_\Delta \times I_a \times k_{ene}^L \times [L]}{\left(k_d + k_q^L \times [L]\right)} \tag{2.6}$$

An increase in the molecular area of the lipid molecule induces surface and volume expansion in the GUVs. Prepared under conditions of equal osmotic concentration inside and

outside the GUV, such a volume expansion would result in a hypertonic solution surrounding the vesicle.[6, 45] The associated membrane fluctuations reflect the dynamic evolution of the GUV toward a new equilibrium as photo-triggered membrane expansion takes place. In turn, the presence of membrane buds and strings attached to the main GUV body provides a way for the membrane to accommodate excess area as lipids expand, preserving constant the volume (concentration) of the vesicle (vesicle cargo).[3, 6, 45]

Our work reveals that membrane expansion and/or shedding occur dominantly following the onset of the *ene* reaction, after time τ, consistent with photo-triggered lipid oxidation and the associated surface increase occurring once the $^1O_2$ scavenger probe H_4BPMHC is consumed. This can be best observed from **Figure 2.4a,b** (**Figure 2.4c,d**) illustrating the relationship between τ and the time at which deformation (shedding) took place in each GUV analyzed, when working with I_2BOAc and methylene blue, respectively. When observed, expansion typically precedes shedding. That 46% of GUVs recorded with methylene blue did not expand but only underwent membrane shedding may well indicate that methylene blue partly elicits oxidation of the probe via a free radical-initiated process.[37, 38] The presence of oxidation processes that involve radical-mediated pathways would generate a variety of secondary products not expected with $^1O_2$, e.g. lipid aldehydes that have a truncate-cone geometry and a decreased surface area, leading to membrane pore formation.[6, 37, 46, 47] This would also explain why the extent of deformation recorded when using methylene blue as a photosensitizer is on average lower than that recorded when employing I_2BOAc.

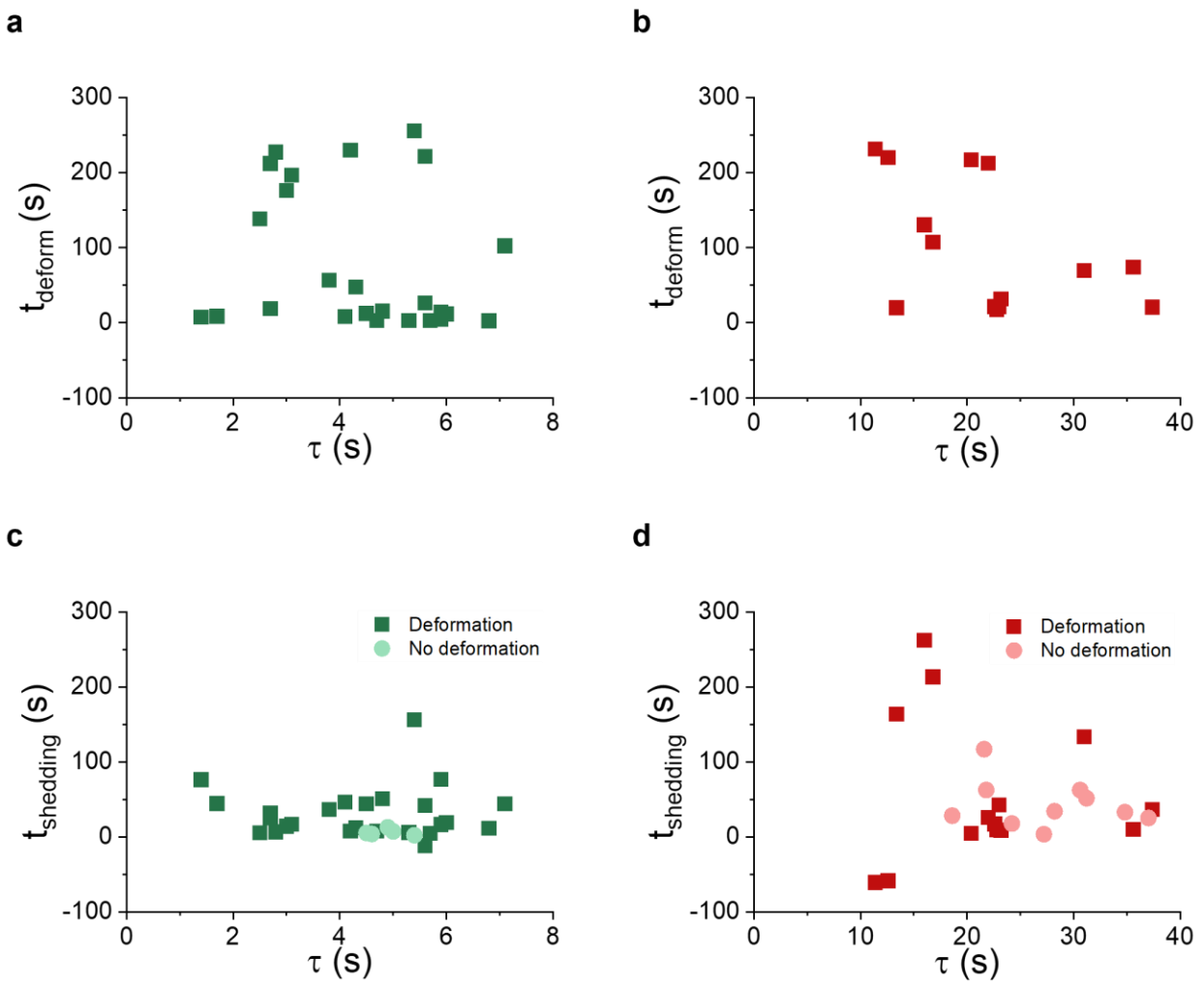

Figure 2.4. Correlation of GUV deformation (a,b) or shedding (c,d) with *τ*. Panels (a,c) correspond to experiments with I_2BOAc, while panels (b,d) correspond to experiments with methylene blue. The data was extracted from single GUVs studied as described in the text and further characterized in **Figure 2.3**. 0.3 μM I_2BOAc was irradiated with 50 μW of a 561 nm laser, while 1.7 μM methylene blue was irradiated with 50 μW of a 647 nm laser.

2.6. Conclusions

Motivated by our interest in understanding the relationship between lipid chemical structure and membrane physical properties, we have developed a highly sensitive assay to monitor in real-time the flux of $^1O_2$ on lipid membranes. At the core of this assay lies the rapid $^1O_2$ quenching kinetics by the chromanol moiety in the two-segment chromanol-BODIPY probe H_4BPMHC. This trick provides an ingenious method to ensure zero-order kinetics for probe consumption. The remarkable sensitivity of H_4BPMHC toward $^1O_2$ permitted spatial and temporal

studies providing quantitative values for $^1O_2$ flux on single GUVs, ultimately enabling the recording of flux values down to a diffraction-limited spot along the membrane. Singlet oxygen-mediated oxidation of the fluorogenic antioxidant H_4BPMHC marked the end of lipid protection by the tocopherol chromanol moiety in H_4BPMHC and the onset of lipid photooxidation via the *ene* reaction. This provided an internal clock for the onset of membrane fluctuations in the form of membrane expansion, deformation, and shedding that are associated with the collective motion of the lipids as the molecules undergo surface area expansion upon their transformation to lipid hydroperoxides. Here, the GUVs are perturbed and seek to accommodate the excess area while keeping intact the internal volume toward minimizing osmotic imbalances. A kinetic analysis based on the recorded times would place an upper bound on the rate constant of lipid oxidation and be comparable to values for $^1O_2$ physical decay in water. Our work shows that while membrane fluctuations (expansion/shedding) may appear rapidly following the onset of lipid photooxidation (after the protection role of the fluorogenic antioxidant probe is gone), their values are spread within a time span of one order of magnitude from those measured for probe oxidation. This large spread is rather remarkable and is the manifestation of complex collective dynamics.

Together, the results presented herein provide a methodology toward exploring with enhanced spatial−temporal resolution $^1O_2$-mediated lipid chemical transformations, membrane morphology, and their collective dynamics.

2.7. Supporting Information

2.7.1. Experimental methods

2.7.1.1. Determination of the rate constant of $^1O_2$ scavenging by H_4BPMHC

The method developed by Young *et al*. was used to determine the rate constant of $^1O_2$ scavenging (k_q) by measuring the inhibition of the photooxidation of DMA (1 μM) by H_4BPMHC (0-100 μM range).[48] DMA is a specific $^1O_2$ trap that irreversibly reacts with this species. Changes in DMA fluorescence intensity as a function of photosensitizer irradiation were recorded with 1 cm × 1 cm quartz cuvettes and a Photon Technology International (PTI) Quanta Master fluorimeter. Samples were excited at 379 nm and emission was collected between 390 and 700 nm. $^1O_2$ was generated by irradiating 0.1 μM I_2BOAc in acetonitrile with a LED setup emitting at 520 nm, with full width at half maximum (FWHM) of 31 nm and with 2.6 mW cm^{-2} irradiance.

The **equation 2.7** below allowed us to obtain values for k_q ($k_q = k_{phy} + k_{ox}$; where k_{phy} is the physical quenching rate constant and k_{ox} is the rate constant for the irreversible reaction) for $^1O_2$ quenching by H_4BPMHC.

$$\frac{S_0}{S_{H_4BPMHC}} = 1 + \frac{k_q}{k_d}[H_4BPMHC] \quad (2.7)$$

where S_0 and $S_{H4BPMHC}$ denote the observed photosensitized degradation rate constants of DMA in the absence and presence of H_4BPMHC, respectively (see **Figure 2.6**). The k_d value is the rate constant for the natural decay of $^1O_2$ to the triplet ground state ($^3O_2$). By plotting the slope ratios *vs.* [H_4BPMHC] and fitting a linear equation to the data, values for k_q/k_d can be obtained. Using a value of $k_d = 1.3\times10^4$ s^{-1} in acetonitrile,[32] k_q was determined to be 4.9×10^8 M^{-1} s^{-1}.

2.7.1.2. Measurement of Log P value of I_2BOAc

I_2BOAc was dissolved in a small amount of acetonitrile (ACN) and the concentration of the solution was determined using a HITACHI U-2800 spectrophotometer and the known extinction coefficient of the photosensitizer.[19] The solution was then diluted with HPLC grade acetonitrile and Milli-Q water (70:30) to a concentration between 30 and 75 μM. 1 μL of formamide (unretained) was added to the solution. The retention time of I_2BOAc was determined using an Agilent 1290 Infinity II HPLC using a reverse phase HPLC column (ZORBAX RRHD Eclipse Plus C18). Here the column temperature was set to 25°C. An isocratic solution of acetonitrile and water (70:30) was used as the mobile phase. The flow rate was set to 1 mL per minute. The stop time was set to 7 minutes. The retention factor of the dye was calculated using **Equation 2.8** below, where t_r is the peak time and t_m is the void time. A standard solution was prepared using formamide (neat, 1 μL, unretained), benzene (neat, 5 μL, log(P)=2.1), toluene (neat, 5 μL, log(P)=2.7), naphthalene (1.0 mg/mL in ACN, 20 μL, log(P)=3.3), anthracene (1.0 mg/mL in ACN, 10 μL, log(P)=4.4), pyrene (1.0 mg/mL in ACN, 10 μL, log(P)=4.88), hexachlorobenzene (1.0 mg/mL in ACN, 20 μL, log(P)=6.18), 1,3,5-tri-tert-butylenzene (10.0 mg/mL in ACN, 100 μL, log(P)=7.6), 529 μL acetonitrile, and 300 μL water. Log(k) of the compounds in the mixture were plotted against log(P) to build a calibration curve (**Equation 2.9**). Samples are injected following the sequence of the calibration curve (ascending log(P)), 45-75 μM solution of the dye,

and 100% pure acetonitrile wash. The sequence was repeated for three time. Fluorescent signals were detected at 509 nm. Log(P) of the dye was determined from the corresponding calibration curve, and the average value of the three independent triplicates was reported.

$$k = \frac{t_r - t_m}{t_m} \tag{2.8}$$

$$\log(k) = a \times \log(P) + b \tag{2.9}$$

2.7.1.3. Liposome preparation

H_4BPMHC (or H_2BPMHC when specified) was dissolved in acetonitrile and added to a glass vial. The solvent was evaporated under a stream of argon, and the desired lipid dissolved in chloroform was added next to the vial such that the ratio of probe to lipid was 1:1000 (1:750 when using H_2BPMHC). A lipid film was formed on the walls of the glass vial by evaporating the chloroform under a stream of argon while slowly rotating the vial. The lipid film was dried under vacuum for 1 h to remove any traces of solvent. The lipid film was rehydrated with PBS and subjected to 4 freeze-thaw-sonicate cycles (5 min in dry ice, followed by 5 min sonication in a room temperature water bath) to increase unilamellarity. The liposome suspension was then extruded 21 times through a 100 nm polycarbonate membrane (Avanti Polar lipids), resulting in a suspension of 100 nm diameter liposomes. For liposomes prepared in D_2O, water was first evaporated from a PBS solution by heating, and the resulting dry salts were dissolved in an equivalent volume of D_2O to maintain initial concentration and ionic strength. The resulting D_2O-phosphate buffer (referred to simply as DPBS in the manuscript) was used to rehydrate the lipid films. Liposome preparation was done as fast as possible and with minimal light exposure, and samples were used within few hours from preparation in order to avoid premature oxidation of lipids and H_4BPMHC.

2.7.1.4. GUV data analysis

Two pieces of information needed to be extracted from the GUVs irradiation movies, namely the time evolution of H_4BPMHC fluorescence intensity (i.e., fluorescence kinetics) and of GUV area (i.e., expansion kinetics). The GUV movies were first corrected for vesicle translational

movements using the "Align Stacks" tool from ImageJ software (version 1.50e). Next, four concentric lines, intersecting at the center of the ring projection of the GUV, were traced along four axes over the ring projection of the GUV (horizontal, vertical, diagonal and anti-diagonal directions, see **Figure 2.3a** for schematic representation). For each of these lines, the macro "StackProfileData" was used to generate intensity profiles along the selected line for the whole image stack (see **Figure 2.3b** for examples of intensity profile along the vertical axis at three different time points). The intensity-time profile from a 4 × 4 pixels background region was used for background-intensity correction. H_4BPMHC intensity was determined by subtracting this background intensity from the two maxima along each of the four lines (at ring-line intersections), and averaging the resulting peak values (8 values total, 2 from each line). H_4BPMHC intensity was plotted as a function of time to generate fluorescence kinetics plots. Enhancement values were calculated by dividing emission intensities over time by the initial intensity value prior to irradiation. To obtain expansion kinetics plots, the distance between both profile maxima (i.e. the vesicle diameter in pixels, see **Figure 2.3a-b**) was calculated for the whole stack (i.e. at each time point) and plotted according to **equation 2.5** (see Results and Discussion section). As further explained in the Results and Discussion section, the ensuing analysis to obtain kinetics parameters consisted in fitting linear equations to enhancement and bleaching kinetics, in order to obtain zero order rate constants.

2.7.2. Derivation of H_4BPMHC oxidation rate equation

The rate of H_4BPMHC oxidation by photosensitized singlet oxygen (**equation 2.1** in manuscript) was derived as explained by Wilkonson et al.[34] The rate of chemical trapping of $^1O_2$ by H_4BMHC ($k_{ox}^{H_4BPMHC}$) is given by **equation 2.10** below.

$$-\frac{\mathrm{d[H_4BPMHC]}}{\mathrm{dt}} = \frac{\mathrm{d[H_4BPMHC_{ox}]}}{\mathrm{dt}} = \mathrm{k_{ox}^{H_4BPMHC}[H_4BPMHC]}\left[\,{}^1\mathrm{O_2}\right] \qquad (2.10)$$

Given that photosensitization is performed under continuous laser excitation, the generation of singlet oxygen proceeds under a steady state condition, where the rate of $^1O_2$ production is equal to the rate of $^1O_2$ decay as described by **equation 2.11**, where I_a is the rate of photosensitizer excitation, Φ_Δ is the photosenistization quantum yield, k_d is the natural decay rate

of singlet oxygen in the absence of quenchers, k_q^L is the rate of quenching of $^1O_2$ by lipids (L), and $k_q^{H_4BPMHC}$ is the rate of quenching of $^1O_2$ by H_4BPMHC. k_q^L and $k_q^{H_4BPMHC}$ are the total rate of quenching of $^1O_2$ through both physical and chemical quenching mechanisms.

$$I_a\Phi_\Delta = \left(k_d + k_q^L \times [L] + k_q^{H_4BPMHC} \times [H_4BPMHC]\right)\left[{}^1O_2\right] \quad (2.11)$$

Equation 2.11 can be rearranged in **equation 2.12** to express the steady state concentration of $^1O_2$.

$$\left[{}^1O_2\right] = \frac{I_a\Phi_\Delta}{k_d + k_q^L \times [L] + k_q^{H_4BPMHC} \times [H_4BPMHC]} \quad (2.12)$$

By substituting the value for $\left[{}^1O_2\right]$ from **equation 2.12** into **equation 2.10**, we obtain **equation 2.13**, a full expression of the rate of oxidation of H_4BPMHC by photosensitized singlet oxygen (**equation 2.1** in the manuscript).

$$-\frac{d[H_4BPMHC]}{dt} = \frac{d[H_4BPMHC_{ox}]}{dt} = \frac{I_a\Phi_\Delta \times k_{ox}^{H_4BPMHC}[H_4BPMHC]}{k_d + k_q^L \times [L] + k_q^{H_4BPMHC} \times [H_4BPMHC]} \quad (2.13)$$

2.7.3. Enhancement and oxidation rate calculations in liposomes

2.7.3.1. Calculation of emission enhancement in liposomes

To calculate the maximum emission enhancement undergone by H_4BPMHC upon its oxidation when liposome embedded, all emission spectra were first corrected by subtraction of a blank curve and of a liposome scattering curve, in two steps. First, a "blank" emission spectrum was obtained by averaging 7 spectra recorded with the solvent (PBS or DPBS) of each sample of each experimental condition (3 samples (triplicates) per condition). This "blank" curve was further multiplied by a factor to match the last 5 points of the higher-wavelength end of the emission spectrum recorded at t=0 min (i.e., the spectrum recorded with H_4BPMHC-embedded liposomes, in the presence of photosensitizer, but prior to any photosensitizer irradiation). The corrected "blank" spectrum was then subtracted from all spectra recorded of the corresponding sample (recorded at different photosensitizer irradiation times). A liposome scattering curve was obtained

by averaging 3 spectra obtained with DOPC liposomes (without H_4BPMHC), and then subtracting the PBS blank as done for the samples (as just described). For each experiment, this curve was further multiplied by a factor in order for it to match the first 3 points of the lower-wavelength end of the spectrum recorded at t=0 min already corrected with the PBS-blank. The resulting curve was then subtracted from all the spectra of the corresponding sample.

The intensity *vs* irradiation time plots depicted in **Figure 2.2** were obtained by plotting the intensity at the maximum emission wavelength of each corrected spectrum (typically obtained at 520-521 nm) against the photosensitizer irradiation time at which that spectrum was recorded. Plotted values correspond to the average and standard deviation of the intensity at the maximum emission wavelength recorded from three independent triplicates. The time stamps of the samples that were not irradiated corresponds to the time since addition of the photosensitizer.

To calculate the emission enhancement underwent by H_4BPMHC, we first calculated the average initial intensity recorded for each experimental condition (average of the intensity at the maximum emission wavelength recorded in the emission scan taken at t= 0 min obtained from the triplicates of a certain experimental condition). The lowest (average) initial intensity recorded in any of the (triplicate) conditions was used to determine the maximum emission enhancement for all experimental conditions. Values reported in **Figure 2.2a** correspond to the average ± standard deviation of the maximum emission enhancements obtained with three triplicates of each experimental condition.

2.7.3.2. Calculation of apparent rate of oxidation

The apparent zero-order rate constant k_{obs} of H_4BPMHC oxidation was calculated as described in the manuscipt. Briefly, the time till full probe consumption, τ, was determined for each sample by fitting with straight lines both the intensity increase and subsequent intensity plateau or deacy of the corresponding emission intensity *vs* irradiation time curve (such as the ones shown in **Figure 2.2**). τ corresponds to the time point at which the two lines interesect (see **Figure 2.1d-e** for schematic representation). Since $[H_4BPMHC]_0 = 1$ μM, τ corresponds to the time it took to genereate 1 μM of H_4BPMHC_{ox}. k_{obs} is then equal to $[H_4BPMHC_{ox}]/\tau = 10^{-6}/\tau$ M min^{-1}. Values for k_{obs} were not reported for any of the controls, and only reported for the samples in which emission enhacement was expected and observed (sample in air-equilibrated PBS/DPBS with photosensitizer and irradiated with light). Values of k_{obs} reported in **Figure 2.2b-c** corresponds to

the average ± standard deviation of the k_{obs} values of the three independent triplicates of those experimental conditions.

In the case of samples containing Methylene Blue in air-equilibrated PBS, an intensity plateau was never reached. Since the ratio of k_{obs} for the different experimental conditions should be equal to the ratio of the slopes of the linear emission intensity increse in the intesnity *vs* irradiation time traces (such as the ones in **Figure 2.2b-c**), the value of k_{obs} in air equilibrated PBS was calculated using **equation 2.14** below, where k_{obs}^{PBS} and $k_{obs}^{D_2O}$ are the apparent zero-order rate constant of H_4BPMHC oxidation by photosensitized singlet oxygen in PBS and DPBS, respectively, and S_{obs}^{PBS} and $S_{obs}^{D_2O}$ are the slopes of the linear increase of emission intensity upon oxidation of H_4BPHMC in PBS and DPBS, respectively. Average values and standard deviations (errors) of $k_{obs}^{D_2O}$, S_{obs}^{PBS}, and $S_{obs}^{D_2O}$ were determined from three independent triplicates, while the error on k_{obs}^{PBS} was determined through the rules of error propagation.

$$\frac{k_{obs}^{PBS}}{k_{obs}^{DPBS}} = \frac{S_{obs}^{PBS}}{S_{obs}^{DPBS}} \tag{2.14}$$

2.7.4. Theoretical ratio of H_4BPMHC oxidation rate with I_2BOAC vs methylene blue

2.7.4.1. Liposome studies

In order to compare the effect of photosensitizer hydrophilicity/hydrophobicity on the rate of oxydation of the probe by photosensitized singlet oxygen, multiple factors need to first be examined and corrected for. This includes (1) different photosensitization quantum yields (Φ_Δ), (2) photosensitizer concentration, (3) efficiency of excitation, including intensity of excitation source and spectral overlap between excitation source and photosensitizer absorbance.

In order to estimate the efficiency of excitation of each photosensitizer by their respective LED lamp, the LED lamp emission spectrum (Power (mW m^{-2}) *vs* wavelength was estimated by a guassian that has the same characteristics mentioned by the manufacturer (peak wavelength, FWHM, and irradiance). The spectrum was then converted from a power *vs* wavelength to a number of photons (per m^2) *vs* wavelength, and the spectral overlap between this resulting spectrum and the absorbance spectrum of the photosensitizer was calculated. This allowed us to

determined that the 520nm LED lamps used were 1.45-fold more efficient at exciting I_2BOAc then the 635 nm LED lamps used were at exciting Methylene Blue.

Taking under consideration that I_2BOAc has a 1.8-fold larger Φ_Δ, and that the concentration of Methylene Blue used in the experiments is 2.5-fold larger than that of I_2BOAc, the amount of singlet oxygen generated by either photosensitizers under our experimental conditions is roughly equal, with the amount of $^1O_2$ generated by I_2BOAc being ~1.044-fold higher than that of Methylene Blue. Any observed difference in the rate of oxidation of H_4BPMHC by singlet oxygen is thus directly related to the ability of the generated $^1O_2$ to oxidize H_4BPMHC, which is largely dependent on the lipophilicity of the photosensitizer (i.e. effective concentration of $^1O_2$ around H_4BPMHC).

One may estimate the relative concentration of I_2BOAc vs Methylene Blue that is able to oxidize H_4BPMHC by singlet oxygen. If we assume all of I_2BOAC is homogenously and equally incorporated in all 100 nm (diameter) liposomes, then the ratio of I_2BOAc:lipid in each liposome is 4:1000 (0.4 μM I_2BOAc and 1 mM lipid). This is equivalent to 306.5 molecules of I_2BOAc per 100 nm lipsome. Since I_2BOAc is lipophilic and liposome-embedded, we assume that the singlet oxygen produced by all 306.5 I_2BOAc molecules may contribute to oxidation of H_4BPMHC. On the other hand, since Methylene Blue is in the water phase, only Methylene Blue that is very close to the liposome can lead to the oxidation of H_4BPMHC, as the generated $^1O_2$ must travel and reach the probe before decaying. The three dimentional mean square displacement of $^1O_2$ in solution $r_{rms} = (6D\tau)^{1/2}$ (where D is the diffusion coefficient of $^1O_2$ and τ is its lifetime) is approximately 210 nm.[49] This means that only $^1O_2$ molecules generated by Methylene Blue present within a roughly 210 nm thick shell around each liposome may lead to the oxidation of the probe, as a good approximaiton. A 210 nm thick shell present around a 100 nm (diameter) lipsome has a volume of 7.37×10^7 nm^3. Given that the concentration of Methylene Blue in solution is 1 μM, an average of 44.3 Methylene Blue molecules will be close enough to the liposomes at any given time to cause oxidation of the probe. This means that I_2BOAc would be 6.92 times better at delivering singlet oxygen to the probe based on these arguments. Next, if we consider that I_2BOAc has a 1.8-fold larger Φ_Δ, and that the spectral overlap between the excitation source and photosensitizer is 1.45-fold larger for I_2BOAc than Methylene Blue, we find that the generated amount of $^1O_2$ that is close enough to the liposome to react with its components is 18-fold larger in the case of I_2BOAc than

it is with Methylene Blue. We would thus expect an 18-fold larger H_4BPMHC oxidation rate with I_2BOAc than with Methylene Blue.

2.7.4.2. GUV studies

In order to calculate the expected ratio of k_{obs} between I_2BOAc *vs* Methylene Blue for the experiments conducted in GUVs, we must take under concideration the same factors discussed above, namely: (1) the different photosensitization quantum yields Φ_Δ, (2) the different photosensitizer excitation rates, and (3) the different effective concentrations if I_2BOAc and Methylene Blue around a GUV.

The fact that the excitation sources used in these experiments are monochromatic lasers renders the comparison of photosensitizer excitation rates much simpler than in the case of liposomes. I_2BOAc was irradiates with the 50 μW output of a 561 nm cw laser, while Methylene Blue was irradiated with the 50 μW output of a 647 nm cw laser. The latter thus has a 1.15-fold larger photon flux than the 561 nm laser. Moreover, Methylene Blue absorbs 647 nm light 1.255 times more effectively than I_2BOAc absorbs 561 nm light. Thus, overall, the excitation rate of Methylene Blue is expected to be 1.45-fold larger than that of I_2BOAc. Considering that the concentration of Methylene Blue used throughout the experiments was 5.67-fold larger than that of I_2BOAc, and that the photosensitization quantum yield of I_2BOAc is 1.8-fold larger than that of Methylene Blue, one estimates that Methylene Blue will generate 4.54-fold more $^1O_2$ than I_2BOAc. However, not all generated $^1O_2$ can reach and interact with the GUV.

As per work in liposomes above, we next need to compare the effective concentration of I_2BOAc *vs* Methylene Blue that is able to generate singlet oxygen close enough to the GUV membrabe to be able to interact with the GUV components. Assuming (a) complete incorporation of I_2BOAc in GUVs, (b) homogenous distribution of I_2BOAc among all the GUVs, and (c) that 100% of the lipids orginally deposited on the PVA film during GUV formation were subsequently resuspended in sucrose and contributed to GUV formation, one may estimate the ratio of I_2BOAc (added to the GUV microscope chamber) to lipid to be 0.00525. The number of lipids per GUV (and thus I_2BOAc per GUV) as a function of GUV radius maybe be estimated from surface area calculations, considering the avearge DOPC lipid head area to be 0.82 nm^2.

As discussed in the above section, only $^1O_2$ generated by Methylene Blue molecules present within a 210 nm thick shell around the GUV may interact with the GUV component. Since the

thickness of the shell is significantly smaller than the average GUV radius (r~8 μm), we can estimate the volume of the shell to be equal to the surface area of the GUV multiplied by the thickness of the shell (210 nm × $4\pi r^2$). We can thus obatin an estimate of the number of Methylene Blue molecules present within this shell as a function of GUV radius.

Having an estimate of both the number of Methylene Blue and I_2BOAc molecules in or around the GUV as a function of GUV radius, we found that under our experimental conditions, the number of I_2BOAc molecules incorporated within the GUV membrane is 59.6-fold larger than the number of Methylene Blue molecules present within a 210 nm shell around the GUV.

Taking under consideration that the excitation rate of Methylene Blue is 1.45-fold larger than that of I_2BOAc, and that I_2BOAc has a 1.8-fold larger Φ_Δ, we estimate that the amount of generated $^1O_2$ that is able to interact with the GUV components is 74-fold larger in the case of I_2BOAc than with Methylene Blue.

2.7.5. Supplementary figures

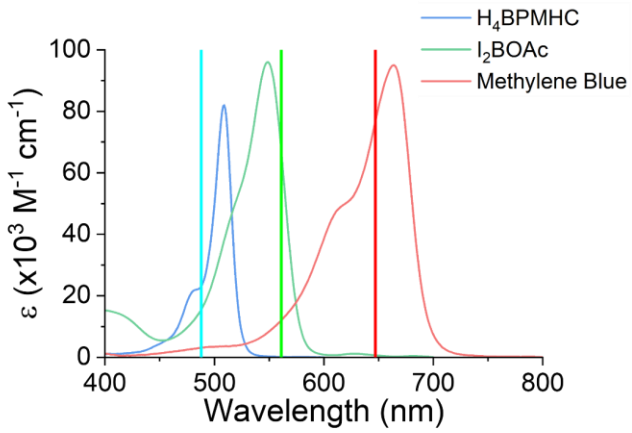

Figure 2.5. Molar extinction coefficients of sensor and photosensitizers used in this study. Blue, green and red lines correspond to 488 nm, 561 nm, and 647 nm laser excitation. The spectra of H_4BPMHC and I_2BOAC were measured in acetonitrile, while the absorbance of methylene blue was measured in ethanol. I_2BOAc cross-excitation by the 488 nm laser line was minimized by optimizing 488 nm vs 561 nm excitation power. Under our microscopy imaging conditions, I_2BOAc excitation rate by the 561 nm laser line is ~19-fold larger than the one by the 488 nm line.

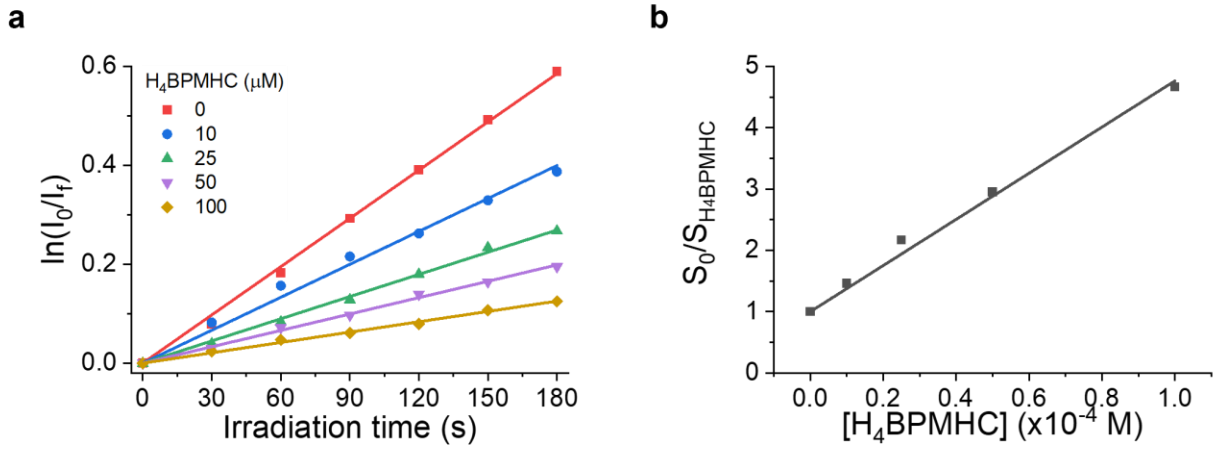

Figure 2.6. (a) Competition assay of DMA photooxidation by H_4BPMHC, employing various H_4BPMHC concentrations. I_0 is the initial emission intensity of DMA and I_f is its final emission intensity (λ_{ex} = 379 nm; λ_{em} = 403 nm). Each line corresponds to a linear fit to the dataset of the corresponding color. (b) Plot of $S_0/S_{H4BPMHC}$ as a function of H_4BPMHC concentration. Note that S_0 and $S_{H4BPMHC}$ are the slopes of the lines in graph (a), in the absence and presence of H_4BPMHC, respecitvely.

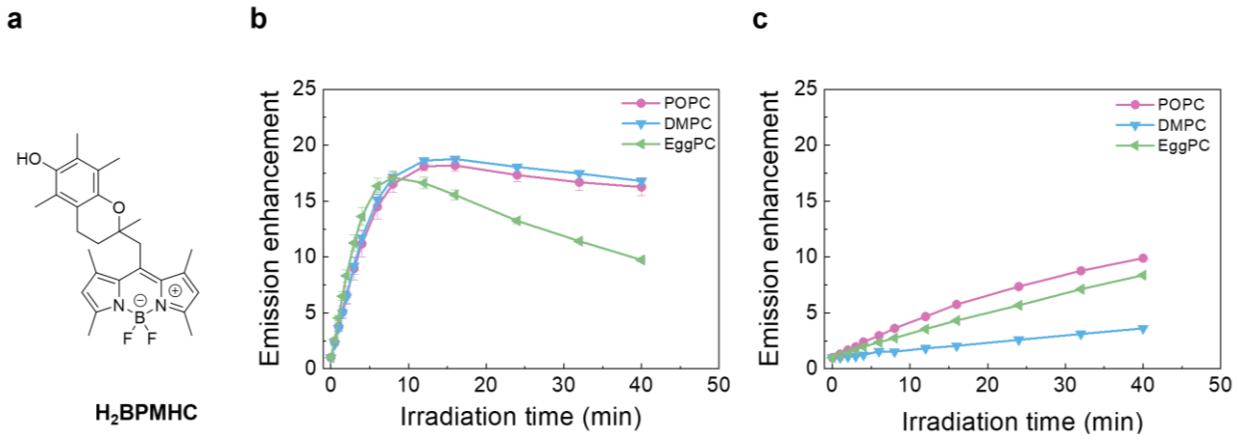

Figure 2.7. Intensity-time profiles of the emission of H_2BPMHC embedded in liposomes formed from lipids with different degrees of unsaturation. (a) Structure of H_2BPMHC. (b) Intensity-time profiles of H_2BPMHC emission in the presence of 0.24 μM I_2BOAc. (c) Intensity-time profiles of H_2BPMHC emission in the presence of 0.24 μM Methylene Blue. [lipid] = 1mM, [H_2BPMHC] = 1.33 μM. I_2BOAc was irradiated with a 520 nm LED lamps. Methylene Blue was irradiated with a 635 nm LED lamps.

Table 2.2. Kinetic parameters extracted from H_4BPHMC oxidation in DOPC liposomes

Photosensitizer/solvent	τ (min)	$^1O_2$ flux ($\times 10^{-4}$ molecules.nm^{-2} s^{-1})
I_2BOAc/PBS	10.24 ± 0.42	3.98 ± 0.17
I_2BOAc/DPBS	8.10 ± 0.76	5.06 ± 0.46
Methylene Blue/PBS	n/a[a]	0.53 ± 0.01[a]
Methylene Blue/ DPBS	15.24 ± 0.33	2.67 ± 0.06

Values correspond to the average ± standard deviation of three independent triplicates. [a]Intensity-time plots did not reach a plateau; oxidation rate and $^1O_2$ flux were calculated from the oxidation rate in DPBS; error is calculated using error propagation rules.

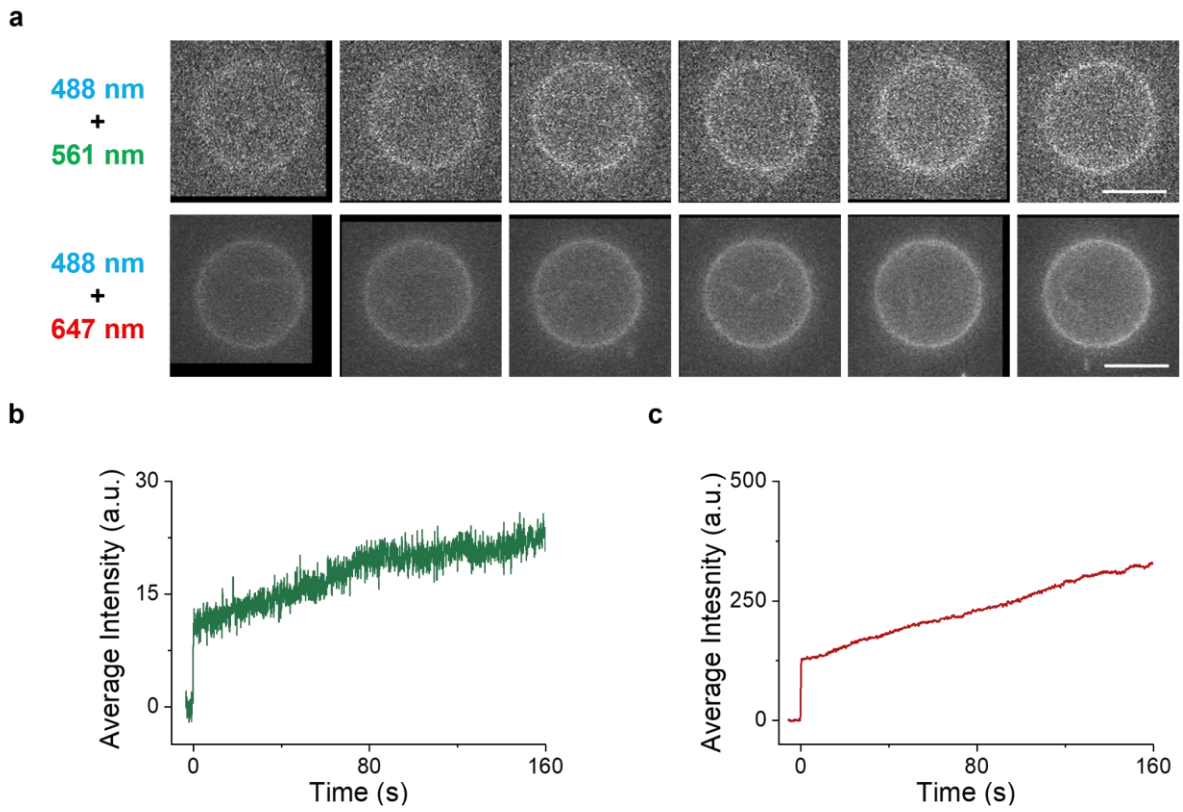

Figure 2.8. Lack of H_4BPMHC activation in GUVs in the absence of photosensitizers. (a) film strips depicting very minimal activation of H_4BPMHC upon irradiation in the absence of photosensitizer and under otherwise identical conditions as the ones used with I_2BOAc experiments (top film strip) or Methylene Blue experiments (bottom film strip). Scale bar = 10 μm. (b) Intensity-time trace of H_4BPMHC emission corresponding to the top film strips shown in panel (a). (c) Intensity-time trace of H_4BPMHC emission corresponding to the bottom film strips shown in panel (a). Images were acquired at a 5 frames/s rate.

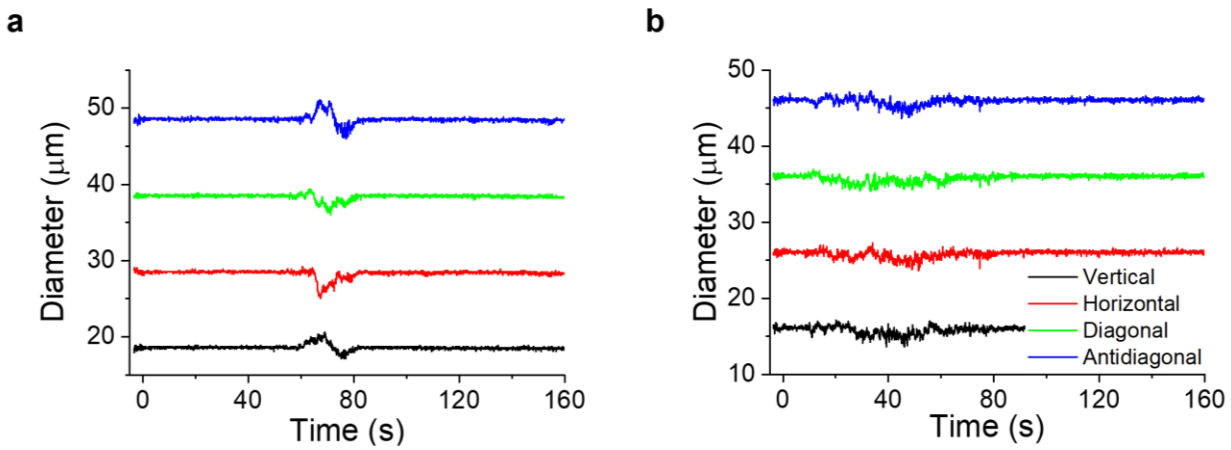

Figure 2.9. Fluctuations in GUV membranes observed along 4 different axes (vertical, horizontal, diagonal, and antidiagonal). Offset = 10 μm. Fluctuation along the 4 diameters were sometimes observed to be correlated (a), however they were predominantly non-correlated (b).

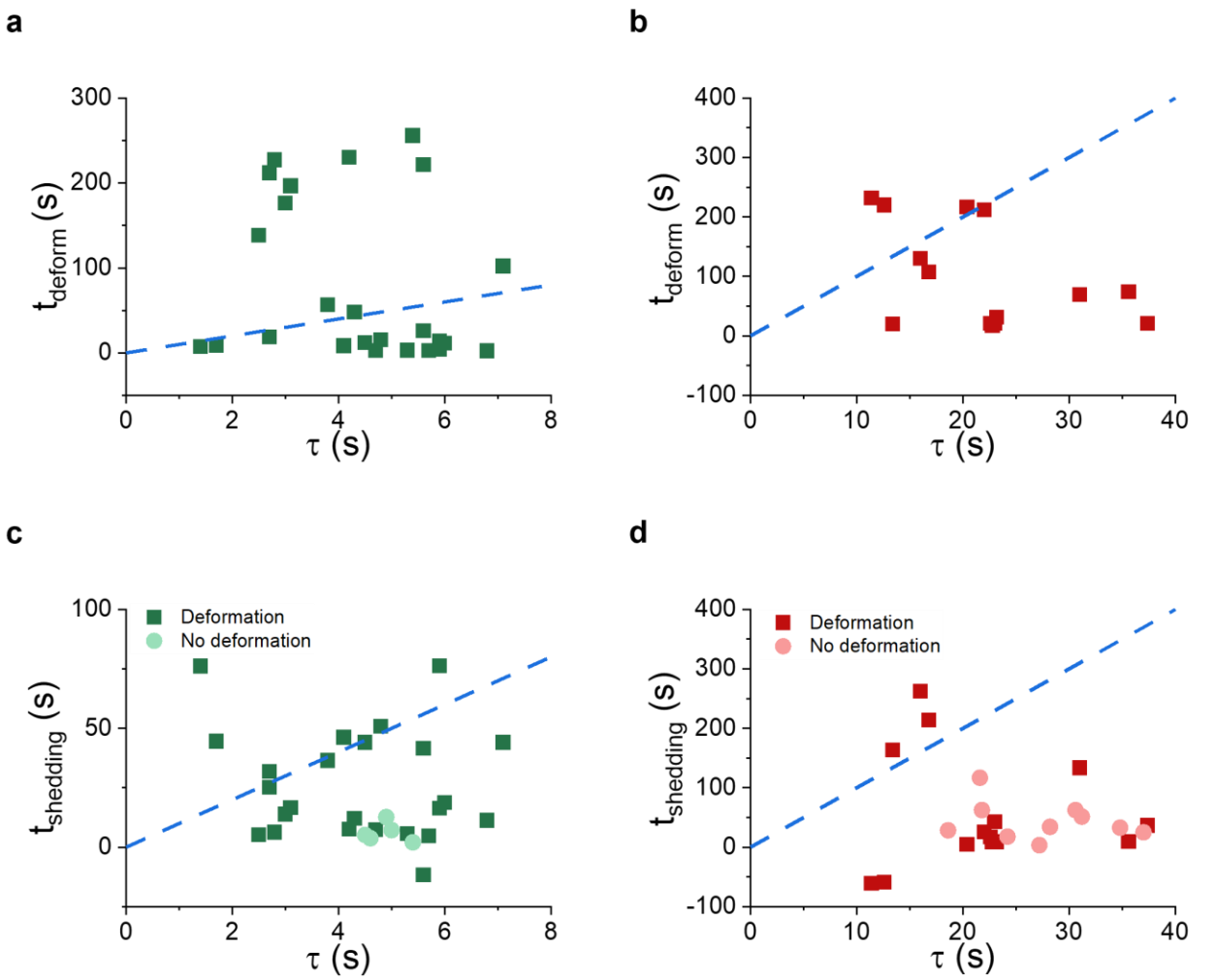

Figure 2.10. Correlation of GUV deformation (a, b) or shedding (c, d) with τ. Expanded version of manuscript **Figure 2.4** highlighting the correlation between τ (associated with rate of probe oxidation) and deformation and shedding onset times (associated to the onset of lipid peroxidation). The blue dashed lines, with a slope = 10, serve as a visual representation of a lipid oxidation rate to probe oxidation rate ratio of 10. Panels (a) and (c) correspond to experiments with I2BOAc, while panels (b) and (d) correspond to experiments with Methylene Blue.

2.8. References

1. Girotti, A. W., Photosensitized oxidation of membrane lipids: reaction pathways, cytotoxic effects, and cytoprotective mechanisms. *J. Photochem. Photobiol. B: Biol.* **2001,** *63* (1), 103-113.
2. Girotti, A. W.; Korytowski, W., Chapter 21 Reactions of Singlet Oxygen with Membrane Lipids: Lipid Hydroperoxide Generation, Translocation, Reductive Turnover, and Signaling Activity. In *Singlet Oxygen: Applications in Biosciences and Nanosciences, Volume 1*, The Royal Society of Chemistry: 2016; Vol. 1, pp 409-430.
3. Zhu, T. F.; Adamala, K.; Zhang, N.; Szostak, J. W., Photochemically driven redox chemistry induces protocell membrane pearling and division. *Proc. Natl. Acad. Sci. U.S.A.* **2012,** *109* (25), 9828-9832.
4. Dreher, Y.; Jahnke, K.; Schröter, M.; Göpfrich, K., Light-Triggered Cargo Loading and Division of DNA-Containing Giant Unilamellar Lipid Vesicles. *Nano Lett.* **2021,** *21* (14), 5952-5957.
5. Tsubone, T. M.; Baptista, M. S.; Itri, R., Understanding membrane remodelling initiated by photosensitized lipid oxidation. *Biophys. Chem.* **2019,** *254*, 106263.
6. Bour, A.; Kruglik, S. G.; Chabanon, M.; Rangamani, P.; Puff, N.; Bonneau, S., Lipid Unsaturation Properties Govern the Sensitivity of Membranes to Photoinduced Oxidative Stress. *Biophys. J.* **2019,** *116* (5), 910-920.
7. Weber, G.; Charitat, T.; Baptista, M. S.; Uchoa, A. F.; Pavani, C.; Junqueira, H. C.; Guo, Y.; Baulin, V. A.; Itri, R.; Marques, C. M.; Schroder, A. P., Lipid oxidation induces structural changes in biomimetic membranes. *Soft Matter* **2014,** *10* (24), 4241-4247.
8. Riske, K. A.; Sudbrack, T. P.; Archilha, N. L.; Uchoa, A. F.; Schroder, A. P.; Marques, C. M.; Baptista, M. S.; Itri, R., Giant vesicles under oxidative stress induced by a membrane-anchored photosensitizer. *Biophys. J.* **2009,** *97* (5), 1362-1370.
9. Aoki, P. H. B.; Schroder, A. P.; Constantino, C. J. L.; Marques, C. M., Bioadhesive giant vesicles for monitoring hydroperoxidation in lipid membranes. *Soft Matter* **2015,** *11* (30), 5995-5998.
10. Mertins, O.; Bacellar, I. O. L.; Thalmann, F.; Marques, C. M.; Baptista, M. S.; Itri, R., Physical damage on giant vesicles membrane as a result of methylene blue photoirradiation. *Biophys. J.* **2014,** *106* (1), 162-171.
11. Ayuyan, A. G.; Cohen, F. S., Lipid Peroxides Promote Large Rafts: Effects of Excitation of Probes in Fluorescence Microscopy and Electrochemical Reactions during Vesicle Formation. *Biophys. J.* **2006,** *91* (6), 2172-2183.
12. Zhao, J.; Wu, J.; Shao, H.; Kong, F.; Jain, N.; Hunt, G.; Feigenson, G., Phase studies of model biomembranes: Macroscopic coexistence of Lα+Lβ, with light-induced coexistence of Lα+Lo Phases. *Biochim. Biophys. Acta* **2007,** *1768* (11), 2777-2786.
13. Haluska, C. K.; Baptista, M. S.; Fernandes, A. U.; Schroder, A. P.; Marques, C. M.; Itri, R., Photo-activated phase separation in giant vesicles made from different lipid mixtures. *Biochim. Biophys. Acta* **2012,** *1818* (3), 666-672.
14. Morales-Penningston, N. F.; Wu, J.; Farkas, E. R.; Goh, S. L.; Konyakhina, T. M.; Zheng, J. Y.; Webb, W. W.; Feigenson, G. W., GUV preparation and imaging: Minimizing artifacts. *Biochim. Biophys. Acta* **2010,** *1798* (7), 1324-1332.

15. Westberg, M.; Bregnhøj, M.; Banerjee, C.; Blázquez-Castro, A.; Breitenbach, T.; Ogilby, P. R., Exerting better control and specificity with singlet oxygen experiments in live mammalian cells. *Methods* **2016,** *109*, 81-91.
16. Greene, L. E.; Lincoln, R.; Cosa, G., Rate of Lipid Peroxyl Radical Production during Cellular Homeostasis Unraveled via Fluorescence Imaging. *J. Am. Chem. Soc.* **2017,** *139* (44), 15801-15811.
17. Fahrenholtz, S. R.; Doleiden, F. H.; Trozzolo, A. M.; Lamola, A. A., On the quenching of singlet oxygen by α-tocopherol. *Photochem. Photobiol.* **1974,** *20* (6), 505-509.
18. Krumova, K.; Friedland, S.; Cosa, G., How Lipid Unsaturation, Peroxyl Radical Partitioning, and Chromanol Lipophilic Tail Affect the Antioxidant Activity of α-Tocopherol: Direct Visualization via High-Throughput Fluorescence Studies Conducted with Fluorogenic α-Tocopherol Analogues. *J. Am. Chem. Soc.* **2012,** *134* (24), 10102-10113.
19. Durantini, A. M.; Greene, L. E.; Lincoln, R.; Martínez, S. R.; Cosa, G., Reactive Oxygen Species Mediated Activation of a Dormant Singlet Oxygen Photosensitizer: From Autocatalytic Singlet Oxygen Amplification to Chemicontrolled Photodynamic Therapy. *J. Am. Chem. Soc.* **2016,** *138* (4), 1215-1225.
20. Weinberger, A.; Tsai, F.-C.; Koenderink, Gijsje H.; Schmidt, Thais F.; Itri, R.; Meier, W.; Schmatko, T.; Schröder, A.; Marques, C., Gel-Assisted Formation of Giant Unilamellar Vesicles. *Biophys. J.* **2013,** *105* (1), 154-164.
21. Ragàs, X.; Jiménez-Banzo, A.; Sánchez-García, D.; Batllori, X.; Nonell, S., Singlet oxygen photosensitisation by the fluorescent probe Singlet Oxygen Sensor Green®. *Chem. Commun.* **2009,** (20), 2920-2922.
22. Gollmer, A.; Arnbjerg, J.; Blaikie, F. H.; Pedersen, B. W.; Breitenbach, T.; Daasbjerg, K.; Glasius, M.; Ogilby, P. R., Singlet Oxygen Sensor Green®: Photochemical Behavior in Solution and in a Mammalian Cell. *Photochem. Photobiol.* **2011,** *87* (3), 671-679.
23. Banerjee, C.; Westberg, M.; Breitenbach, T.; Bregnhøj, M.; Ogilby, P. R., Monitoring Interfacial Lipid Oxidation in Oil-in-Water Emulsions Using Spatially Resolved Optical Techniques. *Anal. Chem.* **2017,** *89* (11), 6239-6247.
24. Burton, G. W.; Ingold, K. U., Vitamin E: application of the principles of physical organic chemistry to the exploration of its structure and function. *Acc. Chem. Res.* **1986,** *19* (7), 194-201.
25. Fukuzawa, K.; Inokami, Y.; Tokumura, A.; Terao, J.; Suzuki, A., Rate constants for quenching singlet oxygen and activities for inhibiting lipid peroxidation of carotenoids and α-tocopherol in liposomes. *Lipids* **1998,** *33* (8), 751-756.
26. Fukuzawa, K.; Matsuura, K.; Tokumura, A.; Suzuki, A.; Terao, J., Kinetics and Dynamics of Singlet Oxygen Scavenging by α-Tocopherol in Phospholipid Model Membranes. *Free Radical Biol. Med.* **1997,** *22* (5), 923-930.
27. Gorman, A. A.; Gould, I. R.; Hamblett, I.; Standen, M. C., Reversible exciplex formation between singlet oxygen, 1.DELTA.g, and vitamin E. Solvent and temperature effects. *J. Am. Chem. Soc.* **1984,** *106* (23), 6956-6959.
28. Christopher, S.; Ching, T.-Y.; Geller, G. G., Chemistry of singlet oxygen—xviii. Rates of reaction and quenching of α-tocopherol and singlet oxygen*. *Photochem. Photobiol.* **1974,** *20* (6), 511-513.
29. Krasnovsky, A.; Kagan, V.; Minin, A., Quenching of singlet oxygen luminescence by fatty acids and lipids: Contribution of physical and chemical mechanisms. *FEBS Lett.* **1983,** *155* (2), 233-236.

30. Vever-Bizet, C.; Dellinger, M.; Brault, D.; Rougee, M.; Bensasson, R. J. P.; photobiology, Singlet molecular oxygen quenching by saturated and unsaturated fatty-acids and by cholesterol. *Photochem. Photobiol.* **1989,** *50* (3), 321-325.
31. Chacon, J. N.; McLearie, J.; Sinclair, R. S., Singlet oxygen yields and radical contributions in the dye-sensitised photo-oxidation in methanol of esters of polyunsaturated fatty acids (oleic, linoleic, linolenic and arachidonic). *Photochem. Photobiol.* **1988,** *47* (5), 647-656.
32. Bregnhøj, M.; Westberg, M.; Jensen, F.; Ogilby, P. R., Solvent-dependent singlet oxygen lifetimes: temperature effects implicate tunneling and charge-transfer interactions. *PCCP* **2016,** *18* (33), 22946-22961.
33. Hackbarth, S.; Bornhütter, T.; Röder, B., Chapter 26 Singlet Oxygen in Heterogeneous Systems. In *Singlet Oxygen: Applications in Biosciences and Nanosciences, Volume 2*, The Royal Society of Chemistry: 2016; Vol. 2, pp 27-42.
34. Wilkinson, F.; Helman, W. P.; Ross, A. B., Rate Constants for the Decay and Reactions of the Lowest Electronically Excited Singlet State of Molecular Oxygen in Solution. An Expanded and Revised Compilation. *J. Phys. Chem. Ref. Data* **1995,** *24* (2), 663-677.
35. Wainwright, M.; Giddens, R. M., Phenothiazinium photosensitisers: choices in synthesis and application. *Dyes Pigm.* **2003,** *57* (3), 245-257.
36. Sakaya, A.; Durantini, A. M.; Gidi, Y.; Šverko, T.; Wieczny, V.; McCain, J.; Cosa, G., Fluorescence-Amplified Detection of Redox Turnovers in Supported Lipid Bilayers Illuminates Redox Processes of α-Tocopherol. *ACS Appl. Mater. Interfaces* **2022,** *14* (11), 13872-13882.
37. Bacellar, I. O. L.; Oliveira, M. C.; Dantas, L. S.; Costa, E. B.; Junqueira, H. C.; Martins, W. K.; Durantini, A. M.; Cosa, G.; Di Mascio, P.; Wainwright, M.; Miotto, R.; Cordeiro, R. M.; Miyamoto, S.; Baptista, M. S., Photosensitized Membrane Permeabilization Requires Contact-Dependent Reactions between Photosensitizer and Lipids. *J. Am. Chem. Soc.* **2018,** *140* (30), 9606-9615.
38. Caetano, W.; Haddad, P. S.; Itri, R.; Severino, D.; Vieira, V. C.; Baptista, M. S.; Schröder, A. P.; Marques, C. M., Photo-Induced Destruction of Giant Vesicles in Methylene Blue Solutions. *Langmuir* **2007,** *23* (3), 1307-1314.
39. Vyšniauskas, A.; Qurashi, M.; Kuimova, M. K., A Molecular Rotor that Measures Dynamic Changes of Lipid Bilayer Viscosity Caused by Oxidative Stress. *Chem. Eur. J.* **2016,** *22* (37), 13210-13217.
40. Krumova, K.; Oleynik, P.; Karam, P.; Cosa, G., Phenol-Based Lipophilic Fluorescent Antioxidant Indicators: A Rational Approach. *J. Org. Chem.* **2009,** *74* (10), 3641-3651.
41. Oleynik, P.; Ishihara, Y.; Cosa, G., Design and Synthesis of a BODIPY-α-Tocopherol Adduct for Use as an Off/On Fluorescent Antioxidant Indicator. *J. Am. Chem. Soc.* **2007,** *129* (7), 1842-1843.
42. Godin, R.; Liu, H.-W.; Cosa, G., Ambient condition oxidation in individual liposomes observed at the single molecule level. *Chem. Sci.* **2014,** *5* (6), 2525-2529.
43. Godin, R.; Liu, H.-W.; Smith, L.; Cosa, G., Dye Lipophilicity and Retention in Lipid Membranes: Implications for Single-Molecule Spectroscopy. *Langmuir* **2014,** *30* (37), 11138-11146.
44. Wong-ekkabut, J.; Xu, Z.; Triampo, W.; Tang, I. M.; Peter Tieleman, D.; Monticelli, L., Effect of Lipid Peroxidation on the Properties of Lipid Bilayers: A Molecular Dynamics Study. *Biophys. J.* **2007,** *93* (12), 4225-4236.

45. Oglęcka, K.; Rangamani, P.; Liedberg, B.; Kraut, R. S.; Parikh, A. N., Oscillatory phase separation in giant lipid vesicles induced by transmembrane osmotic differentials. *eLife* **2014,** *3*, e03695.
46. Boonnoy, P.; Jarerattanachat, V.; Karttunen, M.; Wong-ekkabut, J., Bilayer Deformation, Pores, and Micellation Induced by Oxidized Lipids. *J. Phys. Chem. Lett.* **2015,** *6* (24), 4884-4888.
47. Sankhagowit, S.; Wu, S.-H.; Biswas, R.; Riche, C. T.; Povinelli, M. L.; Malmstadt, N., The dynamics of giant unilamellar vesicle oxidation probed by morphological transitions. *Biochim. Biophys. Acta* **2014,** *1838* (10), 2615-2624.
48. Young, R. H.; Wehrly, K.; Martin, R. L., Solvent effects in dye-sensitized photooxidation reactions. *J. Am. Chem. Soc.* **1971,** *93* (22), 5774-5779.
49. Hackbarth, S.; Röder, B., Singlet oxygen luminescence kinetics in a heterogeneous environment – identification of the photosensitizer localization in small unilamellar vesicles. *Photochem. Photobiol. Sci.* **2015,** *14* (2), 329-334.

Chapter 3

Fluorescence Amplified Detection of Redox Turnovers in Supported Lipid Bilayers Illuminates Redox Processes of α-Tocopherol

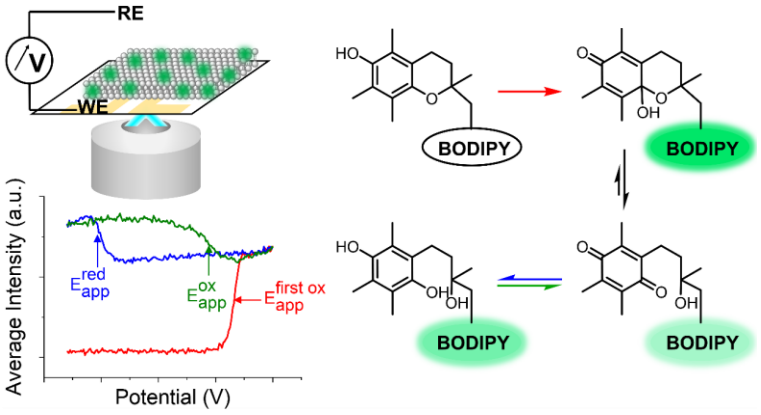

"...by the help of Microscopes, there is nothing so small, as to escape our inquiry; hence there is a new visible World discovered to the understanding"

– Robert Hooke

3.1. Preface

In **Chapter 1**, we presented an overview of the significance of selectively measuring redox reactions in lipid membranes and discussed the existing challenges in this field. We also provided an overview of the current state-of-the-art techniques for measuring and visualizing charge transfer processes within lipid membranes. **Chapter 3** introduced a novel platform designed to sensitively map redox conversions in lipid membranes. In this study, we developed an electrochemical fluorescence microscopy setup that successfully detected the redox conversions undergone by the α-tocopherol fluorogenic analogue, H_4BPMHC, when embedded within an electrode-supported lipid bilayer. The fluorescence amplification offered by our setup enabled the detection of heterogeneous electron transfer reactions originating from extremely low analyte concentrations with a remarkable signal-to-background ratio and allowed the extraction of both thermodynamic and kinetic parameters associated with these electron transfer reactions.

Chapter 3 is reproduced with permission from "Fluorescence Amplified Detection of Redox Turnovers in Supported Lipid Bilayers Illuminates Redox Processes of α-Tocopherol", Aya Sakaya, Andrés M. Durantini, Yasser Gidi, Tara Šverko, Vincent Wieczny, Julia McCain, and Gonzalo Cosa, *ACS Appl. Mater. Interfaces* **2022,** *14* (11), 13872-13882. Copyright 2022 American Chemical Society.

3.2. Abstract

Electron-transfer processes in lipid membranes are key to biological functions, yet challenging to study because of the intrinsic heterogeneity of the systems. Here, we report spectroelectrochemical measurements on indium tin oxide-supported lipid bilayers toward the selective induction and sensing of redox processes in membranes. Working at neutral pH with a fluorogenic α-tocopherol analogue, the dynamics of the two-electron oxidation of the chromanol to a chromanone and the rapid thermal decay of the latter to a chromoquinone are recorded as a rapid surge and drop in intensity, respectively. Continuous voltage cycling reveals rapid chromoquinone two-electron, two-proton reduction to dihydrochromoquinone at negative bias, followed by slow regeneration of the former at positive bias. The kinetic parameters of these different transitions are readily obtained as a function of applied potentials. The sensitivity and selectivity afforded by the reported method enables monitoring signals equivalent to femtoampere currents with a high signal-to-background ratio. The study provides a new method to monitor membrane redox processes with high sensitivity and minimal concentrations and unravels key dynamic aspects of α-tocopherol redox chemistry.

3.3. Introduction

Redox processes within lipid membranes are at the center of our existence, from photosynthesis to cellular respiration. Finely tuned concerted reactions between the different redox proteins within membranes take place where shuttling of electrons occurs via electron transport cofactors such as ubiquinone[1], plastoquinone[2] or vitamin K[3-5] (a naphthoquinone). Notable among membrane-soluble redox-active molecules is α-tocopherol, the most potent naturally occurring lipid-soluble antioxidant.[6-8] α-Tocopherol is a scavenger of lipid peroxyl radicals and a precursor to α-tocopheryl quinone and its reduced dihydroquinone form. Both these metabolites have been suggested to be enzyme cofactors for fatty acid desaturases,[9] and have been most recently suggested to be ferroptosis regulators, playing a similar role to ubiquinone/ubiquinol.[10] Given their biological relevance, it is desirable to develop methods to study the redox properties and associated

dynamics of membrane-soluble redox-active molecules, including α-tocopherol and associated α-tocopheryl quinone and dihydroquinone.

Monitoring and studying membrane-soluble redox-active cofactors within lipid membranes is however significantly more challenging than in homogeneous solutions of organic solvents. To start with, the potentials and rates at which these species form, as well as the intermediates involved, may be very sensitive to the presence of water (as demonstrated for α-tocopherol).[11] The additional membrane capacitance[12, 13] and the complex cellular matrix make it extremely difficult to detect and/or assign any resulting electrochemical signals. Bulk studies on lipid membranes are additionally hampered by the large amount of material required, contrasting the low analyte concentrations encountered within cell membranes. Combining electrochemistry and fluorescence microscopy [electrochemical fluorescence microscopy (ECFM), a form of spectroelectrochemistry] yields a highly sensitive technique where an electrochemical reaction may be readily transduced and amplified in the form of fluorescence.[14-16] By modulating the applied potential and working with redox-active fluorogenic probes (probes that become emissive upon changes in their redox state) charge-transfer currents can be readily detected all the way down to the single-molecule level.[15, 17-21] ECFM enables spatiotemporal mapping of redox reactions on the surface of nanomaterials and heterogeneous environments as a function of applied potentials.[22-24] ECFM provides an opportunity to address redox processes within the confined, ~5 nm-thick 2D mosaic of lipid membranes, so long as one may modulate potential in membranes and work with a suitable fluorogenic probe.

Here, we apply ECFM on indium tin oxide (ITO)-supported lipid bilayers (SLB) to monitor the redox reactions and associated dynamics of the fluorogenic α-tocopherol analogue probe H_4BPMHC (see **Figure 3.1**). H_4BPMHC is a two-segment trap-reporter probe consisting of the chromanol ring of α-tocopherol and a BODIPY moiety (trap and reporter segments, respectively).[25-28] Photoinduced electron transfer (P*e*T) from the chromanol ring moiety in H_4BPMHC quenches the emission from the BODIPY segment. Oxidation of the chromanol ring in turn restores the BODIPY emission resulting in up to 700-fold fluorescence enhancement in homogeneous organic solvent.[27] Working with a total internal reflection fluorescence (TIRF) microscope to maximize signal-to-background ratio, and upon applying an increasing potential, the fluorescence enhancement of membrane-embedded H_4BPMHC was recorded, consistent with the oxidation of the chromanol segment to a chromoquinone. Rapid and irreversible conversion of

the oxidized probe to a partially emissive form was next recorded in a non-potential dependent reaction. The newly formed species was further observed to undergo a reversible interconversion as a function of the applied potential, consistent with an α-tocopheryl quinone to dihydroquinone interconversion. Monitoring the fluorescence intensity as a function of the applied potential enabled retrieving the anodic and cathodic peak potentials for these redox processes, where the detected species are consistent with those reported under standard conditions. The absolute rate constant for the α-tocopheryl hemiketal to α-tocopheryl quinone thermal rearrangement was further determined through these studies. Here, the signal-to-background ratio provided by the setup ultimately allows to readily monitor signals equivalent to currents down to the femtoamperes, corresponding to the detection of just a few hundred molecules in a diffraction-limited spot. Overall, we report, to the best of our knowledge, the first application of TIRF-ECFM on SLBs and provide a new methodology to study electrochemical reactions with a minute amount of material in lipid membranes.

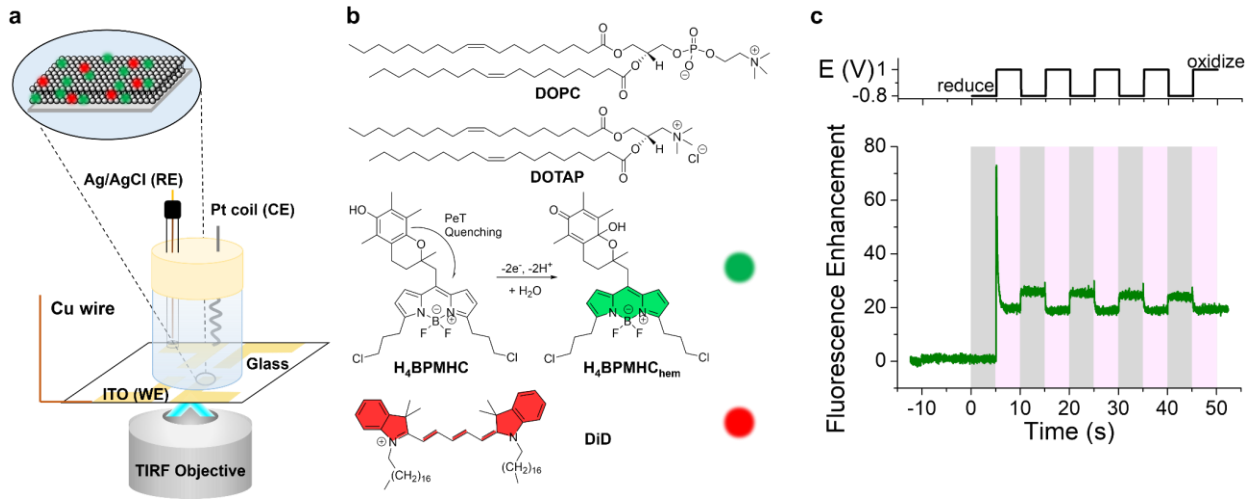

Figure 3.1. (a) ECFM setup utilized in this study. A planar SLB was formed inside a home-built ECFM chamber on top of a glass coverslip coated on four independent regions with ITO, serving as a working electrode (WE). A silver-silver chloride (Ag/AgCl) electrode was employed as a reference electrode (RE) with a coiled platinum wire as a counter electrode (CE). The chamber was mounted on an inverted fluorescence microscope that allowed monitoring fluorescence intensity fluctuations as a function of the applied potential. (b) Structure of the lipids and fluorophores utilized in this study. H_4BPMHC was used as a reporter of the redox chemistry, while DiD was used to independently visualize and characterize the lipid membrane. (c) Typical fluorescence response of membrane-embedded H_4BPMHC (3.4:100 dye/lipid mole ratio) to an applied electrochemical potential square wave (alternating 5 s steps of reductive (−0.8 V, gray-

shaded) and oxidative (1 V, pink-shaded) potentials). λ_{ex} = 488 nm; 100 frames/s acquisition frequency. Time 0 s corresponds to the start of the applied potential.

3.4. Results and Discussion

3.4.1. Formation of a functional ITO supported lipid bilayer

In order to study redox reactions in an environment mimicking cellular membranes, we developed an ECFM technique based on a previously reported setup[29] to monitor changes in the fluorescence intensity of the fluorogenic α-tocopherol analogue H_4BPMHC with the applied potential. Specifically, a functional solid-SLB was assembled on an airtight electrochemical cell consisting of a glass coverslip coated with a thin transparent ITO film that acted as a working electrode (**Figure 3.1a**). The electrochemical cell was mounted on a microscope and, unless otherwise stated, imaged under TIRF modality to minimize unwanted background. Images were captured using an electron multiplying CCD camera (EMCCD) while sweeping the external potential in the electrochemical cell (**Figure 3.1c**). All imaging experiments were conducted at 37 °C. Two emission channels were recorded, one reporting on the membrane-embedded redox-active H_4BPMHC **(Figure 3.1b,c**) and a second one reporting on DiD, a membrane-embedded lipid marker dye.

To assemble the SLB on top of the ITO surfaces, we utilized the vesicle fusion method.[30, 31] Liposomes 50 nm in diameter and consisting of a 15:85 DOTAP/DOPC lipid ratio were used (**Figure 3.1b**), where the choice of small liposomes and the addition of the cationic 1,2-dioleoyl-3-trimethylammoniumpropane (DOTAP) was made to promote liposome rupture and SLB formation. Key to the formation of functional SLB on ITO-coated surfaces was a subsequent slow annealing step, always maintaining the temperature above the glass-transition temperatures of either DOTAP or 1,2-dioleoyl-*sn*-glycero-3-phosphocholine (DOPC). Here, the temperature was gradually increased from 23 to 37 °C, with a 30 min incubation time upon each temperature change (see **Section 3.7.1.1** for further details).

To assess the formation of SLB atop ITO, fluorescence recovery after photobleaching (FRAP) experiments [32-34] were carried out prior to each electrochemical experiment on the ITO-coated surface under study and on an adjacent glass region serving as a control. Here, the lipophilic red-emissive cyanine dye DiD was incorporated at a <0.064:100 DiD/lipid mole ratio. DiD

fluorophores present in a region ~13 μm in diameter were photobleached for 1 min using a 647 nm laser with an excitation power of 3.7 mW over the photobleached area. Rapid recovery of the fluorescence intensity revealed the formation of a well-connected two-dimensional solid-SLB when the SLB was formed upon temperature increase in a stepwise fashion from 23 °C to 27 °C, 34 °C, and finally 37 °C (**Figure 3.2**). Notably, a lack of DiD fluorescence recovery at 23 °C and 27 °C was observed, suggesting the formation of a layer consisting of unruptured liposomes[35, 36] (**Figure 3.2a,b**, green and purple traces), and a "phase transition" to an SLB occurred only upon further heating to 34 and 37 °C (**Figure 3.2a,b,** red and blue traces, respectively). Attempts at forming an SLB on ITO-coated surfaces directly at 37 °C were unsuccessful.

Diffusion coefficients of ~0.33 and ~0.23 $\mu m^2 s^{-1}$ were extracted from FRAP trajectories both on ITO and on adjacent glass surfaces, respectively (see **Section 3.7.1.2** for diffusion coefficient calculations). The extracted diffusion coefficients are on the lower end of values reported for glass-SLBs.[37-40] One possible explanation is the presence of unruptured liposomes that hinder the diffusion of freely moving DiD molecules providing a tortuous path. However, a significant fraction (70 ± 8%) of the initial fluorescence signal was recovered on glass surfaces (62 ± 10% on ITO surfaces), where full recovery is precluded by gradual photobleaching of DiD dyes as a result of the continuous (~20 μW) excitation during acquisition (**Figure 3.2b**, dashed line). This indicates that most of the glass surface is covered by a well-connected SLB and possibly suggests that the presence of only a small amount of unruptured liposomes may significantly hinder diffusion. The DiD fluorescence intensity recorded on the ITO-SLB was on average 20% higher than that recorded on glass (contrary to the expected ~22% drop based solely on ITO transmission efficiency in both the excitation and emission pathways). This may indicate that a fraction of liposomes remains unruptured, yielding a higher fluorophore surface density than would otherwise be expected on an ITO-SLB.

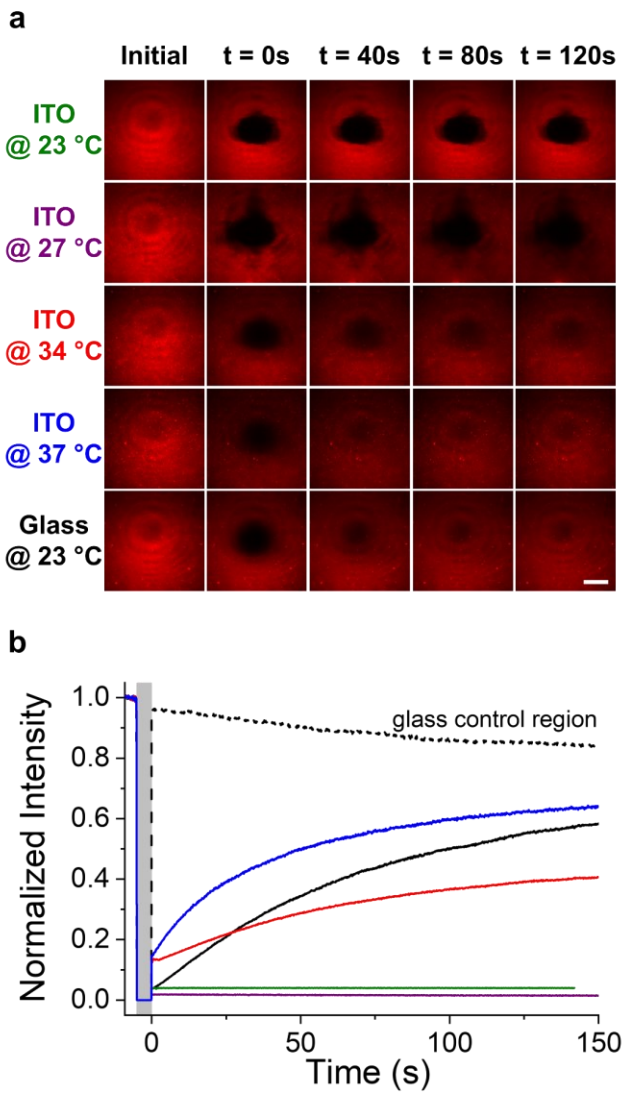

Figure 3.2. Temperature dependence and characterization of the lipid membrane. (a) Images portraying the fluorescence recovery (or its lack thereof) of membrane-embedded DiD (0.064:100 dye/lipid mole ratio) over time after photobleaching a ~13 μm diameter region for 1 min. The experiments were done atop a glass surface or an ITO-coated surface at increasing temperatures. The sample was formed at 23 °C and then heated sequentially to 27 °C and 34 °C and finally to 37 °C, and the resulting lipid membrane was characterized at each temperature step. The first picture to the left of each row depicts the surface prior to photobleaching. Scale bar: 20 μm. (b) Intensity over time trajectories of the DiD fluorescence signal (λ_{ex} = 647 nm) in the photobleached region on the different surfaces (glass at 23 °C (black trace), ITO at 23 °C (green trace), ITO at 27 °C (purple trace), ITO at 34 °C (red trace), and ITO at 37 °C (blue trace)) normalized to the intensity prior to photobleaching. The gray-shaded area indicates 1 min of photobleaching at a maximum excitation intensity (>3.7 mW over the photobleached area). Time 0 s corresponds to the first frame after photobleaching.

3.4.2. Electrochemical actuation along ITO surfaces

To monitor redox processes exploiting fluorescence as an amplification of the electron-transfer reactions, the redox-active fluorogenic probe H_4BPMHC was incorporated within the lipid membrane at dye/lipid mole ratios ranging between 0.26:100 and 5.2:100 (as specified in the text). Here, the neutral and lipophilic BODIPY fluorophore ensures partitioning within the lipid membrane, while the chromanol head is exposed to the water/lipid interface (as revealed by its previously reported reactivity with water-soluble peroxyl radicals[26, 28, 41]), adopting a similar orientation to its parent molecule α-tocopherol.[42-44] Effective electron transfer between the ITO electrode and the probes present in the lower leaflet of the SLB leads to conversion of an otherwise non-emissive dye into an emissive chromophore, where the intensity increase over time is proportional to the electron current associated with the desired redox process. Initial imaging was carried out on a large field of view (409 μm × 409 μm) using a low 20× magnification widefield epifluorescence imaging to observe the fluorescence signal arising from the SLB simultaneously on both ITO and glass. We observed three distinct regions on the coverslip in terms of H_4BPMHC response to the applied electric field, surface topography, and DiD intensity. Thus, a field-responsive ITO-coated region, a non-responsive glass region, and an interface separating the two and spanning ∼100 μm (**Figure 3.3**) were recorded by monitoring H_4BPMHC intensity with the applied potential. Atomic force microscopy (AFM) measurements indicated that the interface exhibits a granular morphology akin to ITO, albeit less pronounced (**Figure 3.7**), suggesting that the interface consists of interspersed "islands" of ITO generated during the coating process that diminishes the conductivity of the glass/ITO interface. Interestingly, we observed a brighter DiD fluorescence signal along this interface than on either ITO or glass (**Figure 3.3a**, where the ITO surface appears dimmer than glass as it is semitransparent), suggesting a larger number of fluorophores per unit area adsorbed along the interface.

To assess the redox properties of H_4BPMHC within the SLB, the potential was swept over time in the form of a square wave between +1 V and −1 V versus the Ag/AgCl reference electrode. These values are above and below, respectively, the reported oxidation potential of the chromanol segment in the probe [2,2,5,7,8-pentamethyl-6-hydroxy-chromanol (PMHC), +0.7 V vs Ag/AgCl[11, 45]], yet do not attain the redox potentials of the BODIPY segment in H_4BPMHC (oxidation and reduction potentials of +1.2 and −1.2 V, respectively[27]). We observed a rapid (∼0.1 s) ∼6-fold intensity enhancement with positive bias in the SLB covering the working electrode

(ITO-coated surface), see **Figure 3.3b,c**. This intensity jump is consistent with oxidation of the chromanol segment in H_4BPMHC and deactivation of the otherwise operating P*e*T. Notably, the intensity rapidly decayed to a residual value (~33% of the maximum intensity) while holding the positive bias. This initial behavior was not replicated in subsequent square wave cycles, indicative of the irreversible nature of the oxidation of H_4BMPHC in lipid membranes. Switching next to negative bias, we recorded a moderate increase in intensity from the residual value. Subsequent steps of positive and negative bias showed intensity modulation between the residual value and the moderate restoration with no noticeable signal fatigue. No intensity modulation with applied potential was recorded either along the lipid bilayer supported on the interface (ITO islands) or on bare glass surfaces, where the probe remained pristine, indicative of their insulating properties (**Figure 3.3b,c**).

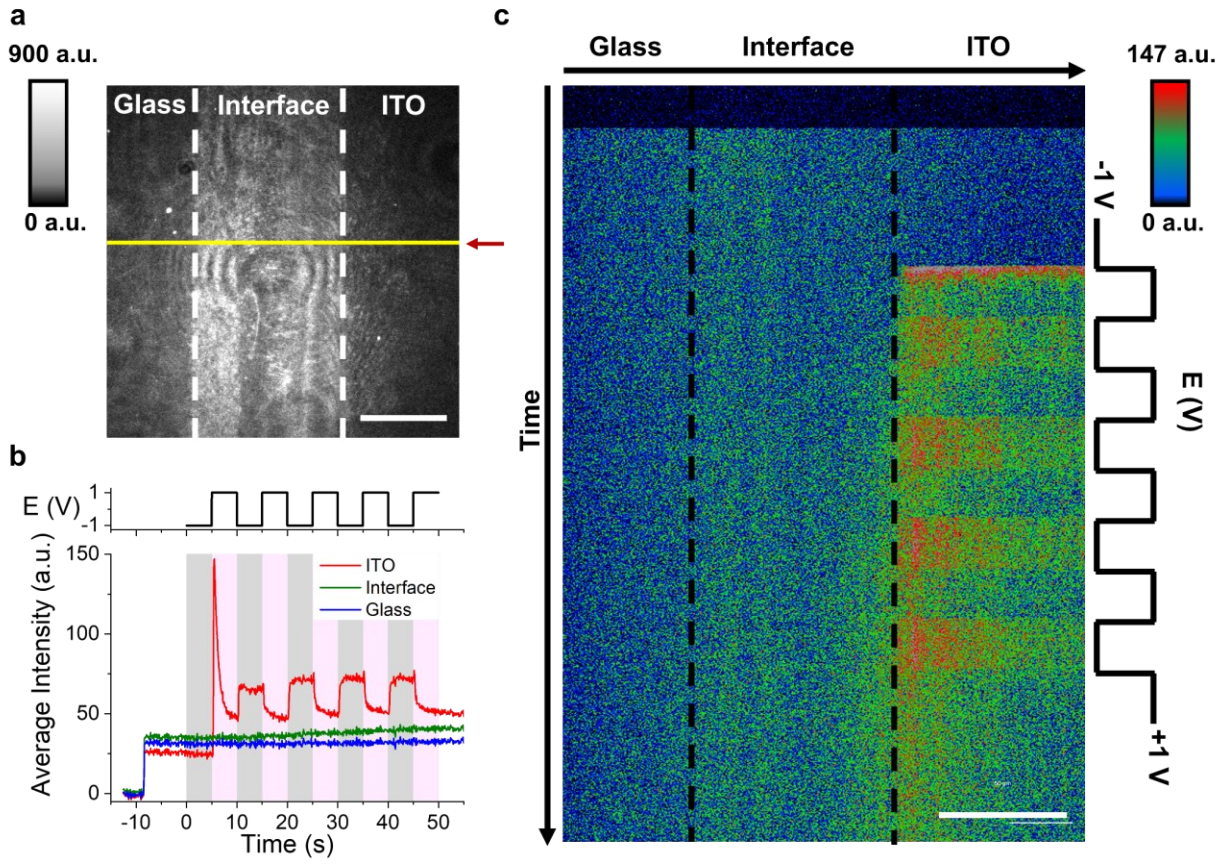

Figure 3.3.Electrochemical actuation along the different surfaces (a) Fluorescence image of membrane-embedded DiD (λ_{ex} = 647 nm, 100 µW) with lipid bilayers supported either on bare glass or on the interface region or the ITO-coated surface (going from left to right). The yellow line and burgundy arrow illustrate the line scan where the kymograph was obtained from (see panel

c). (b) Fluorescence response of H_4BPMHC to the applied square wave potential recorded across the three surfaces, λ_{ex} = 488 nm, 47 μW. (c) Kymograph depicting the evolution of the fluorescence intensity of H_4BPMHC with time while under applied potential. H_4BPMHC and DiD dye/lipid ratios used are 5.1:100 and 0.064:100, respectively. Scale bars: 100 μm, imaging frequency 10 frames/s. The potential square wave consisted of 1 V (pink-shaded areas in panel b) and −1 V (gray-shaded areas in panel b) potential steps. A 20× magnification objective was used.

3.4.3. ECFM sensitivity optimization

To optimize the sensitivity and resolution toward conducting mechanistic studies on redox processes for H_4BPMHC, we next utilized the TIRF imaging modality with a 100× magnification objective. We initially verified that the enhancement recorded for H_4BPMHC upon applying the positive bias matched the intensity value recorded for H_4BCH_3 (**Figure 3.8a**), a control dye that lacks the PMHC segment and thus the P*e*T quenching mechanism (**Figure 3.4a**). We subsequently sought to (i) minimize the background and (ii) enhance the signal. To minimize the background, we incorporated a sacrificial antioxidant (PMHC) to ensure that no pre-activation of the probe took place during sample preparation. Premature oxidation of H_4BPMHC would reduce the dynamic range by increasing the initial intensity value. PMHC was thus added as a sacrificial reagent to the lipid mixture prior to lipid film formation in a 10:1 PMHC/H_4BPMHC mole ratio. No change in either the intensity−time profile or the fluorescence enhancement value was observed in studies conducted with and without PMHC (**Figure 3.4b**, black and purple traces, respectively), suggesting that the observed background level is intrinsic to the system. No background change was observed with differing loadings of H_4BPMHC in the membrane, further indicating that the background is intrinsic to the system and that the probe remains pristine until the positive bias is applied (**Figure 3.8b**).

To enhance the signal, we explored increasing the dye loading, thus better offsetting the intrinsic background of our setup. We reasoned, however, that the loading should be capped at values low enough to prevent homo-energy transfer between neighboring dyes, as that process would otherwise play a detrimental role in the intensity. The optimal value for H_4BPMHC loading was reached at a mole ratio of ~3.4:100 probe/lipid. This loading corresponds to an average probe-to-probe separation of 5.5 nm (assuming a homogeneous distribution of material within the SLB), where the homo-Förster resonance energy-transfer (homo-FRET) radius of H_4BPMHC is 5.40 nm (see **Section 3.7.2** for homo-FRET radius calculations). Under these conditions, we achieved a fluorescence enhancement of ~73-fold upon applying a positive +1 V bias on the ITO electrode.

Lower enhancements were obtained when dye loadings were either below (0.26:100 or 1:100 dye/lipid mole ratio) or above (5.1:100 dye/lipid mole ratio) this optimal value, see **Figure 3.4b**. The recorded fluorescence enhancement values were lower than the ~700-fold enhancement reported in acetonitrile[27] due to the significant background contribution arising from the experimental setup that is not subtracted in these studies.

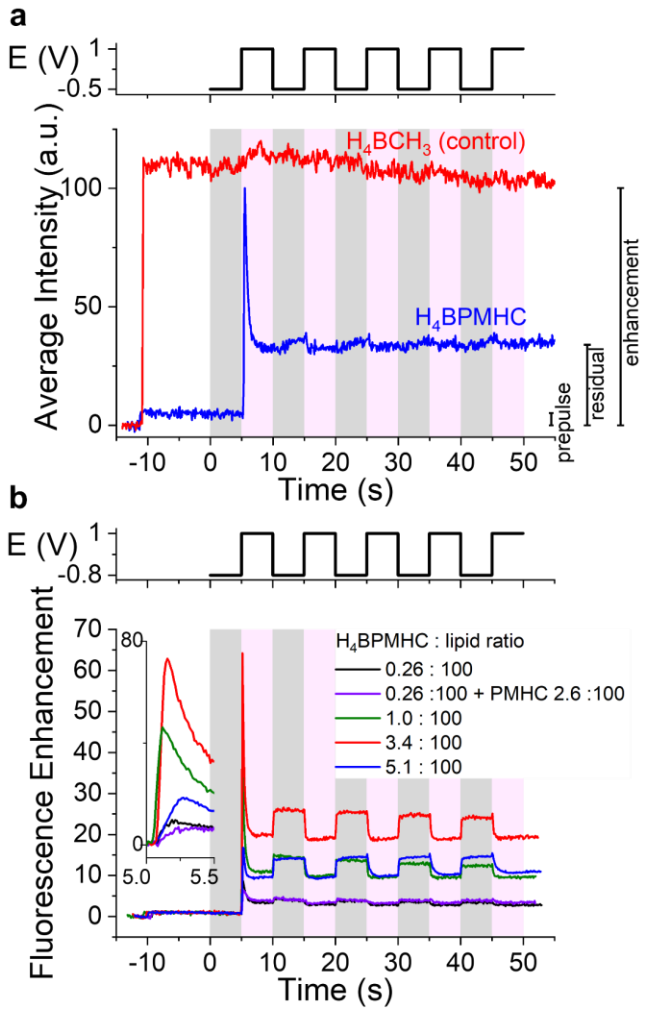

Figure 3.4. Optimization of ECFM sensitivity. (a) Fluorescence response of H_4BPMHC and the control fluorescent dye H_4BCH_3 - lacking the chromanol ring - to the applied potential at 0.26:100 dye/lipid mole ratio acquired at 10 frames/s. (b) Fluorescence response of H_4BPMHC to the applied potential under different probe and antioxidant loading conditions (0.26, 1, 3.4, and 5.1 probe per 100 lipid and a PMHC loading of 2.6:100 lipid when stated). The data was normalized to the pre-pulse intensity (intensity prior to oxidation) to favor comparison of the sensitivity. Movies were acquired at 100 frames/s and re-binned to 10 frames/s. The inset of figure (b) is a zoom-in of the fluorescence enhancement obtained upon oxidation with the data acquired at 100 frame/s, providing better temporal resolution. Time 0 s corresponds to the start of the applied potential. The samples were excited with 5 μW of a 488 nm CW laser. Potential step functions

consisted of 1 V oxidative steps (pink-shaded regions) and −0.5 V (a) and −0.8 V (b) reductive steps (gray-shaded regions).

3.4.4. Oxidation mechanism of H_4BPMHC

To decipher the mechanism of reaction, we next tackled the three distinct features in the response of H_4BPMHC to applied bias, namely, (i) an initial sharp enhancement of the fluorescence emission at +1 V, indicative of the trap segment oxidation, (ii) a fast decrease in intensity to a non-zero residual value while still under oxidative potential, and (iii) the presence of the residual intensity that in turn modulates with the applied potential steps.

To confirm that the sharp emission enhancement in the first oxidative step (i) is consistent with the oxidation of the chromanol segment in H_4BPMHC, we recorded the potential at which emission enhancement occurs. The potential was obtained upon monitoring the fluorescence emission while linearly increasing the potential with time at a constant rate of 100 mV/s (**Figure 3.5a**, red trace), analogous to a standard cyclic voltammogram, where current is recorded as the potential is linearly scanned. Here, the emission intensity versus the potential trajectory is ultimately akin to an integrated form of current versus potential, and the sigmoidal point obtained in the former corresponds to the anodic peak potential "E_{pa}" of the latter. An apparent oxidation potential of +0.67 V versus Ag/AgCl was retrieved from the sigmoidal point. This value matches the oxidation potential reported for PMHC in water.[11] Importantly, we note that the fluorescence intensity enhancement achieved upon initial oxidation through a linearly increasing potential is significantly lower than the one achieved when a step function is applied due to the slower rate of oxidation in the former case, which competes with the rapid decay of the newly formed species (see next paragraph).

To address the rapid intensity decay recorded following the oxidation of the probe (ii), we next explored three pathways that could account for the observation, namely, (a) photoinduced decay, (b) secondary oxidation to a partially emissive product, and (c) chemical rearrangement into a partially emissive product. As the fluorescence decay occurs while still under oxidative potential, reduction was eliminated as a possible decay pathway. To tackle point (a) above, we applied a first cycle of reductive and oxidative steps under no laser excitation (**Figure 3.5b**, black trace), thus preventing any photoinduced decay from occurring. Upon resuming excitation, we observed an intensity identical to the residual intensity of H_4BPMHC when modulated under constant laser excitation (**Figure 3.5b**, red trace). The intensity decay rate was further shown to be

independent of excitation power (**Figure 3.9**). Together, these results point to a "dark" thermal reaction being involved in the rapid decay. To rule out a secondary oxidation (point b) into a partially emissive product following the initial oxidation of the probe, we monitored the intensity over time while applying a short (50 ms) +1 V oxidative pulse (**Figure 3.5c**, highlighted with pink-shaded area in the inset) that is shorter than the time required to reach full enhancement (~100 ms). We observed a rapid intensity decay with an identical decay constant as that recorded in the long oxidative pulse, indicating that the decay process is not associated with the applied potential. Accordingly, the results, we reasoned, are accounted for by a chemical rearrangement, point (c), possibly into the ring-opened quinone form of the probe. Studies on α-tocopherol electrochemical oxidation within films,[45] droplets,[46] and lipid membranes[45, 47] deposited on electrode surfaces and exposed to aqueous buffers have shown that this molecule undergoes a hydration reaction, followed by a quasi-irreversible ring opening to form α-tocopheroquinone.

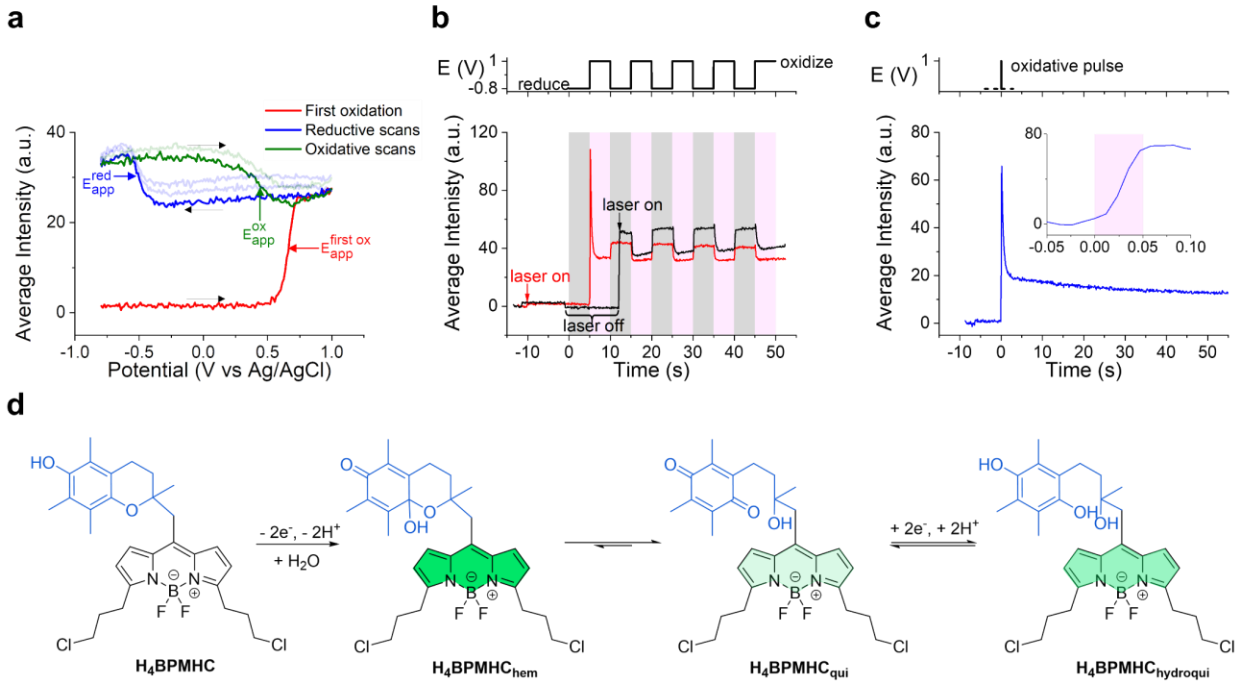

Figure 3.5. Deciphering the redox mechanism of H4BPMHC. (a) Fluorescence response of H4BPMHC to externally applied potential cycling between −0.8 and 1 V at a rate of 100 mV/s. The first segment depicting the irreversible oxidation of H4BPMHC is shown in red (a), after which the probe undergoes a ring opening to form the quinone H_4BPMHC_{qui} that can undergo reversible reduction (blue) and oxidation back to H_4BPMHC_{qui} (green). The curves corresponding to the first reduction and oxidation scans between the quinone and dihydroquinone forms are bolded, and subsequent cycles are shaded. Black arrows indicate the direction of the potential scan. (b) Fluorescence response of H4BPMHC to the applied potential square wave with the first reductive

and oxidative steps applied under laser excitation (red) or in the dark (no laser excitation, black). (c) Fluorescence response of H_4BPMHC to a short oxidative pulse (50 ms), highlighted by the pink-shaded area in the inset. Dashed lines in the potential−time trace correspond to the resting potential. (d) Proposed mechanism depicting the states of H_4BPMHC following its oxidation and subsequent reduction. The samples were excited with 5 μW of a 488 nm CW laser and their fluorescence acquired at 100 frames/s and rebinned to 10 frames/s (the inset of panel (c) shows the data acquired at 100 frame/s). Time 0 s corresponds to the start of the applied potential. The potential step functions consisted of −0.8 V and 1 V steps. Membrane loading was 3.4 dyes: 100 lipids.

The nature of the residual intensity that in turn modulates with the applied potential steps (iii), we reasoned, can then be accounted for via a redox cycling between the probe in its quinone form and its reduced dihydroquinone form. Such a rearrangement is possible for the oxidized product of H_4BPMHC, where the observed modulation in the residual intensity would result from cycling between these two forms of the probe. Density functional theory (DFT) calculations performed on the structures shown in **Figure 3.5d** at the B3LYP 6-31G(d) level[48] reveal that the quinone moiety may readily quench the BODIPY emission via photoinduced electron transfer from the BODIPY segment, while the dihydroquinone may in turn quench the emission through a photoinduced electron transfer to the fluorophore segment (see **Figure 3.6** and **Table 3.3**). Given that the rate constant of P*e*T is dependent on the fluorophore−quencher distance, and considering that an additional bond and also additional flexibility exist in the open cycle of quinone/dihydroquinone, both of these P*e*T processes will only result in the partial quenching of the BODIPY fluorescence, compared to the near-complete fluorescence quenching observed in H_4BPMHC.

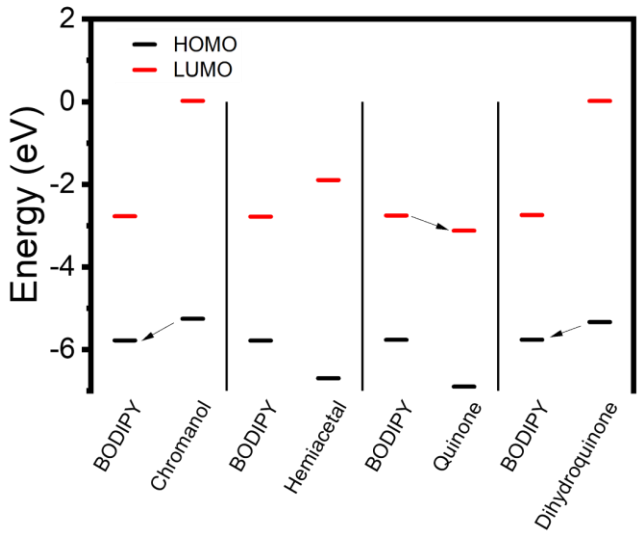

Figure 3.6. Calculated HOMO and LUMO energy levels of BODIPY fluorophore and oxidation products of PMHC. DFT calculations were performed on the structures shown in **Figure 5d**. Molecular orbitals were assigned to the BODIPY fluorophore or the α-tocopherol segment following a previously reported method by our group.[49] Arrows indicate P*e*T processes.

To confirm the cycling between a quinone and dihydroquinone forms of the oxidized probe, we applied a triangular potential function versus time to establish the potentials responsible for the modulation in the residual intensity, **Figure 3.5a** (see **Figure 3.10** for the original intensity−time trajectory). We observed that the residual intensity increases at potentials below ∼−0.50 V, with a sigmoidal point at −0.55 V, in strong agreement with the apparent peak reduction potential value of −0.6 V reported for the conversion of α-tocopheroquinone to α-tocopherodihydroquinone in lipid membranes.[45] Subsequent oxidation restores the residual intensity to its initial value at potentials above +0.25 V, with a sigmoidal point of +0.4 V. We assign this second process to the oxidation of the dihydroquinone back to its quinone form, consistent with literature values of +0.4 V for the apparent oxidation peak of the conversion of α-tocopherodihydroquinone to α-tocopheroquinone in lipid membranes.[45] Based on these observations, we propose the reaction mechanism illustrated in **Figure 3.5d** for the redox-mediated conversion of the probe. H_4BPMHC goes from an initially reduced non-emissive form to an emissive hemiketal form H_4BPMHC_{hemi} formed upon oxidation and hydration. The latter undergoes a quasi-irreversible ring opening to form a partially emissive quinone H_4BPMHC_{qui}, responsible for the observed decay into a residual intensity. Finally, H_4BPMHC_{qui} can be reversibly reduced to the dihydroquinone $H_4BPMHC_{hydroqui}$.

Our ECFM setup thus allows sensitive and accurate detection of the different redox states of the most potent naturally occurring lipid-soluble antioxidant at very low concentrations using 10^8 fold less analyte than previously used to study α-tocopherol oxidation with bulk electrochemical techniques.[45] With our method, we have indirectly measured picoampere currents, on par with the most sensitive electrochemical techniques such as scanning electrochemical microscopy,[50, 51] with a remarkable signal to background ratio. The sensitivity of our method should enable us to readily monitor diffraction-limited single liposomes. Fluorescence signals equivalent to currents down to the femtoampere can be readily sensed through the rapid conversion upon oxidation of an otherwise non-emissive probe into a fluorescent one (see **Section 3.7.3** and **Figure 3.11** for current calculations).

The fast camera acquisition rate at which the experiments were carried out further allowed obtaining the kinetic parameters for the different conversions. All the interconversions followed first-order kinetics when a step function was applied. For the first and second steps of the reaction scheme illustrated in **Figure 3.5d**, we applied a model of consecutive first-order reactions with a non-emissive reactant, a highly emissive intermediate, and a partially emissive final product. The fluorescence signal of the initial peak was thus fit to **eq 3.1** (see **Figure 3.12** and **Section 3.7.4** for derivation). Here, $I_{(t)}$ is the total fluorescence intensity at any given time, I_0 is the initial fluorescence intensity, k_{ox} is the rate constant of H_4BPMHC oxidation to H_4BPMHC_{hem}, k_{op} is the rate constant of the ring opening of H_4BPMHC_{hem} to form H_4BPMHC_{qui}, t is the time, c is the ratio of the quantum yield of H_4BPMHC_{qui} to that of H_4BPMHC_{hem}, and I_{max} is the theoretical maximum intensity gained upon a full conversion of H_4BPMHC to H_4BPMHC_{hem} without a subsequent ring-opening reaction. The quantum yield of non-quenched BODIPY fluorophores being near unity,[27] c can be used as an estimate of the quantum yield of H_4BPMHC_{qui} in lipid membranes (0.26 ± 0.07). The reversible electrochemical transitions between H_4BPMHC_{qui} to $H_4BPMHC_{hydroqui}$ and the reverse process were in turn fit with a first-order exponential growth (reduction step) and decay (oxidation step) functions (**eqs 3.2** and **3.3**, respectively). Here, k_{red}^{q} and k_{ox}^{hq} are the rate constants of the electrochemical reduction and oxidation reactions between H_4BPMHC_{qui} and $H_4BPMHC_{hydroqui}$, respectively, and I_0 and I_∞ are the fluorescence intensities of reactants and products, respectively (see **Figure 3.12**).

$$I_{(t)} = I_0 + \frac{k_{ox}}{k_{op} - k_{ox}}\left(e^{-k_{ox}t} - e^{-k_{op}t}\right)I_{max} + c \times \left(1 + \frac{k_{ox}e^{-k_{op}t} - k_{op}e^{-k_{ox}t}}{k_{op} - k_{ox}}\right)I_{max} \quad (3.1)$$

$$\frac{I_\infty - I_{(t)}}{I_\infty - I_o} = e^{-k_{red}^{q}t} \quad (3.2)$$

$$\frac{I_\infty - I_{(t)}}{I_\infty - I_o} = e^{-k_{ox}^{hq}t} \quad (3.3)$$

The extracted rate constants under the potentials applied throughout this manuscript are listed in **Table 3.1**. The potential dependence of these rate constants was further measured, and the results are depicted in **Figure 3.13**. A six-fold shorter lifetime (**Table 3.1**) was recorded in reducing the quinone (~20 ms lifetime at an applied bias of −0.8 V) than in oxidizing the dihydroquinone (~123 ms lifetime at an applied bias of +1.0 V). The recorded lifetime values for H_4BPMHC oxidation in turn were in the range of 65 ms at an applied bias of +1 V. Considering the reported redox potentials for these species in lipid membranes (−0.6 V and +0.4 V for the quinone reduction and dihydroquinone oxidation, respectively, and +0.7 V for PMHC oxidation, all vs Ag/AgCl[45]), the overpotential applied was higher for the slowest process, indicating that the membrane environment plays a key role in modulating the rates of electron transfer for the quinone/ dihydroquinone redox couple. The difference in the rates of reaction also becomes apparent upon inspection of the intensity time trajectories when a triangular potential function was applied (**Figure 3.5a**). Here, we observe that the bias at which the dihydroquinone oxidation takes place occurs over a large range of potential values while reduction is nearly instantaneous. Ultimately, the ITO-supported bilayers provide an ideal substrate to measure the rates of electron-transfer processes through the reporting enabled by redox-active fluorogenic probes.

Table 3.1. Applied and Extracted Parameters and Rate Constants of Reported Electrochemical Transitions[a]

step	apparent peak potential (V)	applied potential (V)	rate constant (s^{-1})
k_{ox}	+0.6	+1.0	15.4 ± 7.2[b]
k_{op}	N.A.		3.2 ± 1.5[c]
k^{q}_{red}	-0.55	-0.8	47.3 ± 16.0[d]
k^{hq}_{ox}	+0.4	+1.0	8.4 ± 4.4[e]

[a]Rate constants were obtained by averaging values extracted from fitting multiple intensity-time trajectories of the fluorescence response of H_4BPMHC to the applied potential. Errors are the standard deviations obtained from the averaged values. [b]N=6. [c]N=7. [d]N=22. [e]N=17.

3.5. Conclusion

The work reported herein underscores the use of spectro-electrochemical fluorescence microscopy combined with ITO-SLBs and probe design toward studying redox processes in lipid membranes. This combined construct allows real-time, spatiotemporal detection of redox conversion all while circumventing vexing problems from bulk studies associated with membrane capacitance and large amount of material requirements. Provided that chemical selectivity is built in the probe design, it is possible to probe in situ redox processes of biological relevance. The setup reported herein allows us to monitor electron flux equivalent to picoampere currents in a full field of view with extremely high sensitivity. The remarkable signal-to-background ratio provided by the setup ultimately allows us to readily monitor signals resulting from currents down to the femtoamperes, corresponding to the detection of just a few hundred molecules in a diffraction-limited spot.

Utilizing ECFM and α-tocopherol as a case study, we successfully detected with high sensitivity the transitions undergone by H_4BPMHC, a fluorogenic α-tocopherol analogue embedded in an ITO-SLB. Through monitoring changes in fluorescence intensity as a result of applied potential, we successfully induced and detected the oxidation of the α-tocopherol analogue and the reversible interconversion of the ensuing α-tocopheryl quinone analogue into its dihydroquinone form. The rate constants of these processes were readily obtained and showed that

dihydroquinone oxidation is significantly slower than the quinone reduction when in the lipid membrane at physiological pH. The work further provides rate constant values for the rapid two-electron oxidation of α-tocopherol into its hemiketal analogue, as well as the rate constant for the subsequent rapid (thermal) decay of the hemiketal into the open quinone form for membrane embedded substrates. Tocopheryl dihydroquinone (and its oxidized quinone counterpart) is a key metabolite of α- tocopherol that has been reported to play a role in antioxidant protection at the cellular level.[9, 10, 52] The rapid formation of tocopheryl quinone upon rearrangement of α-tocopherone hemiketal underscores that when newly formed α-tocopheroxyl radicals undergo a subsequent one-electron oxidation yielding α-tocopherone hemiketal, they will irreversibly degrade into the resulting quinone. Such rapid rearrangement will preclude α-tocopherol regeneration in membranes via electron injection and highlights the transient nature of the oxidized intermediate tocopherone hemiketal. In general, our work provides a new methodology to study with high sensitivity heterogeneous electron transport processes within SLBs and specifically where quinone/dihydroquinone redox couples serve as electron relays.

3.6. Materials and methods

3.6.1. Materials

H_4BPMHC was synthesized as previously reported.[27] Potassium chloride, HPLC grade solvents (acetone, isopropanol, acetonitrile, and chloroform), and HyClone HyPure Molecular Biology Grade Water were purchased from Fisher. 1,2-dioleoyl-snglycero- 3-phosphocholine (DOPC) and 1,2-dioleoyl-3-trimethylammonium- propane (DOTAP, chloride salt) powders were purchased from Avanti Polar Lipids, Inc. 2,2,5,7,8-Pentamethyl-6-chromanol (PMHC) was purchased from Sigma-Aldrich, Co. Sulfuric acid and hydrogen peroxide were purchased from ACP chemicals. 10× Phosphate-buffered saline (pH 7.4) and 1,1′-dioctadecyl-3,3,3′,3′-tetramethylindodicarbocyanine perchlorate (DiD) oil were purchased from ThermoFisher Scientific (Invitrogen). Anhydrous ethanol was purchased from Greenfield Global, Inc. (Brampton, ON, Canada). All materials were used without further purification.

3.6.2. Liposome preparation

Stock solutions of DOTAP and DOPC (20 mM each) were prepared in chloroform. DiD stock solution (500 μM) was prepared in anhydrous ethanol and its concentration determined by using the extinction coefficient of DiD (2.5×10^5 M^{-1} cm^{-1}). Solutions of H_4BPMHC in acetonitrile were freshly prepared prior to lipid film formation and their concentration determined from the extinction coefficient of H_4BPMHC (8.2×10^4 M^{-1} cm^{-1}).[27] When specified, H_4BPMHC was dissolved in an acetonitrile solution containing a previously dissolved antioxidant (PMHC) to prevent preoxidation of the probe. Here, the final solution was at a 10:1 ratio of PMHC to H_4BPMHC. The DiD stock solution (2.55 μL) was added to a glass vial, and H_4BPMHC was added in the amount specified in the text (5.1×10^{-9}, 6.75×10^{-8}, 2.00×10^{-8}, or 1.02×10^{-7} molecules). The solvents were evaporated under a stream of argon. 85 μL of stock DOPC and 15 μL of stock DOTAP were added to the vial for final concentrations of 17 and 3 mM, respectively. Chloroform was evaporated under a stream of argon, and the resulting lipid film was further dried under vacuum for a minimum of 60 min. The lipid film was hydrated with 100 μL of a 0.1 M KCl phosphate buffer solution to achieve a final lipid concentration of 20 mM. The final DiD-to-lipid ratio is 0.64 DiD molecules per 1000 lipids (12.5 molecules per 50 nm diameter liposome). The H_4BPMHC-to-lipid ratios used were 2.55, 10.00, 33.75, or 51.06 molecules per 1000 lipids (50, 196, 661, or 1000 dyes per liposome, respectively). The suspension was subjected to four freeze−thaw−sonication cycles (5 min in dry ice, followed by 5 min sonication in a room temperature water bath) to increase unilamellarity. The sample was then extruded 17 times through a 50 nm polycarbonate membrane using a mini-extruder (Avanti Polar Lipids, Inc.), resulting in a suspension of 50 nm diameter liposomes.

3.6.3. Electrochemical fluorescence microscopy (ECFM) chamber

Custom-patterned glass coverslips coated in four separate regions with ITO with a sheet resistance of ∼50 Ω/sq (Evaporated Coatings Inc.) were cleaned by sequential sonication in acetone, isopropanol, and HyClone water (three cycles of 10 min, each). A glass tube (∼1 cm inner diameter, ∼3 cm height, cleaned with piranha) was affixed in the center of the coverslip with epoxy glue, then allowed to dry for 5 min, and then cured in a 90 °C oven for 15 min. A copper wire was attached to each of the four ITO sectors to facilitate independent connection to the electrochemical

analyzer. The copper wire−ITO junction was sealed by coating with a SPI Flash-Dry Silver Colloidal Suspension (SPI Supplies).

3.6.4. Supported lipid bilayer (SLB) formation

The ECFM chamber was washed twice with buffer solution (0.1 M KCl in PBS) and then filled with 2 mL of the same buffer solution. Extruded liposomes (20 μL) were added to the chamber at room temperature (23 °C) to a final lipid concentration of 0.2 mM (providing a net lipid surface ~10^8 fold in excess than that required to cover the chamber's coverslip surface). The sample was incubated for a minimum of 60 min and then washed seven times with fresh buffer to remove unruptured or unadhered liposomes. A residual amount of buffer was left inside the chamber during washing to prevent disruption of the hydration layer separating the SLB and the surface. The final volume of the buffer solution inside the chamber was ~1.5 mL. Following the washing of excess, unruptured liposomes, the chamber was slowly annealed using a repurposed Bioptechs Objective Heater and Controller that was placed around the glass cylinder of the ECFM chamber. The temperature of the chamber was increased to 27 °C, 34 °C, and finally to 37 °C and incubated for 30 min at each temperature before the next increase. All measurements were conducted at 37 °C unless otherwise noted.

3.6.5. Microscopy setup

Fluorescence imaging was performed using an inverted Nikon Eclipse Ti microscope equipped with a Perfect Focus System (PFS) to compensate for axial drift. A widefield objective-based TIRF configuration was implemented with a Nikon TIRF illuminator and an oil immersion objective [Nikon CFI SR Apochromat TIRF 100×, numerical aperture (NA) = 1.49] with an effective pixel size of 160 nm. When specified, a lower magnification widefield microscopy setup equipped with an air immersion objective (Nikon CFI Apo VC 20×, NA = 0.75, effective pixel size of 800 nm) was used to image wider areas. A 488 nm laser was used to excite H_4BPMHC, and a 647 nm laser was used for DiD (Agilent MLC400B Monolithic laser combiner). The laser beam was cleaned up using a multiband excitation filter (ZET405/488/561/647×, Chroma Technology) and then coupled into the microscope objective using a multiband beam splitter (ZT405/488/561/647rpc, Chroma Technology). The fluorescence emission collected through the objective was spectrally filtered using a ZET405/488/561/647m emission filter (Chroma

Technology). Emission from H_4BPMHC was further cleaned using a 540/80× bandpass filter (Chroma Technology). Here, the emission filter was manually engaged when images were to be taken to visualize H_4BPMHC, following inspection of DiD.

Fluorescence time-lapse movies consisted of 16-bit, 512 × 512 pixels images with an exposure time of 100 ms per frame or 128 × 128 pixels images with an exposure time of 10 ms per frame (as specified in the text). Fluorescence emission was captured onto a 512 × 512 pixels region (acquiring at 10 frames/s) or a 128 × 128 pixels region (acquiring at 100 frames/s) of a back-illuminated electron-multiplying charge-coupled device (EMCCD) camera (iXon X3 DU-897-CS0-#BV, Andor Technology). The microscope was controlled through the NIS element software from Nikon. The camera was controlled using Micro-Manager Software (Micro-Manager 1.4.13, San Francisco, CA, USA).

3.6.6. ECFM measurements

The ECFM chamber was sealed with a septum pierced with an Ag/AgCl reference electrode (ALS Co., Ltd) and a platinum coil counter electrode. The sample was degassed with argon for a minimum of 40 min to ensure oxygen-free conditions, after which the sample was maintained under a cloud of argon. The electrochemical potential was applied using a CHI600D (CH Instruments) electrochemical analyzer and controlled through the CH Instruments electrochemical software (CHI Version 14.06). The potentials indicated are versus Ag/AgCl. Unless otherwise specified, potential step functions were applied for 5 s/step, and triangular potential functions were applied with a scan rate of 0.1 V/s. Image acquisition was initiated first, followed by the start of laser excitation to record the initial background fluorescence of the sample. Finally, the desired potential waveform was applied, and the fluorescence response to the applied potential was recorded.

Fluorescence movies were analyzed using Fiji/ImageJ software (ImageJ version 1.50e), and the timestamp of each frame was extracted using the "planeTimings.txt" macro from Bio-Formats written by Curtis Rueden. A screen recorder software (iSpring Free Cam 8) was used to accurately detect the fluorescence movie frame number corresponding to the start of the applied potential wave function, thus enabling the correlation of the time stamps extracted from fluorescence movies and electrochemical measurements.

3.6.7. Atomic Force Microscopy

AFM images were acquired using an Asylum MPF3D with a Molecular Force Probe 3D controller and performed under AC mode in air. The probes used were 160-AC-NA from MikroMash (k (nom): 26 N/m and f_o (nom): 300 kHz).

3.6.8. Computational method

DFT calculations were performed using the Gaussian 16 W package. HOMO and LUMO orbital energies were determined from molecular geometries optimized at the B3LYP 6-31G(d) level[48] with an applied polarizable continuum model solvation of acetonitrile. The molecular structures and orbitals were visualized using the GaussView 6.0 package. The molecular orbitals were assigned to the fluorophore or attached α-tocopherol segment as previously reported.[49]

3.7. Supplementary Information

3.7.1. Formation of and diffusion coefficient within ITO-supported lipid bilayers (SLB)

3.7.1.1. Formation of ITO-SLB

To achieve successful and reproducible formation of a well connected, planar supported lipid bilayer atop the ITO electrode, we found that the sample had to be slowly annealed and heated to a final temperature of 37 °C, where attempts to directly form the SLB at 37 °C resulted in the irreproducible and most often unsuccessful formation of an ITO-SLB, forming a supported vesicular layer (SVL) instead, made up of unruptured liposomes adhered to the ITO surface.

After addition of the extruded liposomes to the spectro-electrochemistry (SEC) chamber (see materials and methods for more details about liposome and SEC chamber formation), the liposomes were left to incubate in the chamber for 60 minutes, after which the chamber was washed at least 7 times with fresh buffer solution to remove any non-adhered and/or unruptured liposomes. The chamber was then heated sequentially to 27 °C, 34 °C and finally 37 °C, and left to incubate and equilibrate at each temperature for 30 minutes before the next increase in temperature. Experimental measurements mentioned in the manuscript were taken at 37 °C and only after 30 minutes had passed since the last annealing step. We found that sonication of

liposomes during the freeze/thaw cycles prior to extrusion is crucial for the successful formation of a SLB. Longer incubation time resulting from the slow annealing process is not the reason behind the successful formation of an SLB, as incubating the liposomes for an equal amount of time directly at 37 °C did not result in the formation of an SLB. Thus, the slow annealing and temperature increase is crucial to SLB formation atop an ITO electrode.

3.7.1.2. Extraction of diffusion coefficients from FRAP trajectories

To determine the membrane fluidity and connectivity throughout the SLB formation process, fluorescence recovery after photobleaching (FRAP) traces were taken at each temperature step (and only once the sample had been sitting at that temperature for 30 minutes) upon engaging an iris in the excitation path to photobleach a small area (approximated by a 13 μm diameter circle) in the field of view. Here we monitored DiD lateral diffusion within the resulting membrane (see **Figure 3.2b** for FRAP trajectories). DiD fluorophores (6.4 dye:10 000 lipid) present in the ~13 μm-diameter circular region were photobleached for 1 min with a 647 nm laser (3.7 mW at the exit of the objective once the iris is engaged) laser, after which the recovery of the DiD fluorescence signal was monitored over time. Partial or full recovery is indicative of a homogenous, well connected SLB, whereas a lack of recovery indicates the presence of a layer of unconnected and unruptured liposomes. Upon successful formation of an SLB, diffusion coefficients were extracted from the normalized FRAP trajectories using **Equation 3.4** below.[32, 53] Here, D is the lateral diffusion coefficient of DiD within the SLB, ω is the radius of the photobleached area, and $\tau_{1/2}$ is the time at which the fractional recovery curve $f_{(t)}$ is equal to ½.

$$D = \frac{0.224\omega^2}{\tau_{1/2}} \tag{3.4}$$

The fractional recovery curve is given by **Equation 3.5** below, where $I_{(t)}$ is the fluorescence intensity in the bleached sport at time t, I_0 is the fluorescence intensity of the first frame after photobleaching, and I_∞ is the long-time asymptote of the fluorescence recovery. All intensity values are normalized to the initial intensity pre-photobleaching. I_∞ was estimated by fitting the FRAP curves, normalized to the initial pre-bleaching intensity (such as the ones shown in **Figure 3.2b**), to a mono exponential growth function with a rate constant k, see **Equation 3.6**:

$$f_{(t)} = \frac{I_{(t)} - I_0}{I_\infty - I_0} \tag{3.5}$$

$$\frac{I_\infty - I_{(t)}}{I_\infty - I_0} = e^{-kt} \tag{3.6}$$

Table 3.2 below lists the average diffusion coefficients obtained on ITO and glass surfaces at different temperatures.

Table 3.2. Diffusion coefficients extracted from FRAP trajectories at different temperatures.

Sample	Diffusion coefficient ($\mu m^2 s^{-1}$)
Glass at 23 °C	0.20 ± 0.02
Glass at 37 °C	0.23 ± 0.05
ITO at 37 °C	0.34 ± 0.11
ITO at 34 °C	0.18 ± 0.06
ITO at 27 °C	N/A
ITO at 23 °C	N/A

The sample was formed at 23 ℃ and then heated sequentially to 27℃, 34℃, and finally to 37℃. The resulting lipid membrane was characterized at each temperature step during initial experiments aimed at optimizing SLB formation, and only at the final temperature (37 °C) in later experiments. Values and errors correspond to averages and standard deviations extracted from multiple samples. N=10 for glass samples at 37 °C, N=12 for ITO samples at 37 °C, and N=3 for all other samples.

3.7.2. Calculation of homo-Förster Resonance Energy Transfer (homo-FRET) radius

The homo-FRET radius of energy transfer within H_4BPMHC molecules was calculated using the conventional FRET equation (**Equation 3.7)** with H_4BPMHC being both the donor and the acceptor in this case.

$$R_0 = \left(\Phi_f^D \kappa^2 \left(\frac{9000(\ln 10)}{128\pi^5 N_A n^4}\right) J_{(\lambda)}\right)^{\frac{1}{6}} \quad (3.7)$$

Here, R_0 is the intermolecular distance at which the excited donor transfers its energy to the acceptor with a 50% efficiency, Φ_f^D is the fluorescence quantum yield of the donor, κ^2 is a dipole orientation factor equal to 2/3 for a freely tumbling molecule, N_A is Avogadro's number, n the refractive index of the medium, and $J(\lambda)$ the spectral overlap integral between the donor and acceptor. The overlap integral was calculated from the absorbance spectrum of the acceptor and the emission spectrum of the donor using **Equation 3.8** below[54]. Here $\varepsilon_A(\lambda)$ is the extinction coefficient of the acceptor at wavelength λ and $F_D(\lambda)$ the fluorescence intensity of the donor at wavelength λ, with the area under the emission spectrum of the donor being normalized to 1 and corrected for the detector sensitivity. In our case, $\Phi_f^D = 0.94$ (quantum yield of the BODIPY fluorophore with a methyl in the meso position instead of a PMHC ring)[27], *n* is the refractive index of water (*n* = 1.333), and a value of 2/3 was used for κ^2 for ease of calculation even though the dye is not freely tumbling when embedded within lipid membranes. Using **equations 3.7** and **3.8** and the above-mentioned values, we obtained a homo-FRET radius of 5.40 nm for the energy transfer between neighboring H_4BPMHC molecules.

$$J_{(\lambda)} = \int \varepsilon_{A(\lambda)}(\lambda) F_{D(\lambda)} \lambda^4 d\lambda \quad (3.8)$$

3.7.3. Calculation of minimal current measured with SEC system

To estimate the conversion from fluorescence intensity-time trajectories obtained with our SEC system to an equivalent charge current-time we utilized **Equation 3.9** below. Here, *i* is the estimated current and *t* is the time required to reach maximum enhancement of H_4BPMHC under our experimental conditions (~0.1 s). *C* is the total collected charge in coulombs, equal to the product of the number of electrons transferred/molecule (*n*), the elementary charge ($e = 1.6 \times 10^{-19}$ C) and the total number of oxidized molecules (N_{probe}).

$$i = \frac{C}{t} = \frac{n \times e \times N_{probe}}{t} \quad (3.9)$$

In our case, the smallest loading of probes to lipid oxidized in a field of view was 0.26 probe : 100 lipids. Here the area of the field of view of 128 × 128 pixels is ~419 μm^2 when utilizing a 100× magnification objective. Considering an average lipid head group area of 0.8 nm^2, a 419 μm^2 area bearing a supported lipid bilayer would contain 419 μm^2/ (8×10^{-7} μm^2) = 5.25×10^{10} lipids and N_{probe} = 1.37×10^6 molecules of H_4BPMHC per leaflet, where only probes located in the lower leaflet are expected to be electroactive. Inserting the above numbers into **Equation 3.9** results in an equivalent current of 4.3 pA. However, the measured fluorescence intensity-time trajectory used to estimate this current is of very large signal-to-background ratio despite the very low probe concentration (see **Figure 3.4b**, black trace for the used trajectory). This high sensitivity theoretically enables us to accurately detect the oxidation of a much smaller amount of dye, down to a diffraction limited - 300 nm diameter circle - 0.07 μm^2 area, a ~6,000-fold lower N_{probe} amount and associated current. As a test, extracting the fluorescence signal of H_4BPMHC from a 2 × 2 pixels region (as opposed to from the entire 128 × 128 pixels FOV mentioned above) as a rough estimate of a diffraction limited spot, we are still able to detect the oxidation peak of H_4BPMHC with remarkable accuracy (see associated **Figure 3.12** below). Following the same calculations listed above but for a 2 × 2 pixels region, we find that the fluorescence signal shown in **Figure 3.12** is equivalent to a current of ~1 femtoampere.

3.7.4. Determining rate constants of H_4BPMHC oxidation and subsequent ring opening

The electrochemical oxidation and hydration of H_4BPMHC to H_4BPMHC_{hem}, and its subsequent chemical rearrangement (ring opening) of the latter to form H_4BPMHC_{qui} follow first order kinetics when under a potential step function. The transition from H_4BPMHC to H_4BPMHC_{qui} follows thus the consecutive first order reaction scheme below, where k_{ox} is the rate constant of oxidation of H_4BPMHC to H_4BPMHC_{hem}, and k_{op} is the rate constant of the ring opening of H_4BPMHC_{hem}, forming H_4BPMHC_{qui}.

$$H_4BMPHC \xrightarrow{k_{ox}} H_4BMPHC_{hem} \xrightarrow{k_{op}} H_4BMPHC_{qui} \tag{3.10}$$

Subsequently, the rate expressions for each of the species would be as follows:

$$\frac{d[H_4BMPHC]}{dt} = -k_{ox}[H_4BMPHC] \quad (3.11)$$

$$\frac{d[H_4BMPHC_{hem}]}{dt} = k_{ox}[H_4BMPHC] - k_{op}[H_4BMPHC_{hem}] \quad (3.12)$$

$$\frac{d[H_4BMPHC_{qui}]}{dt} = k_{op}[H_4BMPHC_{hem}] \quad (3.13)$$

Equations 3.11-3.13 can be easily integrated to obtain the concentration of each species as a function of time. Taking under consideration that only H_4BPMHC is initially present, the time dependence of [H_4BPMHC] can be expressed as:

$$[H_4BMPHC] = [H_4BMPHC]_0 e^{-k_{ox}t} \quad (3.14)$$

Equation 3.14 can be substituted into **Equation 3.12**, yielding:

$$\frac{d[H_4BMPHC_{hem}]}{dt} = k_{ox}[H_4BMPHC]_0 e^{-k_{ox}t} - k_{op}[H_4BMPHC_{hem}] \quad (3.15)$$

An expression for the time dependence of [H_4BPMHC_{hem}] is obtained by solving the differential equation above, yielding:

$$[H_4BMPHC_{hem}] = \frac{k_{ox}}{k_{op} - k_{ox}}\left(e^{-k_{ox}t} - e^{-k_{op}t}\right)[H_4BMPHC]_0 \quad (3.16)$$

Given that H_4BPMHC is the only species initially present, we can write:

$$[H_4BMPHC]_0 = [H_4BMPHC] + [H_4BMPHC_{hem}] + [H_4BMPHC_{qui}] \quad (3.17)$$

$$[H_4BMPHC_{qui}] = [H_4BMPHC]_0 - [H_4BMPHC] - [H_4BMPHC_{hem}] \quad (3.18)$$

Substituting **equation 3.14** and **3.16** into **Equation 3.18** yields the following expression:

$$\left[H_4BMPHC_{qui}\right] = \left(1 + \frac{k_{ox}e^{-k_{op}t} - k_{op}e^{-k_{ox}t}}{k_{op} - k_{ox}}\right)[H_4BMPHC]_0 \quad (3.19)$$

Since H_4BPMHC_{hem} and H_4BPMHC_{qui} are the only emissive species during the first oxidative potential step, the fluorescence intensity obtained during this step is the sum of the fluorescence emission arising of these two species. By combining **equations 3.16** and **3.19**, we obtain the following expression for the time dependence of the total intensity upon applying the first oxidative pulse (**equation 3.1** in the manuscript).

$$I_{(t)} = I_0 + \frac{k_{ox}}{k_{op} - k_{ox}}\left(e^{-k_{ox}t} - e^{-k_{op}t}\right)I_{max} + c \times \left(1 + \frac{k_{ox}e^{-k_{op}t} - k_{op}e^{-k_{ox}t}}{k_{op} - k_{ox}}\right)I_{max} \quad (3.20)$$

Here, $[H_4BPMHC]_0$ is replaced by I_{max}, the theoretical intensity contribution of H_4BPMHC at t=0 if it was fully emissive instead of quenched. I_{max} also represents the theoretical fluorescence intensity that would have been gained upon formation of H_4BPMHC_{hem}, if the later did not further decay into H_4BPMHC_{qui} (i.e., at $t=\infty$ and if $k_{op}=0$). The fluorescence contribution of H_4BPMHC_{qui} was multiplied by a factor c ($0 < c < 1$) to account for the fact that H_4BPMHC_{qui} is only partially emissive and does not contribute to the total intensity to the same extent as the fully emissive H_4BPMHC_{hem}. The factor c is equal to the ratio of the quantum yield of H_4BPMHC_{qui} to that of H_4BPMHC_{hem}. Finally, a factor I_0 is added to account for the initial "pre-pulse" fluorescence intensity arising from the intrinsic background intensity of the system.

Equation 3.20 was used to fit the fluorescence signal obtained during the first applied oxidative step to extract the rate constants k_{ox} and k_{op} shown in **Table 3.1** and **Figure 3.13**.

3.7.5. Supplementary figures

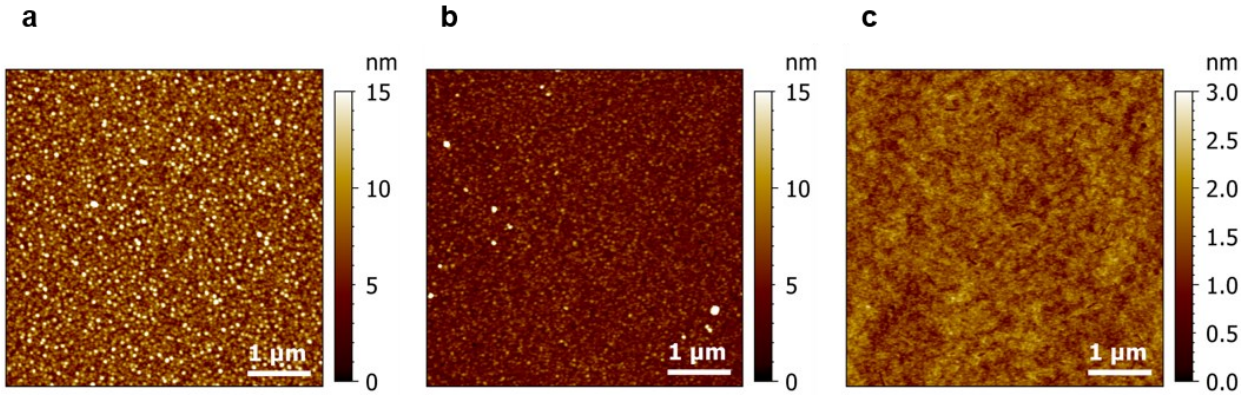

Figure 3.7. Atomic force microscopy images (5 µm^2) of dry surfaces of: ITO-coated surface (a), the interface between glass and ITO (b), and of bare glass surface (c). Scale bar = 1 µm.

AFM measurements show a smooth surface morphology of bare glass (Rq = 0.294 nm) and a granular, rough surface morphology of ITO-coated surfaces (Rq = 2.556 nm). The interface between glass and ITO surfaces shows a granular morphology (Rq = 1.753 nm) akin to ITO, however much less pronounced.

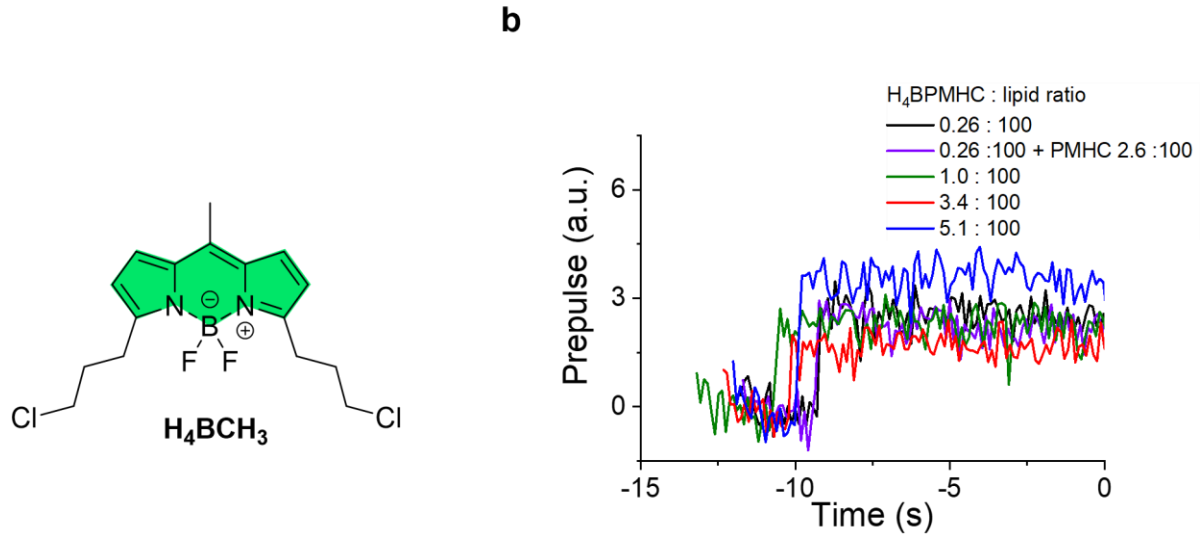

Figure 3.8. (a) Structure of control dye, H_4BCH_3, that lacks a PMHC segment and P*e*T mechanism and is thus always fluorescent. (b) Fluorescence (prepulse) intensity of H_4BPMHC prior to applying any potential function, acquired at varying H_4BPMHC and antioxidant (PMHC) concentrations. Values listed in figure legend correspond to number of molecules per 100 lipids.

Data acquired at 100 frames/s and rebinned to 10 frames/s. Time 0 s corresponds to the start of the applied potential. Samples were excited with a 488 nm, 5μW (at the exit of the objective), CW laser.

The recorded pre-pulse intensities of the different membrane embedded H_4BPMHC samples showed minimal differences despite a 50-fold increase in H_4BPMHC:lipid ratio between the lowest and highest dye loading samples. This indicates that the recorded initial prepulse intensity is independent of dye concentration, and is instead arising from the intrinsic background of the SEC system.

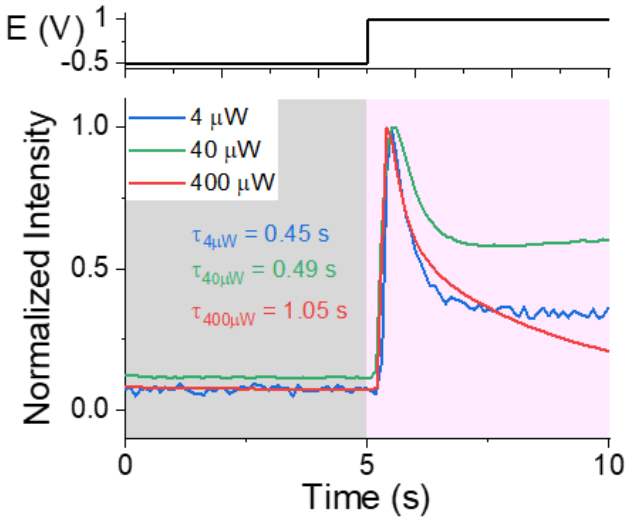

Figure 3.9. Fluorescence response of H_4BPMHC to the applied potential square function (reduction at -0.5 V, grey shaded area, followed by oxidation at 1 V, pink shaded area) with increasing 488 nm excitation power (4 μW, 40 μW, and 400 μW). Data acquired at 10 frames/s. H_4BPMHC to lipid ratio is 0.26 dye/100 lipid. Time 0 s corresponds to the start of the applied potential.

Fluorescence decay lifetimes were extracted from fitting the decay section of the curves to a monoexponential decay function. The extracted decay lifetimes were 0.45 s, 0.49 s and 1.05 s at excitation powers of 4 μW, 40 μW, and 400 μW respectively. The fact that the decay lifetimes/rates do not scale with excitation power is indicative that the observed decay following the first oxidation step is not a result of photobleaching or any other photoinduced process.

Table 3.3. Calculated HOMO and LUMO energy levels of BODIPY fluorophore and oxidation products of PMHC

	α-tocopherol product		BODIPY	
	E_{HOMO} (eV)	E_{LUMO} (eV)	E_{HOMO} (eV)	E_{LUMO} (eV)
H_4BPMHC	-5.25	0.02	-5.78	-2.77
H_4BPMHC$_{hem}$	-6.69	-1.89	-5.78	-2.78
H_4BPMHC$_{qui}$	-6.89	-3.12	-5.76	-2.75
H_4BPMHC$_{hydroqui}$	-5.33	0.02	-5.76	-2.74

DFT calculations were performed on the structures shown in **Figure 3.5d,** and the values correspond to the ones plotted in **Figure 3.6**. HOMO and LUMO orbital energies were determined from molecular geometries optimized at the B3LYP 6-31G(d) level[48] with an applied polarizable continuum model solvation of acetonitrile. Molecular orbitals were assigned to the fluorophore or attached α-tocopherol segment as previously reported.[49]

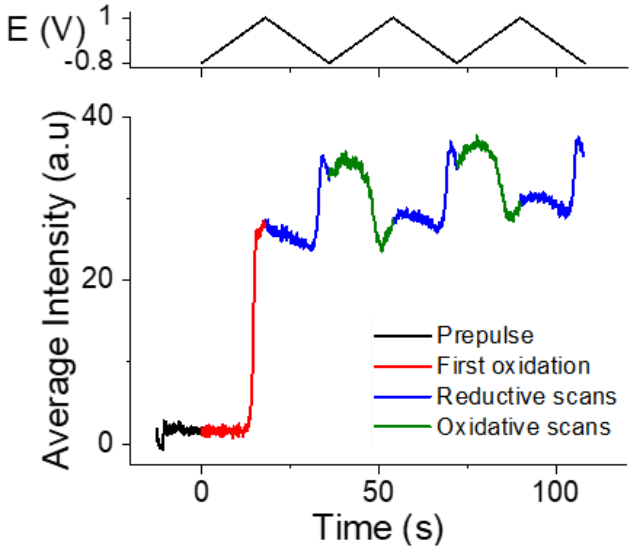

Figure 3.10. Fluorescence response of membrane-embedded H_4BPMHC (3.4 : 100 lipid) to applied triangular wave functions, plotted as intensity vs time traces. This data was used to reconstruct **Figure 3.5a**. The first oxidation scan corresponding to the oxidation and the rearrangement to H_4BPMHC$_{qui}$ is highlighted in red. The reversible reduction of H_4BPMHC$_{qui}$ to

$H_4BPMHC_{hydroqui}$ and the subsequent oxidation of the latter back to H_4BPMHC_{qui} are highlighted in blue and green, respectively. The applied potential was linearly swept between -0.8 V and 1V with a scan rate of 0.1 V/s. Time 0 s corresponds to the start of the applied potential. The sample was excited with a 488 nm (5 µW at the exit of the objective) CW laser.

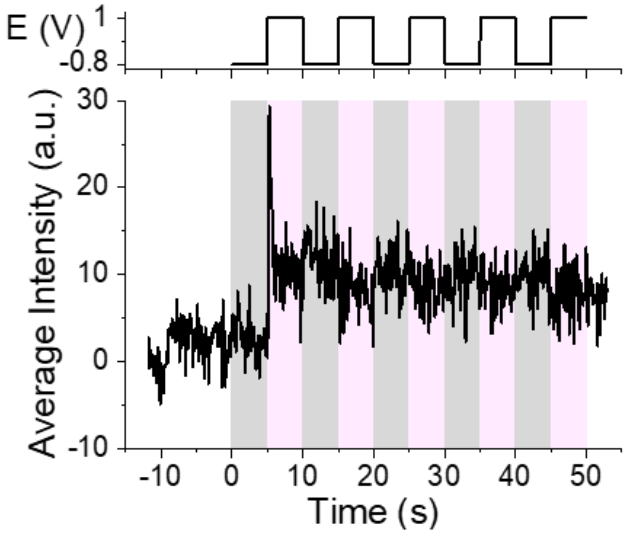

Figure 3.11. Fluorescence response of membrane-embedded H_4BPMHC (0.26:100 dye:lipid mole ratio) in a 2×2 pixels field of view, to an applied electrochemical potential square wave (alternating 5 second steps of reductive (-0.8 V, grey) and oxidative (1 V, pink) potentials). λ_{ex} = 488 nm; 100 frames/s acquisition frequency rebinned to 10 frames/s. Time 0 s corresponds to the start of the applied potential.

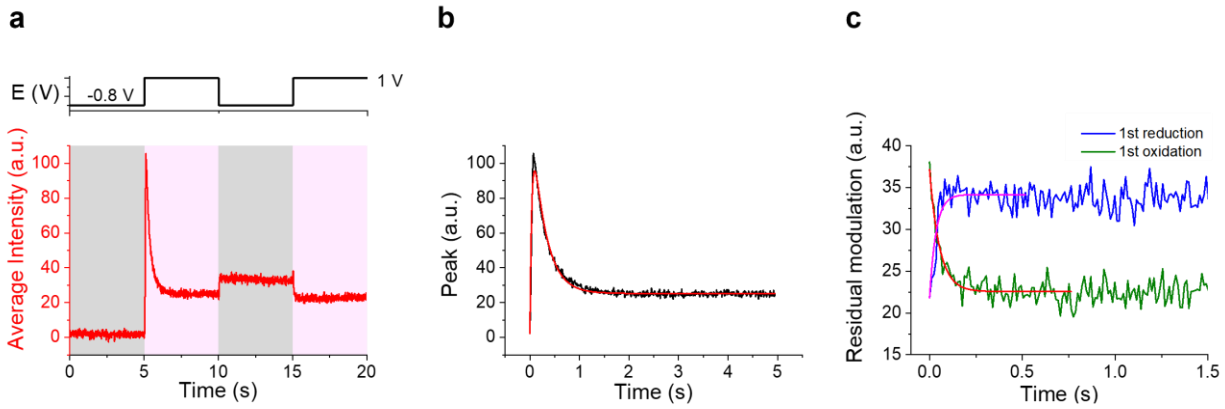

Figure 3.12. Fitting the H_4BPMHC fluorescence response to applied potentials to extract rate constant of transitions undergone by H_4BPMHC upon its oxidation. (a) 5 second steps of -0.8 V (grey areas) or 1 V (pink areas) were applied. Time 0 s corresponds to the start of potential application. (b) Experimental data (black curve) and fitting (red curve) of the fluorescence response of H_4BPMHC to the first oxidative step (time 5-10s in panel a). (c) Experimental data

(blue and green curves) and exponential fit (pink and red curves) of the fluorescence response of the resulting quinone and dihydroquinone forms of H_4BPMHC to the applied reductive and oxidative potentials (time 10-20s in panel a). Time 0 s on panels b and c corresponds to the start of potential application of each potential step. Data acquired at 100 frames/s. The sample was excited with a 488 nm, 5 µW (at the exit of the objective) cw laser. Membrane loading used is 1 dye : 100 lipids.

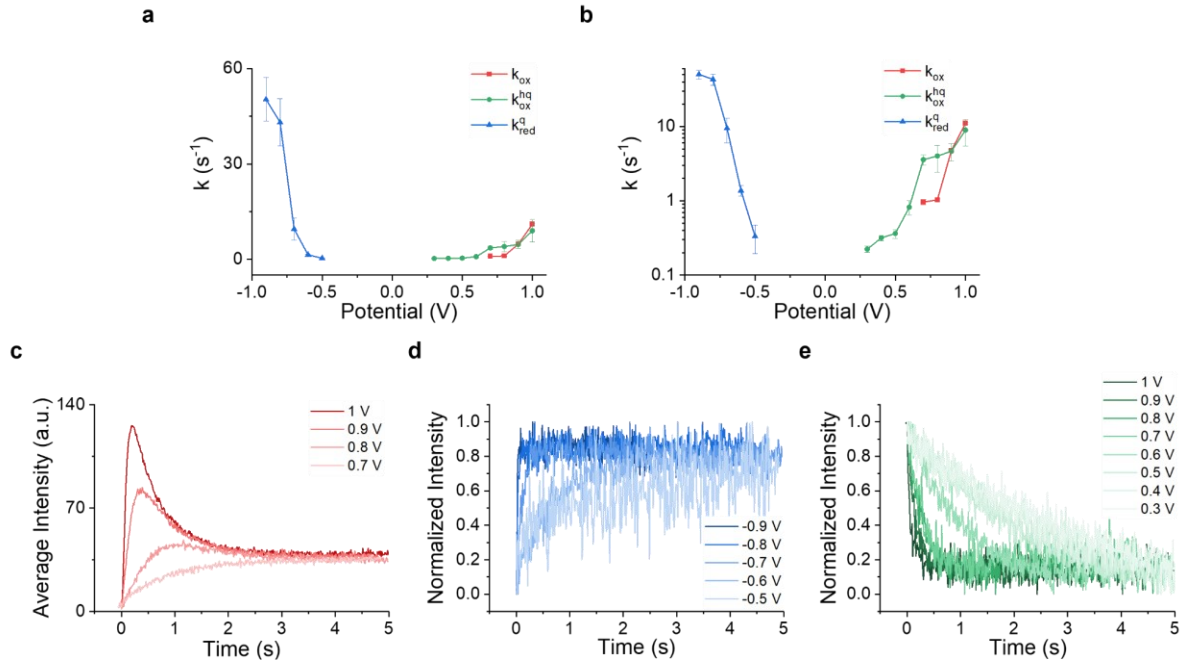

Figure 3.13. Potential dependence of the extracted rate constants of the transitions undergone by H_4BPMHC upon its oxidation. The fluorescence response of H_4BPMHC, H_4BPMHC$_{qui}$, and H_4BPMHC$_{hydroqui}$ was measured under varying applied potentials steps (5s vs Ag/AgCl) and used to extract the rate constants of the transitions undergone by these molecules, namely the oxidation of H_4BPMHC to H_4BPMHC$_{hem}$ (k_{ox}, black traces), the reduction of H_4BPMHC$_{qui}$ to H_4BPMHC$_{hydroqui}$ (k^q_{red}, red traces), and the oxidation of the latter back to H_4BPMHC$_{qui}$ (k^{hq}_{ox}, blue traces). The extracted rate constants are plotted as a function of applied potential under linear (a) and logarithmic (b) scales. (c-e) Intensity-time trajectories depicting the response to various applied potential of (c) H_4BPMHC, (d) H_4BPMHC$_{qui}$, and (e) H_4BPMHC$_{hydroqui}$. Data acquired at 100 frames/s. The sample was excited with a 488 nm, 5 µW (at the exit of the objective) cw laser. Membrane loading used is 3.4 dye : 100 lipids. Data points and error bars of k^q_{red} and k^{hq}_{ox} correspond to the average and standard deviation of 5 fitted traces (10 traces for k^{hq}_{ox} at -0.8V). Since the oxidation of H_4BPMHC is irreversible, only one trace per potential was obtained, and the error bars correspond to the error obtained from the fitting.

3.8. References

1. Zhang, Z.; Huang, L.; Shulmeister, V. M.; Chi, Y.-I.; Kim, K. K.; Hung, L.-W.; Crofts, A. R.; Berry, E. A.; Kim, S.-H., Electron transfer by domain movement in cytochrome bc1. *Nature* **1998,** *392* (6677), 677-684.
2. Umena, Y.; Kawakami, K.; Shen, J.-R.; Kamiya, N., Crystal structure of oxygen-evolving photosystem II at a resolution of 1.9 Å. *Nature* **2011,** *473* (7345), 55-60.
3. Vos, M.; Esposito, G.; Edirisinghe Janaka, N.; Vilain, S.; Haddad Dominik, M.; Slabbaert Jan, R.; Van Meensel, S.; Schaap, O.; De Strooper, B.; Meganathan, R.; Morais Vanessa, A.; Verstreken, P., Vitamin K2 Is a Mitochondrial Electron Carrier That Rescues Pink1 Deficiency. *Science* **2012,** *336* (6086), 1306-1310.
4. Dowd, P.; Ham, S.-W.; Naganathan, S.; Hershline, R., The Mechanism of Action of Vitamin K. *Annu. Rev. Nutr.* **1995,** *15* (1), 419-440.
5. Coates, C. S.; Ziegler, J.; Manz, K.; Good, J.; Kang, B.; Milikisiyants, S.; Chatterjee, R.; Hao, S.; Golbeck, J. H.; Lakshmi, K. V., The Structure and Function of Quinones in Biological Solar Energy Transduction: A Cyclic Voltammetry, EPR, and Hyperfine Sub-Level Correlation (HYSCORE) Spectroscopy Study of Model Naphthoquinones. *J. Phys. Chem. B* **2013,** *117* (24), 7210-7220.
6. Tappel, A. L.; Zalkin, H., Inhibition of Lipid Peroxidation in Microsomes by Vitamin E. *Nature* **1960,** *185* (4705), 35-35.
7. Cummings, M. J.; Mattill, H. A., The Auto-Oxidation of Fats with Reference to Their Destructive Effect on Vitamin E. *J. Nutr.* **1931,** *3* (4), 421-432.
8. Niki, E., Role of vitamin E as a lipid-soluble peroxyl radical scavenger: in vitro and in vivo evidence. *Free Radical Biol. Med.* **2014,** *66*, 3-12.
9. Infante, J. P., A function for the vitamin E metabolite α-tocopherol quinone as an essential enzyme cofactor for the mitochondrial fatty acid desaturases. *FEBS Lett.* **1999,** *446* (1), 1-5.
10. Hinman, A.; Holst, C. R.; Latham, J. C.; Bruegger, J. J.; Ulas, G.; McCusker, K. P.; Amagata, A.; Davis, D.; Hoff, K. G.; Kahn-Kirby, A. H.; Kim, V.; Kosaka, Y.; Lee, E.; Malone, S. A.; Mei, J. J.; Richards, S. J.; Rivera, V.; Miller, G.; Trimmer, J. K.; Shrader, W. D., Vitamin E hydroquinone is an endogenous regulator of ferroptosis via redox control of 15-lipoxygenase. *PLOS ONE* **2018,** *13* (8), e0201369.
11. Tan, Y. S.; Chen, S.; Hong, W. M.; Kan, J. M.; Kwek, E. S. H.; Lim, S. Y.; Lim, Z. H.; Tessensohn, M. E.; Zhang, Y.; Webster, R. D., The role of low levels of water in the electrochemical oxidation of α-tocopherol (vitamin E) and other phenols in acetonitrile. *PCCP* **2011,** *13* (28), 12745-12754.
12. Everitt, C. T.; Haydon, D. A., Electrical capacitance of a lipid membrane separating two aqueous phases. *J. Theor. Biol.* **1968,** *18* (3), 371-379.
13. Monajjemi, M., Cell membrane causes the lipid bilayers to behave as variable capacitors: A resonance with self-induction of helical proteins. *Biophys. Chem.* **2015,** *207*, 114-127.
14. Engstrom, R. C.; Ghaffari, S.; Qu, H., Fluorescence imaging of electrode-solution interfacial processes. *Anal. Chem.* **1992,** *64* (21), 2525-2529.
15. Palacios, R. E.; Fan, F.-R. F.; Bard, A. J.; Barbara, P. F., Single-Molecule Spectroelectrochemistry (SMS-EC). *J. Am. Chem. Soc.* **2006,** *128* (28), 9028-9029.
16. Miomandre, F.; Lépicier, E.; Munteanu, S.; Galangau, O.; Audibert, J. F.; Méallet-Renault, R.; Audebert, P.; Pansu, R. B., Electrochemical Monitoring of the Fluorescence Emission of

Tetrazine and Bodipy Dyes Using Total Internal Reflection Fluorescence Microscopy Coupled to Electrochemistry. *ACS Appl. Mater. Interfaces* **2011,** *3* (3), 690-696.
17. Lei, C.; Hu, D.; Ackerman, E. J., Single-molecule fluorescence spectroelectrochemistry of cresyl violet. *Chem. Commun.* **2008,** (43), 5490-5492.
18. Godin, R.; Cosa, G., Counting Single Redox Turnovers: Fluorogenic Antioxidant Conversion and Mass Transport Visualization via Single Molecule Spectroelectrochemistry. *J. Phys. Chem. C* **2016,** *120* (28), 15349-15353.
19. Fan, Y.; Hao, R.; Han, C.; Zhang, B., Counting Single Redox Molecules in a Nanoscale Electrochemical Cell. *Anal. Chem.* **2018,** *90* (23), 13837-13841.
20. Fan, S.; Webb, J. E. A.; Yang, Y.; Nieves, D. J.; Gonçales, V. R.; Tran, J.; Hilzenrat, G.; Kahram, M.; Tilley, R. D.; Gaus, K.; Gooding, J. J., Observing the Reversible Single Molecule Electrochemistry of Alexa Fluor 647 Dyes by Total Internal Reflection Fluorescence Microscopy. *Angew. Chem. Int. Ed.* **2019,** *58* (41), 14495-14498.
21. Saini, A.; Messenger, H.; Kisley, L., Fluorophores "Turned-On" by Corrosion Reactions Can Be Detected at the Single-Molecule Level. *ACS Appl. Mater. Interfaces* **2021,** *13* (1), 2000-2006.
22. Bizzotto, D., In situ spectroelectrochemical fluorescence microscopy for studying electrodes modified by molecular adsorbates. *Curr. Opin. Electrochem.* **2018,** *7*, 161-171.
23. Bowyer, W. J.; Xie, J.; Engstrom, R. C., Fluorescence Imaging of the Heterogeneous Reduction of Oxygen. *Anal. Chem.* **1996,** *68* (13), 2005-2009.
24. Bouffier, L.; Doneux, T., Coupling electrochemistry with in situ fluorescence (confocal) microscopy. *Curr. Opin. Electrochem.* **2017,** *6* (1), 31-37.
25. Oleynik, P.; Ishihara, Y.; Cosa, G., Design and Synthesis of a BODIPY-α-Tocopherol Adduct for Use as an Off/On Fluorescent Antioxidant Indicator. *J. Am. Chem. Soc.* **2007,** *129* (7), 1842-1843.
26. Krumova, K.; Friedland, S.; Cosa, G., How Lipid Unsaturation, Peroxyl Radical Partitioning, and Chromanol Lipophilic Tail Affect the Antioxidant Activity of α-Tocopherol: Direct Visualization via High-Throughput Fluorescence Studies Conducted with Fluorogenic α-Tocopherol Analogues. *J. Am. Chem. Soc.* **2012,** *134* (24), 10102-10113.
27. Greene, L. E.; Lincoln, R.; Cosa, G., Rate of Lipid Peroxyl Radical Production during Cellular Homeostasis Unraveled via Fluorescence Imaging. *J. Am. Chem. Soc.* **2017,** *139* (44), 15801-15811.
28. Greene, L. E.; Lincoln, R.; Cosa, G., Spatio-temporal monitoring of lipid peroxyl radicals in live cell studies combining fluorogenic antioxidants and fluorescence microscopy methods. *Free Radical Biol. Med.* **2018,** *128*, 124-136.
29. Godin, R.; Palacios, R. E.; Cosa, G., Heterogeneous Charge Mobility in Individual Conjugated Polyelectrolyte Nanoparticles Revealed by Two-Color Single Particle Spectroelectrochemistry Studies. *J. Phys. Chem. C* **2015,** *119* (23), 12875-12886.
30. Keller, C. A.; Kasemo, B., Surface Specific Kinetics of Lipid Vesicle Adsorption Measured with a Quartz Crystal Microbalance. *Biophys. J.* **1998,** *75* (3), 1397-1402.
31. Reimhult, E.; Höök, F.; Kasemo, B., Intact Vesicle Adsorption and Supported Biomembrane Formation from Vesicles in Solution: Influence of Surface Chemistry, Vesicle Size, Temperature, and Osmotic Pressure. *Langmuir* **2003,** *19* (5), 1681-1691.
32. Axelrod, D.; Koppel, D. E.; Schlessinger, J.; Elson, E.; Webb, W. W., Mobility measurement by analysis of fluorescence photobleaching recovery kinetics. *Biophys. J.* **1976,** *16* (9), 1055-1069.
33. Wu, E.; Jacobson, K.; Papahadjopoulos, D., Lateral diffusion in phospholipid multibilayers measured by fluorescence recovery after photobleaching. *Biochemistry* **1977,** *16* (17), 3936-3941.

34. Verkman, A. S., Diffusion in cells measured by fluorescence recovery after photobleaching. In *Methods Enzymol.*, Academic Press: 2003; Vol. 360, pp 635-648.
35. Richter, R. P.; Bérat, R.; Brisson, A. R., Formation of Solid-Supported Lipid Bilayers: An Integrated View. *Langmuir* **2006,** *22* (8), 3497-3505.
36. Kılıç, A.; Fazeli Jadidi, M.; Özer, H. Ö.; Kök, F. N., The effect of thiolated phospholipids on formation of supported lipid bilayers on gold substrates investigated by surface-sensitive methods. *Colloids Surf. B. Biointerfaces* **2017,** *160*, 117-125.
37. Kaufmann, M.; Jia, Y.; Werner, C.; Pompe, T., Weakly Coupled Lipid Bilayer Membranes on Multistimuli-Responsive Poly(N-isopropylacrylamide) Copolymer Cushions. *Langmuir* **2011,** *27* (2), 513-516.
38. Seu, K. J.; Pandey, A. P.; Haque, F.; Proctor, E. A.; Ribbe, A. E.; Hovis, J. S., Effect of Surface Treatment on Diffusion and Domain Formation in Supported Lipid Bilayers. *Biophys. J.* **2007,** *92* (7), 2445-2450.
39. Zhang, Y.; Li, Q.; Dong, M.; Han, X., Effect of cholesterol on the fluidity of supported lipid bilayers. *Colloids Surf. B. Biointerfaces* **2020,** *196*, 111353.
40. Štefl, M.; Kułakowska, A.; Hof, M., Simultaneous Characterization of Lateral Lipid and Prothrombin Diffusion Coefficients by Z-Scan Fluorescence Correlation Spectroscopy. *Biophys. J.* **2009,** *97* (3), L1-L3.
41. Godin, R.; Liu, H.-W.; Smith, L.; Cosa, G., Dye Lipophilicity and Retention in Lipid Membranes: Implications for Single-Molecule Spectroscopy. *Langmuir* **2014,** *30* (37), 11138-11146.
42. Marquardt, D.; Williams, J. A.; Kučerka, N.; Atkinson, J.; Wassall, S. R.; Katsaras, J.; Harroun, T. A., Tocopherol Activity Correlates with Its Location in a Membrane: A New Perspective on the Antioxidant Vitamin E. *J. Am. Chem. Soc.* **2013,** *135* (20), 7523-7533.
43. Takahashi, M.; Tsuchiya, J.; Niki, E., Scavenging of radicals by vitamin E in the membranes as studied by spin labeling. *J. Am. Chem. Soc.* **1989,** *111* (16), 6350-6353.
44. Barclay, L. R. C., 1992 Syntex Award Lecture Model biomembranes: quantitative studies of peroxidation, antioxidant action, partitioning, and oxidative stress. *Can. J. Chem.* **1993,** *71* (1), 1-16.
45. Wei Yao, W.; Mei Peng, H.; Webster, R. D., Electrochemistry of α-Tocopherol (Vitamin E) and α-Tocopherol Quinone Films Deposited on Electrode Surfaces in the Presence and Absence of Lipid Multilayers. *J. Phys. Chem. C* **2009,** *113* (52), 21805-21814.
46. Wain, A. J.; Wadhawan, J. D.; France, R. R.; Compton, R. G., Biphasic redox chemistry of α-tocopherol: Evidence for electrochemically induced hydrolysis and dimerization on the surface of and within femtolitre droplets immobilized onto graphite electrodes. *PCCP* **2004,** *6* (4), 836-842.
47. Yao, W. W.; Lau, C.; Hui, Y.; Poh, H. L.; Webster, R. D., Electrode-Supported Biomembrane for Examining Electron-Transfer and Ion-Transfer Reactions of Encapsulated Low Molecular Weight Biological Molecules. *J. Phys. Chem. C* **2011,** *115* (5), 2100-2113.
48. Frisch, M. J.; Trucks, G. W.; Schlegel, H. B.; Scuseria, G. E.; Robb, M. A.; Cheeseman, J. R.; Scalmani, G.; Barone, V.; Petersson, G. A.; Nakatsuji, H.; Li, X.; Caricato, M.; Marenich, A. V.; Bloino, J.; Janesko, B. G.; Gomperts, R.; Mennucci, B.; Hratchian, H. P.; Ortiz, J. V.; Izmaylov, A. F.; Sonnenberg, J. L.; Williams; Ding, F.; Lipparini, F.; Egidi, F.; Goings, J.; Peng, B.; Petrone, A.; Henderson, T.; Ranasinghe, D.; Zakrzewski, V. G.; Gao, J.; Rega, N.; Zheng, G.; Liang, W.; Hada, M.; Ehara, M.; Toyota, K.; Fukuda, R.; Hasegawa, J.; Ishida, M.; Nakajima, T.; Honda, Y.; Kitao, O.; Nakai, H.; Vreven, T.; Throssell, K.; Montgomery Jr., J.

A.; Peralta, J. E.; Ogliaro, F.; Bearpark, M. J.; Heyd, J. J.; Brothers, E. N.; Kudin, K. N.; Staroverov, V. N.; Keith, T. A.; Kobayashi, R.; Normand, J.; Raghavachari, K.; Rendell, A. P.; Burant, J. C.; Iyengar, S. S.; Tomasi, J.; Cossi, M.; Millam, J. M.; Klene, M.; Adamo, C.; Cammi, R.; Ochterski, J. W.; Martin, R. L.; Morokuma, K.; Farkas, O.; Foresman, J. B.; Fox, D. J. *Gaussian 16 Rev. A.03*, Wallingford, CT, 2016.
49. Greene, L. E.; Lincoln, R.; Cosa, G., Tuning Photoinduced Electron Transfer Efficiency of Fluorogenic BODIPY-α-Tocopherol Analogues. *Photochem. Photobiol.* **2019,** *95* (1), 192-201.
50. Zoski, C. G., Review—Advances in Scanning Electrochemical Microscopy (SECM). *J. Electrochem. Soc.* **2015,** *163* (4), H3088-H3100.
51. Kai, T.; Zoski, C. G.; Bard, A. J., Scanning electrochemical microscopy at the nanometer level. *Chem. Commun.* **2018,** *54* (16), 1934-1947.
52. Neužil, J.; Witting, P. K.; Stocker, R., α-Tocopheryl hydroquinone is an efficient multifunctional inhibitor of radical-initiated oxidation of low density lipoprotein lipids. *Proc. Natl. Acad. Sci. U.S.A.* **1997,** *94* (15), 7885-7890.
53. Soumpasis, D. M., Theoretical analysis of fluorescence photobleaching recovery experiments. *Biophys. J.* **1983,** *41* (1), 95-97.
54. Energy Transfer. In *Principles of Fluorescence Spectroscopy*, Lakowicz, J. R., Ed. Springer US: Boston, MA, 2006; pp 443-475.

Chapter 4

$^1O_2$-mediated remodeling of supported lipid membranes

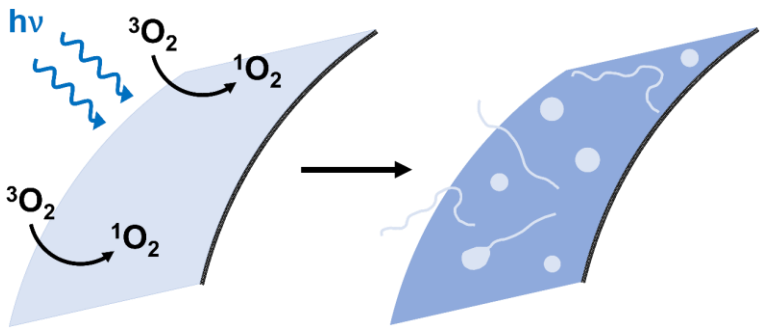

"If everything seems under control, you're not going fast enough"

- Mario Andretti

4.1. Preface

In **Chapter 1**, we provided an introduction to organic bioelectronic devices, highlighting the various classes of organic materials utilized for interfacing biological systems with electronic devices. We discussed the broad range of applications enabled by these devices while addressing the limitations associated with the commonly used organic bioelectronic materials. Moreover, we emphasized the need for new materials possessing improved charge transport properties, stability, and biocompatibility. In **Chapter 2**, we introduced a tool that could be used to assess the potential phototoxicity of optoelectronic material, whereas in **Chapter 3**, we report a novel platform for the mapping of charge transfer reactions within lipid membranes. **Chapter 4** marks the first step towards the application of the tools and platforms developed in **Chapters 2** and **3** for the evaluation of novel organic bioelectronic materials. Specifically, we assessed the integration, photostability, and phototoxicity of electron acceptor-donor-acceptor (ADA) oligomers, which serve as potential building blocks for transmembrane molecular wires. We observe the photoinduced membrane deformation and tubulation and investigate the mechanism behind the observed membrane remodeling. Our work reveals that membrane deformation results from $^1O_2$-mediated damage and exposes a dependence of membrane remodeling on the flux of $^1O_2$, measured by the sensor reported in **Chapter 2**. This work reveals critical insights into the dynamics adopted by a lipid membrane in order to accommodate to different levels of chemical damage.

Chapter 4 is the subject of a manuscript in preparation under the title "$^1O_2$-mediated remodeling of supported lipid membranes" by Aya Sakaya, Yuxuan Che, Dmytro F. Perepichka, and Gonzalo Cosa

4.2. Abstract

Conjugated structures with alternating electron donating and accepting fragments have seen increased use as semiconducting materials and offer great promise as bioelectronic materials owing to their superior charge transfer properties. As we move toward using these conjugated materials as an interface between live cell membranes and electronic components, a major concern rests on their optical and electrochemical stability and potential toxicity. In order to assess their stability, phototoxicity, and potential application as building blocks for bioelectronic materials, in this study, we incorporated a series of conjugated electron acceptor-donor-acceptor (ADA) structures in unsaturated supported lipid bilayers (SLBs). Irradiation of SLB-embedded ADA oligomers resulted in membrane deformation in the form of lipid nanotubes that grew away from the surface up to tens of microns in length and eventually collapsed into disks. Mechanistic studies including irradiation with and without oxygen, addition of a singlet oxygen quencher, and ADA incorporation into phospholipid membranes bearing either saturated or monounsaturated fatty acids all pointed to a mechanism invoking – ADA photosensitized – singlet oxygen mediated lipid peroxidation. Importantly, we show that membrane deformation occurs above a critical threshold of singlet oxygen flux but is not associated with accumulated damage, consistent with the necessity of the membrane to (rapidly) accommodate excess surface on an incompressible substrate. Chemical and physical insights into the driving forces behind membrane deformation and lipid nanotube formation and collapse are discussed herein. Together, our imaging studies reveal key aspects into the dynamics of the response of lipid membranes to chemical damage and ways the SLB adapts to mitigate the change in its chemical (and related physical) membrane composition and properties.

4.3. Introduction

Bioelectronic materials act as an interface between the biotic and abiotic, making it possible to investigate, customize, optimize and regulate the interactions between biological systems and outside electronic components. Among other materials, conjugated polymers have been at the forefront of bioelectronic research and applications. Owing to their tunable optical and

electronic properties, ease of functionalization, improved biocompatibility (compared to their inorganic semiconductor counterparts), and low cost of production,[1-4] these materials have been widely adopted. Conjugated polymers have thus been incorporated in a wide range of biological application, such as biosensing,[5-7] microbial fuel cells,[8, 9] artificial ion pumps,[10] photo-actuation,[11-13] and preclinical and clinical applications.[14] A particular subclass of conjugated polymers, membrane intercalating conjugated oligoelectrolytes (MICOE), have gained increased attention lately. The characteristic structure of MICOEs, a hydrophobic conjugated oligomer backbone of controlled size with polar pendants at both terminals, allows them to spontaneously intercalate within lipid bilayers while also affording a more precise control of their optoelectronic properties (compared to their polymeric counterparts).[15, 16]

Despite great advancements in the performance of conjugated polymers, their charge transport properties are limited by structural and energetic disorder.[17, 18] Conjugated structures with alternating electron donating (donor, D) and electron withdrawing (acceptor, A) fragments offer an attractive alternative, and have been at the center of recent research and advancement in organic semiconducting materials and devices. Their characteristic intramolecular charge transfer (ICT) states and associated low band gap and improved charge transport properties have led to their increased applications not only as semiconducting materials in electronic devices,[19-21] but also in biomedical applications.[22, 23]

As we move toward using these conjugated materials as an interface between live cell membranes and electronic components, a major concern rests on their optical and electrochemical stability and potential toxicity. Some of the most widely used and researched conjugated polymers, polyelectrolytes, and MICOEs demonstrated a degree of electrochemical instability under applied potential,[24-26] as well as cell toxicity and biocidal activity.[27-30] It is thus of paramount importance to assess the effect of incorporating novel bioelectronic material into lipid membranes as a first step before proceeding to testing and applications in bioelectronic devices.

Motivated by our desire to understand the dynamic interaction of ADA oligomers within lipid membranes and their potential phototoxicity, we report herein total internal reflection imaging studies on a series of recently reported thiophene-based acceptor-donor-acceptor (ADA) oligomers[31] – conceived as potential building blocks for MICOEs – when embedded within supported (unsaturated) lipid bilayers (SLBs). Mechanistic studies on ADA oligomer photostability and membrane dynamics revealed supported lipid membrane rearrangement and

formation of elongated nanotubes and disks (**Figure 4.1**). These rearrangements depended on the photon flux, presence of oxygen, and nature of lipids, in a manner consistent with singlet oxygen ($^1O_2$) mediated lipid peroxidation photosensitized by ADA oligomers. Importantly, key to the observed supported membrane dynamics were the rates, rather than just the dose at which $^1O_2$ was delivered, consistent with *how fast*, but not just *how much*, lipid peroxidation damage occurred.

Our work, while highlighting the need to better understand the nature and effect of interfacing ADA oligomers with lipid membranes, serendipitously unraveled key aspects of the response of lipid membranes to chemical stress in the form of $^1O_2$ *ene* reaction, and associated ways the membrane explores toward mitigating the imbalances produced through chemical changes on lipids.

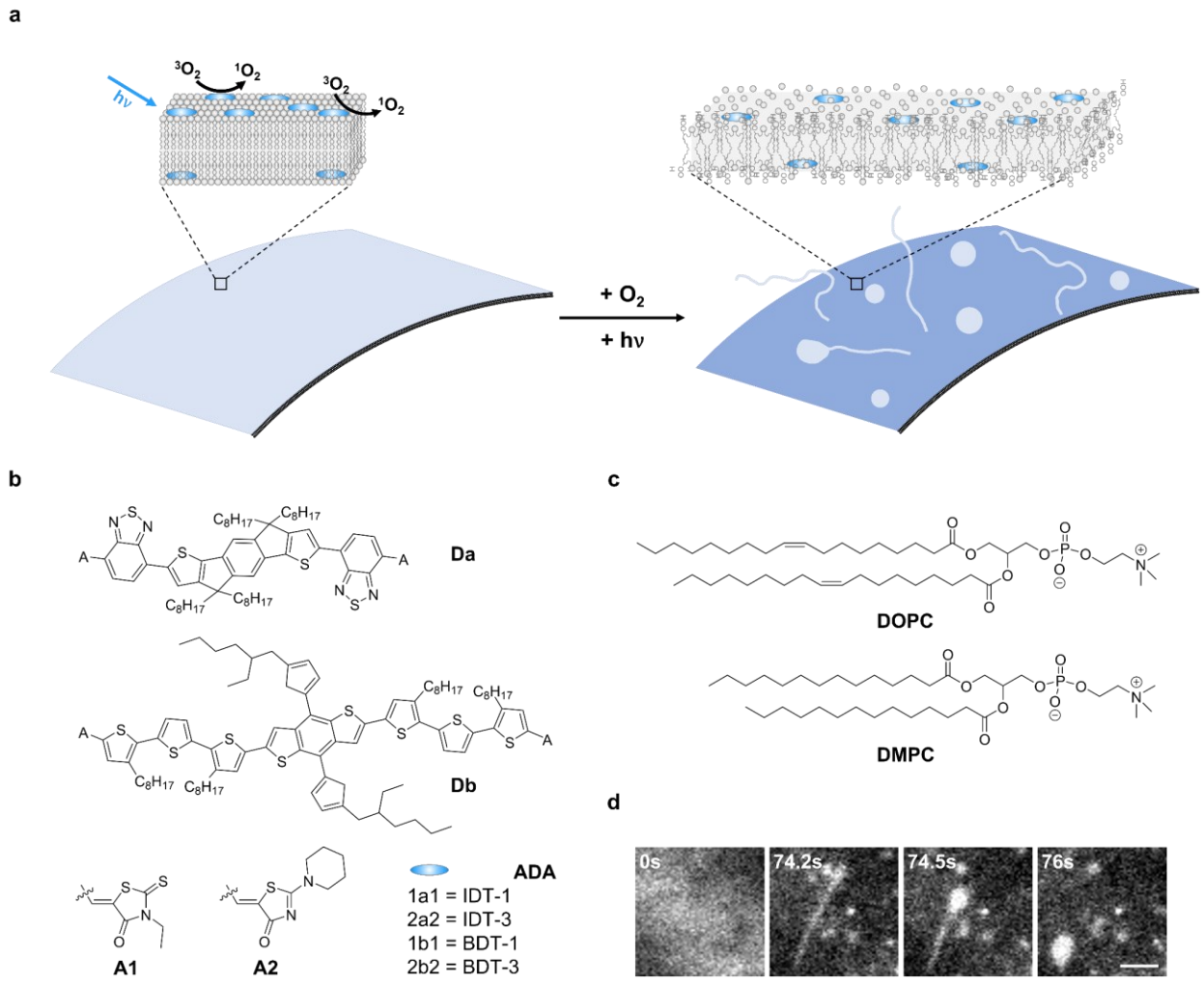

Figure 4.1. Photoinduced phase separation of ADA oligomers in supported lipid bilayers (SLB) (a) Schematic depiction of singlet oxygen ($^1O_2$)-mediated phase separation of ADA

oligomers embedded in SLBs and formation of lipid nanotubes and domains. The photoinduced $^1O_2$ *ene* reaction on lipids in a membrane slab and the ensuing membrane expansion is illustrated as insets above. (b) Structures of ADA oligomers employed in this study.31 (c) Structure of the unsaturated (DOPC) and saturated (DMPC) lipids employed in this study. (d) Image time series depicting the photoinduced phase separation of BDT-3 from a DOPC SLB and formation of lipid nanotubes and disks. Scale bar = 3 μm. BDT-3:DOPC ratio = 1:1000.

4.4. Results and Discussion

4.4.1. Mechanism of photoinduced formation of phase segregated domains

Seeking to explore the potential of thiophene-based ADA oligomers[31] (**Figure 4.1b**) as an assembly backbone to transmembrane wires, we first assessed their photostability within lipid membranes. To that end, ADA-embedded supported lipid bilayers were formed on glass coverslips via the vesicle fusion method,[32, 33] with an ADA oligomer:lipid ratio of 1:1000, and characterized according to procedures described in **Section 4.6.3** (see also **Supporting Figure 4.7**). Supported lipid bilayers were imaged using an inverted Nikon Eclipse Ti microscope. A widefield objective based total internal reflection fluorescence (TIRF) configuration was implemented with a Nikon TIRF illuminator and a 100× oil immersion objective. The ADA oligomers BDT-3, IDT-3, and IDT-1 were excited with the 488 nm, 561 nm, or 647 nm outputs of a laser combiner, respectively. Experiments with the fourth oligomer, BDT-1, could not be conducted as it did not incorporate into the supported lipid bilayers. Emission from the ADA oligomers was collected on the 512 × 512-pixels region of an electron multiplying charge-coupled device (EMCCD camera) with an effective pixel size of 160 nm.

Upon first incorporating BDT-3 oligomers in an SLB composed of the unsaturated lipid DOPC (1,2-dioleoyl-sn-glycero-3-phosphocholine, **Figure 4.1c**) and imaging via TIRF microscopy, we observed to our surprise, the apparent segregation of BDT-3 from the surrounding supported lipid bilayer and the formation of nanotubes and disks (**Figure 4.1a,d**). This segregation was accompanied by a rapid photobleaching of BDT-3 and a pronounced decrease in its fluorescence intensity (**Supporting Figure 4.8**).

In order to pinpoint the mechanism at play in the recorded segregation/phase separation, we investigated the role and effect of each component present in the system, namely: (i) the presence or absence of light, (ii) the presence or absence of oxygen, (iii) the nature of ADA oligomers, and (iv) the nature of lipids (saturated vs monounsaturated).

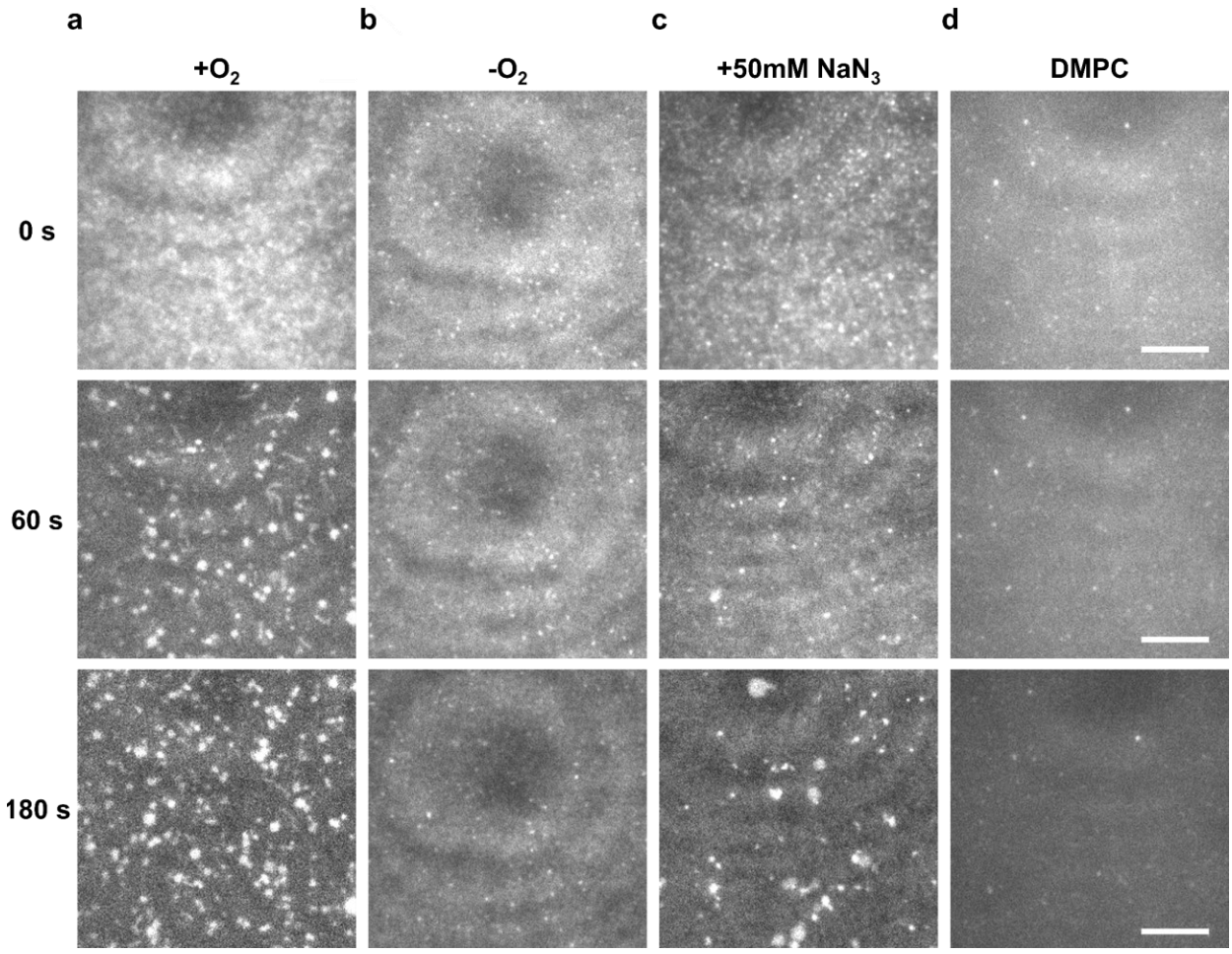

Figure 4.2. Membrane-embedded BDT-3 phase separation (or lack thereof) under different conditions. (a) in a DOPC SLB under air-equilibrated PBS, (b) in a DOPC SLB in the absence of oxygen. (c) in a DOPC SLB under air-equilibrated PBS and in the presence of 50 mM of the $^1O_2$ quencher sodium azide (NaN_3), and (d) in an air-equilibrated SLB formed with the saturated lipid DMPC. Scale bar = 10 μm. BDT-3:lipid ratio = 1:1000. BDT-3 was excited with 100 μW of a 488 nm cw laser. t = 0 s corresponds to the first imaging frame.

Consistent with a light triggered process, we found that the phase separation was only initiated upon laser irradiation, where a lipid bilayer region that had not previously been exposed to any light initially appears homogenous with no signs of phase separated nanotubes or domains (**Figure 4.2a,c**, t = 0 s). Experiments where the light irradiation was interrupted at the first sight of phase separation resulted in the halting of the continued growth of nanotubes and domains (**Supporting Figure 4.9**), consistent with a process that is not only triggered by light, but also requires constant illumination.

We next found that the presence of oxygen is required for the observed photoinduced BDT-3 phase separation to occur. Here, removal of oxygen from the system - through a glucose/glucose oxidase/catalase enzymatic mixture - prevented the formation of nanotubes and segregated domains (**Figure 4.2b**, see also **Section 4.6.4.2** for details on removal of oxygen). Removal of oxygen also led to a remarkable improvement in the photostability of membrane-embedded BDT-3 oligomers, with their fluorescence intensity remaining stable over a long imaging period (4-5 minutes, see **Supporting Figure 4.8**).

Given that the presence of both oxygen and continuous laser irradiation is required for BDT-3 segregation to occur, we reasoned that singlet oxygen ($^1O_2$) was involved in the process, with BDT-3 serving as the photosensitizer under our experimental conditions. This is consistent with the large (63% in chloroform) singlet oxygen photosensitization quantum yield (Φ_Δ) we recorded for BDT-3 (see **Table 4.1** and **Section 4.6.5.2** for Φ_Δ determination). The large Φ_Δ of BDT-3 is attributed to its charge separated-intramolecular charge transfer (ICT) state, which typically presents with reduced excited singlet-triple gaps, and thus an improved intersystem crossing rate.[34-38]

Table 4.1. Photophysical properties of ADA oligomers in chloroform solutions

	Φ_f[a]	Φ_Δ[b]
BDT-3	0.13	0.63
IDT-3	0.14	0.36
IDT-1	0.04	0.39

[a]Values taken from reference 31. [b]Values measured herein using Rose Bengal as reference (Φ_Δ = 0.54 in acetonitrile).[39]

In order to confirm that the observed BDT-3 segregation occurs as a result of $^1O_2$ generation, we next employed sodium azide (NaN_3), a $^1O_2$ physical quencher.[40] BDT-3 segregation in the supported lipid bilayer was successfully minimized by addition of this $^1O_2$ quencher[40] (**Figure 4.2c**), where a minor segregation observed after prolonged irradiation (**Figure 4.2c**, t = 180 s) can be ascribed to membrane-generated $^1O_2$ that cannot be quenched by the water-soluble NaN_3. Further confirmation came from inducing BDT-3 segregation through the irradiation of an

external photosensitizer, methylene blue, at wavelengths where BDT-3 does not absorb (**Supporting Figure 4.10**).

To assess if the phase separation of BDT-3 is a result of the interaction of $^1O_2$ with (i) the monounsaturated lipids in the supported lipid bilayer (i.e., lipid peroxidation via the *ene* reaction), (ii) with the ADA oligomer BDT-3, or (iii) with both, we next incorporated BDT-3 within a supported bilayer composed of a saturated lipid, dimyristoyl phosphatidyl choline (DMPC). Contrary to DOPC, DMPC cannot undergo peroxidation. No BDT-3 segregation was observed upon incorporating and irradiating BDT-3 in lipid membrane formed from DMPC (**Figure 4.1c**), indicating that disk formation, tubulation, and BDT-3 segregation occurs as a result of lipid peroxidation (**Figure 4.2d**). Experiments on the photostability of BDT-3 further cemented lipid peroxidation as the sole chemical change responsible for BDT-3 segregation, disk and nanotube formation. Here, bulk photo-oxidation experiments on DOPC liposomes embedded with BDT-3 were conducted where the sample was continuously irradiated over 48 hours with a 520 nm LED lamp, and the ADA oligomer emission monitored over time. While the emission intensity decreased significantly over time (possibly due to $^1O_2$ mediated photobleaching), no considerable change in the emission spectrum of BDT-3 was recorded (**Supporting Figure 4.11**). This indicates that (i) BDT-3 photo-oxidation products are non-emissive, and (ii) the emission recorded from the phase-separated aggregates during microscopy imaging most likely results from "pristine", non-oxidized BDT-3. This "phase separation" observation is then likely a result of membrane expansion, deformation, and tubulation following an increase in the area of the lipid membrane upon its peroxidation.[41-46]

4.4.2. Singlet oxygen flux threshold required for membrane tubulation

Experiments conducted with different ADA oligomers (**Figure 4.1b**) revealed that the formation of nanotubes and disks is dictated not only by the occurrence of lipid peroxidation through the *ene* reaction, but by the rate at which this *ene* reaction is taking place. As such, while the oligomer IDT-3 produced lipid nanotubes and domains in DOPC supported lipid bilayers (**Figure 4.3a**) following a similar, $^1O_2$-dependent mechanism as BDT-3 (as tested upon removal of O_2 and in DMPC lipid bilayers, see **Supporting Figure 4.12**), the structurally related oligomer IDT-1 showed no domain formation (**Figure 4.3b**) despite having a similar Φ_Δ as IDT-3 when

measured in bulk acetonitrile solutions (**Table 4.1**), and despite both oligomers being excited at identical excitation rates (see **Section 4.6.4.3** for calculation of excitation rates).

We reasoned that the different ADA oligomers could be eliciting different levels of singlet oxygen photosensitization and in turn of *ene* reaction (lipid hydroperoxide formation) when membrane embedded. A different "*in situ*" Φ_{Δ} value would affect the effective flux of $^1O_2$ impinging on DOPC, and the rate at which the membrane is expanding, thus affecting the tendency of the supported lipid membrane to deform in order to accommodate a newly arising mechanical compression induced by the increasing area upon peroxidation.[45, 46] Accordingly, under increasing excitation powers, and concomitant increasing rates of lipid peroxidation, we confirmed photoinduced segregation of IDT-1 (**Supporting Figure 4.13)**.

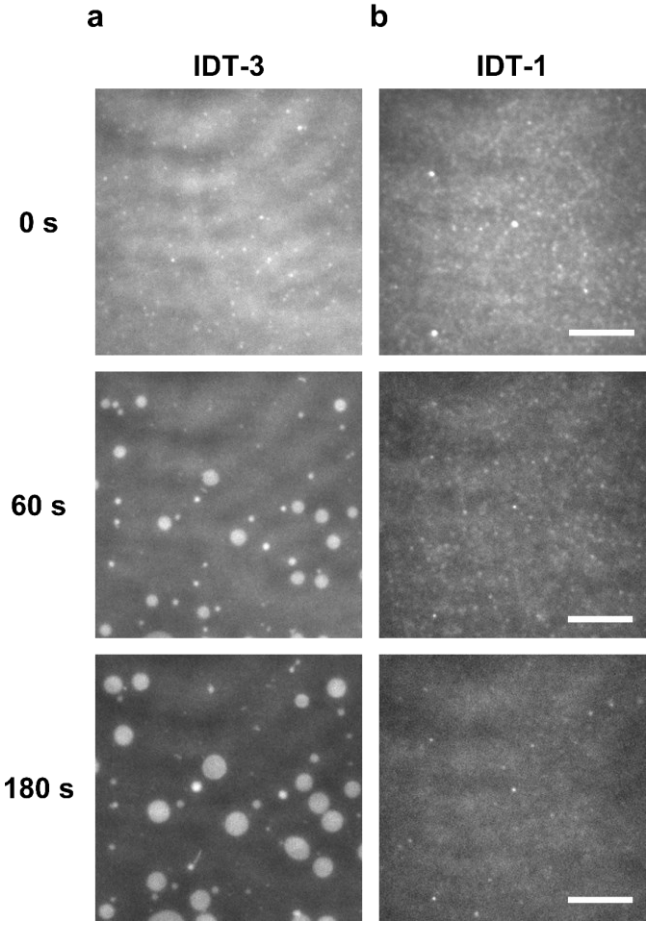

Figure 4.3. Phase separation behavior of membrane-embedded IDT-3 and IDT-1. IDT-3 undergoes a photoinduced phase separation out of the surrounding DOPC SLB (a), while IDT-1 shows no sign of domain formation (b). Scale bar = 10 μm. ADA:DOPC ratio = 1:000. IDT-3 was excited with 108 μW of a 561 nm cw laser. IDT-1 was excited with 66 μW of a 647 nm cw laser.

IDT-3 and IDT-1 were imaged under the same excitation rate used for BDT-3 in Figure 4.2. t = 0 s corresponds to the first imaging frame.

In order to quantify the flux of $^1O_2$ (rate of generation of $^1O_2$ in a given illuminated area) associated to each of these ADA oligomers under our experimental conditions, we resorted to a recently reported method we developed that allows the real-time monitoring and quantification of the flux of $^1O_2$ impinging on giant unilamellar vesicles (GUVs).[47] The method utilizes a fluorogenic α-tocopherol analogue, H_4BPMHC (**Figure 4.4a**),[48] as a $^1O_2$ sensor that is initially non-emissive yet undergoes a >50-fold emission intensity enhancement upon trapping $^1O_2$ (**Figure 4.4b**). Here the zero order reaction kinetics between $^1O_2$ and H_4BPMHC allow for a straightforward and direct determination of $^1O_2$ flux (**Figure 4.4b**).[47]

Analysis of H_4BPMHC emission enhancement trajectories through our method indicated two key findings (see **Section 4.6.7** for $^1O_2$ flux calculations). (i) All three ADA oligomers required a threshold $^1O_2$ flux to elicit lipid domain formation. (ii) The three ADA oligomers required the *same* threshold of $^1O_2$ flux (~0.15 molecules nm^{-2} s^{-1}) to induce membrane deformation, where a lower flux led to no nanotube or lipid domain formation (**Figure 4.4c**). That IDT-1 failed to elicit domain formation initially was thus assigned to a relative lowering of its "*in situ*" value for Φ_Δ when on supported lipid membranes, compared to that for its analogues BDT-3 and BDT-1.

Notably, in our studies with the fluorogenic antioxidant H_4BPMHC, the onset of membrane deformation occurred right after complete oxidation of the probe (end of the antioxidant protection by the α-tocopherol chromanol moiety in H_4BPMHC), and thus immediately following the onset of lipid peroxidation (**Supporting Figure 4.14)**.

Tubulation of SLBs following addition of external small molecules[49] or upon lipid oxidation under photoinduced stress[43] has been reported to be concentration-dependent and explained as needing a threshold amount of damage in order to induce membrane deformation. Our results however indicate that membrane deformation does not require a buildup of a critical lipid hydroperoxide concentration (achieved by irradiating for longer periods of time), but rather requires a minimal rate of lipid hydroperoxide formation. This paradox reveals that a slow buildup of chemical damage and composition change can be accommodated by the membrane, whereas an abrupt and severe chemical insult will result in a change of membrane topology and organization.

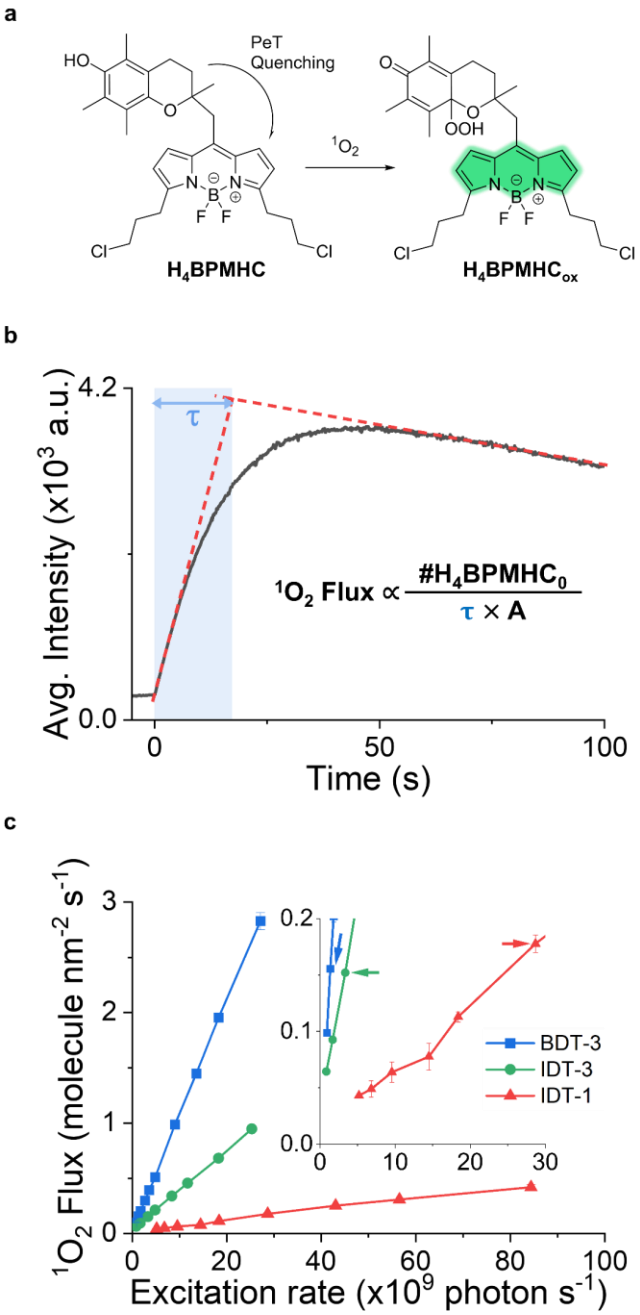

Figure 4.4. Singlet oxygen flux dependence of ADA phase separation. (a) Structure of the $^1O_2$ sensor H_4BPMHC and its oxidized counterpart H_4BPMHC_{ox}. (b) Representative intensity-time trajectory depicting linear enhancement in H_4BPMHC emission intensity upon trapping of ADA-photosensitized $^1O_2$ and correlation between H_4BPMHC reaction time (τ) and $^1O_2$ flux. Here, τ represents the time until full probe consumption occurs (intensity plateau), and A is the area of the field of view (81.9 × 81.9 μm^2). (c) Measured $^1O_2$ flux at different ADA excitation rates. Inset shows the minimum $^1O_2$ flux required to initiate membrane deformation with each membrane-embedded ADA compound (indicated with arrows). ADA:DOPC ratio = 1:1000. H_4BPMHC:DOPC ratio = 1:100. BDT-3, IDT-3, and IDT-1 were excited with a 488 nm, 561 nm, and 647 nm cw lasers, respectively. H_4BPMHC was excited with a 488 nm cw laser.

4.4.3. Dynamics of lipid domains and nanotubes

We next examined over time the morphological response of lipid membranes to photosensitized lipid oxidation by the three ADA oligomers (see **Figure 4.5** for examples of IDT-1 induced deformation and **Supporting Figure 4.15** and **Figure 4.16** for examples of BDT-3 and IDT-3 induced membrane deformation, respectively). Nanotubes first grew lengthwise up to several tens of microns in length (**Figure 4.5a,b** and **Supporting Figure 4.16c**) remaining anchored to the supported lipid bilayer at the tubulation point (**Figure 4.5a,b**), while free at the other end. Most nanotubes maintained their integrity for a prolonged period of time before collapsing into disks (**Figure 4.5b,f**), however, a small fraction of nanotubes characterized by their short length were short-lived, forming and collapsing within one second (**Figure 4.5d** and **Supporting Figure 4.16b**).

Two different dynamics were observed with nanotube-to-disk transitions: "snap-collapse" and "gradual pulling", similar to the dynamics previously reported by Staykova et al. following mechanical compression of SLBs.[50] Shorter nanotubes collapsed instantaneously within a single imaging frame (**Figure 4.5b**, and **Supporting Figure 4.15e,f**, and **Figure 4.16e,f**), while longer nanotubes experience a more dynamic transition into 2D domains. The collapse of longer nanotubes started from a fixed anchor point of the nanotube in the supported lipid bilayer that gradually pulls in the rest of the filament. The disk can start forming from the center of that fixed anchor point (**Figure 4.5b** and **Supporting Figure 4.16c**) or from the mobile end of the filament that is slowly pulled into the anchor (**Supporting Figure 4.15a**).

The appearance of disks did not necessarily require the *a priori* formation of a nanotube that eventually collapsed, as some disks grew gradually and radially from a fixed point in the supported lipid bilayer (**Figure 4.5c** and **Supporting Figure 4.15b,c**). Interestingly, these disks (formed independently or from collapsed nanotubes) were observed to occasionally interact with each other, with nearby disks frequently interacting by approaching each other and eventually merging into one large disk (**Supporting Figure 4.16c,d**).

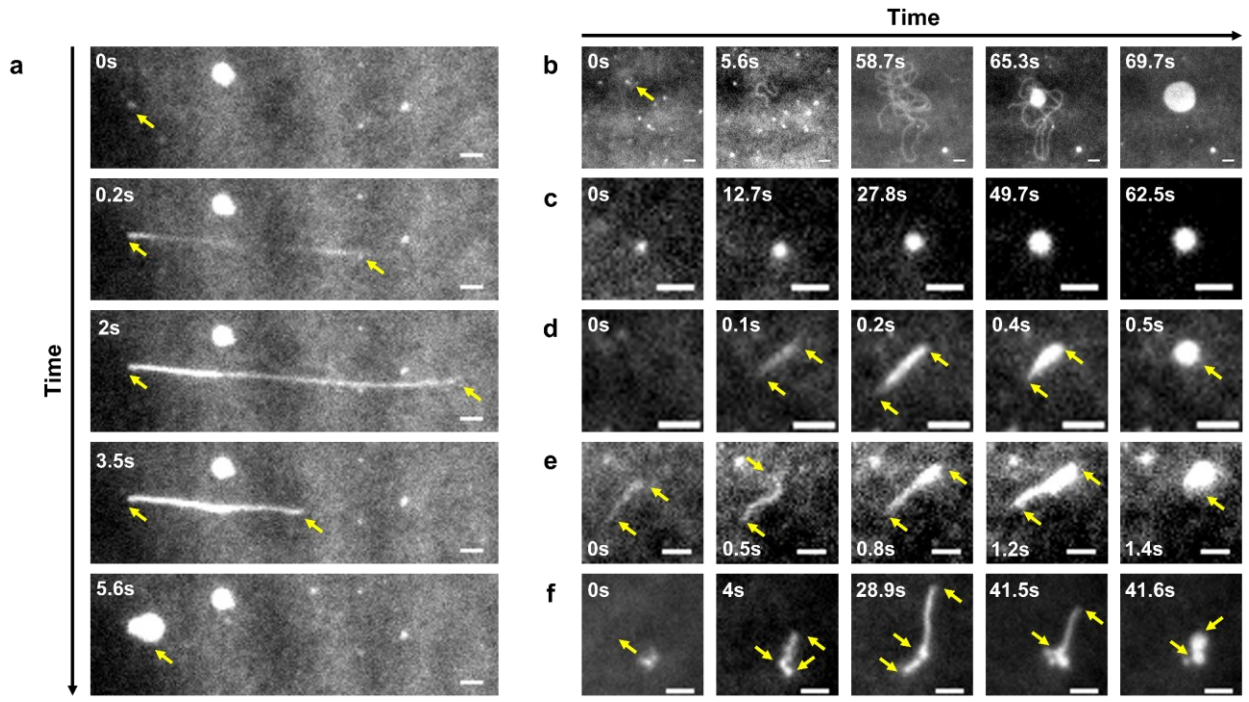

Figure 4.5. Image time series depicting dynamics of membrane deformation induced by IDT-1 (a-b) Formation and collapse of a long nanotubes by gradual pulling into SLB. (c) Radial growth of a disk. (d-e) Instantaneous formation and snap-collapse of short nanotubes. (f) Snap-collapse of long-lived nanotubes. Scale bar = 2 μm. Yellow arrows highlight features of interest such as nanotube extremities and disks. IDT-1:DOPC ratio = 1:1000. SLB also contained H_4BPMHC in a 1:100 probe:lipid ratio. IDT-1 was excited with the 100 μW (a-c) or 200 μW (d-f) output of a 647 nm cw laser. Any H_4BPMHC emission was filtered out and only IDT-1 emission was collected.

In order to further characterize the nature of the observed nanotubes and disks, their photosensitized formation was recorded while keeping the microscopy imaging plane 1 – 3 μm above the supported lipid bilayer plane and while exciting perpendicularly to the glass-lipid interface surface. Most nanotubes were observed to be in focus well above the supported lipid bilayer plane, indicating they are freely floating above – rather than lying flat on top of – the lipid membrane (**Figure 4.6** and **Supporting Figure 4.17**). On the other hand, by initially setting the focus at the supported lipid bilayer plane and then slowly moving it away from the glass-bilayer-water interface into the buffered solution, any initially observed disk went completely out of focus simultaneously with the bilayer. This confirms that the circular structures correspond to disks[51] rather than three dimensional vesicle protrusions or hemispherical caps atop the supported lipid bilayer, as previously reported.[43, 49, 52-55] This is further confirmed by the homogenous fluorescence intensity across the disks, as opposed to presenting a bright perimeter ring as previously observed upon the formation or addition of giant vesicles to SLBs.[50, 56]

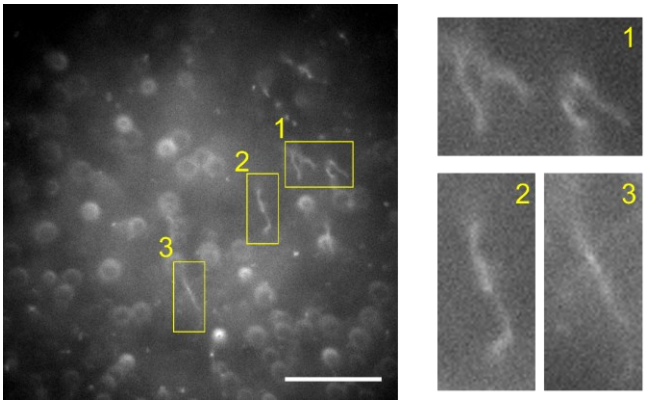

Figure 4.6. Membrane deformation imaged above the SLB plane. Photosensitized membrane deformation was initiated by irradiating IDT-3 and setting the imaging plane 1 μm above the supported lipid bilayer plane. Scale bar = 20 μm. IDT-3:DOPC ratio = 1:1000. The supported lipid bilayer also contained H_4BPMHC in a 1:100 probe:lipid ratio. IDT-3 was excited with 2 mW of a 561 nm cw laser. The incident beam was perpendicular to the sample plane. Any H_4BPMHC emission was filtered out and only IDT-3 emission was collected.

Formation of lipid nanotubes has been reported to occur in both giant unilamellar vesicles and supported lipid bilayer model lipid membranes and is initiated following disruption of the lipid membrane by physical or chemical stressors such as mechanical strain,[50, 57, 58], lipid peroxidation,[41, 43] or addition of either small molecule drugs,[49] proteins and peptides,[51, 56] single chain amphiphiles, [52-54, 59] or nanoparticles.[60, 61] In most cases, those lipid nanotubes retracted to form disks. Tubulation of planar lipid membranes has been explained by Lipowsky to be driven by membrane tension resulting from spontaneous curvature acquired upon the addition of external agents to the membrane such as small molecules and peptides.[62] This explanation however relies on the presence of an asymmetric stress where only the upper SLB leaflet is exposed to the external stressors. Membrane tubulation in our case, however, occurs as a result of lipid peroxidation undergone by both SLB leaflets upon the irradiation of membrane-bound photosensitizers. As such, it cannot be explained through a mechanism relying on asymmetric stress, and is better explained by a strain-driven mechanism[58] - mechanical compression - resulting from membrane area expansion upon lipid peroxidation in a confined space.[41, 42, 44-46]

While the nanotube-to-disk transition has been previously reported with a range of chemical stressors,[43, 49, 51, 55, 60] the mechanism and driving force behind this transition are still debated. Previous reports explain this transition as resulting from relieving an initial asymmetric stress applied on the SLB via transmembrane translocation or "flip-flop" that re-equilibrates the membrane composition in both leaflets.[49, 55] Again, such explanation is not applicable to our

system as we expect membrane damage to be symmetric between the two bilayer leaflets. The nanotube-to-disk transition in our case is likely a result of by-products of oxidized lipids generated through both Type I and Type II photosensitization. These oxidation products typically have cleaved tails ending with an aldehyde or a carboxyl group,[63, 64] and possess a reduced lipid area, resulting in further changes in membrane geometry and organization and membrane pore formation.[65-68] Furthermore, these lipid oxidation products have been recently reported to induce membrane deformation and bending following their asymmetric desorption from the outer leaflet of lipid membranes.[69] As membrane deformation is driven by strain, bending energies, and spontaneous curvatures, we believe that a transition to truncated lipids of different polarity, size, curvature, and geometry to non-oxidized and peroxidized DOPC would naturally result in a change in membrane geometry and packing and thus be the driving force behind the nanotube-to-domain transition.

4.5. Conclusion

Motivated by our desire to use ADA oligomers as building blocks for transmembrane molecular wires, we conducted imaging studies of a series of ADA oligomers incorporated in SLBs in order to assess their stability and potential membrane phototoxicity. Our studies revealed that upon irradiation, the ADA oligomers induce membrane deformation in the form of lipid nanotube and domain formation. Our studies thus highlight a caveat and limitation to the use of ADA structures in bioelectronic devices, as the same photophysical principles behind their great charge transfer properties lead to their membrane phototoxicity.

An in-depth investigation into the mechanism behind the photoinduced membrane damage revealed that membrane tubulation occurs as a result of ADA photosensitized lipid peroxidation, confirmed by the successful inhibition of membrane deformation upon the removal of oxygen, the addition of $^1O_2$ quenchers, or the incorporation of ADA oligomers in saturated SLBs. Lipid hydroperoxides occupy a larger area/lipid than their non-oxidized counterparts, and thus their generation leads to an increase in lipid membrane area. This abrupt area increase and mechanical compression is mitigated by SLBs through the formation of three-dimensional lipid nanotubes protruding away from the SLB surface in one direction, as the other direction is constrained by the glass substrate. The lipid nanotubes eventually collapsed into flat disk on top of the SLB, possibly

due to the formation of lipid hydroperoxide by-products, such as truncated lipid aldehydes, which occupy a smaller area/lipid and lead to a decrease in total membrane area and changes in membrane curvature. Power dependence studies in the presence of H_4BPMHC, an α-tocopherol fluorogenic analogue serving as a $^1O_2$ sensor, revealed that a certain threshold of $^1O_2$ flux needs to be exceeded in order for membrane deformation to be observed. The fact that lipid nanotubes and disks start to form right at the end of the antioxidant protection offered by H_4BMHC (upon its complete oxidation by $^1O_2$) demonstrates that the dependence of $^1O_2$ flux is a function of *how fast* membrane damage is done, and not just *how much* damage has accumulated.

Overall, our imaging studies report key aspects of the response of a lipid membrane to chemical stress and provide insights regarding the dynamics and ways in which a membrane accommodates changes to its chemical composition.

4.6. Supplementary Information

4.6.1. Materials

H_4BPMHC, BDT-3, IDT-3, and IDT-1 were synthesized as previously reported.[31, 48] 1,2-dioleoyl-sn-glycero-3-phosphocholine (DOPC) and 1,2-dimyristoyl-sn-glycero-3-phosphocholine (DMPC) were purchased from Avanti Polar Lipids, Inc. D-(+)-glucose(≥99.5% GC), 9,10-dimethylanthracene (DMA), methylene blue, Rose Bengal, sodium azide, glucose oxidase (from *Aspergillus niger*, type VII, G2133), catalase C30 (from bovine liver, C30), 2,2'-azobis(4-methoxy-2.4-dimethyl valeronitrile) (V70), and HPLC grade chloroform (≥99.8%, amylene stabilized) were purchased from Sigma Aldrich. HPLC grades solvents (acetone and acetonitrile), sulfuric acid, sodium bicarbonate, 10× phosphate-buffered saline (PBS, pH 7.4, Invitrogen), and HyClone Water (Molecular Biology Grade, Cytiva) were purchased from Thermo Fisher Scientific. Hydrogen peroxide was purchased from ACP chemicals. All materials were used without further purification.

4.6.2. Liposome preparation

Stock solutions of DOPC and DMPC (20 mM each) were prepared in HPLC grade chloroform. Dilute solutions of BDT-3, IDT-3, IDT-1 (in chloroform), and H_4BPMHC (in

acetonitrile) were prepared right before lipid film formation and their concentrations were determined by absorbance measurements using their published extinction coefficients (82×10^3, 93×10^3, 81×10^3, and 82×10^3 M^{-1} cm^{-1}, respectively).[31, 48] DOPC and the desired ADA oligomer were mixed in a vial in a 1:1000 ratio of ADA:lipid. When specified, H_4BPMHC was added in a 1:100 probe:lipid ratio. Chloroform was evaporated while rotating under a gentle stream of argon, then all traces of solvent were evaporated from the resulting lipid film under vacuum for 1 hour. The lipid film was then hydrated in PBS to a final lipid concentration of 20mM, subjected to four freeze-thaw-sonicate cycles (5 minutes in dry ice followed by 5 minutes of sonication in a room temperature water bath), and extruded 21 times through a 100 nm polycarbonate membrane (Avanti Lipids, Inc), resulting in a suspension of 100 nm liposomes. When DMPC was used as a lipid, the PBS buffer and water bath were heated above the phase transition temperature of DMPC (24 ℃).

4.6.3. Supported lipid bilayer formation and characterization

4.6.3.1. SLB formation

Supported lipid bilayers (SLBs) were formed via the vesicle fusion method.[32, 33] Glass coverslips (25 mm × 25 mm, Fischer scientific) and glass cylinders (~1 cm diameter × 3 cm height) were first cleaned by sonication in piranha (3:1 95-98% H_2SO_4 : 30% H_2O_2) then by sequential sonication in molecular biology-grade water and HPLC grade acetone. An imaging chamber was formed by adhering a glass tube to a coverslip using epoxy glue, which was left to dry for 5 minutes then cured in a 90 ℃ oven for 15 minutes. The imaging chamber was then washed with 2 × 1 mL buffer and filled with 2 mL PBS buffer. Extruded liposomes (20 μL) were then added to the chamber and incubated at room temperature for 1 hour in order to rupture and form the SLB. The resulting SLB was washed with 12 × 1 mL buffer to remove any unruptured liposomes. A small amount of buffer was always left in the chamber while washing to prevent disruption of the hydration layer separating the SLB from the glass support. The final volume in the imaging chamber was 2 mL and all measurements were conducted at room temperature. When DMPC was used as a lipid, the buffer was heated above the transition temperature of DMPC (24 ℃), and the imaging chamber was heated to 37 ℃ on top of the microscope stage using a repurposed Bioptechs Objective Heater and Controller tied around the cylinder of the imaging chamber.

4.6.3.2. SLB characterization

To assess whether SLBs successfully formed, we conducted fluorescence recovery after photobleaching (FRAP) experiments. FRAP experiments consisted of photobleaching a circular area of the SLB (~13 μm in diameter) by closing an iris in the excitation path and increasing the laser power to its maximum (~ 47 mW, 58 mW, and 93 mW for the 488 nm, 561 nm, and 647 nm laser outputs, respectively) for 5 seconds. Successful formation of an SLB was confirmed by observing a recovery of the fluorescence signal in the photobleached region over time for all three ADA oligomers, indicating the presence of a fluid, well connected membrane with freely diffusing fluorophores (**Supporting Figure 4.7**). However, accurate diffusion coefficients could not be extracted from the FRAP trajectories due to the strong photobleaching observed as a result of the photosensitizing nature of the ADA oligomers.

4.6.4. Fluorescence microscopy measurements

4.6.4.1. Microscopy setup

SLBs were imaged using an inverted Nikon Eclipse Ti microscope equipped with a Perfect Focus System (PFS) to compensate for axial drift. A widefield objective based TIRF configuration was implemented with a Nikon TIRF illuminator and an oil immersion objective [Nikon CFI SR Apochromat TIRF 100×, numerical aperture (NA) = 1.49]. Unless otherwise specified, the circularly polarized incident beam was brought in above the critical angle in order to achieve total internal reflection. BDT-3, IDT-3, and IDT-1 were excited with the 488 nm, 561 nm, or 647 nm outputs of an Agilent MLC400B Monolithic laser combiner, respectively. When present, H_4BPMHC was excited with the 488 nm laser output. The excitation beam was first passed through a ZET405/488/561/647× multiband excitation filter (Chroma Technology) and directed towards the sample with a ZT405/488/561/647rpc multiband beam splitter (Chroma Technology). Fluorescence emission was collected through the objective and spectrally filtered through a ZET405/488/561/647m multiband emission filter (Chroma Technology). The emission of the individual fluorophores was further cleaned up by secondary emission filters. IDT-3 and IDT-1 fluorescence emission was passed through an ET705/72m emission filter (Chroma Technology). BDT-3 emission was cleaned up with an ET600/50m emission filter when alone and a HQ647/75m in the presence of H_4BPMHC to better spectrally filter their respective emissions (see **Supporting Figure 4.18** for the absorbance and emission spectra of H_4BPMHC and the ADA oligomers).

H_4BPMHC was filtered through a 540/80× bandpass filter when incorporated with IDT-3 and IDT-1, while an HQ517/30m filter was used when H_4BPMHC was incorporated with BDT-3.

Emitted photons were collected on the 512 × 512 pixels region of a back illuminated electron multiplying charge-coupled device (EMCCD camera, iXon X3 DU-897-CS0-#BV, Andor Technology). 16-bit images were collected with an effective pixel size of 160 nm. Timelapse movies were typically acquired at a 10 frames/s rate, using an EM-gain amplification setting of 100. The EM-gain and acquisition frequency were however adjusted when needed to accommodate for high intensity imaging or fast reaction kinetics. The microscope and lasers were controlled through the NIS element software from Nikon. The camera was controlled using Micro-Manager Software (Micro-Manager 1.4.13, San Francisco, CA, USA).

4.6.4.2. Oxygen removal

Oxygen was removed from the imaging chamber when desired with an oxygen scavenging solution (GODCAT) consisting of D-(+)-glucose (3% w/w), glucose oxidase (165 units/mL), and catalase C30 (2170 units/mL) prepared in PBS buffer in molecular biology grade water. Experiments typically involved forming and initial imaging of the SLB in air-equilibrated PBS. The buffer in the imaging chamber was then removed (leaving a small amount to keep the SLB hydrated) and the chamber was washed with 2 × 1 mL GODCAT solution. The final GODCAT volume in the imaging chamber was 2 mL. Imaging was resumed 15 minutes after introduction of the GODCAT solution to allow for the oxygen concentration to equilibrate.

4.6.4.3. Determining ADA excitation rate

ADA excitation rates were calculated in order to ensure equal ADA excitation when required, or to correlate with the ensuing $^1O_2$ flux (**Figure 4.4**). This involved accounting for the different extinction coefficients (tendency to absorb photons) of each ADA oligomer at their respective excitation wavelength. Excitation rates were calculated using **equation 4.1** below, where I_{ex} is the rate of incident photons (photon/s) obtained from the laser power measured out of the objective, σ is the fluorophore cross section (in cm^2/molecule), N is the number of fluorophores present in the excitation area, and A is the excitation area/beam cross section (in cm^2), which in our setup can be estimated as the area of the field of view (81.9 × 81.9 μm^2).

$$\text{Excitation rate (photon s}^{-1}) = \frac{I_{ex} \times \sigma \times N}{A} \quad (4.1)$$

N is calculated by first estimating the number of lipids per field of view (using a DOPC lipid head area of 0.82 nm^2, ref 70) and then multiplying by the fluorophore-to-lipid ratio (1:1000 in our case), and by 2 to account for the fact that the membrane is a bilayer. σ is calculated using **equation 4.2**, where ε_λ is the extinction coefficient of the fluorophore at the excitation wavelength λ (in M^{-1} cm^{-1}), and N_A is Avogadro's number (molecules/mol).

$$\sigma = \frac{1000 \times \ln(10) \times \varepsilon_\lambda}{N_A} \quad (4.2)$$

ε_λ was determined from the measured absorbance spectra of the ADA oligomers (see **Section 4.6.5.1** and **Figure 4.18**) and their reported extinction coefficients at their maximum absorbance wavelength.[31]

4.6.5. Photophysical characterization

4.6.5.1. Absorbance and emission spectra

Absorbance spectra were recorded using a Hitachi U-2800 spectrophotometer. Spectra were recorded in chloroform (ADA oligomers) or acetonitrile (H_4BPMHC) solutions in 1 cm × 1 cm quartz cuvettes. Emission spectra were recorded on a Photon Technology International (PTI) Quanta Master fluorimeter in 1.0 cm × 1.0 cm quartz cuvettes. All slits were set to 2 nm. Emission spectra were recorded with solutions having a maximum absorbance less than 0.1. BDT-3, IDT-3, IDT-1, and H_4BPMHC were excited at 488 nm, 561 nm, 647 nm, and 480 nm, respectively. As H_4BPMHC is initially non-emissive, the recorded emission spectrum corresponds to its oxidized counterpart, generated by oxidizing it with 0.2 mM of the radical initiator V-70 (2,2'-azobis(4-methoxy-2.4-dimethyl valeronitrile)). All emission spectra were automatically corrected for the wavelength dependent PMT (detector) sensitivity when recorded with the PTI Felix32 software (version 1.2).

4.6.5.2. Determination of singlet oxygen quantum yields

Singlet oxygen ($^1O_2$) quantum yields (Φ_Δ) were measured by following the kinetics of DMA photooxidation, using Rose Bengal (RB) as a reference photosensitizer (Φ_Δ = 0.54 in acetonitrile).[39] Solutions of BDT-3, IDT-3, IDT-1, and RB containing 50 μM DMA were prepared (in chloroform for ADA oligomers and acetonitrile for RB) such that they have the same absorbance (0.12 in our case) at 532 nm. Kinetics of $^1O_2$ generation and DMA oxidation were determined by irradiating the solutions at several intervals followed by measuring the absorbance of DMA after each irradiation interval. Solutions were irradiated in a 1 cm × 1 cm quartz cuvette at 532 nm using a pulsed Nd:YAG laser with a 10 Hz pulsing frequency at 10 mJ/pulse. Absorbance spectra were recorded using a Hitachi U-2800 spectrophotometer.

The extinction coefficient of DMA at 398 nm (ε_{DMA}) was first determined by averaging the absorbance spectrum of four separate 50 μM DMA samples (without addition of any photosensitizer) and dividing by the DMA concentration. To account for any photosensitizer contribution to the absorbance value at 398 nm, the concentration of DMA after every irradiation interval ($[DMA]_t$) was calculated using **equation 4.3** below instead of by directly using the Beer-Lambert law. Here $[DMA]_0$ is the initial DMA concentration (50 μM in our case), and A_0 and A_t are the absorbance value at 398 nm pre-irradiation and after irradiating for a cumulative time t, respectively (e.g. t = 20 s after two irradiation intervals of 10 s each).

$$[\mathrm{DMA}]_t = [\mathrm{DMA}]_0 - \frac{A_0 - A_t}{\varepsilon_{DMA}} \tag{4.3}$$

Values of Φ_Δ for each compound were determined from **equation 4.4** using the slope (S) of a semilogarithmic plot of DMA photooxidation kinetics ($\ln([DMA]_0/[DMA]_t)$ vs t) and the refractive index (n) of each solution. The superscript/subscript "*st*" designates the standard (RB). Here, the slope is equal to the pseudo-first order rate constant of $^1O_2$ quenching by DMA.

$$\Phi_\Delta = \Phi_\Delta^{st} \times \frac{S}{S_{st}} \times \left(\frac{n}{n_{st}}\right)^2 \tag{4.4}$$

4.6.6. Bulk photooxidation of BDT-3 in liposomes

Bulk photooxidation of BDT-3 was carried out in DOPC liposomes in order to detect the possible generation of BDT-3 oxidation products. A solution of 100 nm DOPC liposomes embedded with BDT-3 was irradiated for 48 hours under 520 nm LED lamps (LED-GR, Luzchem, FWHM = 31 nm, irradiance = 2.6 mW cm^{-2} in the peak wavelength range) in a 1 cm × 1 cm glass cuvette. Solutions were prepared in PBS with a final concentration of 1 mM in DOPC and 1 μM in BDT-3. The emission spectrum of the solution was taken at regular time intervals using a Photon Technology International (PTI) Quanta Master fluorimeter. The solution was excited at 488 nm and all slits were set at 2 nm. The emission spectra were automatically corrected for the wavelength-dependent sensitivity of the PMT detector, and further corrected for liposome scattering using the emission spectrum of a DOPC liposome solution not containing any fluorophore.

4.6.7. $^1O_2$ flux measurement

The flux of $^1O_2$ impinging on the lipid membranes was determined using a recently reported method by our research group.[47] H_4BPMHC, an α-tocopherol fluorogenic analogue,[48] is used a $^1O_2$ sensor. H_4BPMHC is non-emissive in its native form but undergoes a large enhancement in its emission intensity upon trapping $^1O_2$ and other reactive oxygen species (see **Figure 4.4a** for H_4BPMHC structure). When $^1O_2$ quenching by H_4BPMHC outcompetes its natural decay in solvent or its quenching by lipids, the rate of H_4BPMHC oxidation, and thus the rate of generation of its oxidized counterpart H_4BPMHC_{ox}, follows zero-order kinetics as seen in **equation 4.5** below,[47] where Φ_Δ and I_a are the singlet oxygen quantum yield and excitation rate of the photosensitizer, respectively. $k_{ox}^{H_4BPMHC}$ is the rate constant of chemical quenching (i.e. oxidation) of $^1O_2$ by H_4BPMHC, and $k_q^{H_4BPMHC}$ is the total quenching rate constant (chemical + physical quenching) of $^1O_2$ by H_4BPMHC.

$$\frac{d[H_4BPMHC_{ox}]}{dt} = \frac{\Phi_\Delta \times I_a \times k_{ox}^{H_4BPMHC}}{k_q^{H_4BPMHC}} \quad (4.5)$$

It follows that if a certain amount of probe (H_4BPMHC_0) present in a certain area (*A*) was fully oxidized in an amount of time (τ), the amount of $^1O_2$ generated in this time τ can be estimated using **equation 4.6**, and thus the flux $^1O_2$ impinging on the membrane could be calculated using **equation 4.7**.

$$H_4BPMHC_0 = \frac{k_{ox}^{H_4BPMHC}}{k_q^{H_4BPMHC}} \times {}^1O_2 \tag{4.6}$$

$$^1O_2\text{Flux} = \frac{^1O_2}{\tau \times A} = \frac{H_4BPMHC_0}{\tau \times A} \times \frac{k_q^{H_4BPMHC}}{k_{ox}^{H_4BPMHC}} \tag{4.7}$$

Equations 4.6 and **4.7** highlight the fact that only a fraction of the generated $^1O_2$ is chemically quenched, and thus sensed, by H_4BPMHC. The percentage of α-tocopherol that is chemically quenched has been previously reported to be between 0.8-7%.[71-74] We used a value of 1% in our calculations to provide an upper bound value of $^1O_2$ flux. The number of H_4BPMHC molecules in an area *A* is calculated by first determining the number of lipids present in the area A (taking a DOPC lipid head size of 0.82 nm^2), taking under consideration the presence of two lipid layers, then multiplying by the H_4BPMHC to lipid ratio (1:100 in our case). The time until full probe consumption, τ, is determined from the intersection of two straight lines tangential to the linear growth in probe intensity and subsequent plateau/decay, as depicted in **Figure 4.4c**.

4.6.8. Supplementary figures

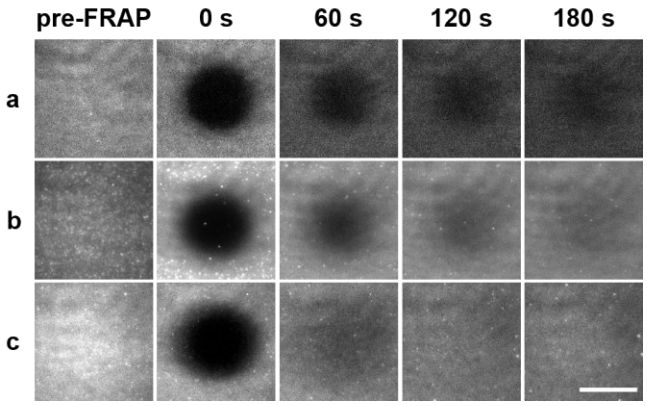

Figure 4.7. Film strips of ADA fluorescence recover after photobleaching. Film strips depicting recovery of BDT-3 (a), IDT-3 (b), and IDT-1 (c) fluorescence signal after photobleaching an area of the SLB, confirming the successful formation of a well connected SLB. Scale bar = 20 μm. ADA:lipid ratio = 1:1000. BDT-3 was imaged with 20 μW of a 488 nm cw laser. IDT-3 was imaged with 20 μW of a 561 nm cw laser. IDT-1 was imaged with 18 μW of a 547 nm cw laser. t = 0 s corresponds to the first frame after photobleaching. "pre-FRAP" frames in (a) and (b) are visualized on a different dynamic range that the rest of the frames in their corresponding film strips due to the strong photobleaching observed in these two samples.

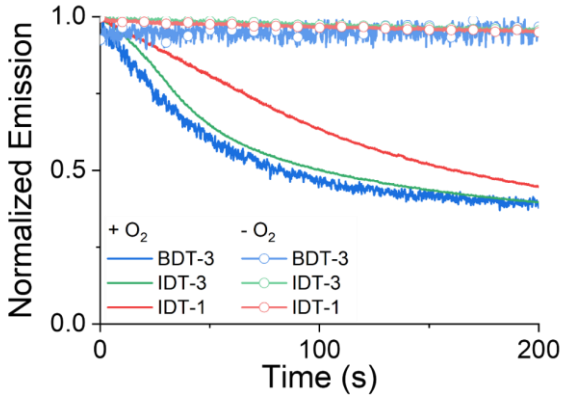

Figure 4.8. Photostability of ADA oligomers in a DOPC supported bilayer (SLB) in the presence and absence of oxygen. Normalized emission intensity-time curves of BDT-3 (blue traces), IDT-3 (green traces), and IDT-1 (red traces) in the presence (solid traces) and absence (traces with symbols) of oxygen. ADA:lipid ratio = 1:1000. BDT-3 was excited with 27 μW of a 488 nm cw laser. IDT-3 was excited with 29 μW of a 561 nm cw laser. IDT-1 was excited with 19 μW of a 647 nm cw laser. Laser powers were measured out of the objective. All three ADA oligomers were imaged using identical excitation rates, accounting for extinction coefficients of ADA oligomers at their corresponding excitation wavelength.[31]

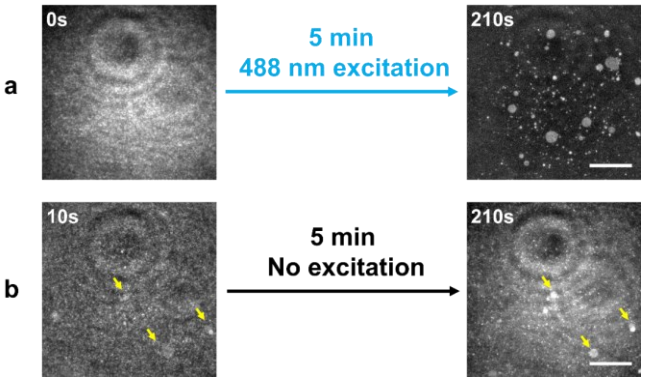

Figure 4.9. Lack of membrane-embedded BDT-3 phase separation following interrupted excitation. (a) Phase separation of BDT-3 under continuous irradiation for 5 min. (b) Irradiation was interrupted upon the first sighting of phase separation. Irradiation was resumed after 5 min. Yellow arrows indicate the phase segregated domains formed before and after interruption of irradiation. Scale bar = 20 µm. BDT-3:lipid ratio = 1:1000. BDT-3 was excited with 100 µW of a cw 488 nm laser.

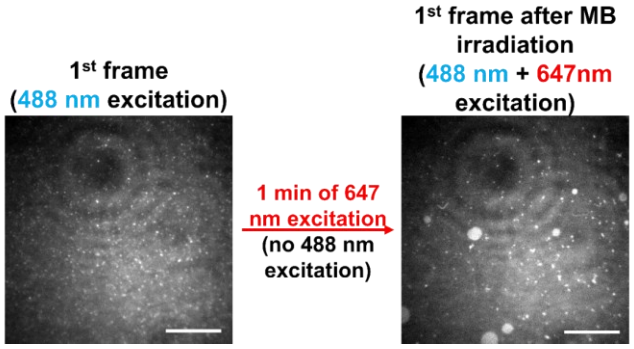

Figure 4.10. Initiation of membrane-embedded BDT-3 phase separation by methylene blue. A snapshot of BDT-3 emission was taken (left image) by exciting with a 488 nm cw laser, followed by interruption of BDT-3 excitation and irradiation of methylene blue (MB) with a 647 nm cw laser for 1 minute. After 1 minute, BDT-3 excitation was resumed, and its emission collected (right image). Scale bar = 20 µm. BDT-3:lipid ratio = 1:1000. [MB] = 1.7 µM. BDT-3 was excited with 100 µW of a 488 nm laser. Methylene blue was excited with 3.6 mW of a 647 nm laser.

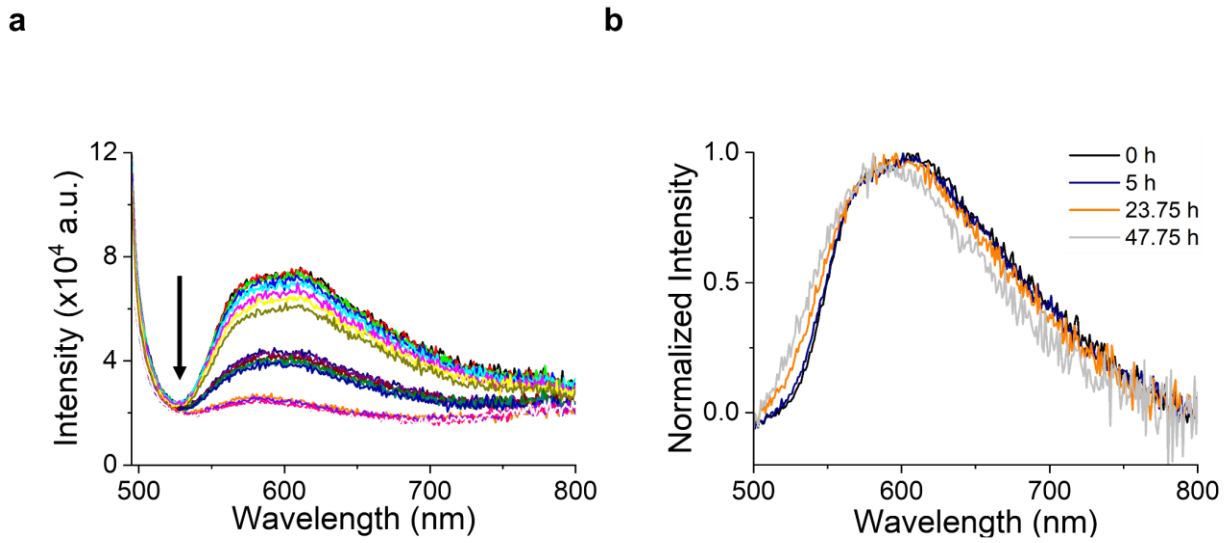

Figure 4.11. Bulk photooxidation of BDT-3 in DOPC liposomes. (a) Raw data depicting decrease in BDT-3 emission intensity over 48 hours of 520 nm LED excitation. (b) Normalized emission spectra corrected for 100 nm DOPC liposome scattering, depicting lack of change in BDT-3 emission properties. BDT-3:DOPC ratio = 1:1000. λ_{ex} = 488 nm. Excitation and emission slits were set at 2 nm.

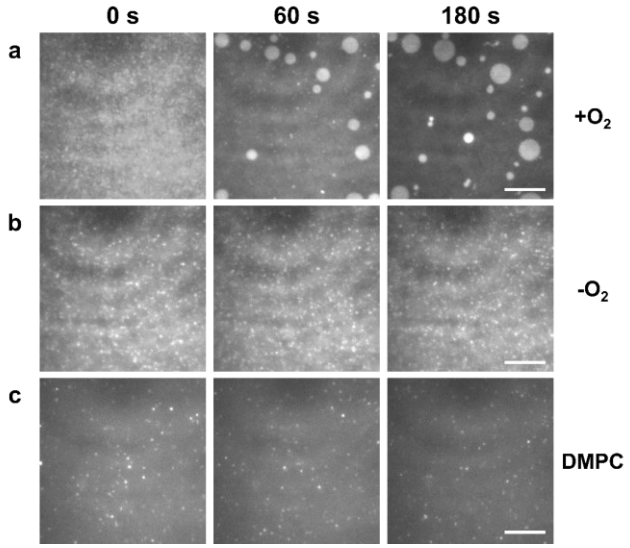

Figure 4.12. Membrane-embedded IDT-3 phase separation under different imaging and SLB conditions. (a) Photoinduced IDT-3 phase separation in air-equilibrated PBS and DOPC SLB. (b) Lack of phase separation in a DOPC SLB and under oxygen-deprived conditions. (c) Lack of phase separation in a DMPC SLB in air-equilibrated PBS. Scale bar = 10 μm. IDT-3:DOPC ratio = 1:1000. IDT-3 was excited with 50 μW (a, b) or 108 μW (c) of a 561 nm cw laser.

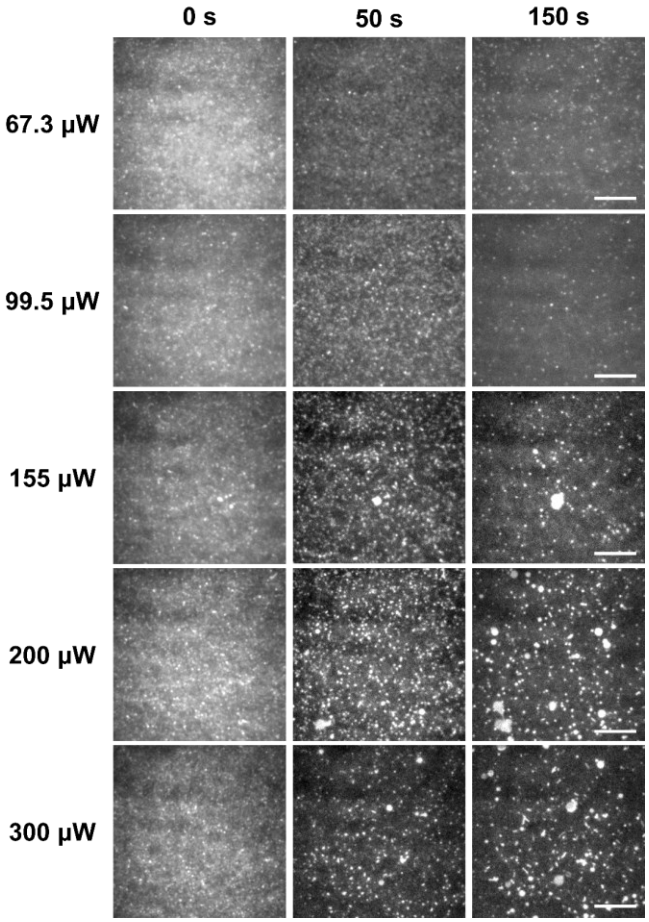

Figure 4.13. Initiation of membrane-embedded IDT-1 phase separation at increasing excitation powers. Scale bar = 10 µm. IDT-1:DOPC ratio = 1:1000. IDT-1 was excited with a 647 nm cw laser using the powers indicated at the left of each row of images.

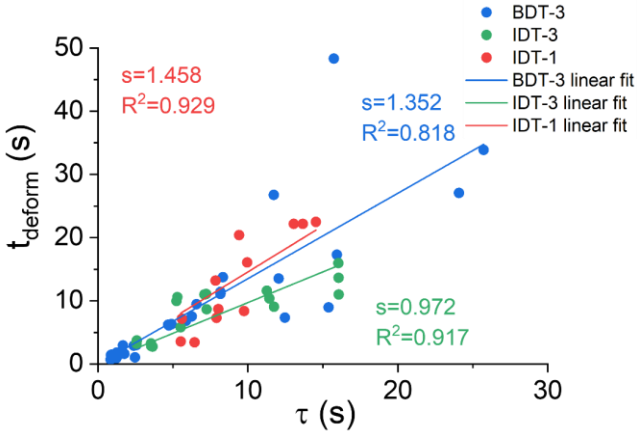

Figure 4.14. Correlation of time till onset of membrane deformation (t_{deform}) and time till end of antioxidant protection (τ). ADA oligomers were irradiated at increasing excitation rates in the presence of $^1O_2$ sensor H_4BPMHC. The time it took to initially observe membrane deformation (i.e. tubulation and domain formation) was correlated with the time it took for all H_4BPMHC

present in the field of view to react with $^1O_2$, and thus the time till end of antioxidant protection. ADA:DOPC ratio = 1:1000. H_4BPMHC:DOPC ratio = 1:100. BDT-3, IDT-3, and IDT-1 were excited with a 488 nm, 561 nm, and 647 nm cw lasers, respectively. H_4BPMHC was excited with a 488 nm laser.

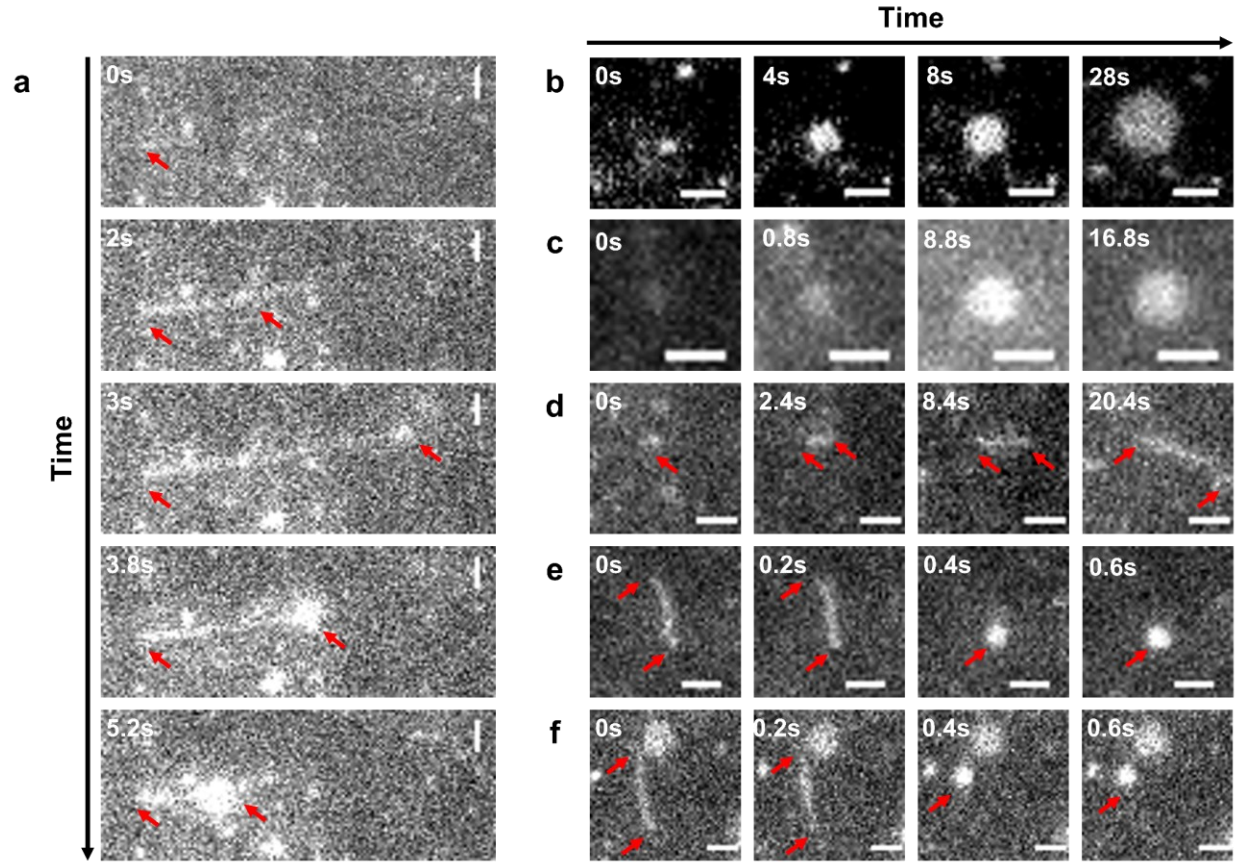

Figure 4.15. Image time series depicting dynamics of membrane deformation induced by BDT-3. (a) Formation and collapse of a nanotube by gradual pulling into SLB. (b-c) Radial growth of a disk. (d) Gradual formation of a long-live nanotube. (e-f) Snap-collapse of short nanotubes. Scale bar = 2 μm. Red arrows highlight features of interest such as nanotube extremities and disks. BDT-3:DOPC ratio = 1:1000. SLB also contained H_4BPMHC in a 1:100 probe:lipid ratio. H_4BPMHC and BDT-3 were excited with 50 μW of a 488 nm cw laser. H_4BPMHC emission was filtered out and only BDT-3 emission was collected.

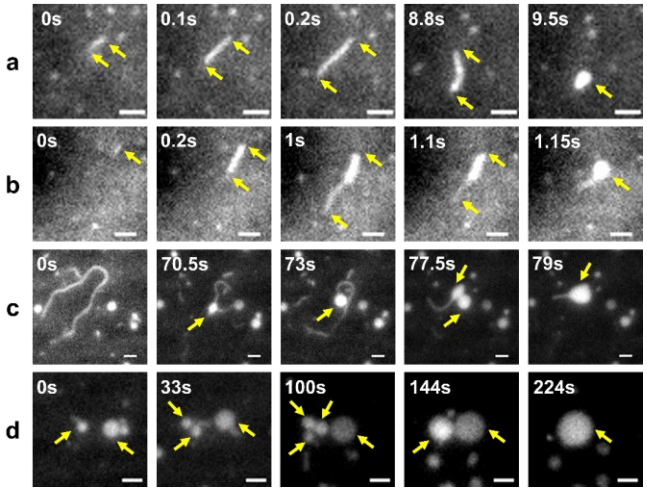

Figure 4.16. Image time series depicting dynamics of membrane deformation induced by IDT-3. (a) Formation and eventual collapse of a long-lived nanotube. (b) Instantaneous formation and snap-collapse of a short-lived nanotube. (c) Collapse of a large, long-lived, nanotube by gradual pulling into a domain in the SLB. (d) Absorption and coalescence of neighboring disks. Scale bar = 2 μm. Yellow arrows highlight features of interest such as nanotube extremities and disks. IDT-3:DOPC ratio = 1:1000. SLB also contained H_4BPMHC in a 1:100 probe:lipid ratio. IDT-3 was excited with 150 μW of a 561 nm cw laser. Any H_4BPMHC emission was filtered out and only IDT-3 emission was collected.

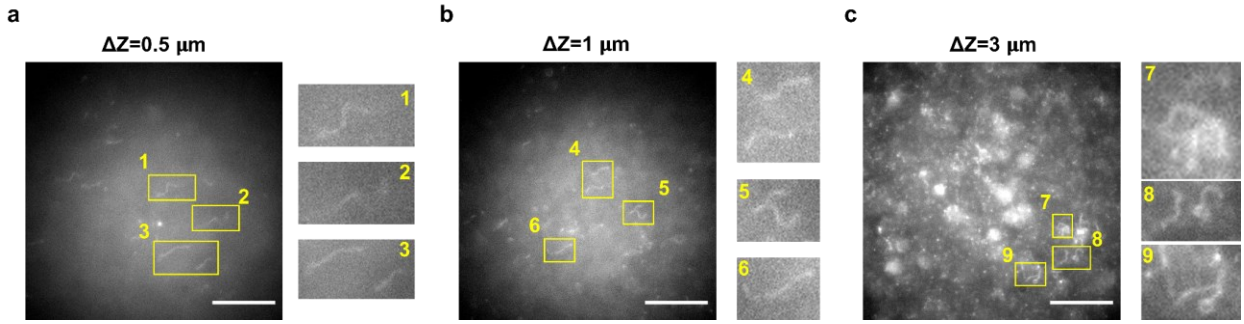

Figure 4.17. Imaging IDT-1 and BDT-3 photosensitized nanotubes above SLB plane. Photosensitized membrane deformation was initiated by irradiating IDT-1 (a,b) or BDT-3 (c) and setting the imaging plane 0.5 μm, 1 μm, or 3 μm above the SLB plane in (a), (b), and (c), respectively. Scale bar = 20 μm. ADA:DOPC ratio = 1:1000. SLB also contained H_4BPMHC in a 1:100 probe:lipid ratio. In (a) and (b), IDT-1 was excited with 1 mW of a 647 nm cw laser; H_4BPMHC emission was filtered out and only IDT-1 emission was collected. In (c) BDT-3 and H_4BPMHC were excited with 1 mW of a 488 nm cw laser; BDT-3 emission was filtered out and H_4BPMHC emission was collected. Incident beam was perpendicular to sample plane.

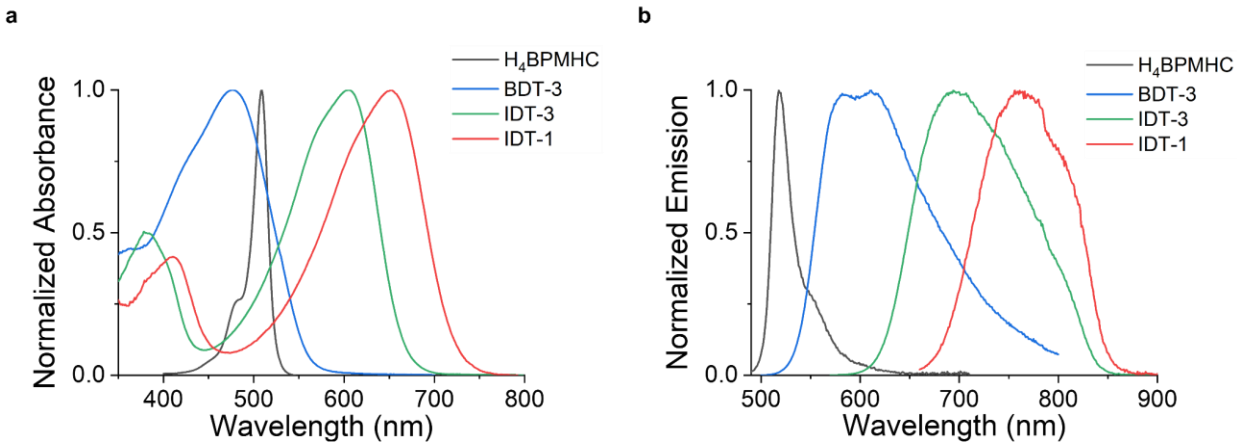

Figure 4.18. Absorbance and emission spectra of the ADA oligomers and H_4BPMHC. ADA spectra were recorded in chloroform solutions. H_4BPMHC spectra were recorded in acetonitrile. H_4BPMHC emission spectrum was recorded following its oxidation by a radical initiator (2,2'-azobis(4-methoxy-2.4-dimethyl valeronitrile) , V-70).

4.7. References

1. McCuskey, S. R.; Chatsirisupachai, J.; Zeglio, E.; Parlak, O.; Panoy, P.; Herland, A.; Bazan, G. C.; Nguyen, T.-Q., Current Progress of Interfacing Organic Semiconducting Materials with Bacteria. *Chem. Rev.* **2022,** *122* (4), 4791-4825.
2. Higgins, S. G.; Lo Fiego, A.; Patrick, I.; Creamer, A.; Stevens, M. M., Organic Bioelectronics: Using Highly Conjugated Polymers to Interface with Biomolecules, Cells, and Tissues in the Human Body. *Adv. Mater. Technol.* **2020,** *5* (11), 2000384.
3. Pitsalidis, C.; Pappa, A.-M.; Boys, A. J.; Fu, Y.; Moysidou, C.-M.; van Niekerk, D.; Saez, J.; Savva, A.; Iandolo, D.; Owens, R. M., Organic Bioelectronics for In Vitro Systems. *Chem. Rev.* **2022,** *122* (4), 4700-4790.
4. Berggren, M.; Głowacki, E. D.; Simon, D. T.; Stavrinidou, E.; Tybrandt, K., In Vivo Organic Bioelectronics for Neuromodulation. *Chem. Rev.* **2022,** *122* (4), 4826-4846.
5. Butina, K.; Löffler, S.; Rhen, M.; Richter-Dahlfors, A., Electrochemical sensing of bacteria via secreted redox active compounds using conducting polymers. *Sensors Actuators B: Chem.* **2019,** *297*, 126703.
6. Parlak, O.; Keene, S. T.; Marais, A.; Curto, V. F.; Salleo, A., Molecularly selective nanoporous membrane-based wearable organic electrochemical device for noninvasive cortisol sensing. *Sci. Adv.* **2018,** *4* (7), eaar2904.
7. Golabi, M.; Padiolleau, L.; Chen, X.; Jafari, M. J.; Sheikhzadeh, E.; Turner, A. P. F.; Jager, E. W. H.; Beni, V., Doping Polypyrrole Films with 4-N-Pentylphenylboronic Acid to Enhance Affinity towards Bacteria and Dopamine. *PLOS ONE* **2016,** *11* (11), e0166548.
8. Lai, B.; Tang, X.; Li, H.; Du, Z.; Liu, X.; Zhang, Q., Power production enhancement with a polyaniline modified anode in microbial fuel cells. *Biosens. Bioelectron.* **2011,** *28* (1), 373-377.
9. Pu, K.-B.; Ma, Q.; Cai, W.-F.; Chen, Q.-Y.; Wang, Y.-H.; Li, F.-J., Polypyrrole modified stainless steel as high performance anode of microbial fuel cell. *Biochem. Eng. J.* **2018,** *132*, 255-261.
10. Bernacka-Wojcik, I.; Huerta, M.; Tybrandt, K.; Karady, M.; Mulla, M. Y.; Poxson, D. J.; Gabrielsson, E. O.; Ljung, K.; Simon, D. T.; Berggren, M.; Stavrinidou, E., Implantable Organic Electronic Ion Pump Enables ABA Hormone Delivery for Control of Stomata in an Intact Tobacco Plant. *Small* **2019,** *15* (43), 1902189.
11. Ghezzi, D.; Antognazza, M. R.; Maccarone, R.; Bellani, S.; Lanzarini, E.; Martino, N.; Mete, M.; Pertile, G.; Bisti, S.; Lanzani, G.; Benfenati, F., A polymer optoelectronic interface restores light sensitivity in blind rat retinas. *Nat. Photon.* **2013,** *7* (5), 400-406.
12. Tortiglione, C.; Antognazza, M. R.; Tino, A.; Bossio, C.; Marchesano, V.; Bauduin, A.; Zangoli, M.; Morata, S. V.; Lanzani, G., Semiconducting polymers are light nanotransducers in eyeless animals. *Sci. Adv.* **2017,** *3* (1), e1601699.
13. Hopkins, J.; Travaglini, L.; Lauto, A.; Cramer, T.; Fraboni, B.; Seidel, J.; Mawad, D., Photoactive Organic Substrates for Cell Stimulation: Progress and Perspectives. *Adv. Mater. Technol.* **2019,** *4* (5), 1800744.
14. Liu, Y.; Feig, V. R.; Bao, Z., Conjugated Polymer for Implantable Electronics toward Clinical Application. *Adv. Healthc. Mater.* **2021,** *10* (17), 2001916.
15. Yan, H.; Catania, C.; Bazan, G. C., Membrane-Intercalating Conjugated Oligoelectrolytes: Impact on Bioelectrochemical Systems. *Adv. Mater.* **2015,** *27* (19), 2958-2973.

16. Zhou, C.; Chia, G. W. N.; Yong, K.-T., Membrane-intercalating conjugated oligoelectrolytes. *Chem. Soc. Rev.* **2022,** *51* (24), 9917-9932.
17. Noriega, R.; Rivnay, J.; Vandewal, K.; Koch, F. P. V.; Stingelin, N.; Smith, P.; Toney, M. F.; Salleo, A., A general relationship between disorder, aggregation and charge transport in conjugated polymers. *Nat. Mater.* **2013,** *12* (11), 1038-1044.
18. Venkateshvaran, D.; Nikolka, M.; Sadhanala, A.; Lemaur, V.; Zelazny, M.; Kepa, M.; Hurhangee, M.; Kronemeijer, A. J.; Pecunia, V.; Nasrallah, I.; Romanov, I.; Broch, K.; McCulloch, I.; Emin, D.; Olivier, Y.; Cornil, J.; Beljonne, D.; Sirringhaus, H., Approaching disorder-free transport in high-mobility conjugated polymers. *Nature* **2014,** *515* (7527), 384-388.
19. Goetz, K. P.; Vermeulen, D.; Payne, M. E.; Kloc, C.; McNeil, L. E.; Jurchescu, O. D., Charge-transfer complexes: new perspectives on an old class of compounds. *J. Mater. Chem. C* **2014,** *2* (17), 3065-3076.
20. Zhang, J.; Xu, W.; Sheng, P.; Zhao, G.; Zhu, D., Organic Donor–Acceptor Complexes as Novel Organic Semiconductors. *Acc. Chem. Res.* **2017,** *50* (7), 1654-1662.
21. Zhang, G.; Zhao, J.; Chow, P. C. Y.; Jiang, K.; Zhang, J.; Zhu, Z.; Zhang, J.; Huang, F.; Yan, H., Nonfullerene Acceptor Molecules for Bulk Heterojunction Organic Solar Cells. *Chem. Rev.* **2018,** *118* (7), 3447-3507.
22. Nguyen, V.-N.; Kumar, A.; Lee, M. H.; Yoon, J., Recent advances in biomedical applications of organic fluorescence materials with reduced singlet–triplet energy gaps. *Coord. Chem. Rev.* **2020,** *425*, 213545.
23. Li, W.; Zhang, J.; Gao, Z.; Qi, J.; Ding, D., Advancing biomedical applications via manipulating intersystem crossing. *Coord. Chem. Rev.* **2022,** *471*, 214754.
24. Di Pietro, R.; Fazzi, D.; Kehoe, T. B.; Sirringhaus, H., Spectroscopic Investigation of Oxygen- and Water-Induced Electron Trapping and Charge Transport Instabilities in n-type Polymer Semiconductors. *J. Am. Chem. Soc.* **2012,** *134* (36), 14877-14889.
25. Quigley, A. F.; Wagner, K.; Kita, M.; Gilmore, K. J.; Higgins, M. J.; Breukers, R. D.; Moulton, S. E.; Clark, G. M.; Penington, A. J.; Wallace, G. G.; Officer, D. L.; Kapsa, R. M. I., In vitro growth and differentiation of primary myoblasts on thiophene based conducting polymers. *Biomater. Sci.* **2013,** *1* (9), 983-995.
26. Picca, R. A.; Manoli, K.; Macchia, E.; Tricase, A.; Di Franco, C.; Scamarcio, G.; Cioffi, N.; Torsi, L., A Study on the Stability of Water-Gated Organic Field-Effect-Transistors Based on a Commercial p-Type Polymer. *Front. Chem.* **2019,** *7*.
27. Zajdel, T. J.; Baruch, M.; Méhes, G.; Stavrinidou, E.; Berggren, M.; Maharbiz, M. M.; Simon, D. T.; Ajo-Franklin, C. M., PEDOT:PSS-based Multilayer Bacterial-Composite Films for Bioelectronics. *Sci. Rep.* **2018,** *8* (1), 15293.
28. Kirchhofer, N. D.; Rengert, Z. D.; Dahlquist, F. W.; Nguyen, T.-Q.; Bazan, G. C., A Ferrocene-Based Conjugated Oligoelectrolyte Catalyzes Bacterial Electrode Respiration. *Chem* **2017,** *2* (2), 240-257.
29. Ji, E.; Corbitt, T. S.; Parthasarathy, A.; Schanze, K. S.; Whitten, D. G., Light and Dark-Activated Biocidal Activity of Conjugated Polyelectrolytes. *ACS Appl. Mater. Interfaces* **2011,** *3* (8), 2820-2829.
30. Zhu, C.; Yang, Q.; Liu, L.; Lv, F.; Li, S.; Yang, G.; Wang, S., Multifunctional Cationic Poly(p-phenylene vinylene) Polyelectrolytes for Selective Recognition, Imaging, and Killing of Bacteria Over Mammalian Cells. *Adv. Mater.* **2011,** *23* (41), 4805-4810.

31. Che, Y.; Zhang, Y.; Yang, Y.; Liu, C.-H.; Izquierdo, R.; Xiao, S. S.; Perepichka, D. F., Understanding the Photovoltaic Behavior of A–D–A Molecular Semiconductors through a Permutation of End Groups. *J. Org. Chem.* **2020,** *85* (1), 52-61.
32. Brian, A. A.; McConnell, H. M., Allogeneic stimulation of cytotoxic T cells by supported planar membranes. *Proc. Natl. Acad. Sci.* **1984,** *81* (19), 6159-6163.
33. Cremer, P. S.; Boxer, S. G., Formation and Spreading of Lipid Bilayers on Planar Glass Supports. *J. Phys. Chem. B* **1999,** *103* (13), 2554-2559.
34. Busmann, H. G.; Staerk, H.; Weller, A., Solvent influence on the magnetic field effect of polymethylene-linked photogenerated radical ion pairs. *J. Chem. Phys.* **1989,** *91* (7), 4098-4105.
35. Schmidt, K.; Brovelli, S.; Coropceanu, V.; Beljonne, D.; Cornil, J.; Bazzini, C.; Caronna, T.; Tubino, R.; Meinardi, F.; Shuai, Z., Intersystem crossing processes in nonplanar aromatic heterocyclic molecules. *J. Phys. Chem. A* **2007,** *111* (42), 10490-10499.
36. Endo, A.; Sato, K.; Yoshimura, K.; Kai, T.; Kawada, A.; Miyazaki, H.; Adachi, C., Efficient up-conversion of triplet excitons into a singlet state and its application for organic light emitting diodes. *Appl. Phys. Lett.* **2011,** *98* (8).
37. Xu, S.; Yuan, Y.; Cai, X.; Zhang, C.-J.; Hu, F.; Liang, J.; Zhang, G.; Zhang, D.; Liu, B., Tuning the singlet-triplet energy gap: a unique approach to efficient photosensitizers with aggregation-induced emission (AIE) characteristics. *Chem. Sci.* **2015,** *6* (10), 5824-5830.
38. Liu, S.; Zhang, H.; Li, Y.; Liu, J.; Du, L.; Chen, M.; Kwok, R. T. K.; Lam, J. W. Y.; Phillips, D. L.; Tang, B. Z., Strategies to Enhance the Photosensitization: Polymerization and the Donor–Acceptor Even–Odd Effect. *Angew. Chem. Int. Ed.* **2018,** *57* (46), 15189-15193.
39. Wilkinson, F.; Helman, W. P.; Ross, A. B., Quantum Yields for the Photosensitized Formation of the Lowest Electronically Excited Singlet State of Molecular Oxygen in Solution. *J. Phys. Chem. Ref. Data* **1993,** *22* (1), 113-262.
40. Hall, R. D.; Chignell, C. F., Steady-State Near-Infrared Detection of Singlet Molecular Oxygen: A Stern-Volmer Quenching Experiment with Sodium Azide. *Photochem. Photobiol.* **1987,** *45* (4), 459-464.
41. Riske, K. A.; Sudbrack, T. P.; Archilha, N. L.; Uchoa, A. F.; Schroder, A. P.; Marques, C. M.; Baptista, M. S.; Itri, R., Giant vesicles under oxidative stress induced by a membrane-anchored photosensitizer. *Biophys. J.* **2009,** *97* (5), 1362-1370.
42. Itri, R.; Junqueira, H. C.; Mertins, O.; Baptista, M. S., Membrane changes under oxidative stress: the impact of oxidized lipids. *Biophys. Rev.* **2014,** *6* (1), 47-61.
43. Baxter, A. M.; Jordan, L. R.; Kullappan, M.; Wittenberg, N. J., Tubulation of Supported Lipid Bilayer Membranes Induced by Photosensitized Lipid Oxidation. *Langmuir* **2021,** *37* (19), 5753-5762.
44. Tsubone, T. M.; Baptista, M. S.; Itri, R., Understanding membrane remodelling initiated by photosensitized lipid oxidation. *Biophys. Chem.* **2019,** *254*, 106263.
45. Mertins, O.; Bacellar, Isabel O. L.; Thalmann, F.; Marques, Carlos M.; Baptista, Maurício S.; Itri, R., Physical Damage on Giant Vesicles Membrane as a Result of Methylene Blue Photoirradiation. *Biophys. J.* **2014,** *106* (1), 162-171.
46. Weber, G.; Charitat, T.; Baptista, M. S.; Uchoa, A. F.; Pavani, C.; Junqueira, H. C.; Guo, Y.; Baulin, V. A.; Itri, R.; Marques, C. M.; Schroder, A. P., Lipid oxidation induces structural changes in biomimetic membranes. *Soft Matter* **2014,** *10* (24), 4241-4247.
47. Sakaya, A.; Bacellar, I. O. L.; Fonseca, J. L.; Durantini, A. M.; McCain, J.; Xu, L.; Vignoni, M.; Thomas, A. H.; Baptista, M. S.; Cosa, G., Singlet Oxygen Flux, Associated Lipid

Photooxidation, and Membrane Expansion Dynamics Visualized on Giant Unilamellar Vesicles. *Langmuir* **2023,** *39* (1), 442-452.
48. Greene, L. E.; Lincoln, R.; Cosa, G., Rate of Lipid Peroxyl Radical Production during Cellular Homeostasis Unraveled via Fluorescence Imaging. *J. Am. Chem. Soc.* **2017,** *139* (44), 15801-15811.
49. He, N.; Zhao, T., Propranolol induces large-scale remodeling of lipid bilayers: tubules, patches, and holes. *RSC Advances* **2023,** *13* (11), 7719-7730.
50. Staykova, M.; Holmes, D. P.; Read, C.; Stone, H. A., Mechanics of surface area regulation in cells examined with confined lipid membranes. *Proc. Natl. Acad. Sci.* **2011,** *108* (22), 9084-9088.
51. Jepson, T. A.; Hall, S. C.; Chung, J. K., Single-molecule phospholipase A2 becomes processive on melittin-induced membrane deformations. *Biophys. J.* **2022,** *121* (8), 1417-1423.
52. Yoon, B. K.; Jackman, J. A.; Kim, M. C.; Cho, N.-J., Spectrum of Membrane Morphological Responses to Antibacterial Fatty Acids and Related Surfactants. *Langmuir* **2015,** *31* (37), 10223-10232.
53. Yoon, B. K.; Park, S.; Ma, G. J.; Kolahdouzan, K.; Zhdanov, V. P.; Jackman, J. A.; Cho, N.-J., Competing Interactions of Fatty Acids and Monoglycerides Trigger Synergistic Phospholipid Membrane Remodeling. *J. Phys. Chem. Lett.* **2020,** *11* (13), 4951-4957.
54. Yoon, B. K.; Jackman, J. A.; Park, S.; Mokrzecka, N.; Cho, N.-J., Characterizing the Membrane-Disruptive Behavior of Dodecylglycerol Using Supported Lipid Bilayers. *Langmuir* **2019,** *35* (9), 3568-3575.
55. Gahan, C. G.; Patel, S. J.; Chen, L. M.; Manson, D. E.; Ehmer, Z. J.; Blackwell, H. E.; Van Lehn, R. C.; Lynn, D. M., Bacterial Quorum Sensing Signals Promote Large-Scale Remodeling of Lipid Membranes. *Langmuir* **2021,** *37* (30), 9120-9136.
56. Arouri, A.; Kiessling, V.; Tamm, L.; Dathe, M.; Blume, A., Morphological Changes Induced by the Action of Antimicrobial Peptides on Supported Lipid Bilayers. *J. Phys. Chem. B* **2011,** *115* (1), 158-167.
57. Rossier, O.; Cuvelier, D.; Borghi, N.; Puech, P. H.; Derényi, I.; Buguin, A.; Nassoy, P.; Brochard-Wyart, F., Giant Vesicles under Flows: Extrusion and Retraction of Tubes. *Langmuir* **2003,** *19* (3), 575-584.
58. Staykova, M.; Arroyo, M.; Rahimi, M.; Stone, H. A., Confined Bilayers Passively Regulate Shape and Stress. *Phys. Rev. Lett.* **2013,** *110* (2), 028101.
59. Thid, D.; Benkoski, J. J.; Svedhem, S.; Kasemo, B.; Gold, J., DHA-Induced Changes of Supported Lipid Membrane Morphology. *Langmuir* **2007,** *23* (11), 5878-5881.
60. Chelladurai, R.; Debnath, K.; Jana, N. R.; Basu, J. K., Spontaneous formation and growth kinetics of lipid nanotubules induced by passive nanoparticles. *Soft Matter* **2022,** *18* (37), 7082-7090.
61. Yu, Y.; Granick, S., Pearling of Lipid Vesicles Induced by Nanoparticles. *J. Am. Chem. Soc.* **2009,** *131* (40), 14158-14159.
62. Lipowsky, R., Spontaneous tubulation of membranes and vesicles reveals membrane tension generated by spontaneous curvature. *Faraday Discuss.* **2013,** *161* (0), 305-331.
63. Paillous, N.; Fery-Forgues, S., Interest of photochemical methods for induction of lipid peroxidation. *Biochimie* **1994,** *76* (5), 355-368.
64. Gardner, H. W.; Plattner, R. D., Linoleate hydroperoxides are cleaved heterolytically into aldehydes by a Lewis acid in aprotic solvent. *Lipids* **1984,** *19* (4), 294-299.

65. Sankhagowit, S.; Wu, S.-H.; Biswas, R.; Riche, C. T.; Povinelli, M. L.; Malmstadt, N., The dynamics of giant unilamellar vesicle oxidation probed by morphological transitions. *Biochim. Biophys. Acta* **2014,** *1838* (10), 2615-2624.
66. Vignoni, M.; Urrutia, M. N.; Junqueira, H. C.; Greer, A.; Reis, A.; Baptista, M. S.; Itri, R.; Thomas, A. H., Photo-Oxidation of Unilamellar Vesicles by a Lipophilic Pterin: Deciphering Biomembrane Photodamage. *Langmuir* **2018,** *34* (50), 15578-15586.
67. Tsubone, T. M.; Junqueira, H. C.; Baptista, M. S.; Itri, R., Contrasting roles of oxidized lipids in modulating membrane microdomains. *Biochim. Biophys. Acta* **2019,** *1861* (3), 660-669.
68. Bacellar, I. O. L.; Oliveira, M. C.; Dantas, L. S.; Costa, E. B.; Junqueira, H. C.; Martins, W. K.; Durantini, A. M.; Cosa, G.; Di Mascio, P.; Wainwright, M.; Miotto, R.; Cordeiro, R. M.; Miyamoto, S.; Baptista, M. S., Photosensitized Membrane Permeabilization Requires Contact-Dependent Reactions between Photosensitizer and Lipids. *J. Am. Chem. Soc.* **2018,** *140* (30), 9606-9615.
69. Jin, R.; Baumgart, T., Asymmetric desorption of lipid oxidation products induces membrane bending. *Soft Matter* **2021,** *17* (32), 7506-7515.
70. Lis, L.; McAlister, D.; Fuller, N.; Rand, R.; Parsegian, V., Interactions between neutral phospholipid bilayer membranes. *Biophys. J.* **1982,** *37* (3), 657-665.
71. Christopher, S.; Ching, T.-Y.; Geller, G. G., Chemistry of Singlet Oxygen—XVIII. Rates of Reaction and Quenching of α-Tocopherol and Singlet Oxygen*. *Photochem. Photobiol.* **1974,** *20* (6), 511-513.
72. Fahrenholtz, S. R.; Doleiden, F. H.; Trozzolo, A. M.; Lamola, A. A., On the quenching of singlet oxygen by α-tocopherol. *Photochem. Photobiol.* **1974,** *20* (6), 505-509.
73. Kaiser, S.; Di Mascio, P.; Murphy, M. E.; Sies, H., Physical and chemical scavenging of singlet molecular oxygen by tocopherols. *Arch. Biochem. Biophys.* **1990,** *277* (1), 101-108.
74. Stevens, B.; Small Jr, R. D.; Perez, S. R., The Photoperoxidation of Unsaturated Organic Molecules-XIII. $O_2{}^1\Delta_g$ Quenching by α-Tocopherol*. *Photochem. Photobiol.* **1974,** *20* (6), 515-517.

Chapter 5

Summary, Discussion, and Outlook

"We are at the very beginning of time for the human race.
It is not unreasonable that we grapple with problems.
But there are tens of thousands of years in the future.
Our responsibility is to do what we can, learn what
we can, improve the solutions, and pass them on."

- Richard Feynman

5.1. Summary and contributions to knowledge

This thesis presents a comprehensive exploration of the application of fluorescence microscopy in the study of charge transfer processes occurring within lipid membranes. Through a series of meticulously designed experiments and analyses, this research provides valuable insights into the fundamental mechanisms and dynamics of redox processes within lipid membranes. The findings reported in this thesis serve as a steppingstone for the advancement of opto-bioelectronic devices, paving the way for the development of innovative technologies that leverage the interplay between light and biomolecular systems. By elucidating the intricate details of charge transfer phenomena in lipid membranes, this work contributes to our understanding of the fundamental principles governing these processes and opens up new avenues for future research in this field.

In **Chapter 2**, we reported a highly sensitive assay to monitor in real-time the flux of $^1O_2$ impinging on lipid membranes. The assay capitalizes on the rapid $^1O_2$ decay associated to quenching by an α-tocopherol analogue, the fluorogenic probe H_4BPMHC, where this intermolecular decay process vastly outcompetes all other $^1O_2$ decay pathways. H_4BPMHC thus intercepts $^1O_2$ following zero-order kinetics, through both physical and chemical processes, where the chemical reaction is accompanied by a >360-fold linear enhancement in H_4BPMHC fluorescence emission intensity. Combined, the intensity increase and its linear temporal behavior yield characteristics that allow for the straightforward, real-time quantification of the flux of $^1O_2$. We demonstrated the sensing properties of H_4BPMHC in both bulk spectroscopic studies in liposome suspensions and at the single vesicle level through the fluorescence microscopy imaging of giant unilamellar vesicles (GUVs). The remarkable sensitivity of H_4BPMHC to $^1O_2$ allowed us to map the spatiotemporal morphological response of GUVs to oxidative chemical insult in the form of lipid *ene* reactions and correlate their deformation dynamics with the source and flux of $^1O_2$. The antioxidant properties of H_4BPMHC render it an internal clock for the onset of lipid peroxidation, which, when correlated with the time of onset of membrane deformation, allows to extract an upper bound limit for the rate of lipid peroxidation. Our results provide a methodology for investigating $^1O_2$-mediated lipid chemical transformations, associated membrane morphological changes, and their collective dynamics. This methodology and its underlying physical principles can be readily adapted and implemented across multiple fields of chemical

biology to explore the dose-dependent response of biological membranes to chemical stressors. This is particularly relevant, we posit, toward developing photodynamic therapy (PDT) dose response curves in the future.

In **Chapter 3**, we introduce a novel approach using TIRF-based electrochemical fluorescence microscopy (ECFM) for the simultaneous optical and electrochemical investigation of redox reactions in electrode-supported lipid bilayers. In this work, α-tocopherol is used as a case study, and its redox conversions upon the application of an electrochemical potential are transduced as changes in the fluorescence intensity of the fluorogenic probe H_4BPMHC. Through a detailed investigation of factors influencing signal sensitivity and optimization of experimental conditions, we achieve the detection of redox reactions and subsequent chemical transitions of H_4BPMHC and its by-products where the equivalent of currents as low as femtoamperes can be readily detected through the removal of electrons from H_4BPMHC. Notably, this level of sensitivity is achieved with significantly lower probe concentrations compared to conventional bulk electrochemical measurements, while maintaining remarkable sensitivity and signal-to-background ratios. Furthermore, our ECFM setup enables the extraction of important thermodynamic and potential-dependent kinetic parameters of the electrochemical and chemical transitions of H_4BPMHC. Overall, this work offers a novel methodology for the spatiotemporal mapping and characterization of heterogeneous electron transfer processes within electrode-supported lipid bilayers.

Equipped with the tools developed in Chapters 2 and 3, namely a way to investigate charge transfer processes in lipid membranes, as well as a means to monitor the impact of optical (light) stimulation on optoelectronic materials within membranes in the context of their potential photoinduced damage, we next moved towards their application in the assembly of bioelectronic interfaces using novel organic semiconducting oligomers as transmembrane wires (π-MWs). The first step of this process is the motivation behind **Chapter 4**, where we assessed the integration, photostability, and phototoxicity of electron acceptor-donor-acceptor (ADA) semiconducting oligomers to be used as building blocks for the assembly of novel π-MWs. Our fluorescence imaging studies of ADA oligomers incorporated within supported lipid bilayers revealed that the photoexcitation of these oligomers resulted in strong, abrupt, and dynamic morphological changes in the lipid membrane in the form of anchored lipid nanotubes that eventually collapsed into flat disks on top of the lipid membrane. A detailed investigation into the chemical mechanism behind

these observed deformations revealed that they result from membrane disruption and area expansion triggered by ADA-photosensitized, $^1O_2$ induced, lipid peroxidation. Notably, studies utilizing the $^1O_2$ flux sensor reported in **Chapter 2** indicated that a minimum threshold flux of $^1O_2$ (rather than a minimal total dose/amount) was required to induce membrane remodelling, below which the membrane was able to accommodate the changes to its chemical composition without any visible deformations. Our studies emphasize the importance of early-stage assessment of the biocompatibility of proposed bioelectronic materials, as the properties responsible for the remarkable charge carrying capabilities of ADA oligomers also underlie their phototoxicity. Most importantly, our work reveals critical aspects into the response of a lipid membrane to chemical stress and provides insights regarding the dynamic mechanisms by which a membrane adapts to changes in its chemical composition.

Overall, this thesis has introduced innovative methodologies that significantly contribute to the understanding of chemically and electrochemically induced redox processes in lipid membranes. Through the application of these methodologies, crucial insights into the response of lipid membranes to photosensitized damage have been gained. The findings presented in this work have the potential to propel the advancement of bioelectronic interfaces and pave the way for further investigations into the dynamic behavior of lipid membranes under chemical insult.

5.2. Discussion and future work

5.2.1. Enhancing $^1O_2$ quenching kinetics toward new sensors

In **Chapter 2**, we demonstrated the use of H_4BPMHC as a sensor that enables the real-time quantification of the flux of $^1O_2$. Central to this activity is the $^1O_2$ quenching kinetics of H_4BPMHC that must outcompete all other $^1O_2$ decay pathways such as deactivation in solvent or quenching by lipids and other biomolecules present in the system to ensure zero-order $^1O_2$ trapping kinetics. To achieve this, the inequality stated in **eq 5.1** must hold, where k_q represents bimolecular quenching rate constants, k_d denotes the rate of $^1O_2$ deactivation in solvent, and *S*, *L*, and *BM* refer to the sensor, lipids, and other biomolecules, respectively.

$$k_q^S[\text{sensor}] \gg k_d + k_q^L[L] + k_q^{BM}[BM] \tag{5.1}$$

We demonstrated the validity of this inequality under our carefully controlled experimental conditions, where the ratio of H_4BPMHC to the monounsaturated lipid DOPC was 1:100. However, H_4BPMHC, at this probe-to-lipid ratio, might fail to outcompete all other $^1O_2$ decay pathways at different experimental conditions, such as when using lipids with higher degrees of unsaturation (presenting with faster $^1O_2$ quenching kinetics compared to monounsaturated lipids), or when conducting *in vivo* measurements, where cell membranes consist of complex mixtures of lipids and other biomolecules (e.g., proteins). In such cases, two approaches could be taken to ensure that the inequality described in **eq 5.1** holds: increasing the sensor concentration or developing sensors with improved $^1O_2$ quenching rate constants. The former approach is less favored, as increasing the sensor concentration in model lipid membranes might disrupt the properties of the membrane, while increasing the sensor concentration for *in vivo* applications might encounter challenges in controlling the uptake of the sensor by the cell membrane and would certainly impact the cell redox homeostasis.

It follows from the above that the development of $^1O_2$ sensors with improved quenching rate constants is therefore highly desirable. As addressed in **Section 1.4.1.3** of **Chapter 1**, physical quenching of $^1O_2$ (the main quenching pathway by α-tocopherol) typically proceeds via the formation of an excited state charge transfer complex (exciplex) between $^1O_2$ and the singlet ground state quencher (chromanol moiety in α-tocopherol), with the latter transferring an electron (either partially or completely) to the $^1O_2$.[1] Consequently, a correlation exists between the energetics of this charge transfer step and the rate of $^1O_2$ physical quenching. As described in **Section 1.1.3.3**, the energy and rate of electron transfer reactions depend on the redox potentials of the electron donor (quencher) and electron acceptor ($^1O_2$). While the latter is fixed, the structure of the quencher can be modified to reduce its redox potential (making it a better reductant) and consequently increase the rate of electron transfer. This correlation between the rate constants of electron transfer and $^1O_2$ quenching has been previously demonstrated to occur for a range of compounds such as amines, benzenes, sulfides, and phenols.[1]

Given that α-tocopherol is one of the most potent naturally occurring lipid soluble antioxidants, the structure of its redox active chromanol moiety, PMHC (**Scheme 5.1**), serves as a great scaffold for designing new $^1O_2$ quenchers. One very promising candidate with improved redox properties is naphthyridinol (**Scheme 5.1**), an antioxidant that is structurally similar to PMHC, with electron donating nitrogen groups that elevate the HOMO energy level and where

electron delocalization stabilizes the SOMO level of the associated radical obtained upon H-atom transfer, thus destabilizing the O-H bond, rendering naphthyridinol a better reducing agent and radical trapping antioxidant. In fact, naphthyridinol-based antioxidants were shown to be over 30-fold more reactive to radicals than α-tocopherol and to have significantly lower redox potentials than PMHC (0.25 V *vs* NHE, compared to 0.98 V for PMHC), reported in a study using fluorogenic probes developed by our research group in high throughput assays of antioxidant potency.[2] We thus predict that naphthyridinol-based $^1O_2$ sensors would present with an improved rate of $^1O_2$ quenching that would enable their use as reporters on $^1O_2$ flux in diverse and complex biological systems.

Scheme 5.1. Structure of the redox active segments of α-tocopherol and naphthyridinol-based antioxidants

PMHC **Naphthyridinol**

5.2.2. Elucidating the relationship between membrane shape, composition, and response to peroxidative damage

In **Chapter 2**, we mapped the morphological response of giant unilamellar vesicles (GUVs) to oxidative damage in the form of $^1O_2$-induced lipid peroxidation. We observed two ways in which the GUVs accommodated the increase in lipid head group area due to peroxidation: (1) expansion of surface area and increase in GUV size, and (2) shedding of membrane material. The prevalence of these mechanisms correlated with the source (hydrophilic or hydrophobic photosensitizers) and flux of $^1O_2$. In **Chapter 4**, we found that the morphological response of solid-supported lipid bilayers (SLBs) to photosensitized lipid damage resulted in nanotube formation and disc assemblies, where membrane deformation required a minimum threshold of $^1O_2$ flux.

Investigating the dependence of the mechanisms by which a lipid membrane adapts to a change in its composition on membrane morphology and dimensionality could provide valuable insights into the response of organisms with varying sizes, shapes, and spatial confinement to oxidative damage. In particular, we propose the need for a study to examine (1) whether the

reported morphological response in GUVs (i.e., membrane expansion and deformation or membrane shedding) also require a minimum flux of $^1O_2$, (2) whether these two distinct morphological responses observed in GUVs each require a separate $^1O_2$ flux threshold to occur, and (3) whether this threshold $^1O_2$ flux matches or correlates with the one reported in **Chapter 4** for identical membrane compositions.

In parallel, we propose a separate study to examine the influence of membrane composition on its morphological response to peroxidative damage. This proposal stems from the findings of several studies, which indicate that the morphology and prevalence of membrane deformations upon the addition of external stressors such as peptides, proteins, and surfactants, are dependent on the lipid composition of the membrane.[3-5] Notably, these studies reveal that the addition of external chemical stressors elicits varying extent and forms (tubes, spheres, patches, etc.) of membrane protrusions depending on the specific lipid head group, with negative curvature phosphatidylethanolamine (PE), positive curvature phosphatidylglycerol (PG), and neutral phosphatidylcholine (PC) each resulting in different responses. However, morphological responses are not solely determined by the lipid head group, as they also exhibit dependence on the nature of the applied external chemical stressors (e.g., peptide, protein, or sphingolipid). Furthermore, the response of a lipid bilayer to asymmetric stress resulting from preferential addition of external stressors to the outer leaflet may differ from the response observed during symmetric peroxidation of both leaflets. Thus, a comprehensive investigation is necessary to elucidate how the lipid composition of a membrane regulates its morphological response to $^1O_2$-mediated lipid peroxidation. This study should encompass not only the properties of the lipid head group but also delve into the impact of lipid unsaturation levels (and consequently, the number of lipid peroxidation sites) on the dynamics of membrane deformation. These studies should be conducted using both two-dimensional SLBs and three-dimensional GUVs to assess the influence of spatial confinement on the observed dependence on membrane chemical composition.

5.2.3. Exerting spatial control over chemical reactions in lipid membranes

The methodologies and findings presented in this thesis offer the potential for precise spatial control of chemical reactions within lipid membranes. For instance, a recent study by Jepson et al. reveals the chemical mechanism underlying the synergistic effect of melittin and phospholipase A_2 (PLA_2).[6] The study demonstrates that melittin induces the remodeling of the

lipid membrane, leading to the formation of elongated nanotubes that eventually collapse into flat disks on top of the membrane, akin to our findings in **Chapter 4**. PLA_2 was then shown to preferentially reside and process inside these newly formed disks, resulting in a 25-fold increase in PLA2 activity within the membrane deformities compared to the surrounding areas. Separately, the activity of PLA_2 was previously shown to be higher in peroxidised membranes compared to non-oxidized membranes, however the chemical mechanism behind this increased activity remains unknown.[7, 8] We thus propose a study that addresses and expands upon these aforementioned observations. The first aim of this study would be to investigate if the enhanced activity of PLA_2 in peroxidised membranes results from prolonged dwelling in membrane deformities generated by photosensitized membrane damage, such as those reported in **Chapter 4**. The subsequent step involves examining whether these membrane deformities act as a scaffold for enhancing the activity of other non-enzymatic small molecule drugs. Building upon the findings of this second step, one could envision the development of an enhanced photodynamic therapy (PDT) treatment where cell death is cause by both photosensitized membrane damage and pore formation in parallel to selectively increasing the activity of biocidal agents.

The methodologies described in this thesis also offer a compelling opportunity for achieving spatially and temporally controlled reagent generation. This approach exploits the interface between insulating and conducting surfaces within the ECFM (Electrochemical-Fluorescence Microscopy) chamber reported in **Chapter 3**. One can envision the possibility of an on-demand generation of reactants of interest on the conductive surface that would eventually diffuse and react on the insulating side. Such a setup is particularly relevant in situations where a required reactant is a short lived and unstable species, or when an automated timely and constant supply of a reactant is required.

5.2.4. ECFM of single cells and vesicles

In **Chapter 3**, we report an ECFM setup that enables to monitor redox conversions in supported lipid bilayers with currents equivalent to pico- and femtoampere and with a remarkable signal-to-background ratio. Building upon this achievement, we propose expanding the application of our setup to enable the imaging of redox conversions at the single particle level, such as liposomes and GUVs, and potentially even at the single molecule level by incorporating a single probe per liposome. As described in **Section 1.3.2.2** of **Chapter 1**, previous studies, including

ones conducted by our research group, have reported the use of spectroelectrochemical fluorescence microscopy for the imaging of redox conversions at the single molecule or single particle level.[9-12] However, there has been limited research focusing on fluorescence mapping or redox conversions in lipid membranes, either in bulk or at the single molecule/particle level. Conducting such studies would provide valuable insights into the heterogeneities in thermodynamics and kinetics of redox processes without compromising the required membrane environment. Our reported ECFM setup could also be further used to map selectively induced redox conversion in individual prokaryotic or eukaryotic cells.

5.3. Publications

Articles 1-5 have been published. Articles 6-9 are in preparation. The symbol ‡ denotes joint first authorship.

1. Gidi, Y.; Robert, A.; Tordo, A.; Lovell, T. C.; Ramos-Sanchez, J.; Sakaya, A.; Götte, M.; Cosa, G.*; Binding and Sliding Dynamics of the Hepatitis C Virus Polymerase: Hunting the 3' Terminus.*ACS Infect. Dis*. **2023**. *In press*.
2. Sosa, M.J.‡; Fonseca, J.L.‡; Sakaya, A.; Urrutia, M.N.; Petroselli, G.; Erra-Balsells, R.; Quindt, M.I.; Bonesi, S.M.; Cosa, G.; Vignoni, M.; Thomas, A.H.*; Alkylation converts riboflavin into an efficient photosensitizer of phospholipid membranes. *Biochim. Biophys. Acta Biomembr*. **2023**, *1865* (5), 184155
3. Sakaya, A.‡; Bacellar, I. O. L.‡; Fonseca, J. L.; Durantini, A. M.; McCain, J.; Xu, L.; Vignoni, M.; Thomas, A. H.; Baptista, M. S.; Cosa, G.*; Singlet oxygen flux, associated lipid phooxidation, and membrane expansion dynamics visualized on giant unilamellar vesicles. *Langmuir* **2023**, *39* (1), 442-452
4. Sakaya, A.; Durantini, A. M.; Gidi, Y.; Šverko, T.; Wieczny, V.; McCain, J.; Cosa, G.*; Fluorescence Amplified Detection of Redox Turnovers in Supported Lipid Bilayers Illuminates Redox Processes of α-Tocopherol. *ACS Appl. Mater. Interfaces* **2022,** *14* (11), 13872-13882.
5. Lincoln, R.‡; Zhang, W.‡; Lovell, T. C.; Jodko-Piórecka, K.; Devlaminck, P.A.; Sakaya, A.; Van Kessel, A.; Cosa, G.*; Chemically Tuned, Reversible Fluorogenic Electrophile for Live Cell Nanoscopy. *ACS Sensors*. **2022**, *7* (1), 166-174.

6. Sakaya, A.; Che, Y.; Perepichka, D. F.; Cosa, G.*; $^1O_2$-mediated remodeling of supported lipid membranes. *In preparation*.
7. Topić, F.; Sakaya, A.; Hamroff, S.; Cosa, G.; Friščić, T.*; Assembly of new crystalline solids from unsubstituted polycyclic aromatics through α---π recognition with progesterone steroid. *In preparation*.
8. Vignoni, M.; Fonseca, J. L.; Sosa, M. J.; Sakaya, A.; Junqueira, H. C.; Itri, R.; Cosa, G.; Baptista, M. S.; Thomas, A. H.*; Photosensitized oxidation of lipid membranes: dependence of the efficiency and structural damage of the lipid composition. *In preparation*.
9. Gidi, Y.‡; Ramos-Sanchez, J.‡; Payne, L.; Sakaya, A.; Lovell, T. C.; Cosa, G.*; Experimentally Calibrated In-silico Prediction of PeT-based Triplet Quenchers for Cyanine's Enhanced Photocontrol. *In preparation*.

5.4. References

1. Schweitzer, C.; Schmidt, R., Physical Mechanisms of Generation and Deactivation of Singlet Oxygen. *Chem. Rev.* **2003,** *103* (5), 1685-1758.
2. Li, B.; Harjani, J. R.; Cormier, N. S.; Madarati, H.; Atkinson, J.; Cosa, G.; Pratt, D. A., Besting Vitamin E: Sidechain Substitution is Key to the Reactivity of Naphthyridinol Antioxidants in Lipid Bilayers. *J. Am. Chem. Soc.* **2013,** *135* (4), 1394-1405.
3. Stachowiak, J. C.; Hayden, C. C.; Sasaki, D. Y., Steric confinement of proteins on lipid membranes can drive curvature and tubulation. *Proc. Natl. Acad. Sci.* **2010,** *107* (17), 7781-7786.
4. Arouri, A.; Kiessling, V.; Tamm, L.; Dathe, M.; Blume, A., Morphological Changes Induced by the Action of Antimicrobial Peptides on Supported Lipid Bilayers. *J. Phys. Chem. B* **2011,** *115* (1), 158-167.
5. Inaba, T.; Murate, M.; Tomishige, N.; Lee, Y.-F.; Hullin-Matsuda, F.; Pollet, B.; Humbert, N.; Mély, Y.; Sako, Y.; Greimel, P.; Kobayashi, T., Formation of tubules and helical ribbons by ceramide phosphoethanolamine-containing membranes. *Sci. Rep.* **2019,** *9* (1), 5812.
6. Jepson, T. A.; Hall, S. C.; Chung, J. K., Single-molecule phospholipase A2 becomes processive on melittin-induced membrane deformations. *Biophys. J.* **2022,** *121* (8), 1417-1423.
7. Salgo, M. G.; Corongiu, F. P.; Sevanian, A., Enhanced Interfacial Catalysis and Hydrolytic Specificity of Phospholipase A2 toward Peroxidized Phosphatidylcholine Vesicles. *Arch. Biochem. Biophys.* **1993,** *304* (1), 123-132.
8. Litvinko, N. M.; Skorostetskaya, L. A.; Gerlovsky, D. O., The interaction of phospholipase A2 with oxidized phospholipids at the lipid-water surface with different structural organization. *Chem. Phys. Lipids* **2018,** *211*, 44-51.
9. Jeuken, L.; Orrit, M.; Canters, G., Single-molecule fluorescence in redox chemistry. *Curr. Opin. Electrochem.* **2023,** *37*, 101196.
10. Palacios, R. E.; Fan, F.-R. F.; Bard, A. J.; Barbara, P. F., Single-Molecule Spectroelectrochemistry (SMS-EC). *J. Am. Chem. Soc.* **2006,** *128* (28), 9028-9029.
11. Godin, R.; Cosa, G., Counting Single Redox Turnovers: Fluorogenic Antioxidant Conversion and Mass Transport Visualization via Single Molecule Spectroelectrochemistry. *J. Phys. Chem. C* **2016,** *120* (28), 15349-15353.
12. Godin, R.; Palacios, R. E.; Cosa, G., Heterogeneous Charge Mobility in Individual Conjugated Polyelectrolyte Nanoparticles Revealed by Two-Color Single Particle Spectroelectrochemistry Studies. *J. Phys. Chem. C* **2015,** *119* (23), 12875-12886.

"We live on an island surrounded by a sea of ignorance.
As our island of knowledge grows, so does the shore of our ignorance."

- John Archibald Wheeler